On-joint Mechanics of the Lumbar Facet Capsular Ligament

A DISSERTATION SUBMITTED TO THE FACULTY OF
UNIVERSITY OF MINNESOTA
BY

Elizabeth Gacek

IN PARTIAL FULFILLMENT OF THE REQUIREMENTS
FOR THE DEGREE OF
DOCTOR OF PHILOSOPHY

Advisor: Dr. Victor H. Barocas

JUNE 2023

Acknowledgements

I have greatly enjoyed my time as a graduate student and this is due, in large part, to my advisor: Victor Barocas. I'm deeply grateful for his unwavering encouragement, mentorship, and patience (particularly with respect to music and musical references). I've grown tremendously both as a scientist and as a person with him as my mentor. Thank you.

It takes a village to finish a thesis. Thank you to all the past and present members of the Barocas Lab. Your input, both academically and personally, has been instrumental in shaping this work. Thank you to Vahhab, Rohit, Chris, Emily, Hernan, Tiffany, David, Shion, Jill, Marisa, Carly, Shannon, and Hadi. A special thanks to Shannen Kizilski, Lauren Bersi-Larson, and Ryan Mahutga for daily coffee and crossword breaks. I would also like to give a special thanks to Elizabeth Shih and Taylor Rothermel for the countless hours spent together in and out of the lab.

I wish to extend my thanks to the members of my thesis committee, Dr. Patrick Alford, Dr. Henryk Stolarski, and Dr. Kyoko Yoshida for their careful review and valuable feedback on my dissertation. I would especially like to thank my committee chair, Dr. Arin Ellingson, for his invaluable knowledge on spine anatomy and biomechanics.

I am especially grateful to my parents, Maria and Andrzej, my siblings, Matt, Monica, Tom, Mike, Jacob, Andrew, and Maryia, my partner, Ivan, and my best friends, Jess and Rebecca, for all their love and encouragement. Ivan, without you, the completion of my thesis would not have been possible at the time that it was. My family are the epitome of love, courage, hard work, and dedication. Thank you for your unwavering support that has carried me through hard times.

Last, but not least, I would like to acknowledge the funding support provided by the National Institutes of Health via the T32 Musculoskeletal Training Award. I would like to thank the staff and donors of the University of Minnesota Anatomy Bequest Program and the Minnesota Supercomputing Institute for providing the resources needed for this work.

Abstract

Chronic pain presents a substantial socioeconomic burden and public health challenge, with low back pain (LBP) being the primary reason for activity restriction in individuals under 45 years of age in the United States. Between 70 to 85% of the entire adult population in the US will experience LBP, often idiopathic, at some point in their lives. While numerous factors can contribute to LBP, the facet joint and the surrounding facet capsular ligament (FCL) are recognized as potential sources. Given the FCL's possible role in LBP and its innervation with nociceptive (pain) and proprioceptive (position) nerve endings, there is considerable interest in its mechanical behavior. Unfortunately, the unloaded *in situ* configuration and the internal loading state of the FCL is often unknown, presenting challenges when simulating realistic mechanical response. The goal of this dissertation was to determine the on-joint *in vivo* behavior of the ligament. Here we show how the variation in collagen and elastin fibers within the microstructure affects bending mechanics, and why pressurization of the inner joint space and ligament-bone attachment is mechanically important. We found that collagen content, distribution, and crimp length are vital to the ligament's through-thickness mechanics. Furthermore, we found that the lumbar facet capsular ligament is under constant tensile strain *in vivo* due to its attachment to the bone and inner joint pressure. Both have large effects on overall on-joint ligament stresses and strains. Our novel enhanced multiscale finite element model of on-joint mechanics of the lumbar facet capsular ligament demonstrates the complex behavior of the ligament and how it remains in tension even when it is unstretched or compressed relative to the neutral joint position. Multiscale model facilitates further insights on *in vivo* ligament mechanics and influence therapeutic approaches to low back pain.

Table of Contents

List of tables

List of figures

List of abbreviations

Abbreviation	Meaning
LBP	low back pain
FCL	lumbar facet capsular ligament
G&R	growth and remodeling
ECM	extracellular matrix
ROI	region of interest
CI	confidence interval
S	superior
I	inferior
M	medial
L	lateral
CFD	computational fluid dynamics
FSI	fluid-structure interactions
FEA	Finite element analysis
FEM	Finite element method
MAP	mean arterial pressure
NC	normotensive chronic
HA	hypertensive acute
HC	hypertensive chronic
FVF	fiber volume fraction

1 Introduction

1.1 Lumbar Facet Capsular Ligament's role in low back pain

Low back pain (LBP) reduces quality of life and imposes a steep financial burden on patients, particularly elderly and low-income persons [1]. Between 70 and 85% of Americans will experience LBP at some point [1], with nearly 90% of patients being diagnosed with non-specific lower back pain. Weight and age are two notable factors contributing to spinal degeneration, making it a critical concern in light of our aging society and increasing obesity rate. LBP research has focused primarily on the intervertebral disc[2], [3], but the lumbar facet capsular ligament, which degrades concurrently with the disc, has been increasingly suggested as a source of LBP [4], [5]. Due to the nature of facet capsular ligament degeneration, our current understanding of how the ligament contributes to LBP is limited, and medical intervention is confined to superficially treating FCL joint pain, which may result in a poor outcome with reoccurring pain.

1.2 Lumbar Facet Capsular Ligament Anatomy, Structure, and Function

The facet capsular ligament (FCL)[*] encases the facet joint, which spans between the superior and inferior articular processes of each vertebra, and encapsulates the synovial fluid lubricating the joint [4], [6], [7]. The geometry of the facet joints varies across the regions of the spine; the cervical and thoracic facets are flatter and allow for a greater range of motion, while the facet joints in the lumbar regions are curvier and more vertically oriented [6]. This orientation limits the range of motion in the lumbar region but better protects the intervertebral disc and spinal cord from motions that could cause injury or paralysis. The FCL is a strong, flexible, highly innervated ligament that is composed of two primary regions: (1) a highly aligned collagen fiber portion on the exterior (posterior) side and (2) an elastin-rich portion on the interior (anterior) side. It plays both a structural and mechanosensory role, supporting spinal motions and sending proprioceptive (position)

---

[*] In this document, "facet capsular ligament" and "FCL" always refer to those in the lumbar spine

and nociceptive (pain) signals to the brain [4]. These characteristics make the FCL a primary target for LBP research. Although research has shown that the FCL degrades with the disc, there is little information on how FCL degradation changes structural and mechanical properties, what drives FCL degradation, and how degradative changes alter spinal kinematics.

The synovium is a very thin membrane that secretes and maintains the synovial fluid in the joint space between adjacent facets [6]. It has been estimated that the joint space has the potential capacity of 1-2 mL[8], and the synovial fluid helps maintain and lubricate the articular cartilage of the facet joints. The synovial fluid serves as the interface between the avascular articular cartilage and the blood vessels within the surrounding tissue. It also acts as a joint stabilizer by providing an adhesive seal in the joint space due to its viscous properties [4]–[6]. Very little is known about the mechanics of the synovial fluid and how the inner capsular pressure affects the loading mechanics on the facet capsular ligament. Defining these underlying mechanics of the synovial fluid would further our understanding of the ligament-fluid interactions.

Both the capsular ligament and the synovium are highly innervated with both proprioceptive and nociceptive nerve endings [6], [9]. The FCL is innervated by the medial branch of the primary dorsal rami at both the current vertebral level as well as from the level above [8]. These nerve endings are believed to be controlled by stretch-activated ion channels, and large deformations could cause the nerve to send a pain signal to the brain. The central nervous system will activate the surrounding muscles if the duration or magnitude of the pain response is abnormal. In this way, the nerves provide feedback and correct the loading on the joint for less pain [6].

The capsular ligament covers the synovium and fully encapsulates adjacent facet joint pairs. As noted above, the ligament is composed of two primary regions: the elastin-rich region and the collagen-rich region [4]. The elastin-rich portion contains primarily isotropic elastin fibers [10]. The collagen-rich portion of the ligament is characterized by highly aligned Type I collagen fibers that are predominately oriented in the medial-lateral direction, or the bone-to-bone direction. Additionally, this region contains off-axis fibers that contribute to the shear behavior, as reported by Claeson *et al.* [10]. These collagen fibers are believed to be crimped when unloaded, and the crimping factor does not vary greatly along the length of the ligament [4]. It is also believed that the collagen fiber crimps allow the joint capsule to undergo large strains before the fibers lock out (uncrimp) and reach their mechanical loading limit [4]. Little is known, however, about how these crimped collagen fibers contribute to the modulus of the collagen-rich region and whether the modulus varies between the collagen-rich region and the elastin-rich region. It is theorized that these fibers also play a large role in the range of motion allowed per vertebral pair [6], [8]. Little *et al.* [4] have demonstrated that as the crimped fibers are being straightened out, the modulus of the tissue is similar to the elastin region. At low strains, the elastin dominates the contribution to the mechanical support of the tissue. Once the fibers are uncrimped, however, they have a higher load-bearing capacity and greatly exceed the mechanical stiffness of the elastin region and, therefore, dominate the observed mechanical behavior.

1.3 Prior Mechanical Characterization of the Lumbar Facet Capsular Ligament and Their Limitations

Excised, off-bone lumbar facet capsular ligaments have been previously well characterized with a series of planar mechanical tests, including uniaxial [4], biaxial [10], or shear [11] testing. These studied observed key characteristics, such as fiber alignment and tissue stiffness, and defined the structural-mechanical relationship of the ligament, such as its on- and off-axis mechanical behavior. The mechanical response of an excised, off-bone facet capsular ligament (1) undergoes a long toe region within which the elastin component may dominate the tissue's response while the collagen fibers remain crimped and unloaded, and (2) is nonlinear when stretched parallel to the primary collagen fiber alignment [4], [10], [12]. In contrast, the ligament is more linear and more compliant in the transverse direction to primary fiber alignment, although off-angle fibers contributing to the tissue's mechanics have been observed in shear tests [11]. The facet capsular ligament is typically excised and flattened prior to traditional planar mechanical testing, and it is not clear how the mechanics of the unloaded free ligament relate back to the in vivo, on-bone state. Consequently, it is difficult to determine the significance of the strain fields across the facet capsular ligament during physiologic motion [9] and to specify correctly the undeformed, unloaded ligament state in whole-motion-segment finite-element models [13].

1.4 Multiscale Models of the Lumbar Facet Capsular Ligament

Finite element modeling is a perfect tool for modeling *in vivo* loading scenarios that are otherwise not feasible for benchtop testing. Prior work has been done on simulating both macroscale and microscale deformations on the lumbar spine and its constituents. Ellingson *et al.* modeled the full unit of lumbar spine, including connective soft tissues and the intervertebral disc [14]. The facet capsular ligaments within this model are treated as wire elements, with realistic assigned ligament material properties. Cleason *et al.* created a multiscale spine-ligament model by applying spine kinematics to a realistic fact capsular ligament model obtained from μ-CT [15]. Zarei *et al.* expanded on the work of both Ellingson *et al.* and Cleason *et al* by applying the resultant kinematics of a full range of realistic spine motions on the facet capsular ligament model, determining the effect of macroscale spinal kinematics on the microstructural collagen and elastin fibers as well as the embedded nerve endings [16], [17]. Although the models of Ellingson *et al.*, Cleason *et al.*, and Zarei *et al.* provided valuable information on spine-ligament interaction and macroscale to microscale coupling, the model of the facet capsular ligament is limited to mechanical behavior observed during planar mechanical testing and the true behavior of the ligament *in-vivo* is unclear.

1.5 Motivations and Open Questions

In recent years, there has been a collective effort to define the mechanics of the facet capsular ligament and bridge the gap between macroscale spinal motions and microscale fiber mechanics. Despite these advances, however, our understanding of the true on-joint behavior of the ligament is limited to extending planar ligament mechanics onto *in vitro* multiscale computation models of the lumbar spine. Very little is still known about the on-joint *in vivo* behavior of the ligament, how the variation in collagen and elastin fibers within the microstructure affect bending mechanics, and whether pressurization of the inner joint space is mechanically important.

The objective of my thesis was, firstly, to define key experimental areas that have been previously overlooked when mechanically characterizing the ligament, secondly, to validate a multiscale facet capsular ligament computation model using the observed on-joint strain field obtained during an on-joint inflation experiment, and, thirdly, to capture ligament constriction when releasing the ligament's residual stress. Having accomplished these objectives, this work was further extended to consider the role that growth and remodeling of collagen and elastin fibers had on the observed structural and mechanical state of soft tissues.

1.6 Summary of Accomplishments

Determining the on-joint mechanical state of the lumbar facet capsular ligament, both during healthy adulthood and its potential progression throughout growth, has resulted in four studies which are organized as chapters in my thesis.

Through-thickness Regional Variation in the Mechanical Characterization of the Lumbar Facet Capsular Ligament (Chapter 2) [12]

The mechanics of the lumbar facet capsular ligament, and its ability to shield the ligament from harmful spinal motions, depends largely on the contribution of the microstructural collagen and elastin fibers. However, previous studies conducted on the facet capsular ligament failed to elucidate the specific role of the collagen fibers compared to the more compliant elastin fibers. The first chapter of my thesis describes a stretch-and-bend technique that was developed to study the tension-compression asymmetry of the FCL due to varying collagen and elastin fiber density throughout the thickness of the tissue. This study determined that the ligament was stiffest when 3 conditions were met: the collagen fibers were (1) aligned in the direction of loading and (2) were in tension, and (3) the ligament was stretch ~16% from the off-bone, undeformed state. Therefore, collagen composition and distribution, as well as crimp length, are important factors when considering how planar facet capsular ligament mechanics may be related back to the on-joint ligament.

In Situ Lumbar Facet Capsular Strains due to Joint Pressurization and Residual Strain (Chapter 3) [18]

Having determined that the mechanics of the collagen heavily depend on crimp length and loading direction, the objective of this study was to determine how excising the ligament for planar mechanical tests changed the undeformed state of the ligament relative to its *in vivo* state. To measure this, a series of experiments were conducted to determine ligament deformation due to both residual strain and joint pressurization strain. Briefly, to measure strains due to pressurization of the encapsulated synovial fluid, 3D strain tracking was utilized to track the posterior portion of the ligament as the joint space was inflated with an injected saline solution, a substitute for the synovial fluid. Having restored the ligament back to the original, undeformed on-joint state, the same region of interested on the posterior portion was tracked as the ligament was cut off the bone. Based on these measurements, and the results of the previous experiment described in Chapter 2, we conclude that the normal in vivo state of the facet capsular ligament is in tension, and that the collagen fibers within the ligament are likely uncrimped even when the spine is not loaded.

Exploring On-Joint Mechanics of the Lumbar Facet Capsular Ligament: Accounting for Residual Strain, Joint Pressurization, and Microstructural Heterogeneity (Chapter 4)

Chapter 3 concluded with the idea that collagen fibers within a pressurized capsular ligament are in tension before motion and any observed on-joint strain underestimates the total applied strain to the fibers in that it doesn’t account for pressurization strain or residual strain. All previous planar mechanical tests conducted on the facet capsular ligament observed large toe regions where the collagen fibers were uncrimping. However, we have also noted a potential unloaded state of the ligament *in vivo* in which the collagen fibers are not uncrimped fully. This implies that the results from planar mechanical tests are overestimating the extent of stretch a ligament can endure before the collagen lock-out state is achieved. Additionally, we explored how the organization and distribution of the collagen and elastin fibers through the thickness of the ligament, the focus of chapter 1, contribute to on-joint ligament strains.

Hybrid Discrete-Continuum Multiscale Model of Tissue Growth and Remodeling (Chapter 5) [19]

Tissue growth and remodeling (G&R) is central to understanding both the development of a structure into a healthy tissue and its progression during a diseased state. In this chapter, we develop a discrete-continuum modeling scheme for analyzing G&R, in which we apply changes directly to a discrete cell and extracellular matrix (ECM) architecture, modeled as a network of various fiber types, and pass changes occurring on a microscale level up to a finite-element macroscale geometry. Growing and remodeling the tissue directly on the network level allows us to gather information on microstructural changes along with information on local material inhomogeneities, which are critical areas in understanding initiating events in growth, remodeling, and failure. The cases studies presented in this chapter are focused on G&R of cardiovascular tissues, due to the wealth of prior knowledge on their progression. However, the applicability of this technique is broad in that one can model any tissue with any microstructure in any finite element software, making it a highly accessible approach for multiscale mechanic simulations. Further work is still needed to broaden our understanding of the observed growth and remodeling phenomenon in the facet capsular ligament. However, the research presented in this thesis provide a solid foundation for this work.

2 Through-thickness Regional Variation in the Mechanical Characteristics of the Lumbar Facet Capsular Ligament

The contents of this chapter were previously published as a research article in the Journal of Biomechanics and Modeling in Mechanobiology by Gacek, Bermel, Ellingson, and Barocas [12].

2.1 Summary

The human lumbar facet capsule, and the facet capsular ligament (FCL) that forms its primary constituent, is a common source of lower back pain. Prior studies on the FCL were limited to in-plane tissue behavior but due to the presence of two distinct yet mechanically different regions, a novel out-of-plane study was conducted to further characterize the roles of the collagen and elastin regions. An experimental technique, called stretch-and-bend, was developed to study the tension-compression asymmetry of the FCL due to varying collagen fiber density throughout the thickness of the tissue. Each healthy excised cadaveric FCL sample was tested in four conditions depending on primary collagen fiber alignment and regional loading. Our results indicate that the FCL is stiffest when the collagen fibers (1) are aligned in the direction of loading, (2) are in tension, and (3) are stretched ~16% from its off-the-bone, undeformed state. An optimization routine was used to fit a four-parameter anisotropic, hyperplastic model to the experimental data. The average elastin modulus, E, and the average collagen fiber modulus, ξ, were 13.15 ± 3.59 kPa and 18.68 ± 13.71 MPa (95% CI), respectively.

2.2 Introduction

Low back pain (LBP), the most common cause of activity limitation in the United States for persons under 45 years old, imposes significant quality-of-life and financial burdens [1]. Between 70 and 85% of all adults in the United States experience LBP at some point in their lives. Although LBP is attributable to many sources and is often idiopathic

[20], the facet joint and the surrounding facet capsular ligament (FCL) have been identified as possible contributors [21]. Facet joint pairs line the spinous processes along the length of the spine from cervical level 3 to sacrum. The FCL is a curved ligament that surrounds the facet joint and is innervated with nociceptive and proprioceptive nerve endings [22].

Given the FCL's possible role in LBP, there is considerable interest in its mechanical behavior. Much research has focused on the tissue as a whole [4], [9], [10], but the FCL is not a monolithic structure. The FCL is viscoelastic [4], anisotropic [10], heterogenous [23]–[25], and layered [26]. In terms of the layering, Yamashita *et al.* (1996) reported that the FCL is composed of two primary regions: (1) the highly aligned collagen-rich fibrous portion on the posterior side (i.e., the portion of the FCL farther from the joint space) and (2) an elastin-rich portion on the anterior side (i.e., the portion in contact with the joint space). Another structurally important feature is the collagen fiber alignment in the FCL. The primary fiber alignment is in the bone-to-bone direction, with additional fibers aligned off-axis [10], [11]. We know from other tissues [27]–[30] and our own work [10], [23]–[25] that structural anisotropy begets mechanical anisotropy, particularly in light of evidence that the fibers are the primary load bearing structure in the FCL [4], [10]. The mechanical impact of the bilayered anisotropic structure of the FCL has not been quantified and requires a non-standard experimental approach.

Most mechanical tests (e.g. uniaxial extension [4]) cannot distinguish through-thickness variation. Three-point bending, which places part of the sample in tension and part in compression, has been used to distinguish mechanical differences between tissue layers in other soft tissues [31]–[35] and in bone [36]. The soft and compliant elastin-rich region dominates at small strains while the collagen-rich region of the FCL is expected to be very stiff under tension but compliant under compression[4], together making the FCL a prime candidate for determining through-thickness modulus variations with the 3-point bend test's application of tension and compression to different regions. However, as we observed previously [37], the traditional 3-point bend test does not uncrimp the FCL's collagen fibers fully and therefore fails to load the fibers and elucidate differences between the two regions (**Figure 1**a). To overcome this challenge, we bring the collagen fibers closer to their uncrimped state by initially stretching the tissue to 10% before bending, in a method we call stretch-and-bend (**Figure 1**b-c). A similar principle – introducing a deformation to bring the collagen fibers into tension before the mechanical test – were applied to study the tension-compression asymmetry of bovine articular cartilage [38] by using osmotic swelling prior to compression.

The objective of this work was to characterize the cadaveric human lumbar FCL mechanically, via a novel stretch-and-bend test sensitive to the mechanical difference between the layers of the tissue. We hypothesized that tissue regions largely composed of highly aligned collagen fibers would be stiffer than regions containing primarily elastin.

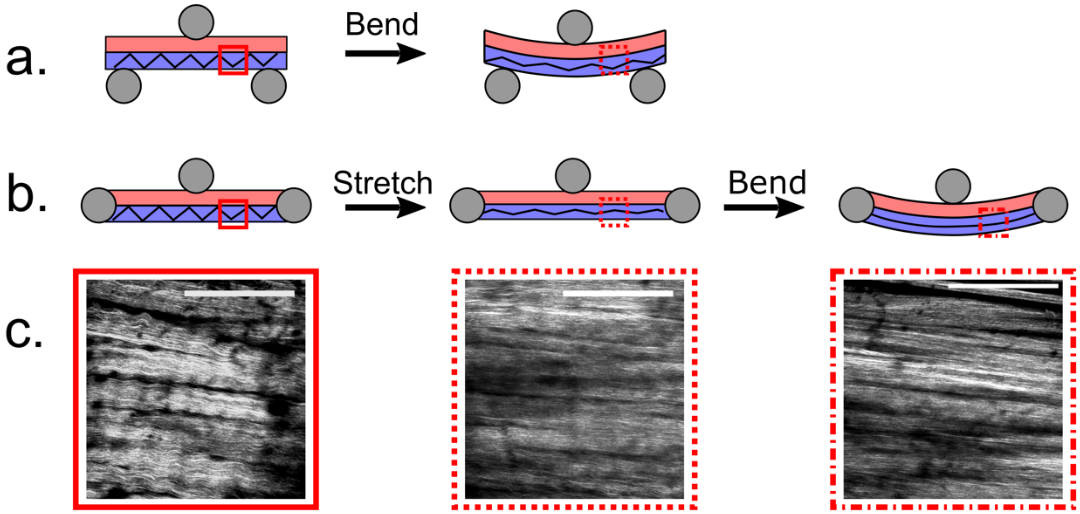

Figure 1 ***(a.)*** *A traditional 3-point bend test does not generate enough train to uncrimp the collagen fibers in the FCL.* ***(b.)*** *The stretch portion of the stretch-and-bend test brings the collagen fibers close to uncrimping, after which a stiffness increase is observed when the bend portion of the test puts the collagen in tension.* ***(c.)*** *Representative second harmonic generation images of FCL collagen fibers at 0% (solid), 10% (dotted), and 20% (dashed) strain. Blue = collagen region, Red = elastin, Black = collagen fibers. Scale bars = 150 um*

2.3 Methods

2.3.1 Sample Preparation and Mounting

Three cadaveric lumber spine specimens (F, aged 26-65 years) without history of spinal pathologies, were obtained through the University of Minnesota Anatomy Bequest

Program, as approved by institutional review. The spinal health of each specimen was assessed via MRI. Scans of the samples were reviewed, and none displayed advanced signs of degeneration or pathology. The spines were cleared of superficial tissue, taking special care to keep the FCLs fully intact. Rectangular FCL samples were resected from L2L3, L3L4, and L4L5 vertebral segments (N = 16), such that the bone-to-bone direction, which corresponded to the main collagen fiber alignment, was parallel to the short side of the sample. FCL samples were visually healthy with no indication of osteophyte formation.

Sample dimensions were measured using digital calipers. The mean[1] and range for parallel and perpendicular samples are shown in **Table 1** and are listed in full in *Appendix B* - **Supplementary Table 3** .

Table 1 *Average sample dimensions as measured parallel and perpendicular to the primary collagen fiber alignment.*

	Parallel Samples		**Perpendicular Samples**	
	Mean	**Range**	**Mean**	**Range**
Width (mm)	9.37 ± 1.40	[7.43,12.64]	13.61 ± 2.74	[9.43,17.77]
Length (mm)	13.49 ± 2.82	[8.94,17.77]	9.49 ± 1.53	[7.43,12.64]
Thickness (mm)	1.70 ± 0.29	[1.16,2.17]	1.70 ± 0.29	[1.16,2.17]

An Instron-Sacks planar biaxial mechanical testing machine (Instron, Norwood, MA, USA) was fitted with three dynamic load cells. Two load cells (500N, 0.05%, Instron) were fitted on one axis of the machine, henceforth referred to as the *grip* axis. The remaining load cell (5N, 0.05%, Instron) was fitted on the axis perpendicular to the grip axis, henceforth referred to as the *cantilever* axis. All load cells recorded normal forces. The biaxial machine was fit with a custom stretch-and-bend apparatus (**Figure 2**a-b) comprised of three vertical steel pins, one for each load cell. Hollow grip attachments cut from plastic tubing were attached to the sample using a cyanoacrylate adhesive. The grip attachments slid over the grip axis pins such that the sample was allowed to rotate freely about the pin. The rigid pin on the cantilever axis, i.e., the cantilever, was aligned with the center of the sample and moved perpendicular to the grip axis.

---

[1] Unless otherwise noted, data in this chapter are reported as mean ± 95% confidence interval.

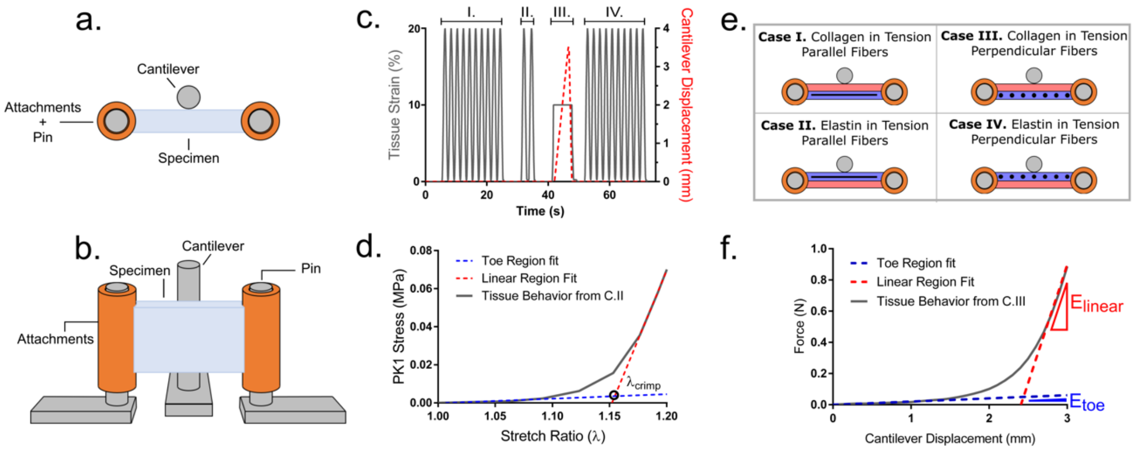

***Figure 2** A view of the prepared, mounted sample is shown in **(a.)** a top-down view and **(b.)** in a side view. The pin is connected to individual load cells. **(c.)** Tissue strain (left axis) of a single axis arm and cantilever displacement (right axis) for **(I.)** 10 cycles of preconditioning, **(II.)** 2 uniaxial stretches, **(III.)** a stretch-and-bend test, and **(IV.)** 10 cycles of postconditioning. **(d.)** Representative bilinear fit analysis of the uniaxial data to derive the degree of fiber crimp. **(e.)** Representative bilinear fit of the cantilever force-displacement data from c. III to derive the toe and linear region stiffness. **(f.)** Top-down view of the 4 test cases*

2.3.2 Preconditioning and Estimation of Crimp Stretch

The samples were initially stretched until a preload of 0.1N was achieved. Each sample was preconditioned with 10 cycles to 20% uniaxial stretch (**Figure 2**c., region I). Following preconditioning, the samples were twice stretched uniaxially to 20% to estimate the degree of fiber crimp (**Figure 2**c.II). A toe and a linear region were defined by fitting two lines to the uniaxial stress-stretch curve (**Figure 2**d), one at low stretch (the toe region) and one at high stretch (the linear region), following methods used previously [39], [40]. The intersection of the two lines, which marks the transition point between the toe and linear regions, was taken to be the stretch at which the fibers transition from crimped to uncrimped, or the degree of fiber crimp.

2.3.3 Stretch and Bend Experiment

Based on the measured transition strains in preliminary samples, samples were next stretched to 10% and held at 10% stretch while being bent by a cantilever displaced in the direction transverse to stretch (**Figure 2**c.III). To prevent off-axis loading during preconditioning, the cantilever was initially located away from the sample. The reference position of the cantilever was then determined during data analysis as the initial point of contact with the sample. The recorded data were trimmed to run from the point of first cantilever-sample contact to the point of 3 mm cantilever travel. Each sample was tested four times total, following the 2 x 2 design shown in **Figure 2**e

I. collagen fibers parallel to the grip axis and bending placing the collagen layer in tension
II. collagen fibers parallel to the grip axis and bending placing the elastin layer in tension
III. collagen fibers perpendicular to the grip axis and bending placing the collagen layer in tension
IV. collagen fibers perpendicular to the grip axis and bending placing the elastin layer in tension

Samples were first tested in one fiber orientation (Case I-II or Case III-IV) before being carefully removed from the plastic tubing and reattached for testing in the opposite orientation. Previous studies [4], [10] suggest minimal viscoelastic effects for stretch rates of around 2%/s, so all tests were conducted on at a 2.4%/s stretch rate (for stretch along the grip axis) or a 1 mm/s cantilever displacement rate (for bending). The protocol concluded with 10 cycles of postconditioning, similar to the preconditioning cycles, to ensure that the sample was not damaged during the experiment (**Figure 2**c. IV).

2.3.4 Data Analysis: Stretch-and-Bend Response

An estimate of fiber crimp length was experimentally derived from the uniaxial stretch tests conducted on each sample prior to the stretch-and-bend test. As shown in figure 2d, the toe-region and linear-region of the resulting stress-λ curve were linearly fit. The resulting intercept between these two lines provided a measure of the sample's degree of fiber crimp.

A sample's small-strain and high-strain bending stiffnesses were computed from the cantilever force-displacement curves for each test case. The toe-region stiffness (small-strain) and the linear-region stiffness (high-strain) were computed in the range of 0.0 - 1.5 mm and 2.7 - 3.0 mm cantilever displacement, respectively (**Figure 2**f). Significance of differences between collagen or elastin regions as measured by toe stiffness was determined using paired t-test between cases with the same fiber orientation (Case I and II or Case III and Case IV) and unpaired t-tests between cases with different fiber orientations (Case I and Case III or Case II and Case IV). The same was done when comparing a region's linear stiffnesses across cases.

2.3.5 Finite Element Composite Model

Although the characterization methods described above provide a sense of the FCL's behavior, they do not translate well to other geometries and thus cannot be used to simulate the *in situ* joint behavior. To specify a full constitutive model of the FCL, sample-specific finite element models were created on the FEBio finite element platform [41] using experimental FCL sample dimensions; the ratio of the collagen layer to the elastin layer was set to 1:1, roughly consistent with the observations of Bermel [37]. To reduce computational complexity, a quarter of each sample was modeled using symmetry planes bisecting the *x*- and *z*-axes (**Figure 3**a). The grip pin and the cantilever were modeled as rigid bodies, with a rigid interface between the grip and the sample. A sliding contact boundary condition was used to define the interface between the cantilever and the sample. During the stretch portion of the stretch-and-bend test, the grip was constrained to displace only in the *x*-direction, and the cantilever was held fixed out of contact with the sample. During the bend portion of the test, the grip was only allowed to rotate freely about the *z*-axis to mimic the rotation of the sample grip attachments, and the cantilever was constrained to displacement in the *y*-direction. Both the grip and cantilever were displacement-controlled to match the experimental protocol.

To aid in parameter optimization, the uniaxial stretch test for a sample when loaded parallel to the collagen fiber direction was also modeled using the same quarter symmetry planes described above, and the grip was displaced to match the experimental protocol. The cantilever was omitted from this model since it was not used in the uniaxial tests.

A hyperelastic strain energy density function was used to describe the tissue behavior. The collagen layer was modeled as a coupled solid mixture with a single fiber family embedded in a compressible neo-Hookean matrix with the following strain energy function *W*:

$$W = \frac{\mu}{2}(I_1 - 3) - \mu \ln J + \frac{\lambda}{2}(\ln J)^2 \tag{2.1}$$

where μ and λ are the Lamé parameters; I_1 is the first invariant[†] (i.e., the trace) of the right Cauchy-Green tensor ($I_1 = C_{ii}$; $C_{ij} = F_{ki}F_{kj}$), and J is the determinant (i.e., the third invariant) of the deformation gradient tensor F [41], [42]. The collagen fibers were described using an exponential fiber constitutive equation:

$$\psi_n(I_n) = \frac{\xi}{\alpha\beta}\left(\exp^{\alpha(I_n - 1)^\beta} - 1\right) \tag{2.2}$$

In equation (2.2), ξ is the fiber small-strain modulus, α and β are the coefficient and power of the exponential, respectively, and I_n is the square of stretch in fiber direction. The collagen fiber orientations were defined with a 2D von Mises distribution [42], [43]:

$$R(\boldsymbol{n}) = \frac{\exp^{b\left(2n_1^2 - 1\right)}}{2\pi I_0(b)} \tag{2.3}$$

where (n_1, n_2, n_3) are the components of the fiber direction vector $\boldsymbol{n}$, b is the concentration parameter, and I_0 is a modified Bessel function of the first kind of order 0. The concentration parameter was set to 8, consistent with a highly aligned fiber network in our previous equibiaxial studies [10]. FEBio uses a trapezoidal integration scheme to integrate the distribution over the 2D unit circle [41], [42].

The elastin layer was modeled as neo-Hookean (Eqn. 2.1). The collagen layer was modeled as nearly incompressible by setting the Poisson's ratio to 0.4999. The elastin layer was modeled as slightly compressible by setting the Poisson's ratio to 0.45.

[†] It is unfortunate that a capital I with a numeric subscript is used both for the invariants of a tensor (as here) and for the modified Bessel function of the first kind (as in Eq. 2.3), and that both are needed in this paper. To emphasize, I_1, here and throughout this chapter, refers to the first invariant of the tensor C; I_0 in Eq. 2.3 and throughout this chapter, refers to the modified Bessel function of the first kind and order 0.

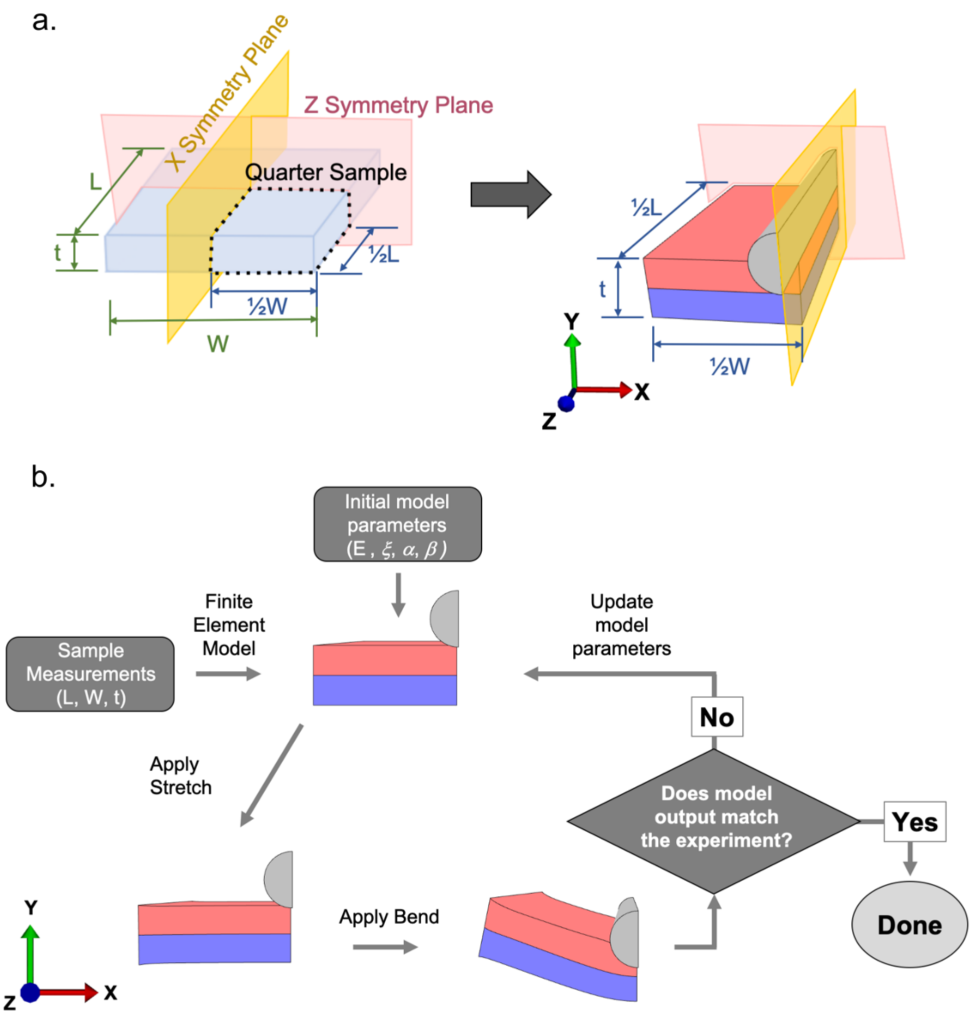

Figure 3 (a.) *The dimensions of a single representative FCL sample shown as width (W), length (L), and thickness (t). A quarter of the sample was modeled in FEBio and two symmetry planes were used as outlines.* ***(b.)*** *Steps of the optimization routine used to determine FCL elastin and collagen material parameters (E, ξ, α, β)*

Optimizing Model Parameters

The reaction force at the cantilever and at the grip were output by the model at each displacement step, and MATLAB's *fminsearch* algorithm was used to obtain the set of material parameters $\{E, \xi, \alpha, \beta\}$ that minimized the sum of squared error (**Figure 3**b) between the cantilever experimental and computation data points for all four testing configurations in **Figure 2**e as well as grip force for the sample's uniaxial stretch test, shown in **Figure 2**d.

A segregated approach was used to accelerate the fitting process and reduce the likelihood of local minima polluting the results. The response of the tissue during the perpendicular-fiber test cases (III and IV) was assumed to be wholly dependent on the elastin. Therefore, the elastin modulus (E) was fitted only to the two perpendicular test cases (III-IV) with a negligible collagen fiber modulus. The fitted elastin modulus was then held fixed when optimizing the collagen parameters ξ, α, β using the parallel test cases (I-II) and the uniaxial stretch response. The fitting algorithm was modified to constrain the parameter β to be less than 10 because larger values produced unreasonable results for the other parameter values from the fitting routine. An approximate 95% confidence interval for each parameter was calculated based on the error linearized about the minimal point, as described in Draper and Smith [44] and the work by Claeson et al.[10]. The FEBio simulations and optimization routine were computed using one core at the University of Minnesota Supercomputing Institute. A single sample was discarded due to a much stiffer response of the perpendicular collagen fibers of Case III, which more closely resembled Case I than Case IV. Our fitting routine failed to capture this tissue's behavior in all four loading cases.

2.3.6 Sensitivity Analysis

As noted above, the Poisson's ratio of the elastin layer was set 0.45 due to the experimentally observed compression of the tissue's elastin region. A sensitivity analysis was conducted to determine the effect of the elastin region's Poisson's ratio on model results. The Poisson's ratio was varied between 0.43 (more compressible), and 0.49 (nearly incompressible) and compared against the optimized results of Case I, Case II, Case III, Case IV, and the uniaxial stretch (Poisson's ratio of 0.45).

2.4 Results

2.4.1 Mechanical Testing

A traditional planar uniaxial stretch test identifies nonlinear behavior of materials (**Figure 2**d). The mean stretch ratio, or λ_{crimp}, at which the L2-L5 FCLs transitioned from crimped to uncrimped was 15.9 +/- 0.2 % stretch (95% CI). The mean λ_{crimp} for all samples tested with parallel collagen fibers (cases I-II) was 15.9 +/- 0.3% and with perpendicular collagen fiber orientation (cases III-IV) was 15.9 +/- 0.2% (**Figure 4**). No statistically significant difference was found between loading directions or between spinal levels ($p > 0.1$ for all comparisons). Our results suggest that there is low sample-to-sample variability in the crimp of the collagen fibers in the lumbar spine, which is consistent with previous studies done on the FCL and other soft tissues [4], [45]. Samples were considered not damaged over the course of the testing protocol since there was an average 6% difference between the pre- and postconditioning cycles.

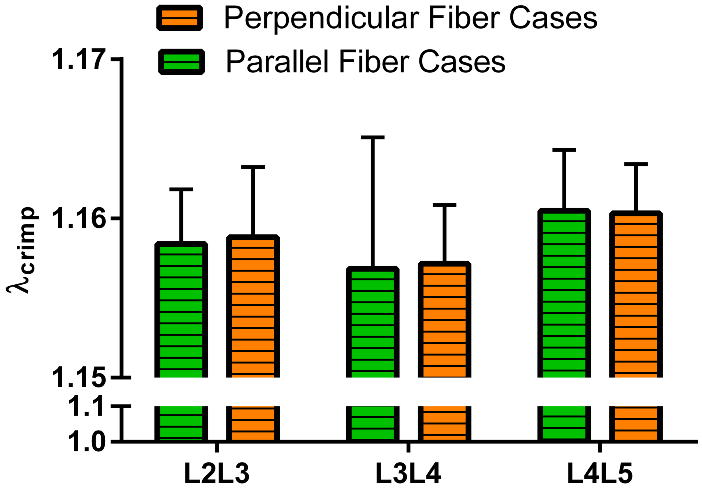

Figure 4 *A measure of collagen fiber crimp derived from the bilinear fit of the uniaxial stretch data. Shown is the mean of the parallel fiber cases (Case I – II) and perpendicular fiber cases (Case III – IV) with 95% CI. No significant difference was found for any comparison*

The stretch-and-bend results for two samples were discarded due to experimental errors, leaving the 14 data sets shown collectively in **Figure 5**, which highlight the FCL's bilayered, anisotropic nature. As reported previously [4], the FCL is much stiffer when the collagen fibers are loaded in tension (**Figure 5**a,b vs, c,d; summarized in **Figure 5**e). Using the mean stretch ratio of roughly 16% as the starting point at which collagen fiber contribution to the observable mechanical behavior, our results indicate that the collagen fibers in Case II remain crimped and unloaded due to the relatively small loads in comparison to Case I (**Figure 5**b).

The experimentally-derived tissue stiffness values for small and large cantilever displacements are shown in **Figure 6**a-b. The linear-region stiffness of the tissue when the collagen is in tension with parallel collagen fibers (i.e., Case I) was 1.20 ± 0.57 N/mm, which was significantly higher than all other testing conditions ($p < 0.001$, Fig. 6b) and smaller than previously reported lumbar FCL stiffness by Little et al. [4].

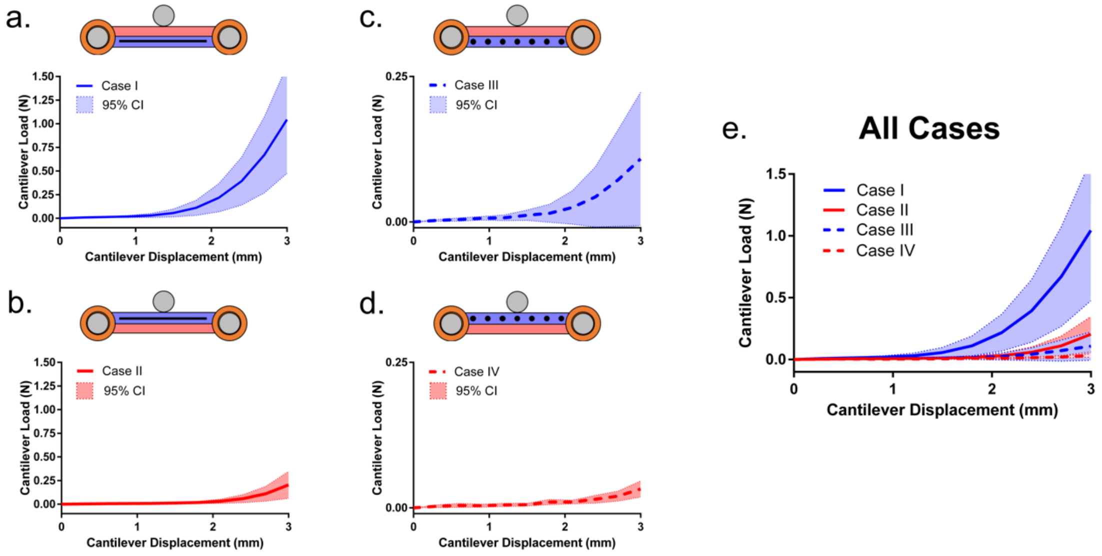

Figure 5 (a.-d.) *Cantilever load-displacement curves for all 14 samples tested in all 4 test cases. Note differing scale bars.* ***(e.)*** *Plots of a.-d. shown on the same scale demonstrate the greater stiffness in the parallel-to-fibers collagen-in-tension cases. These curves are the result of the stretch-and-bend test shown in figure 2c.III. (n = 14 for all plots)*

The difference with a change in collagen orientation (Case I vs. Case III) is consistent with previous planar mechanical tests [10], [46] demonstrating pronounced anisotropy in the ligament. Sample stiffness was positively correlated between collagen-in-tension and elastin-in-tension tests (**Figure 6**c-d). The linear regression of both lines indicates that samples that are stiffer when the elastin-rich region is in tension tend to be stiffer when the collagen region is in tension. However, there was no apparent correlation between linear-region stiffness and sample thickness ($p > 0.45$, $r^2 = 0.047$ (Case I); data not shown).

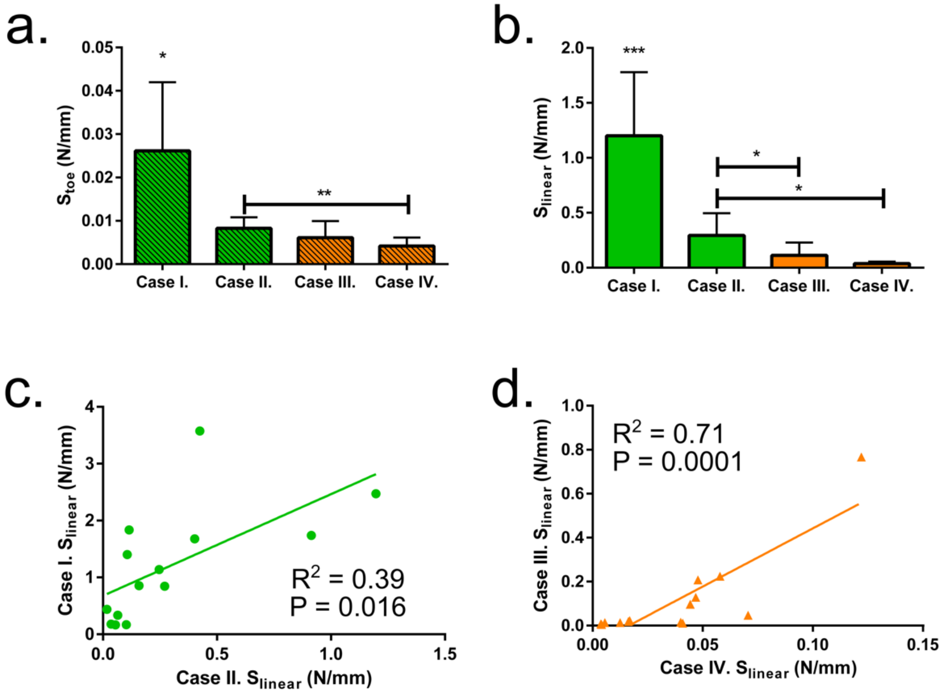

Figure 6 *Tissue stiffness derived from the cantilever force-displacement curves of each case during stretch-and-bend.* ***(a.)*** *The toe region stiffness (S_{toe}) was fit to the curves from 0 – 1.5mm cantilever displacement and* ***(b.)*** *the linear region stiffness (S_{linear}) was fit the curves from 2.7 – 3.0 mm cantilever displacement. Mean and 95% CI error bars are shown (n=14). Plot of each sample's S_{linear} for* ***(c.)*** *parallel collagen fiber test cases (Case I - II) and* ***(d.)*** *perpendicular collagen fiber test cases (Case III - IV)*

** denotes significant difference for $p \leq 0.05$*

*** denotes significance for $p \leq 0.01$*

**** denotes significance for $p \leq 0.001$*

2.4.2 Computational Model

The four model parameters (E, ξ, α, and β) were fit using the experimental stretch-and-bend data for all four cases and the uniaxial stretch of Case I. In general, Case I and Case II contributed more to the error than Case III-IV or the uniaxial stretch, as shown for the cantilever load versus displacement for a single representative sample (**Figure 7**a-c). As can be seen in **Figure 7**a, when the collagen stresses are set to zero for an elastin-only model of the perpendicular-collagen-fibers cases, Equation (2.1) provides a reasonable fit but does not display as much nonlinearity as the tissue; a more complicated model could be introduced to capture that nonlinearity, but we chose not to do so since the elastin contribution is very small compared to the collagen. For the parallel-collagen-fibers cases in both bending (**Figure 7**b) and uniaxial stretch (**Figure 7**c), the model captured but underpredicted the asymmetry between the collagen-in-tension (Case I) and elastin-in-tension (Case II) bending experiments, and it produced results consistent between the bending and stretching data using the same set of model parameters. The range for the RMS error was [0.051, 1.08] N when fitting ξ, α, and β and was [0.0011, 0.030] N when fitting E. The normalized mean of each parameter is shown in **Figure 7**d, and all optimized model parameter values are shown in **Figure 7**e. For α, the calculated upper and lower 95% confidence interval bounds were infinite for all 13 model fits and could not be shown in **Figure 7**d. This suggests that α had very little effect on the observable model fiber behavior provided that it was not approaching zero. All other parameters were considered well estimated as they had normalized value greater than one (**Figure 7**d). The calculated 95% confidence bounds for each sample's parameter set is shown in *Appendix B* - **Supplementary Table 4**. The average elastin modulus, E, was 13.15 ± 3.59 kPa, the average collagen fiber modulus, ξ, was 18.68 ± 13.71 MPa, and the average coefficient, α, and power, β, of the exponential were 0.079 ± 0.073 and 7.58 ± 0.98, respectively (**Figure 7**e).

A sensitivity analysis of the elastin region Poisson's ratio concluded that the difference between a more compressible (Poisson's ratio of 0.43) or a more incompressible (Poisson's ratio of 0.49) and our own material (Poisson's ratio of 0.45) was small, signifying that the response of the tissue depends more on the collagen fibers than on the elastin. At most, there was a 9.7% change in the results for the parallel-fiber, collagen-in-tension case, with negligible change to the other cases.

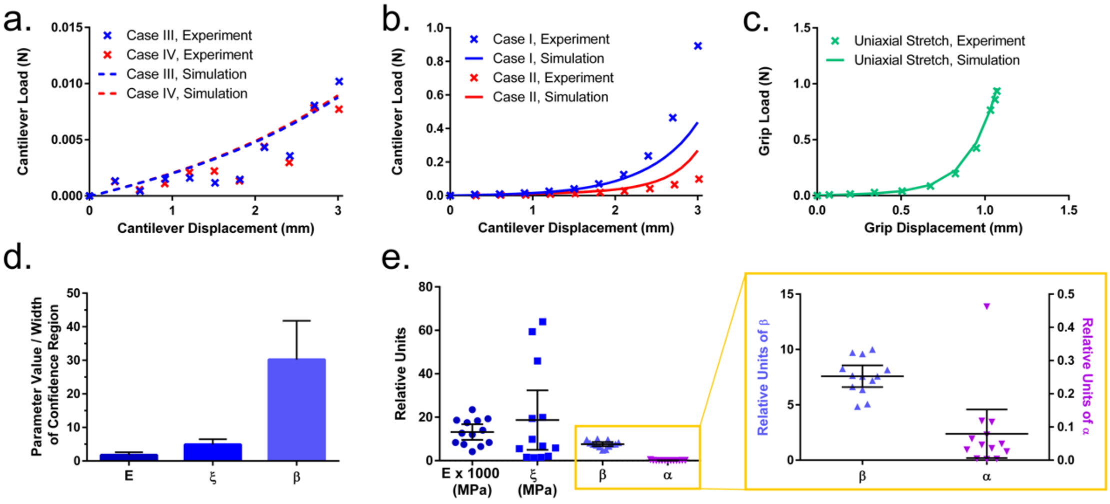

Figure 7 *Representative model fits (lines) fit to a representative experimental data set (n=1) for* ***(a.)*** *Cases III and IV,* ***(b.)*** *Case I and II, and* ***(c.)*** *a uniaxial stretch test (shown in Figure 2c.II) done on a sample with fibers aligned parallel to the loading direction* ***(d.)*** *The normalized mean of each parameter obtained by dividing the parameter value by its respective 95% confidence region width, which gives us a measure of goodness of fit. Parameter values greater than 1 are considered a good fit.* ***(e.)*** *The results of the optimized parameter, E, ξ, α, and β, for all optimized models (n=13). The parameter α was not divided by its confidence region width because all individual model values had infinite bounds*

Figure 8 shows the Green-Lagrange strain along the *x*- and *y*-axis for a single representative sample; results for all samples were qualitatively similar. The sample has much higher maximum strains when tested with the collagen region in tension and fibers parallel to the grip axis (Case I). In that Case, there is a region of high *X*-extension (E_X ~ 1.70) and *Y*-compression (E_Y ~ -0.45) directly below the cantilever. This large deformation is due to the compression of the elastin region, and it closely mimics the tissue's experimental behavior. There is relatively little strain in the much stiffer collagen-rich region. While each case has an applied 10% prestretch before bending, that stretch is small compared to the peak strains of 67-170% observed throughout all four cases. Therefore, the observed peak tissue strains in **Figure 8** can be largely attributed to the bending portion of the stretch-and-bend experiment and show the tension-compression asymmetry of the FCL. The neutral axis, calculated in the midplane at 3 mm cantilever displacement, shows where the tissue transitions from a tensile stress to a compressive stress. For Case I, the neutral axis lies at the boundary between the elastin and collagen regions. Cases II-IV show similar behavior, with the largest X-extension and Y-compression at the midplane and on the surface opposite the indenter (i.e., the concave surface), as one would expect from linear beam theory. There is also an edge effect from the rigid grip. The neutral axis lies in the region closest to the cantilever for Case II-IV, indicating that there is a portion of this region that is in tension. While this shift does not appear to increase cantilever load for Cases III and IV (**Figure 7**a), it could explain the increased load shown in the optimized model results of **Figure 7**b. A portion of the collagen fibers are in tension and contributing to the observed response.

Figure 9 shows the 1st, and 2nd principal stresses for Case I and Case II and is broken down to show the contribution of the collagen fibers compared to the elastin matrix. The 3rd principal stress is very similar to the 2nd principal stress and thus not shown. The 1st principal stress roughly aligns with the x-axis while the 2nd and 3rd align with the z- and y-axis, respectively. The collagen fibers contribute more to the total 1st principal stress than the elastin matrix but not when the collagen fibers are compressed, as shown by the 2nd principal stress (**Figure 9**a). In Cases I and II, the stiff collagen fibers lead to large stresses in the collagen region even though the strains there are much lower than in the elastin region (cf. **Figure 8**). Our results also indicate that there is a region of high tensile stress in the collagen region near the neutral axis of Case II (**Figure 9**b), which is the most-strained portion of the collagen region in that geometry.

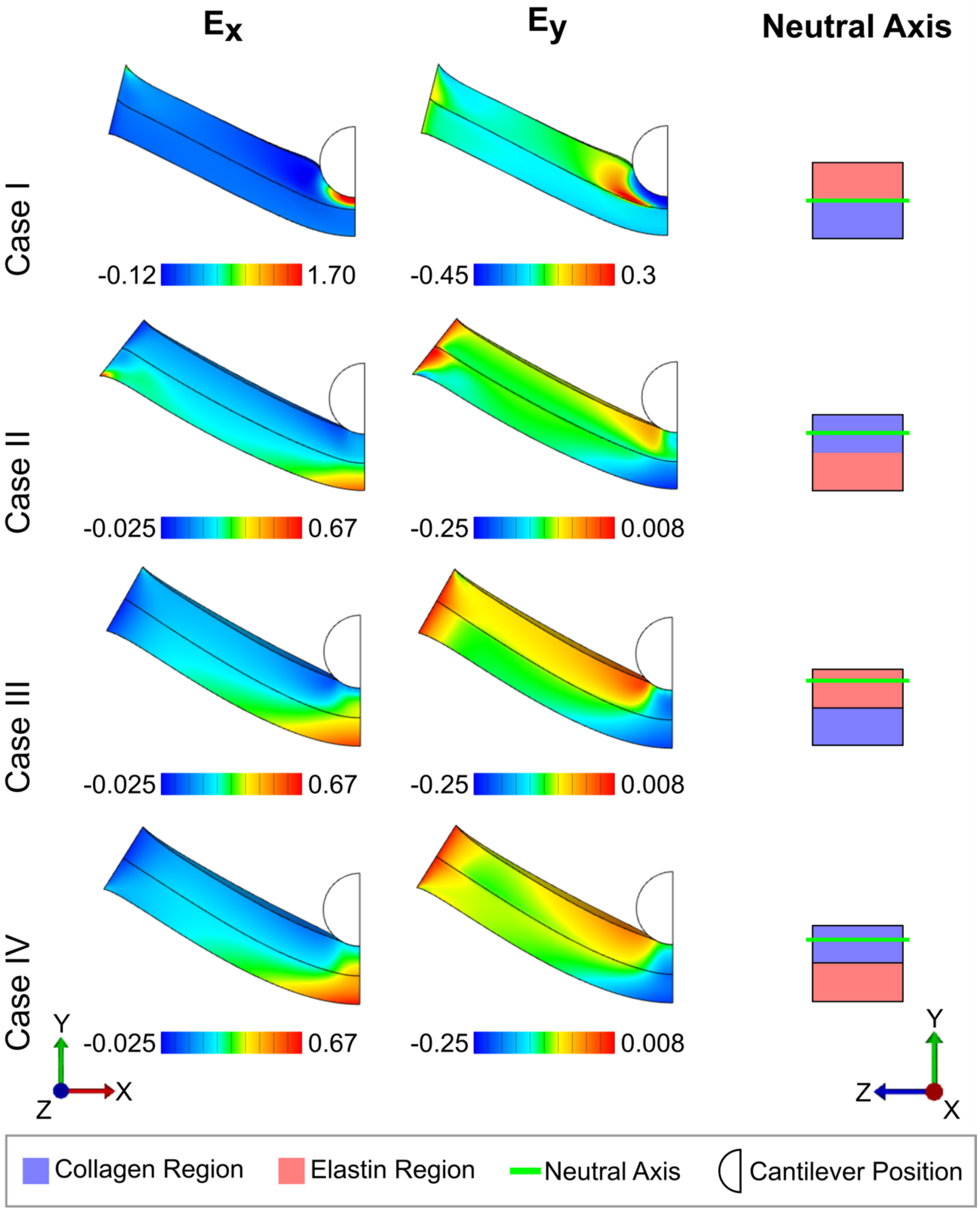

Figure 8 *The Green-Lagrange strain along the x-axis (E_x) and along the y-axis (E_y) for a single representative FCL sample for all four test cases. The neutral axis was determined as the location with zero stress at the end point of the experiment (cantilever displacement of 3mm) for all test cases.*

2.5 Discussion

We used a novel stretch-and-bend test to capture the through-thickness variation in the mechanical response of L2-L5 FCLs. Using experimental data, we optimized a set of model material parameters that matched the behavior observed experimentally. To our knowledge, this is the first characterization of the mechanical variation through the thickness of the lumbar FCL, and it consistent with previous observations of structural and compositional variation [26]. The anisotropy and heterogeneity of the FCL cause large variability in the tissue's strength in relation to direction of tissue loading. The tissue has the highest strength parallel to the collagen fibers due to the presence of highly aligned collagen fiber bundles [4], [26].

In their uniaxial experiment, Little *et al.* [4] demonstrated that the FCL exhibits nonlinear material behavior when loaded parallel to the collagen fibers and was an order of magnitude stiffer than the linear material behavior of the sample when loaded perpendicular to the collagen fibers. In their morphological assessment of lumbar FCLs, Yamashita *et al.* [26] observed anatomical and histological differences between the outer (collagenous) and inner (elastin) portion of the ligament. Our own previous histological assessment [37] supports this observation, which led us to hypothesize that there will be some level of variability between the mechanics of the outer and inner portion of the FCL. The presence of two distinct regions, a collagen-rich region and an elastin-rich region, through the thickness of the FCL indicate that the observation by Little *et al.* [4] could change if the collagen region were not under tension when loaded parallel to the collagen fibers. Our results indicate that the FCL is stiffest when three conditions are met: (1) the collagen fibers are aligned parallel to the direction of loading, (2) the collagen region is placed under tension, and (3) the tissue stretch is at least 16% from its undeformed state. Following these three criteria, the FCL collagen fibers must be fully uncrimped and loaded to contribute significantly to the stiffness of the tissue. Outside of these three conditions, the elastin structure dominates the response during loading.

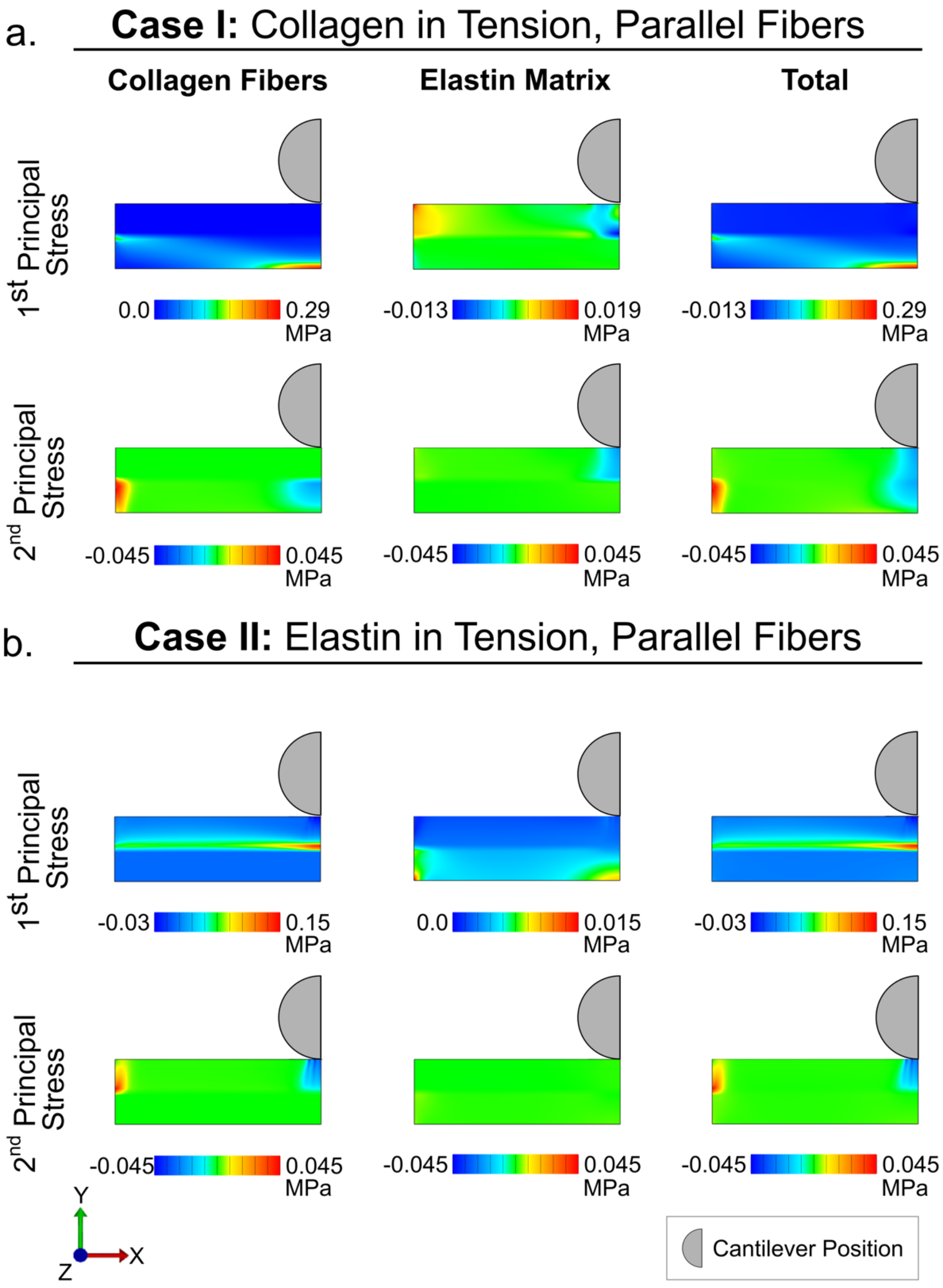

Figure 9 *The principal stresses of the collagen fibers, elastin matrix, and the total sample response for a single representative FCL sample are shown for* ***(a.)*** *Case I and* ***(b.)*** *Case II. The 1st, and 2nd principal stresses are roughly aligned along the x-axis, and z-axis, respectively*

The lumbar FCL's microstructure plays a large role in providing stability and strength for everyday spinal motions [13]. The collagen fiber orientation is an important microstructural component that prevents painful motions by stiffening and resisting tissue shear in response to loads parallel to the fiber orientation [24]. Fiber orientation and crimp has been shown to cause nonlinear stress-strain behavior of the lumbar FCL in tension [4], and many previous studies have mathematically captured this orientation-functionality relationship [4], [16], [23], [24]. However, most experimental studies done on the lumbar FCL have been limited to excised, planar tissue samples. Little is known about the state of the collagen fibers *in situ* and whether removing the tissue from the bone induces or further causes crimp of the collagen fibers. It is possible, perhaps even likely, that a combination of constraints due to attachment to the vertebrae and pressure from the synovial fluid contained within the capsule lead to a degree of tissue strain *in vivo*, even when the joint is not loaded. Further, the rest states of the collagen and elastin may not be the same, an effect well studied in vascular mechanics [47]–[49].

Previous mechanical tests on lumbar FCLs focused on the mechanical behavior of planar samples. In addition to the uniaxial test done by Little *et al.* [4], Claeson *et al.* [10] performed a planar equabiaxial experiment to determine in-plane normal and shear behavior. Again, Claeson *et al.* concluded that the tissue is stiffer when loaded in the direction of the collagen fibers but that there was some contribution to the load from fibers at an angle to the load direction. Both the uniaxial and biaxial experiments demonstrated a significant difference in the response of the tissue depending on the load direction, but these studies were limited to describing the tissue's in-plane behavior. Our study indicated that there is a scenario in which the FCL is loaded parallel to the collagen fibers but, due to through-thickness tension-compression asymmetry, there is no observable stiffening of the tissue at similar cantilever displacements (Case II, **Figure 5**). The slight upturn in the cantilever load of Case II may be due to the shift of the neutral axis of bending into the collagen region so that there is a small portion of the collagen region in tension. Therefore, the through-thickness inhomogeneity of the microstructure is an important consideration when modeling the lumbar facet joint.

To compare our experimental results with those of Claeson *et al.* [10] and Little *et al.* [4], we simulated a 10% and 20% uniaxial extension test by deforming a 1x1x1 mm cube, with both a collagen and elastin region, either parallel or perpendicular to the fiber direction. The average calculated material parameters were used (E=13.15 kPa, ξ=18.68 MPa, α=0.079, and β=7.58). The parallel elastic modulus at 10% and 20% strain was 0.17 MPa and 7.72 MPa, respectively. The simulated 10% parallel elastic modulus was smaller than that reported by Claeson et al. (4.34 ± 1.25 MPa) but the 20% parallel elastic modulus was similar to Claeson et al. (7.82 ± 3.13 MPa). The simulated perpendicular elastic modulus at 10% and 20% strain was 0.040 MPa and 0.037 MPa, respectively. Again, this is smaller than those reported by Claeson et al. (0.52 ± 0.34 MPa and 1.17 ± 0.79 MPa, respectively). The maximum stress in the direction of loading at 10% parallel strain (0.0071 MPa) for our model was similar to the stress derived from the exponential stress-strain relationship reported by Little et al. (0.0082 MPa) but the strain at 20% (0.17 MPa) was larger than Little et al (0.022 MPa). However, the stress perpendicular to fiber orientation at 10% (0.0042 MPa) and 20% (0.0080 MPa) strain was similar to Little et al. (0.0070 and 0.010 MPa, respectively). Differences between data sets may be due to differences in estimation of the collagen layer fraction. Claeson *et al.* [10] had a homogenous-though-thickness model that did not account for a separate collagen and elastin region. Additionally, Little *et al.* [4]reported a smaller parallel modulus when compared to the perpendicular modulus up to strains of 40% which our model cannot capture.

During physiological spinal motion, both the lumbar [9] and cervical FCLs [6] simultaneously experience compressive and tensile strains. These motion-specific strain fields could play a role in sensory perception by the embedded proprioceptive nerve endings [16], [50]. Simultaneous compressive and tensile surface strains could also cause regions of fairly complaint tissue next to regions of very stiff tissue as the collagen fibers are loaded in tension, which could also produce a shearing interface. Ianuzzi *et al.* [9] reported the highest observed FCL maximum principal strain was 14.6% during spine flexion. In the representative sample shown in **Figure 8**, the maximum 1st principal strain was 167% in Case I and 81.8% in Case II. The large model strain for Case I is due to the compression of the elastin by the cantilever and a more appropriate comparison may be found on the outer edge of the collagen region, which reached a maximum 1st principal strain of approximately 25.2%. Comparatively, at the same point on the outer edge of the elastin region in Case II, the maximum 1st principal strain was 56.0%. It is important to recognize that the Ianuzzi *et al.* [9] study observed strains of the ligament while on the joint. In our own study, the ligament was removed from the bone, and any pre-stain that the ligament would have experienced *in vivo* was released during sample preparations.

The stretch and bend test was not designed to mimic the in vivo loading conditions but rather to isolate the effect of the non-uniform, layered structure of the FCL. Examination of our previous study of on-joint (homogeneous-through-thickness) FCL mechanics under various realistic spinal motions [16] showed curvature differences greater than mm^{-1}, especially in the simulated spinal motion of extension. There are changes in ligament curvature *in vivo* that would involve bending of the ligament which could not be assessed in planar mechanical tests. While it is not clear whether the change in curvature produced stresses of any significance when compared to the stresses generated within the plane of the ligament, the fact that the curvature does change suggests that through-thickness heterogeneity should be considered because the stretch on the inner and outer surfaces of the tissue will not be the same. Our study seeks to understand the through-thickness regional difference in the FCL which is needed to fully understand the *in situ* role of the FCL and whether the observed change in curvature is physiologically important for healthy FCL mechanics.

Viscoelasticity of the FCL is an important spinal characteristics that has been studied by others [4], [51], [52]. Our study is limited to characterizing the elastic behavior of the elastin and collagen regions since the experiment was preformed slow enough that viscoelastic effects were negligible, making any analysis on the through-thickness viscoelastic effects impossible. Additionally, there is a high degree of variability between FCL samples, as initially observed by Little et al. [4], and supported by our own observations of the FCL bending behavior. Therefore, while the global fiber alignment in the FCL has been observed to be predominately in the bone-to-bone direction, it was not possible to measure the sample's actual fiber alignment in this study, which may contribute to the larger loads observed in Case III compared to Case II and IV (**Figure 5**c-d). The

Poisson effect was not measured in the third dimension, which would give a better insight into the compressibility of the regions when computationally modeling the experimental results.

Finally, we observe that this experiment can be easily applied to other tissues that also exhibit regional variations in its microstructure. Currently, a 3-point bend test is the only method for measuring through-thickness variations in a tissue modulus by localizing tensile and compressive strains via the applied moment of bending. Previously, Yu *et al.* [30] used a traditional 3-point bending apparatus to quantify the neutral axis and Young's modulus of the arterial wall layers [30]. This technique was later expanded to quantify the flexural properties of heterograft biomaterials [32]. The 3-point bend test is limited in that it generates relatively small strains if the sample is thin. The stretch-and-bend technique could be used to study layer-dependent arterial mechanics during larger strains, which may give more insight into the tissue's layers functionality. This technique could also be used to the cervical FCL which differs from the lumbar FCL in size and anatomical orientation; such a study might provide insight into differences between cervical and lumbar FCL and common injurious loading conditions (traumatic neck injury versus chronic lower back pain).

3 In Situ Lumbar Facet Capsular Strains due to Joint Pressurization and Residual Strain

The contents of the chapter were previously published as a research article in the Journal of Biomedical Engineering by Gacek, Ellingson, and Barocas. [18]

3.1 Summary

The lumbar facet capsular ligament, which surrounds and limits the motion of each facet joint in the lumbar spine, has been recognized as being mechanically significant and has been the subject of multiple mechanical characterization studies in the past. Those studies, however, were performed on isolated tissue samples and thus could not assess the mechanical state of the ligament *in vivo*, where the constraints of attachment to rigid bone and the force of the joint pressure lead to non-zero strain even when the spine is not loaded. In the current work, we quantified these two effects using cadaveric lumbar spines (5 spines, 20 total facet joints harvested from L2-L5). The effect of joint pressure was measured by injecting saline into the joint space and tracking the 3-D capsule surface motion via digital image correlation, and the prestrain due to attachment was measured by dissecting a large section of the tissue from the bone and by tracking the motion between the on-bone and free states. We measured joint pressures of roughly 15-40kPa and local 1st principal strains of up to 25-50% when 0.3 mL of saline was injected into the joint space; the subsequent increase in pressure and strain were more modest for further increases in injection volume, possibly due to leakage of fluid from the joint. The largest stretches were in the bone-to-bone direction in the portions of the ligament spanning the joint space. When the ligament was released from the vertebrae, it shrank by an average of 4-5%, with local maximum (negative) principal strain values of up to 30%, on average. Based on these measurements and previous tests on isolated lumbar facet capsular ligaments, we conclude that the normal in vivo state of the facet capsular ligament is in tension, and that the collagen in the ligament is likely uncrimped even when the spine is not loaded.

3.2 Introduction

The lumbar facet capsular ligament, which contributes to the health and stability of the lumbar spine, connects adjacent vertebrae by spanning between, and fully encapsulating, the superior articular process of the inferior vertebra and the inferior articular process of the superior vertebra. The interfacing surfaces of the articular processes are covered with cartilage and are lubricated by the synovial fluid contained within the joint space. The articular processes, along with the synovium and synovial fluid, are considered the compressive load bearers of the joint, while the fibrous facet capsular ligament limits motion by resisting tensile loads [4], [6], [7]. The lumbar facet joints were previously reported [53] to bear 3-25% of a compressive load applied to the spine, such as body weight, with the remainder being shared by the intervertebral disc. The collagen fibers found within the facet capsular ligament's microstructure are highly aligned with a primary orientation in the bone-to-bone direction[26]. These collagen fibers are load-bearing under tension and are believed to help maintain spinal health by restricting harmful translations and rotations of adjacent vertebrae [4], [10].

Although the facet capsular ligament has been recognized as a possible source of low back pain (LBP) for over a century [21], prior LBP research has focused primarily on the intervertebral disc. To date, mechanical testing of the lumbar facet capsular ligament has been limited to planar mechanical tests of excised, off-bone samples, such as uniaxial [4], biaxial [10], or shear [11] testing. The facet capsular ligament's structural-mechanical relationship has been well defined with these tests, with key observations having been made about fiber alignment and measured tissue stiffness. Briefly, the mechanical response of the facet capsular ligament is nonlinear when stretched parallel to the primary collagen fiber alignment. There is a long toe region within which the elastin component may dominate the tissue's response while the collagen fibers remain crimped and unloaded [4], [10], [12]. In contrast, the ligament is more linear and more compliant in the transverse direction, and shear tests provide evidence of off-angle fibers contributing to the tissue's mechanics [11]. For these traditional planar mechanical tests, the facet capsular ligament is cut off the bone and flattened prior to testing, and it is not clear that the unloaded state of the free ligament is relevant to the in vivo, on-bone state. As a result, it is difficult to interpret the strain fields of the facet capsular ligament during physiologic motion [9] and to specify correctly the ligament state in whole-motion-segment finite-element models [13]. For example, the facet joint capsule may be pressurized due to the encapsulation of the synovial fluid within the joint cavity. Although there has been limited research on the pressure within *in vivo* facet capsular joints, previous studies on the contact pressure of adjacent articular facet surfaces of the lumbar spine observed peak contact pressures of up to 6.1 MPa on the dorsal region of the articular cartilage during combined loading [6]. A further study of contact pressure within the cervical spine observed mean contact pressures of 158 kPa during extension, with measured contact pressure varying across the articular surface [6], [54]. However, these studies do not consider the increase in contact pressure due to the fluid pressure alone. Additionally, these studies do not account for pressure increases during rapid, high load dynamic motions due to the relative incompressibility of the synovial fluid and little time for it to permeate out of the capsule space to retain baseline pressure. Further analysis on the strain contribution of pressurized facet capsular ligaments may help further our understanding of how facet joint effusions can lead to degenerative pathologies, such as spondylolisthesis [55].

In this study, we considered two factors so as to address the limited knowledge of the on-joint mechanical state:

(1) *Joint pressurization* via the encapsulated synovial fluid, measured by an inflation experiment on an intact cadaveric facet joint, and

(2) *Residual strain* in the ligament due to its attachment to the vertebrae, addressed by a study of deformation when the ligament is released from the bone.

3.3 Methods

3.3.1 Sample Preparation

Five donor lumbar spines (31M, 41F, 46M, 71M, 73F) were obtained through the Anatomy Bequest Program at the University of Minnesota, Twin Cities. Twenty facet capsular samples, from a variety of lumbar levels (L2-L5) and from both the left and right portion of the spine, were obtained from the donor spines. Each spine was scanned in a 3T MRI (Siemens MAGNEtoM Prisma) at the University of Minnesota Center for Magnetic

Resonance Research, and the health of the facet joint was graded on the Fujiwara scale [56]. The spine was cleared of the surrounding soft tissue to expose the posterior region of both the left and right L2-L5 facet capsular ligaments. To prepare the samples for strain tracking via digital image correlation, dried powdered Verhoeff-Van Gieson stain was used to speckle the surface of the facet capsular ligament samples [10], [11].

3.3.2 Inflation Testing

Each facet joint specimen (n=20) was injected with approximately 0.55 mL of 1% phosphate-buffered saline (PBS) at a rate of 1 mL/min by passing a needle (outer diameter of 0.53 mm) through the ligament and into the joint space between adjacent facet pairs. The chosen needle gauge was confirmed to be sufficiently small to pass into the joint space between adjacent articular processes by acquiring x-ray images of a representative sample (**Figure 10**). A pressure transducer (Harvard Apparatus) measured the pressure within the joint space for a given volume of injected PBS, and a baseline pressure drop due to flow through the needle was established prior to insertion into the joint space and subtracted from the measurement. The PBS was withdrawn from the joint space at the conclusion of the test to return the facet capsular ligament to its original, uninflated state and to prepare the sample for the residual strain test. Speckle displacements were tracked over the course of the experiment using open-source 3D strain-tracking software [57]; details can be found below in the section *3D Strain Tracking*.

***Figure 10** X-ray image of needle of the syringe pump inserted into the joint space of a L3L4 facet capsular ligament. The arrow denotes the needle inserted into the joint space.*

3.3.3 Residual Strain Testing

Following inflation testing, the facet capsular ligament was cut into a rectangular sample using a 15-blade scalpel, with the longer edge cuts occurring parallel to the spinous process (superior-inferior axis) and the shorter edge cuts occurring along the medial-lateral axis. Careful consideration was taken to prevent speckle smearing and to release the underside (anterior) of the ligament fully from the bone. The deformation of the ligament due to the release of the residual strain was continuously tracked in 3D.

3.3.4 3D Strain Tracking

Facet capsular ligament surface displacement was tracked in 3D using a three-camera stereo system (Canon EOS Rebel T3i with Canon 100 mm f/2.8 Macro lens, Canon EOS Rebel T3i with Canon 18-55 mm f/3.5-5.6 lens, and Canon EOS Rebel T2i with Canon 105mm Macro lens) with stereo planes of 15 degrees between adjacent camera pairs. A focal distance was chosen such that the entire sample was within the camera's field of view. Each camera recorded at 1920x1280 30fps, and videos were synced using an audio cue in Cyberlink PowerDirector 19.

A quarter-cylinder calibration object with a known, uniform speckling pattern was used to calibrate the three-camera system. The calibration object was placed on top of the sample and within the field of view of each camera at the start of testing. The calibration images were then analyzed, using MultiDIC [57], to relate the positions of the calibration pattern within the image to its known position in 3D space. This step also served to relate the positioning of the three cameras relative to one another with the calibration outputs. Reconstruction errors were calculated, and, due to incompatible overlap between adjacent camera pairs, the camera pair resulting in the lowest reconstruction error was chosen for further analysis. Samples with reconstruction errors under 10% were considered for further analysis.

Ligament strains were also analyzed using MultiDIC, which initially uses the open-source, subset based 2D strain tracking software NCorr [58], to calculate the speckle displacement from stereo-image pairs before a 3D reconstruction algorithm computes full-field 3D ligament displacement, surface strains, and other rigid-body motion. For the 2D portion of the analysis, a region of interest (ROI) was selected to include the released area and the area immediately surrounding it. Each ROI is discretized based on the specified subset size and spacing, and points correlated between images are triangulated into individual elements within the ROI. For inflation analysis, a subset size of 26 pixels and a subset spacing of 13 pixels was chosen for each sample. For residual strain analysis, a subset size of 40 pixels and a subset spacing of 20 pixels was chosen. Additionally, a backwards analysis was conducted on the residual strain to ensure that the chosen region of interest included only the portion of the ligament that was released from the bone. These subset sizes and spacing ensured that 3-5 speckles were viewed within the subset's region. The image dataset for the residual strain analysis included the same image of the undeformed sample, prior to inflation testing, as the inflation analysis image dataset. This process ensured that the deformations from each test were related back to the same undeformed, reference ligament configuration. All strains reported in this study are Green-Lagrangian strains.

Some portions of the ROI were untrackable due to a high normalized correlation coefficient between the tracked stereo images. A cut-off correlation coefficient of 0.7 was chosen to remove outliers due to bad tracking. Both increasing and decreasing area changes were observed in some samples. For this reason, the mean area change for a sample was calculated over the middle portion of the tracked ROI.

3.3.5 Analysis – Inflation Testing

Nine facet capsular ligament samples that leaked were removed from the inflation testing analysis, leaving a total of 11 facet capsular ligament samples taken from different lumbar motion segments (L2-L5). A relationship between inner capsular pressure and volume of injected saline was found for each inflated sample. For each point along the pressure-volume curve, the maximum area change was calculated for each sample as the largest surface Jacobian of the elements within the sample's strain-tracked region of interest that successfully tracked over the entire testing time span. Additionally, the maximum 1st principal strains (i.e., the largest eigenvalue of the strain tensor) were measured for the point at which the maximum area change occurs. An angle of the 1st principal strain was calculated in reference to the medial-lateral axis of the sample as the dot product of the 1st principal strain vector with the global medial-lateral axis. A positive angle is defined as clockwise towards the superior direction of a given sample. To represent more clearly the deformation of the ligament in 3D space during inflation, the 2D change in curvature for the ligament was also calculated. An estimate of the facet joint location was obtained by overlaying the 3D ligament surface obtained from strain tracking onto the segmented bone geometries for each representative sample.

3.3.6 Analysis – Residual Strain Testing

The mean surface area change during the residual strain test was calculated as the determinant of the resulting surface deformation gradient tensor from 3D strain tracking. The mean area change was calculated for all elements in the tracked ROI as well as for the center portion of the tracked ROI. As in the inflation tests, the center portion was examined to reduce the influence of any outlier elements on the outside edge of the ROI.

3.3.7 Analysis – Total Deformation

For the eleven samples that underwent both inflation and residual strain analysis, three deformation tensors were obtained for each discretized element on the tracked ROI related by the formula (**Figure 11**):

$$\boldsymbol{F} = \boldsymbol{F}_{\boldsymbol{I}}\,\boldsymbol{F}_{\boldsymbol{R}}^{-1} \tag{3.1}$$

The three deformation gradients are as follows:

- $\boldsymbol{F}$ is the deformation from the truly unloaded tissue state to the inflated state, representing the deformation state of the facet capsular ligament on a pressurized joint with no other loading,
- $\boldsymbol{F_I}$ is the deformation experienced by the facet capsular ligament on the joint from the uninflated to the inflated state, and
- $\boldsymbol{F_R}^{-1}$ is the deformation form the truly unloaded tissue state to the uninflated on-joint state. This tensor is the inverse of the deformation gradient calculated when the tissue was released from the bone.

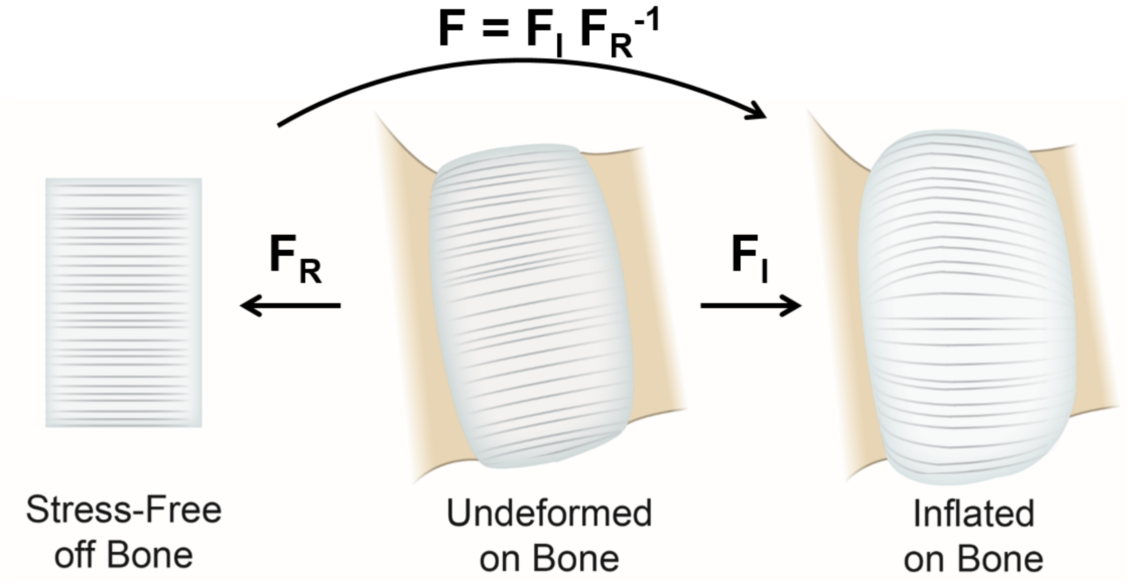

Figure 11 *Posterior view of the FCL in a stress-free state, the unloaded on-bone state, and the inflated state. The total deformation (F) of the ligament from its stress-free configuration is the combined deformation of the residual and inflated states.*

3.3.8 Statistical Analysis

The relationship between the area change when maximally inflated and the area change when release during the residual strain test was determined by plotting each area change for a given element on the tracked ROI. Linear regression was performed to determine the relationship and its significance. This process was repeated to determine the relationship between 1st principal strain during inflation and 1st contractile strain upon release. All values are shown as mean ± 95% confidence interval (CI).

3.3.9 Comparison to Facet Capsular Strains during Physiological Motion

For a better understanding of the contribution of joint pressurization and residual strain on total ligament strain, the principal strains during flexion reported by Ianuzzi et al. [9] were recalculated to include both contributions. The global coordinate system was chosen to match [9] where E_1 during flexion was observed to most closely align in the medial-lateral direction and E_2 in the superior-inferior direction. A representative element within the tracked ROI was chosen from the representative sample 1 and used for the analysis. The total deformation tensor accounting for joint motion, inflation, and residual strain was obtained by the following:

$$F_T = F_M F_I' F_R'^{-1} \tag{3.2}$$

The four deformation gradients are as follows:

- $\boldsymbol{F_T}$ is the deformation from the undeformed state to the inflated state with joint motion, representing the deformation state of the facet capsular ligament on a pressurized joint with physiological motion,
- $\boldsymbol{F_M}$ is the deformation experienced during flexion for a left L3L4 motion segment, calculated from [9],
- $\boldsymbol{F_I'}$ is the deformation experienced from the uninflated to the inflated state with an injected volume of 0.5 mL, and rotated into the coordinate system described in [9]
- $\boldsymbol{F_R'^{-1}}$ is the deformation from the truly unloaded tissue state to the uninflated on-joint state. This tensor is rotated from its local coordinate system into the global coordinate system described in Ianuzzi, et al. [9]

The Green-Lagrangian strain tensor was then calculated from $\boldsymbol{F_T}$. E_1 is the largest eigenvalue and E_2 was the smallest eigenvalue of the strain tensor.

3.4 Results

3.4.1 Inflation of the Joint Space

Contrary to the nonlinear behavior of off-bone planar samples, pressure within the joint space increased linearly with volume for most samples, but there were some samples that exhibited an initial linear increase in pressure with volume before tapering off (**Figure 12**a). This sublinear response may have been due to minor leakage of the joint fluid or a shift in the facet joints that relieved some of the pressure. Despite a variance in the lumbar spine levels, ranging from L2-L3 to L4-L5, of the facet capsules studied, most samples had very similar initial slopes. For injected volumes up to 0.25 mL, the volumetric compliance (i.e., the inverse slope of the lines in **Figure 12**a) over the samples was 0.011 ± 0.0018 mL/kPa (mean ± 95% CI). The maximum local area change (**Figure 12**b) and 1st principal strain at maximum area change (**Figure 12**c) showed considerably more spread.

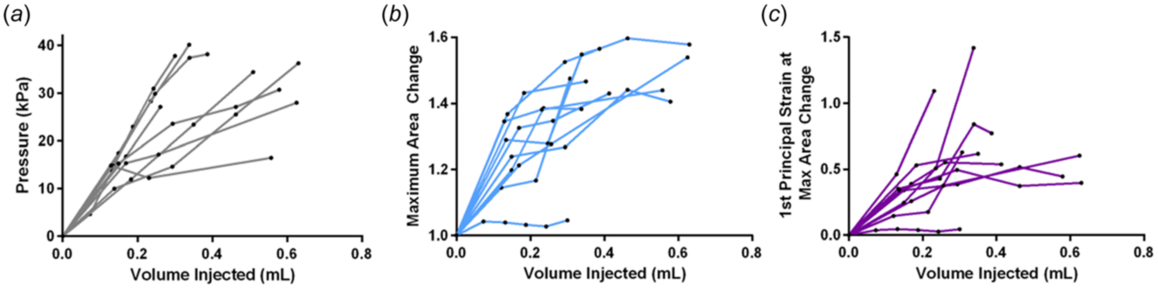

***Figure 12 a**.) The pressure-volume relationship of the capsular joint space of all inflated samples. **b**.) The maximum area change vs. volume of injected saline for each sample. **c.)** The 1st principal strain at the location of maximum area change vs. volume of injected saline.*

Looking into three representative samples in more detail, we can see that the greatest principal strains are observed in two locations: (1) the portion of the ligament spanning across the joint gap, and (2) the portion of the ligament at the enthesis (**Figure 13**). A rough estimate of the bone location under the facet capsular ligament is shown in **Figure 13** a1-a3. This effect is most clearly shown in Sample 1 (**Figure 13** a1,b1, and d1). The direction of the 1st principal strain is generally in the bone-to-bone direction (**Figure 13** b1), which ranges from 15-70 degrees in the axial plane in the lumbar spine, with larger angles towards the lower L4 – L5 spine region [6], [59]. In the case of sample 1, the 1st principal strain is oriented from bone-to-bone. Similarly, although to a lesser degree, the same trend is observed in Sample 2 (**Figure 13** b3 & d3). Here the maximum 1st principal strain is observed in the portion of the ligament spanning the joint gap and closest to the site of needle insertion. The direction of max 1st principal strain (**Figure 13**b2-b3) is oriented bone-to-bone in the region with the highest 1st principal strain (**Figure 13**d2-d3).

Figure 14a displays the location of two slices taken from the 3D strain tracking results of sample 1. One slice runs roughly bone to bone, and the other along a bone surface. The greatest change in the surface contour is observed in the portion of the ligament that spans across the joint gap (**Figure 14**b vs c). This region initially inflates outwards before a pressure threshold is surpassed, at which point the two facet surfaces move away from each other and the joint gap is further inflated. The behavior is reflected in the slices at three pressures: (1) uninflated at P = 0 kPa, (2) outward inflation at P = 10 kPa, and (3) outward inflation with facet motion at P = 36 kPa. A slice along the joint shown in **Figure 14**c shows different behavior. The slice, taken close to the enthesis of the facet capsular ligament, exhibits very little deformation. For this representative sample, the change in curve length at maximum inflation with facet motion, when the pressure = 36 kPa, in the bone- to-bone direction is +4.63% compared to -1.46% along the joint direction.

Summarizing the inflation results, we saw a nearly linear pressure-volume relationship for the joint space during inflation, with a heterogeneous strain field arising in the facet capsular ligament. The largest principal strains, which were on the order of 50% for a joint volume of 0.3 mL for most samples, occurred in the region of the facet capsular ligament above the joint space and in the bone-to-bone direction.

3.4.2 Release of Residual Strains

Viewed grossly, the facet capsular ligament shrank upon release from its attachments to the vertebrae. The area change upon release is shown in **Figure 15** for the same samples as in **Figure 13**. To avoid confusion, in this section and in **Figure 15**, we use the phrase "1st contractile strain" to mean the more negative of the two eigenvalues of the strain tensor, and its corresponding eigenvector. There was no clear primary direction of contraction, with the majority of contraction upon release occurring in the bone-to-bone (**Figure 15**a1) or along-bone (**Figure 15**a2) direction. Tissue retraction was roughly uniform, with 1st contractile strain values mostly in the range -0.05 to -0.1% (**Figure 15**c1-c3) Similar behavior was seen in the area change (**Figure 15** d1-d3) with values in the range of 0.9 to 1. The red outline in **Figure 15** d1-d3 depict the same tracked ROI in its undeformed state. When tissue contraction was particularly small, as observed in Sample 3, the edges of the undeformed ROI almost perfectly overlap with those of the deformed ROI (**Figure 15** d3).

Sample 1 showed nonuniform area change with higher measurements found at the edge of the tracked ROI, possibly due to edge effects that were not resolved with the correlation coefficient (**Figure 15** d1). Both sample 2 and sample 3 appear to have a uniform area change across the surface of each ligament (**Figure 15** d2-d3) with mean area changes of 0.910 and 0.957 for all tracked points in the ROI, respectively.

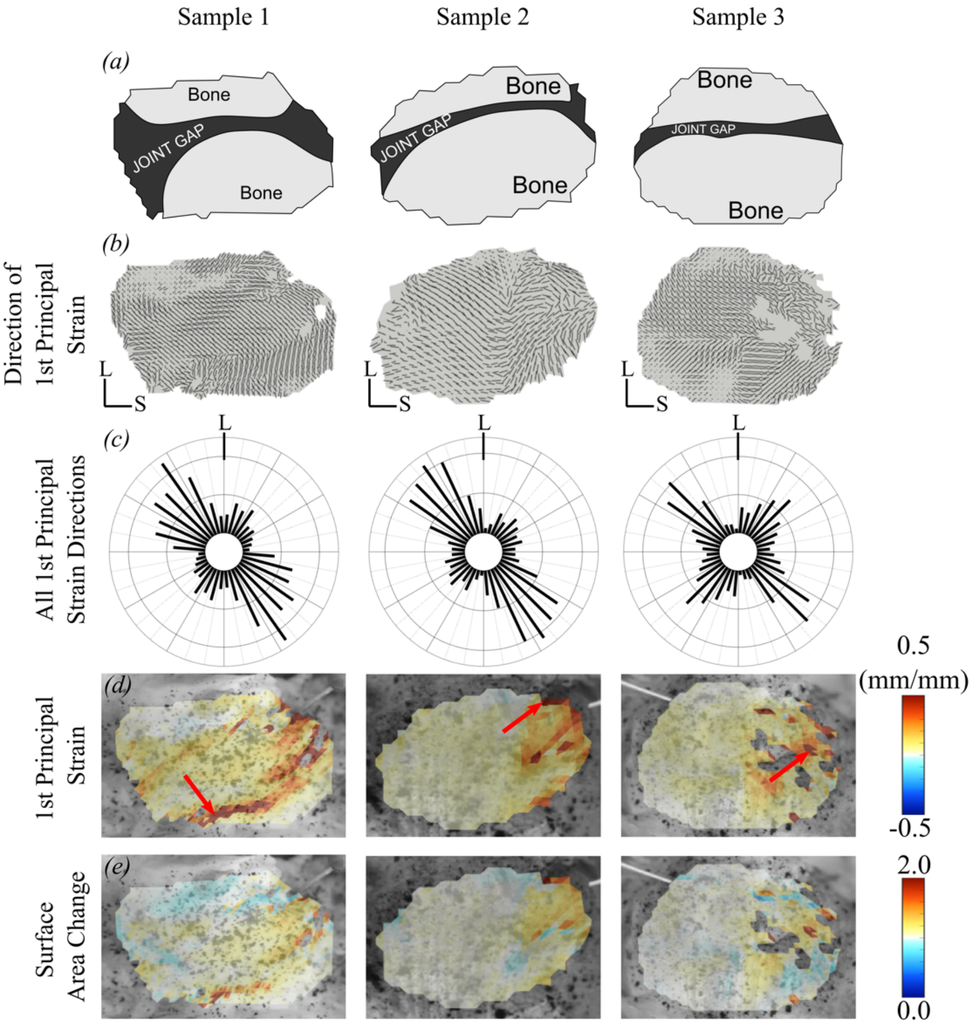

Figure 13 a.) *The location of the facet joint within the ROI estimated from the overlay of the tracked ROI onto CT segmentation of three representative samples.* ***b-c.)*** *The direction of and* ***d.)*** *the maximum principal strain fields at maximum inflation for three representative samples. The angles shown in* ***c.)*** *are the principal direction with respect to the medial-lateral axis of a sample. Red arrows denote the location of maximum strain. Sample 1 and 2 are from the left side. Sample 3 is from the right side; images of sample 3 are mirrored for easier comparison to samples 1 and 2. The needle tip for each sample can be seen in the upper right corner of each image for sample 1 and 2 and in the upper left corner of the image for sample 3. Axes denote the superior (S) and lateral (L) direction for each sample.* ***e.)*** *The surface area change at maximum inflation.*

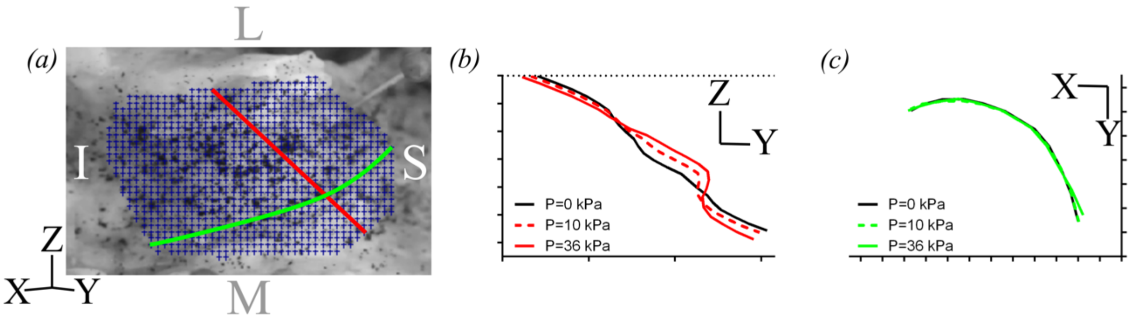

Figure 14 *Anatomy is as described in* ***Figure 13*** *a-c.* ***a.)*** *En face image of sample 1 (same as* ***Figure 13****a) with lines drawn in the bone-to-bone (thick red line) and along-bone (thin green line) direction.* ***b.)*** *Surface contour along bone-to-bone line shows motion upon outward inflation (P = 10 kPa) and inflation with facet motion (P = 36 kPa).* ***c.)*** *Along-bone line shows no significant motion because of anchorage to the bone. The superior (S), inferior (I), medial (M), and lateral (L) are shown on the representative sample in panel A. Tick spacing in panel b and c is 2mm.*

The distribution of the 1st principal strains during inflation and the 1st contractile strains upon release for all samples is shown in **Figure 16**. The direction of the principal and contractile strain is the angle off the medial-lateral axis, which is taken as being the bone-to-bone direction, with a positive angle behind defined towards the superior axis for a given sample. The average 1st principal strains for the tracked elements within all samples was 0.11 ± 0.0070 mm/mm (**Figure 16**a), with a predominate alignment ±55° off of the medial-lateral axis (**Figure 16**b). The average magnitude of 1st contractile strain for all tracked elements in all samples was -0.078 ± 0.0019 mm/mm (**Figure 16**c). The 1st contractile strains were less aligned, with a peak angle of 50° off the medial-lateral axis but with a relatively high frequency of strains aligned between 120-160° (**Figure 16**d).

Figure 7 shows a summary of the area change, 1st principal strain, and 1st contractile strain for all samples. The mean area change over all tracked points within the ROI was 0.953 ± 0.017, indicating roughly 5% area loss upon release (**Figure 17**a). The average area change for elements within the middle portion of the total tracked ROI was 0.965 ± 0.016. The mean area change at maximum inflation was 1.014 ± 0.011 (**Figure 17**b). **Figure 17**c displays the spread of all elements' area change due to residual strain and maximum inflation. Each point represents a single element within the tracked ROI for both the inflation experiment and the residual strain experiment. There was a slight positive

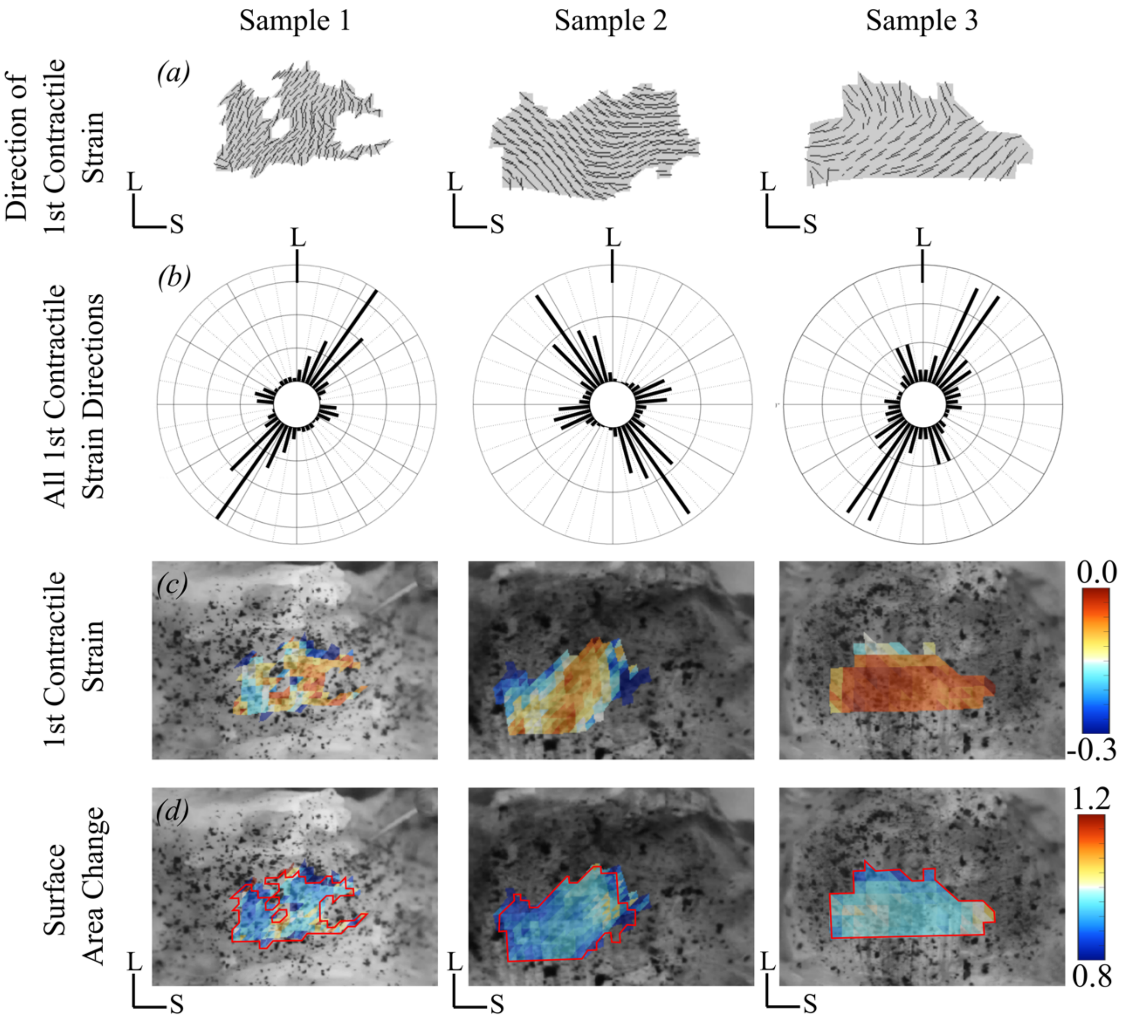

Figure 15 a-b.) *The direction and* ***c.)*** *magnitude of the 1st contractile strain, measured as the most negative eigenvalue of the strain tensor and its corresponding eigenvector, of the same three representative samples shown in* ***Figure 13****. The angles shown in B. are the component of the 1st contractile strain vector with respect to the medial-lateral axis of the sample.* ***d.)*** *The surface area change across the tracked ROI for the residual strain test. Area change and 1st contractile strain are shown in 2D on the undeformed sample surface. The red outline in d. depicts the size and shape of the undeformed ROI for each of the three samples. Axes denote the superior (S) and lateral (L) direction for each sample.*

correlation between the area change during inflation and the area change upon release ($r^2 = 0.015$, $p < 0.0001$). It appeared that portions of the facet capsular ligament that contracted more during the residual strain test had a smaller area change when inflated. However, the r^2 value is reported very close to zero, so any relationship between the two measurements may be influenced by outliers beyond the 20% area change. To eliminate the extreme values, **Figure 17**d zooms in on a portion of the graph in **Figure 17**c. The mean max 1st contractile strain for all tracked points and the middle portion was -0.283 ± 0.043 and -0.223 ± 0.041, respectively (**Figure 17**e), while the mean max 1st principal strain during inflation was 0.588 ± 0.226 (**Figure 17**f). The relationship between the 1st contractile strain upon release and the 1st principal strain upon inflation for each element for all samples is shown in **Figure 17**g. The equation $Y = -0.048*X - 0.057$, with $r^2 = 0.003$ and P value = 0.002, was fit to all the data points in all samples tracked in both the residual strain test and the inflation test. There was little to no relationship between the 1st contractile strain and the 1st principal strain. Again, **Figure 17**h zooms in on a portion of the graph in **Figure 17**g.

To summarize, the facet capsular ligament shrank upon release from the bone, with no clear primary direction of contraction. However, most samples appeared to contract either bone-to-bone or along the bone (**Figure 15** a1-a3). Due to the anatomy of the facet joint and the location of the joint gap within the ROI of the tracked samples, most samples were released with the majority of the ligament over and attached to the bone. Consequently, the tissue contracted about 4-5% upon release (**Figure 17**a). There was neither a clear correlation between area change upon release and upon inflation (**Figure 17**c-d) nor with the 1st contraction strain upon release and 1st principal strain upon inflation (**Figure 17** g-h).

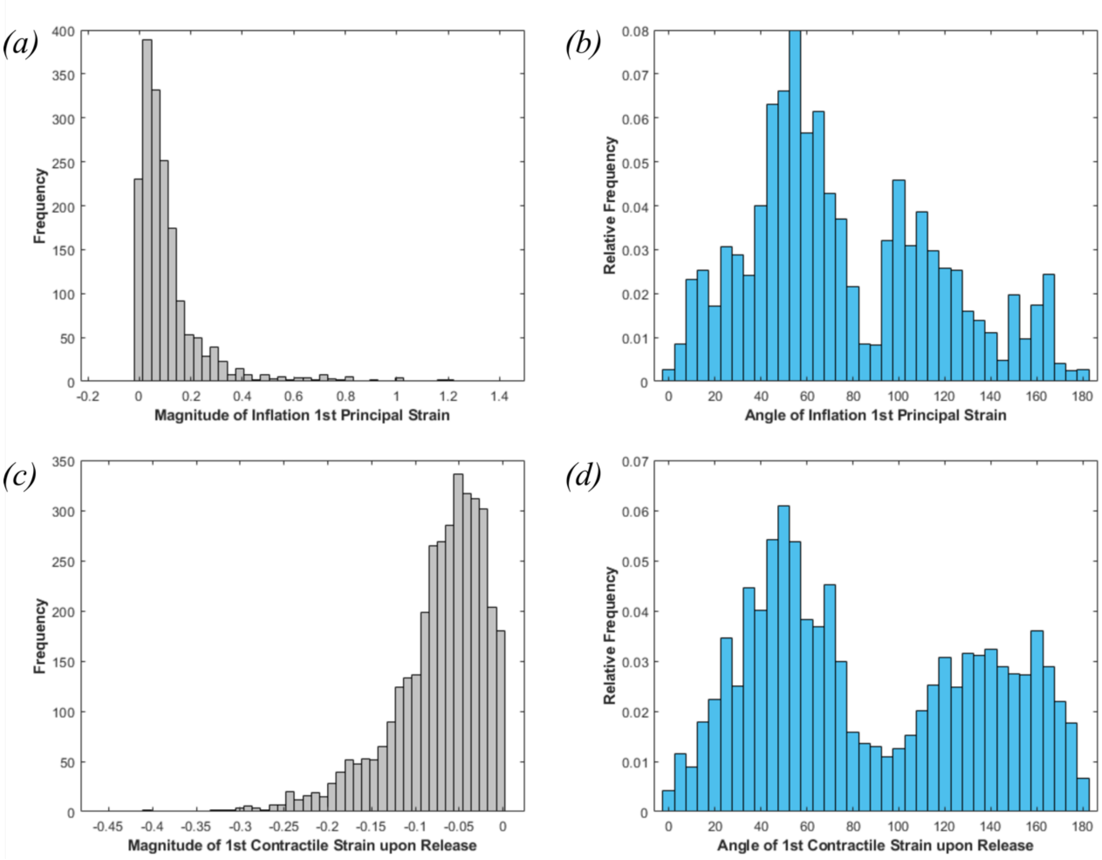

***Figure 16** The distributions of the **a.)** magnitude and **b.)** direction with respect to the medial-lateral axis of the 1^{st} principal strain during inflation for all samples. Similarly, the distributions of the **c.)** magnitude and **d.)** direction, with respect to the medial-lateral axis, of the 1^{st} contractile strain upon release for all samples. The direction of the inflation and residual strain vectors are weighted by the element's magnitude of the strain and normalized to the total magnitude of all samples.*

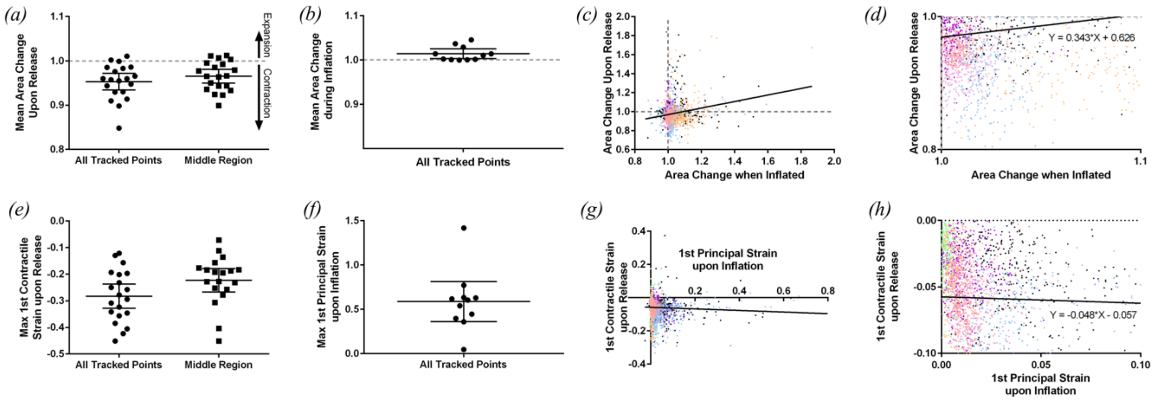

***Figure 17 a.)** The average surface area change tracked in the ROI during the residual strain test. Both the results for all tracked points as well as points taken from the middle region of the ROI are shown. The grey line indicates no area change on release. **b.)** The average surface area change in the ROI during maximum inflation **c.)** Plot of the area change during inflation versus the area change upon release for every element within the ROI. Only samples that inflated and released successfully are shown. **d.)** Zooms in on a region of interest of the data presented in (**c**). **e.)** The maximum 1st contractile strain upon release across the entire tracked ROI as well as points taken from the middle region of the ROI to reduce error due to boundary outliers. **f.)** The max 1st principal strain during maximum inflation and **g.)** a plot of 1st contractile strain during release versus 1st principal strain during inflation for each element with the ROI of all samples, with **h.)** a zoom in on a region of interest.*

3.4.3 Total Deformation of In Situ Facet Capsular Ligament Samples

To account for the combined effect of residual strain and joint pressurization, the total deformation due to both was calculated; the results for sample 1 are shown as surface area changes in **Figure 18**. To clarify, the residual surface area change is the hypothetical deformation required to take a planar, off-joint sample and place it back on the joint (**Figure 18**a). This deformation gradient is calculated as the inverse of the deformation gradient tensor of the residual strain test. Due to the current absence of in situ facet capsular ligament joint capsule pressure measurements, we have shown the total deformation at three pressure levels: approximately 12 kPa (low), 22 kPa (mid), and 36 kPa (high) (**Figure 18**b-d). The residual surface area change shown in **Figure 18**a appears as the dominant strain in the total strain state (**Figure 18**b-d). This may be due to less overlap between the area observed during inflation and the tracked area during the residual strain test.

Figure 19 demonstrates the change in the observed on-joint ligament strains with motion when including the joint pressurization and residual strain contribution, calculated as described under Methods in *__Comparison to Facet Capsular Strains during Physiological Motion__*. The black line, labeled M, is the principal strains on an on-joint left L3L4 facet capsular ligament due to flexion as measured by Ianuzzi *et al.* [9]. The blue line, labeled M + I + R, represents the principal strains on the ligament due to joint pressurization, residual strain, and joint motion. The inflation contribution, labeled I, added 20% strain in the E_1, or superior-inferior, direction. The residual strain contributions, labeled R, an addition 4% strain in the E_1 direction, giving a total of 24% strain on the ligament before spinal motion. This indicates that the collagen fibers are in tension in both the E_1 (bone-to-bone) and E_2 (alone-joint) direction before the addition of spinal motions such as flexion.

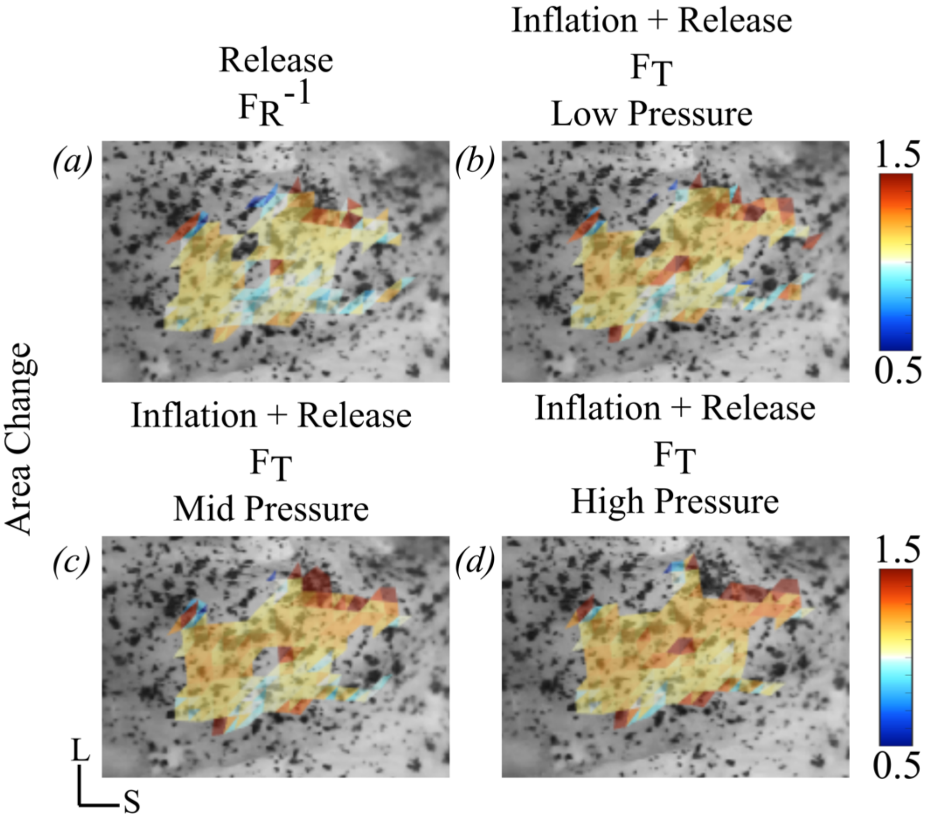

Figure 18 *The surface area change for sample 1* ***a.)*** *needed to place the off-bone, planar ligament back on to its on-joint state, as well as the total deformation due to residual strain and pressurization to roughly* ***b.)*** *12 kPa,* ***c.)*** *22 kPa and,* ***d.)*** *36 kPa are shown. All surface area changes are shown in 2D on the undeformed ligament surface.*

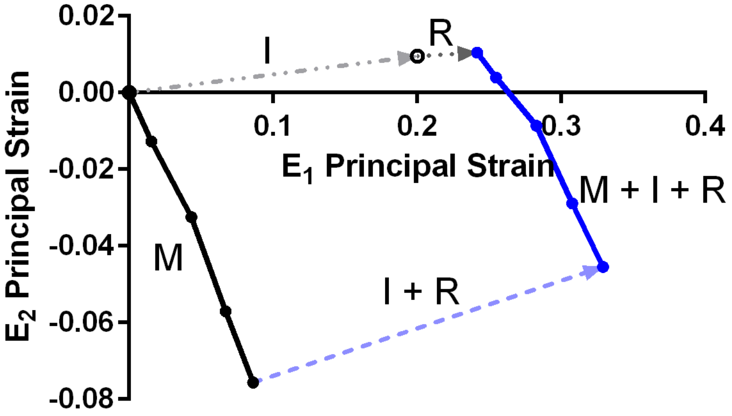

Figure 19 *E_1 and E_2 lumbar facet joint capsule strains during joint motion (M), residual strain (R), and inflation (I) strain for an injected volume of approximately 0.5 mL. Strains for joint motion were obtained from Ianuzzi et al. in their study of facet capsular ligament strains during flexion. The new total strain was calculated to include the contributions from joint pressurization and the residual strain, in addition to those observed on the ligament during flexion. E_1 was aligned in the medial-lateral direction and E_2 was aligned in the superior-inferior direction.*

3.5 Discussion

In this study, we measured the facet capsular ligament strains due to both joint pressurization and residual strain, both of which have been unaccounted for in previous studies that characterized the facet capsular ligament with planar mechanical tests. Using 3D strain tracking, we determined ligament strain at a given volume of injected saline, as well as the inner capsular pressure (**Figure 12**, **Figure 13**). We also measured contraction of the ligament upon the release of the residual strain (**Figure 15**). To our knowledge, this is the first study of the deformation state of the facet capsular ligament on an unloaded joint, providing a bridge between the results of previous whole lumbar spine studies [9] and traditional planar mechanical testing of isolated lumbar facet capsular ligaments [4], [10], [11], [24], [46].

The major conclusion of this study is that even when the spine is not loaded, the facet capsular ligament is under constant tensile strain due to its attachment to the bone and the influence of the joint pressure (**Figure 15** & **Figure 17**). The strain is not merely a non-zero quantity but could have mechanical significance for in vivo function of the lumbar facet capsular ligament. The toe region for uniaxial loading of the lumbar facet capsular ligament is roughly 10-12 % strain [4], [12], and for biaxial loading it is roughly 6-8 % strain [10], [60], measured from the true undeformed state. These numbers are comparable to the strains we calculated for the facet capsular ligament due to prestrain and joint pressure, suggesting that the collagen fibers in the facet capsular ligament are never crimped in vivo, or perhaps only in the case of a spinal motion that would put the facet capsular ligament into compression relative to the neutral spine state. This result has bearing on whole-joint models of the lumbar spine [13], [14], [16] and on attempts to use in vitro experimental data to understand in vivo tissue mechanics [17], [24]. For example, an analysis based on facet capsular ligament strain from its true unloaded state rather than from the neutral spine state would overestimate the facet capsular ligament laxity at low strains and thus would overestimate the range of motion for any motion restricted by the facet capsular ligament.

The range of pressures in the lumbar facet joint is, to our knowledge, unmeasured. Jaumard *et al*. [6], [54] measured the joint pressure in the cervical facet joint, but their device measured the pressure on the cartilage surface, not the pressurization of the synovial fluid. It is conceivable that the joint pressure could be measured via an instrumented syringe during intra-articular injection for low back pain, but to our knowledge, no such measurement has been made; since such injections are typically 0.5-1.5 ml [61] it might also be possible to measure the joint pressure-volume relationship in vivo. Our cadaveric joint results showed a significant pressure rise for 0.5 ml of injection (**Figure 12**), however, without knowing the *in vivo* pressure range of the joint capsule, the applicability of our inflation results are unknown. Our study is also limited to characterizing the truly undeformed state of the lumbar facet capsular ligament from isolated donor spine units, without musculature or body weight, which is not the true resting state *in vivo*. Additionally, in our study the facet joints are unconstrained which, when pressurized, may cause motions that are potentially not possible *in vivo*. Computationally modeling the results of our study with realistic geometries and boundary conditions may provide further insights into the significance of these limitations.

There was a great degree of variability observed in the direction of the 1st principal and 1st contractile strain (**Figure 13**b-c, **Figure 15**a-b, **Figure 16**). Some samples displayed a clear predominate direction of 1st principal strain, aligning roughly in the bone-to-bone direction (**Figure 13** b1-b2), while others had a less clear preference (**Figure 13** b3). Difference in the location and direction of the highest strain in the facet capsular ligament joint gap region may be due to the increase in angle from the axial plane of the two articulating facet surfaces. The orientation angle of the two surfaces, and thus that of the joint gap, becomes more aligned in the sagittal plane further down the lumbar spine [6]. Sample 1 and 2 were both taken from the left facet capsular ligament. Sample 3, however, was taken from the right side of the spinous process. This is observed to a lesser degree in the direction of the 1st contractile strain upon release (**Figure 15**a-b), however, the amount of trackable area is smaller than in inflation. While the sum distribution of all 1st contractile strain directions has a peak angle of 50° off the medial-lateral axis, a bimodal distribution is observed with strain directions occurring 100-120° off the medial-lateral axis with a high relative frequency (**Figure 16**d). Although the overall fiber alignment is taken as being bone-to-bone, previous studies have demonstrated a high degree of heterogeneity in the local collagen fiber orientation [23]. Further studies on the relationship between the direction of the principal strains and the predominate local alignment of the collagen microstructure are needed to explain this variability and the lack of correlation seen between the 1st principal inflation strain and the 1st contractile strain (**Figure 17**c-d & g-h).

Previous studies have demonstrated that planar off-bone facet capsular ligament samples are uncrimped until about 16% stretch [12]. We determined the total ligament strain from a truly unloaded, planar state to being on-joint with applied motion by adding the contributions due to joint pressurization and residual strain to the on-joint strain observation by Ianuzzi et al. [9]. We looked at the strains due to flexion for a left L3L4 sample with primary axis in the medial-lateral (E_1) direction and superior-inferior (E_2) (**Figure 19**). The largest magnitude strains were those in the E_1 direction. Considering that this is roughly the bone-to-bone direction, the strains due to inflation and residual strain have the potential to uncrimp the collagen fibers fully from the truly unloaded to the on-joint state without considering an additional strain due to joint motion (**Figure 19**). The collagen fibers in the facet capsular ligament on a pressurized joint are in tension before motion causing the on-joint observation of ligament strain fields to underestimate the total applied strain.

The potential role of fluid pressurization in determining the lumbar facet capsular ligament's mechanical state also suggests that one may need to consider how the available facet joint volume changes during spinal motion. If a motion causes the joint space to lose volume, and the synovial fluid cannot escape quickly, it would be expected that the fluid would pressurize and push the facet capsular ligament out so as to maintain volume; a similar but opposite effect would be seen if the joint space volume were increased, possibly creating a negative (suction) pressure and pulling the facet capsular ligament into the joint space. If the configuration were maintained for an extended period of time, however, synovial fluid turnover could allow re-equilibration of the joint pressure within the facet capsular ligament.

The potential role of pressurization also compels some discussion of the anatomy of the lumbar facet capsular ligament, which contains an inner elastin-rich layer and an outer collagen-rich layer [12], [26]. By analogy with arterial wall mechanics, we can hypothesize that the elastin component provides elastic restoration under small loads, such as might arise due to synovial fluid pressurization during normal motions, and the collagen component provides stiffness resistance to pressure overload, due to abnormal motions. This hypothesis could be explored in various ways, including leveraging the large volume of work and methodological development for arterial mechanics.

4 Exploring On-Joint Mechanics of the Lumbar Facet Capsular Ligament: Accounting for Residual Strain, Joint Pressurization and Microstructural Heterogeneity

The contents of the chapter are in preparation to be submitted as a journal article by Gacek, Ellingson, and Barocas.

4.1 Summary

Modeling the lumbar facet capsular ligament's mechanical behavior under various physiological motions has often been a challenge due to limited knowledge about the on-joint ligament loads arising from attachment to the bone or other internal loads. Building on prior work, this study presents an enhanced computational model incorporating residual strain, joint pressurization strain, and through-thickness variation of collagen and elastin distribution, factors often neglected in prior models. Further, the model can predict strain and stress distribution across the ligament under various spinal motions, highlighting the influence of the ligament's attachment to the bone, internal synovial fluid pressurization, and distribution of collagen fiber alignment. Joint space inflation was found to notably influence the total observed stress and strain fields, both at rest and during motion. A significant portion of the ligament was found to be in tension, even in the absence of external load. Additionally, the model's ability to account for strain in the predominate collagen fiber direction offers a more realistic portrayal of the collagen fibers and elastin matrix’s role in ligament mechanics. This study's findings could significantly enhance our understanding of spine and ligament biomechanics, bone health, and could potentially contribute to prevention strategies for spinal diseases and instabilities. It also expresses important considerations for modeling the lumbar facet capsular ligament or other synovial ligaments.

4.2 Introduction

The lumbar facet capsular ligament (LFCL) is a vital component of the lumbar spine, playing a crucial role in maintaining spinal stability. Despite its significance, the LFCL has historically received less attention than the interverbal disc and spinal muscles, especially as a possible source of lower back pain, which serves as the leading cause of activity limitation among individuals under the age of 45 and imposes considerable financial burden [62], [63]. However, recent advances in computational model have allowed us to model the complex behavior of the lumbar facet capsular ligament and its implication for spinal health and degeneration.

Most biomechanical scientific research on disease and degeneration of the LFCL fails to translate between microstructural phenomenon and macroscale motion and medical therapeutics. This is, in part, due to a technological limitation on imaging and measuring ligament behavior *in vivo* and with no clear experimental link between clinical studies and their benchtop counterparts. In recent years, advances in computational modeling techniques have provided a powerful tool to simulate the complex behavior of soft tissues under various loading conditions and have allowed us to bridge the experimental-clinical gap by circumventing many of the limitations experienced in traditional experiments. Finite element modeling is often used for performing material parameter extraction on various tissues with realistic boundary conditions [10], [12], [13], analyzing macroscale tissue deformations driven by microstructural mechanics[16], [23], [25], and as a method of estimating the growth and remodeling phenomenon of soft tissues in response to its local microenvironment [19]. More importantly, finite element modeling has the potential to link measurable experimental metrics, such as ligament strain, with unmeasurable quantities that drive tissue failure and degeneration, such as ligament stress, paving the way for improved therapeutic strategies for disease and degeneration. Unfortunately, there exists a fundamental challenge when developing biomechanical finite element models that the unloaded configuration of the tissue is often unknown, as is the *in situ* loading state – even in the absence of external loads on the joint.

In this study, we build upon the lumbar facet capsular ligament computational model of Zarei *et al.* [16], which links macroscale spinal motions with microscale ligament deformations. We further explore the impact of the facet capsular ligament's microstructural composites, inner capsular pressure, and residual strain on the observed stress and strain fields across the ligament. Initially, we expanded the model by incorporating inner capsular pressure and residual strain, as previously measured in Gacek *et al.*[18], to evaluate the lumbar facet capsular ligament's response under physiological spinal motions and compare it to a non-pressurized, zero-stress ligament. Next, we investigated the influence of the collagen and elastin layer on ligament mechanics by altering the concentration of each component throughout the thickness of the ligament and measuring the response under identical spinal motions. Thus, we computationally evaluate the hypothesis that the lumbar facet capsular ligament remains in tension even when it is unstretched or compressed relative to the neutral joint position.

4.3 Methods

The first step was to build upon the foundational work of both the lumbar spine finite element model of Ellingson *et al.* [14] and the facet capsular ligament multiscale model framework of Zarei *et al.* [16]. The macroscale boundary conditions provided by the ligament's attachment to the boney facets were obtained by simulating desired L4L5 motion using the model of Ellingson *et al.* [14]. We studied the effect of 6 spinal motions on ligament mechanics: flexion, extension, ipsilateral and contralateral bending, and ipsilateral and contralateral axial rotation. The L5 vertebrae remained fixed in space. Each motion was simulated by first applying a downwards, axial load of 500N to the L4 vertebrae to simulate body weight, followed by a 7.5 Nm moment in the desired direction of motion. The resulting displacements and rotations (U_x, U_y, U_z, R_x, R_y, and R_z) of the reference point of the L4 vertebral rigid body was passed down to the smaller-scale model of the lumbar facet capsular ligament (**Figure 20**).

An existing finite element representation of the L4L5 facet capsular ligament, with realistic microstructural fiber alignment and orientation and as described in [16], [23], [24], was used. Briefly, a geometric model of the ligament was obtained via μ-CT and morphed onto the facet joint geometries of the L4L5 motion segment model (Abaqus 2018). Realistic fiber architecture was obtained by analyzing fiber orientation and alignment from

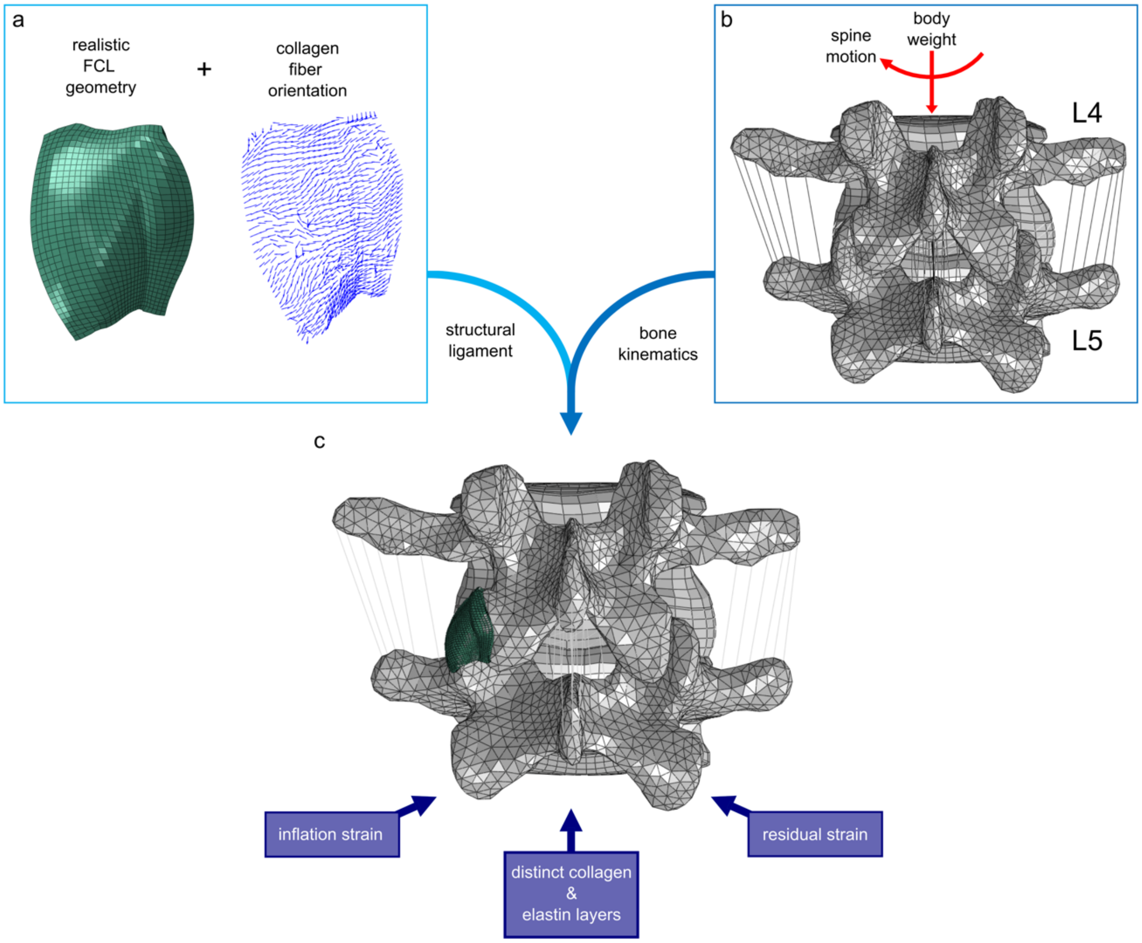

Figure 20 - The model setup: *The enhanced model combines* ***(a)*** *realistic lumbar facet capsular ligament (LFCL) geometry with structural fiber orientation data* [16] *and* ***(b)*** *the bone kinematics obtained from a L4L5 motion segment model* [14]. *Body weight and a moment to simulate desired spinal motions were applied.* ***(c)*** *Final model includes contribution from inflation of the joint space, residual strain, and through-thickness variation between the collagen and elastin regions.*

polarization-sensitive optical coherence tomography of 6 donor lumbar facet capsular ligaments. The spatial distribution of fiber alignment was then morphed over the finite element representation of the L4-L5 facet capsular ligament such that each element had a unique primary fiber direction and degree of alignment. While the geometry of the L4-L5 facet capsular ligament remained consistent across all models, the 6 resultant FCL models reflect the sample-specific microstructure of the 6 distinct donor samples.

The ligament model was assembled using FEBioStudio 1.9.0. The original lumbar facet capsular ligament model geometry had one layer of elements through the thickness of the tissue. For more resolution, the model was partitioned to have 6 layers of hex8 elements through the thickness of the ligament, for a total of 5,400 hex8 elements. The ligament was partitioned to preserve the unique, sample-specific fiber architectures of the original models of Zarei *et al.* [16]. Each set of element partitions was modeled using a hyperelastic strain energy density function in which the collagen fibers were modeled as a coupled solid mixture with a single fiber family embedded in a compressible neo-Hookean matrix representing the elastin fibers. The primary alignment direction of the fiber family was set to match the fiber distribution measured in the 6 donor samples from Zarei *et al.* The strain energy density function of the neo-Hookean matrix is as follows:

$$W = \frac{\mu}{2}(I_1 - 3) - \mu \ln J + \frac{\lambda}{2}(\ln J)^2 \tag{4.1}$$

where μ and λ are the Lamé parameters; I_1 is the first invariant (i.e., the trace) of the right Cauchy-Green tensor ($I_1 = C_{ii}$; $C_{ij} = F_{ki}F_{kj}$), and J is the determinant of the deformation gradient tensor F [64]. The collagen fibers were modeled using an exponential fiber constitutive equation:

$$\psi_n(I_n) = \frac{\xi}{\alpha\beta}\left(\exp^{\alpha(I_n - 1)^\beta} - 1\right) \tag{4.2}$$

where ξ is the fiber small-strain modulus, α and β are the coefficient and power of the exponential, respectively, and I_n is the square of stretch in fiber direction. A 2D von Mises distribution was used to describe the collagen fiber orientations, with the orientation and strength of alignment as described in Zarei *et al.* [16]:

$$R(\boldsymbol{n}) = \frac{\exp^{b\left(2n_1^2 - 1\right)}}{2\pi I_0(b)} \tag{4.3}$$

where (n_1, n_2, n_3) are the components of the fiber direction vector $\boldsymbol{n}$, b is the concentration parameter, and I_0 is a modified Bessel function of the first kind of order 0. A trapezoidal integration scheme was used in FEBio to integrate the distribution over the 2D unit circle [64]. Mean collagen and elastin region material constants, as described in Gacek *et al.* [12], were used and are shown in **Table 2**.

***Table 2:** Model parameters for collagen fibers and elastin matrix*

Variable	Value	Units
E	13.15	kPa
v	0.499	
ξ	18.68	MPa
α	0.079	
β	7.58	

We computed the percentage of collagen fibers in tension ($\lambda_f \geq 1.16$), neutral ($1 \leq \lambda_f < 1.16$), and compression ($1.0 > \lambda_f$) at rest, or directly preceding the application of motion, and at the end of each applied motion. Fiber stretch is denoted by λ_f and was calculated as:

$$\lambda_f^2 = n_i n_j C_{ij} \tag{4.4}$$

where **n** is the unit vector along the direction of the fiber and **C** is the right Cauchy green tensor [41], [64].

Two rigid bodies were defined to model the L4 and L5 vertebral bodies, and their centers of mass were defined to match those of Ellingson *et al.* [14]. Each of the 6 motions were applied by setting the displacement and rotation of the L4 rigid body to that of the resultant displacement and rotation L4 vertebra output of the macroscale spinal motion model (i.e., all motion was defined relative to L5). Similarly, the L5 rigid body was fixed in space. The medial insertion points on the ligament were set as rigid contact points to the L4 rigid body while the lateral insertions points were set as rigid contact points to the L5 rigid body. Due to a lack of *in situ* lumbar facet capsular joint pressure measurements, we have chosen to model joint pressurization with a modest pressure of 5kPa, defined as an applied pressure on the inner facet of the ligament [18]. Residual strain, as measured by Gacek *et al.*, was prescribed by defining a prestrain tensor, F_R, for each element such that the ligament expanded 4% in the bone-to-bone direction and 0.089% in the direction perpendicular to it, or along the joint. A zero-stress ligament state was found such that the deformed ligament with applied prestrain will match the geometry of the original, undeformed ligament.

The influence of through-thickness variation in collagen and elastin was modeled by partitioning our ligament geometry such that the ratio of collagen to elastin was 1:1 through-thickness, as described by [12].The collagen region was modeled using equations 4.1-4.3, as described above, while the elastin region was modeled as purely neo-Hookean (eq. 4.1). Material constants are shown in **Table 2**. For each of the 6 FCL models, and for each of the 6 applied spinal motions, the following combinations were tested:

Table 3: *Tested model factor combinations*

Case	Motion?	Residual Strain?	Pressurization?	Collagen & Elastin Layers?
I	Yes	No	No	No
II	Yes	Yes	Yes	No
III	Yes	No	No	Yes
IV	Yes	Yes	Yes	Yes

Cases I and III will hereafter be referred to as cases of apparent motion and Cases II and IV will hereafter be referred to as cases of true motion.

The influence of each of these factors was assessed by comparing the maximum principal Lagrange strains across all elements in each model, after which we also compared maximum principal Cauchy stresses for all models in all cases. For a comparison of motion in the predominate fiber direction, we compared the strains in the 1-direction (E_{11}), or in the bone-to-bone direction. These strains were compared against the strains in the along-joint direction (E_{22}), or 2-direction. Additionally, the resultant stress across the ligament were compared in both the 1-direction (σ_{11}) and 2-direction (σ_{22}) for apparent and true motion models.

4.4 Results

4.4.1 Contribution of Model Factors

We compared the contribution of residual strain, inflation strain, and strain due to spinal flexion, including the contribution of body weight, on total ligament strain, shown

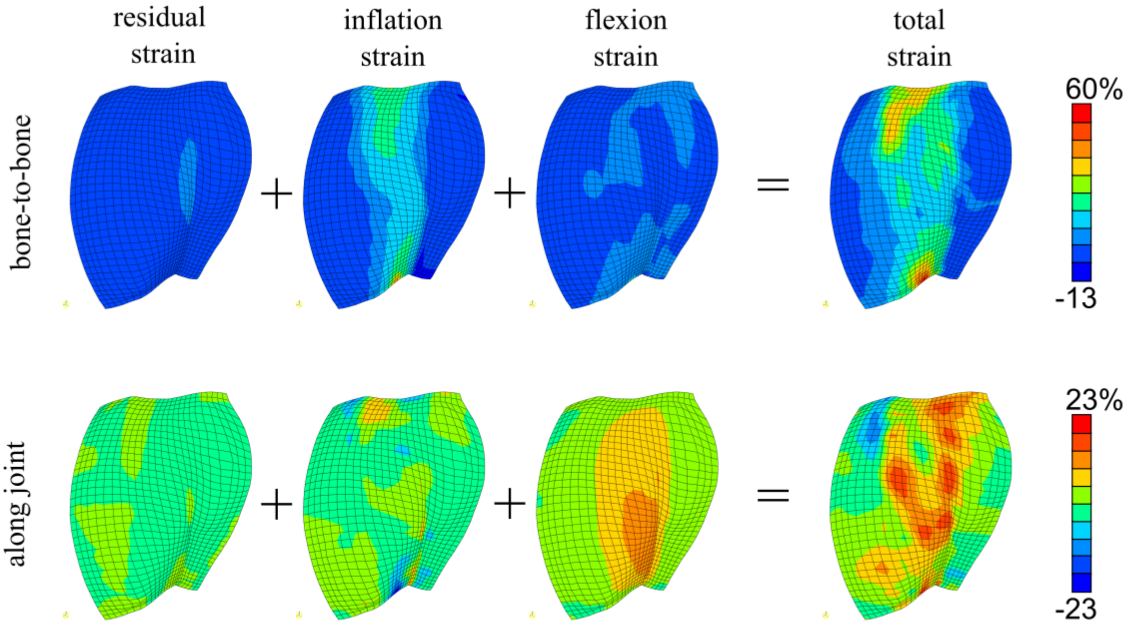

Figure 21 - The contribution of residual strain, inflation strain, and flexion strain on total ligament strain in both the bone-to-bone direction and along the joint: *In the bone-to-bone direction, inflation strains due to pressurization of the joint space have the largest apparent impact on the total strain field, when compared to strain from residual and flexion strain. When observing strains along the joint, flexion strains have the largest area of highest magnitude when compared to inflation strain and residual strain. All corresponding strains are plotted as on the same scale for clarity. All data is shown for a single representative sample.*

from the posterior portion, or top face, of the ligament (**Figure 21**). Strains are shown in the bone-to-bone (1) direction, which is generally the primary direction of collagen fiber alignment, as well as strains along-the-joint (2) direction. The largest contribution to total flexion strain is from inflation of the joint space, at about 41.2% E_{11} strain and 10.6% E_{22} strain, with the second largest contribution coming from flexion of the spine, at about 9.8% E_{11} strain and 11.7% E_{22} strain (Fig 2). The max total strain observed during flexion was 60.0% E_{11} strain and 20.7% E_{22} strain.

We also compared the contribution of residual stress, inflation stress, and flexion stress on the total stress of the ligament (**Figure 22**). Again, we observed modest contributions to ligament stress from the incorporation of a residual stress and a larger contribution from inflation of the joint space. When comparing stress contributions of each

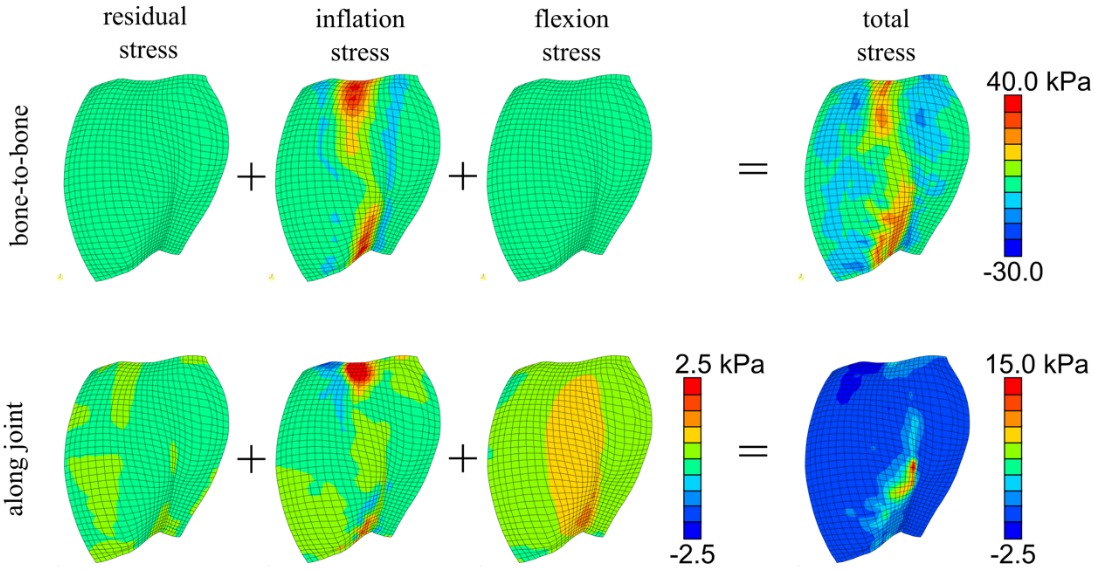

Figure 22: - Stress contribution from residual strain, inflation, and joint motion of flexion of the total stress of the ligament: *Stress σ_{11} (bone-to-bone) and σ_{22} (along the joint) are shown. Stress from incorporating residual strain has a negligible impact on total stress when compared to the contribution from inflation and joint motion of flexion. In both directions, inflation stress has the region of highest stress magnitude, but flexion stress has the widest spread across the surface of the ligament. All data is shown for a single representative sample.*

modeling factor, we observe a smaller contribution to ligament stress from joint motion, perhaps due to smaller contributions of motion to overall ligament strain. The largest contribution to total flexion stress was again from joint inflation, at about 40.3 kPa σ_{11} stress and 5.5 kPa σ_{22} stress, with the second largest contribution coming from flexion of the spine, at about 2.0 kPa σ_{11} stress and 1.1 kPa σ_{22} stress (**Figure 21**). The max total stress observed during flexion was 34.7 kPa σ_{11} stress and 16.8 kPa σ_{22} stress.

4.4.2 Model Predictions for Flexion and Extension

The aggregated results for model predications of flexion and extension for a single representative sample are shown in **Figure 23**. In the case of true motion, the max principal strain during both flexion and extension were higher than that of the observed max principal strains during apparent motion (**Figure 23**a). The regions of highest max principal strain were generally found at the enthesis. Looking at the max principal stress field of both cases, we saw that the stresses, like the strains, were higher in both flexion and

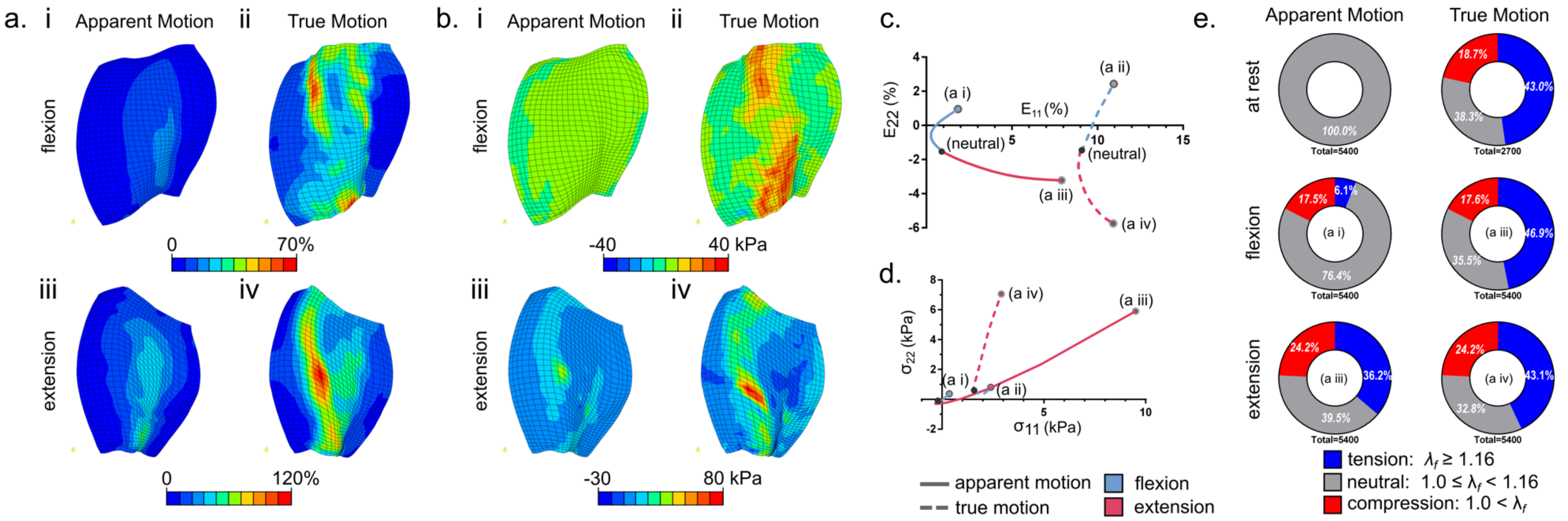

Figure 23 - Results for simulated flexion and extension: (a) *Max principal strain and plotted for spinal motions of flexion (i-ii) and extension (iii-iv).* ***(b)*** *Max principal stress for same motions. Both stress and strain from apparent motion (i and iii) and the true motion (ii and iv), incorporating residual strain, inflation, and motion, are shown at peak motion.* ***(c)*** *The full motion progression of mean bone-to-bone strain (E_{11}) and mean along-joint strain (E_{22}) are shown. As in (a) and (b), the true motion cases for both flexion and extension show higher strains (c).* ***(d)*** *The full motion progression of mean bone-to-bone stress (σ_{11}) and mean along-joint stress (σ_{22}) are also shown. Black dot denotes neutral position in both plots.* ***(e)*** *The percentage of collagen fibers in tension, neutral, and compression are shown for all cases. Additionally, the percentage of collagen fibers in tension, neutral, and compression are shown for the "at rest" position, which precedes motion but, in the case of true motion, includes stretch contributions from the incorporation of residual strain and inflation of the joint space. All data is shown for a single representative sample.*

extension for the case of true motion (**Figure 23**b). During true motion, the regions of high principal stress during flexion did not align with the regions of high principal strains, indicating that the principal stress and strain axes did not align. Instead, the area of highest stress is seen in the middle of the ligament, over the joint space. Conversely, the region of highest stress during extension did align with the region of highest strain (**Figure 23**b).

Figure 23c displays the mean on-joint strains in the 1- and 2-direction during apparent motion and true motion of flexion and extension. The incorporation of residual strain and inflation significantly increases both the mean 1- and 2-direction strains during flexion and extension (**Figure 23**c). The mean apparent strain starts close to zero, with the only observed motion due to the body weight. After a slight initial drop, E_{11}^{app} rises in both flexion and extension, whereas E_{22}^{app} is positive for flexion but negative for extension. When residual strain and inflation pressure are considered, E_{11}^{true} is much larger but shows less increase with flexion, presumably due to the stiffening of the collagen at large strains. E_{22}^{true} is similar to E_{22}^{app} but of larger magnitude. When we consider mean apparent stress, it again starts very close to zero. With a large rise in E_{11}^{app}, σ_{11}^{app}rises sharply for extension but not as much for flexion, due to only a small percentage of collagen fibers in tension and a misalignment of high strain and high stress regions (**Figure 23**a-b, d, e). With similar amount of collagen fibers in tension, we observed similar magnitudes of σ_{11}^{true}. However, in both the apparent and true motion models, we observed a large increase in σ_{22}^{true} in extension (**Figure 23**d). As expected, all collagen fibers are in neutral ($1 \leq \lambda_f < 1.16$) when "at rest", or before the application of motion, in all apparent motion models (**Figure 23**e). With the incorporation of residual strain and inflation during rest, the percentage of collagen fibers in tension ($\lambda_f \geq 1.16$) rises to 43.0%, with an additional 18.7% of fibers in compression ($1.0 > \lambda_f$). With only small changes in strain in the 1-direction (**Figure 23**c), which is generally considered the predominant fiber alignment direction, the percentage of fibers in tension during flexion rises to 6.1% and 46.9% during apparent motion and true motion, respectively. In the case of apparent extension, the large changes in 1-direction strain and force on bone translates to a 36.2% increase in the total percentage of collagen fibers in tension and 24.2% of fibers in compression (**Figure 23**e). Since extension moves the facet surfaces apart, there is little difference in stretch distribution between the apparent and true models.

4.4.3 Model Predictions for Contralateral and Ipsilateral Bending

The same representative sample shown for flexion and extension in **Figure 23** is also shown for contralateral and ipsilateral bending in **Figure 24**. Again, we observed higher max principal strains (**Figure 24**a) and max principal stresses (**Figure 24**b) during the cases of true motion. Both the stress and the strain fields are heterogeneous, as is expected with an heterogenous distribution of collagen fiber orientations, and most peak principal strains are observed at the enthesis. The two motions produce max principal strain and stress fields of similar magnitude.

Two striking differences can be seen between the apparent and true strains in **Figure 24**c, especially for ipsilateral bending. First, the true strain, E_{11}^{true}, is much larger than the apparent strain; second, the *changes in strain* are much smaller in the true model. This difference arises because the contributions of residual strain and inflation are significant enough to place and maintain the collagen fibers in the 2-direction into tension from compression, whereas the apparent motion model of contralateral bending had tensile collagen fibers in the 1-direction become compressive by the end of the motion (**Figure 24**c). This is further seen when comparing the apparent and true stress in the 1-direction (**Figure 24**d). During true motion, the distribution of collagen fibers in tension, neutral, and compression are fairly uniform between ipsilateral and contralateral bending (**Figure 24**e). However, the apparent and true stress in the bone-to-bone (1) direction rises during ipsilateral bending but remains practically unchanged for contralateral bending, further indicating the compressive effect of contralateral bending on collagen fibers (**Figure 24**d). Additionally, the small changes in strain during true motion has a large effect on the true stress in the 1-direction for ipsilateral bending, indicating a large portion of the collagen fibers in tension being very near their ultimate lock-out state. There is low apparent strain in the predominant fiber direction during contralateral bending, as shown by a lack of collagen fibers in tension, and approximately half (50.3%) of collagen fibers in compression (**Figure 24**e) While the true percentage of collagen fibers in tension increases

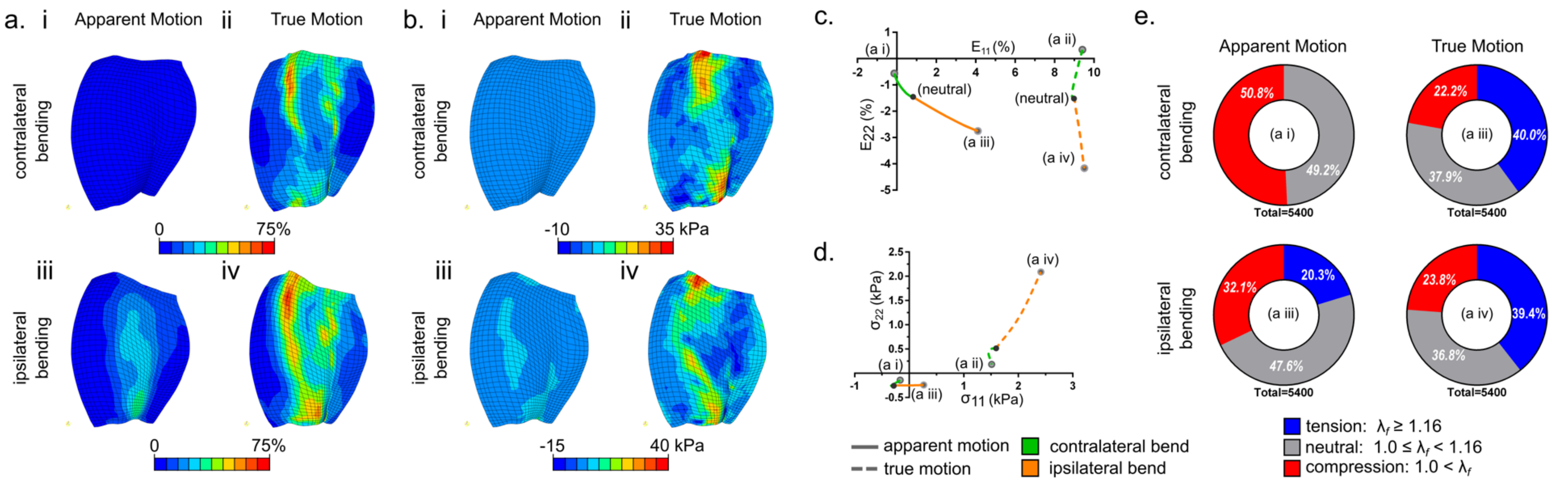

Figure 24- Results for simulated contralateral and ipsilateral bending: ***(a)*** *Max principal strain plotted for spinal motions of contralateral bending (i-ii) and ipsilateral bending (iii-iv).* ***(b)*** *Max principal stress for same motions. Both stress and strain from apparent motion (i and iii) and the true motion (ii and iv), incorporating residual strain, inflation, and motion, are shown at peak motion. In all cases of motion, max principal strains and stresses were higher during true motion (a.ii, a.iv, b.ii, and b.iv) compared to apparent motion (a.i, a.iii, b.i, and b.iii).* ***(c)*** *Strain in the bone-to-bone (E_{11}) and along-joint (E_{22}) are plotted for the full motion of contralateral bending and ipsilateral bending for all cases.* ***(d)*** *The mean bone-to-bone stress (σ_{11}) and mean along-joint stress (σ_{22}) are also shown. Black dot denotes neutral position in both plots.* ***(e)*** *Total percentage of fibers in tension, compression, and neutral at the end of motion for each scenario. All data is shown for a single representative sample.*

to 40.0% during contralateral bending, this is still close to the true at rest results shown in **Figure 23**e. These results indicate that the residual strain and joint pressure dominate ligament mechanics during lateral bending, with the effect of the joint motion relatively small.

4.4.4 Model Predictions for Contralateral and Ipsilateral Axial Rotation

Figure 25 concludes our display of motion results for a single representative sample by displaying the model predictions for contralateral and ipsilateral axial rotation. As was the case for flexion-extension and contralateral-ipsilateral bending, the predicted max principal strain is higher in the cases of true motion for both contralateral and ipsilateral axial rotation (**Figure 25**a). In the case of contralateral axial rotation, we observed a buckling of the ligament at peak motion, leading to very low apparent strains (**Figure 25**a) and stresses (**Figure 25**b). Regions of high predicted max principal stress are found near the regions of high predicted max principal strains (**Figure 25**b). The max principal stresses observed during true contralateral-ipsilateral axial rotation were comparable to those observed in true flexion-extension and true contralateral-ipsilateral bending (**Figure 23**b, **Figure 24**b, and **Figure 25**b). The predicted strain in the bone-to-bone direction (E_{11}) is large for the true contralateral axial rotation case and both the apparent and true ipsilateral axial rotation models (**Figure 25**c). Smaller strains were observed for E_{22} for all three models, with large changes in strains for apparent contralateral axial rotation. Collagen fibers that are initially in tension or compression at the start of motion remain in tension or compression in the case of ipsilateral axial rotation. This is further shown as a large rise in σ_{11} stress for both apparent and true ipsilateral axial rotation models (**Figure 25**d). The 1-direction stress becomes more compressive in both apparent and true contralateral axial rotation, however, with the inclusion of inflation and residual strain, the total change in σ_{11}^{true} is smaller. When comparing all 6 motions, contralateral and ipsilateral axial rotation had the largest apparent changes in percentage of collagen fibers in compression or flexion, respectively (**Figure 25**e). Approximately 73.9% of collagen fibers are in apparent compression at the end of contralateral axial rotation, but this percentage decreases to 52.0% percent with the

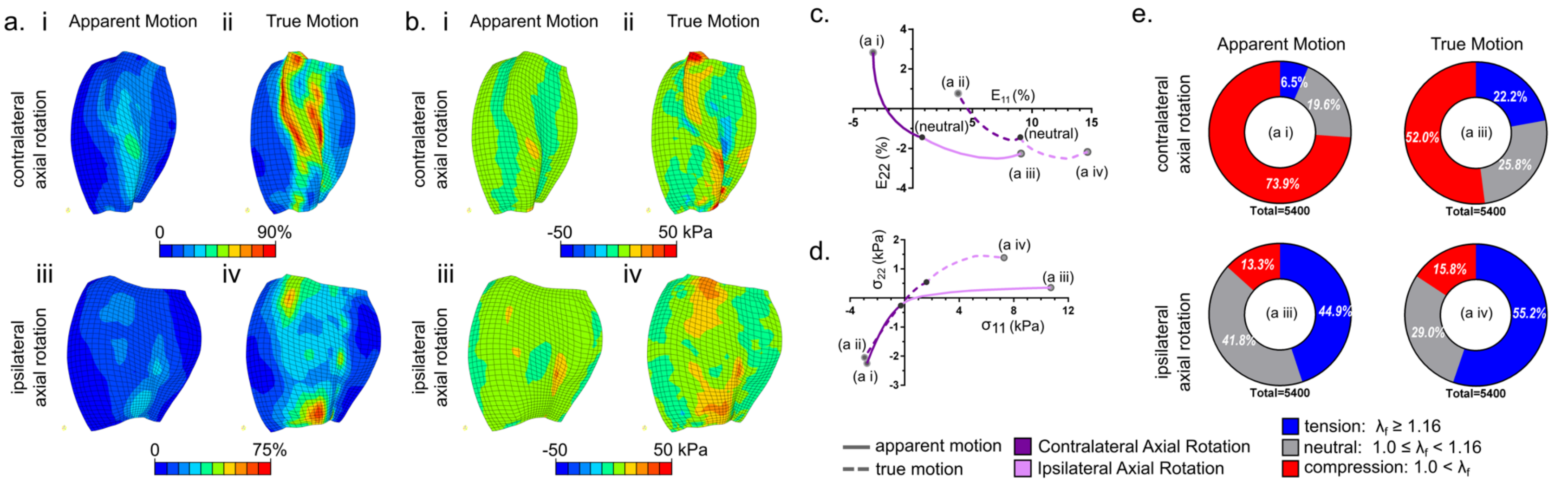

Figure 25 - Results for simulated contralateral and ipsilateral axial rotation: ***(a)*** *Max principal strain during contralateral axial rotation (i-ii) and ipsilateral axial rotation (iii-iv).* ***(b)*** *Max principal stress for same motions. Both stress and strain from apparent motion (i and iii) and the true motion (ii and iv), incorporating residual strain, inflation, and motion, are shown at peak motion.* ***(c)*** *Comparison between* E_{11} *and* E_{22} *strain and* ***(d)*** *between* σ_{11} *and* σ_{22} *stress. Black dot denotes neutral position in both plots.* ***(e)****Total percentage of fibers in tension, neutral, or compression at the end of loading. All data is shown for a single representative sample*

addition of residual strain and inflation in the true motion cases. This result indicates that, as for lateral bending, the addition of residual strain and inflation is enough to load the ligament’s collagen fibers despite the compressive effect of the vertebral motion.

4.4.5 Aggregated Model Predictions

For an aggregated comparison of all model motions, in both apparent and true motion, for all 6 fiber distributions tested, the average maximum and minimum principal strains and stresses are shown in **Figure 26**. For easier comparison, all stresses and strains are plotted as the change in magnitude from the start and end of a given motion. Most motions exhibit mild nonlinearity in the stress and strain with increasing respective IVAs. The highest average maximum principal strain is observed for the true motion case of extension, followed by the case of apparent motion extension. Contralateral bending, flexion and ipsilateral axial rotation generated lower strains at all IVAs (**Figure 26**a-c). These observations are consistent with the observations of Zarei *et al*. [16]. Similarly, the highest observed stress is for extension, with true stress higher than apparent (**Figure 26**a).

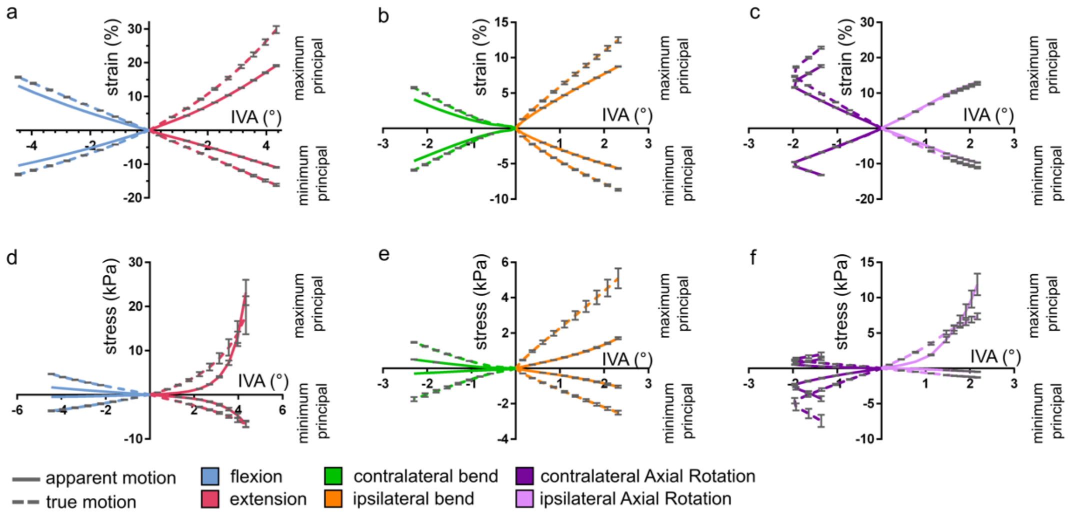

Figure 26 Comparison of average maximum and minimum principal strain with respect to interverbal angle (IVA): *(a) Flexion-extension strains. (b) Contralateral-ipsilateral bending strains. (c) Contralateral-ipsilateral axial rotation strains. (d) – (f) Corresponding maximum and minimum principal strains. For easier comparison, all stresses and strains are plotted as the change in magnitude from the start and end of a given motion. All error bars indicate 95% CI with n=6 for each motion case.*

In most cases, the average max and min principal strains are higher for the cases of true motion compared to the apparent motion models (**Figure 26**d). The average max principal stress is highly nonlinear for increasing IVAs during both cases of extension (**Figure 26**d). We observed a similar behavior for apparent ipsilateral axial rotation (**Figure 26**f), but not during the case of true ipsilateral axial rotation. This observation indicates increased recruitment of collagen fibers during apparent motion, whereas in actual motion many of those fibers were already recruited prior to the start of the motion.

This effect can be seen strikingly in **Figure 27**, which shows the effect of adding residual stress and joint pressure on the fiber stretch distribution for each spinal motion. Our results suggest there is a higher percentage of collagen fibers in tension during all cases of true motion (**Figure 27**a). The percentage of fibers in neutral or compression decreases or remain unchanged from apparent motion to true motion models (**Figure 27**b-c).

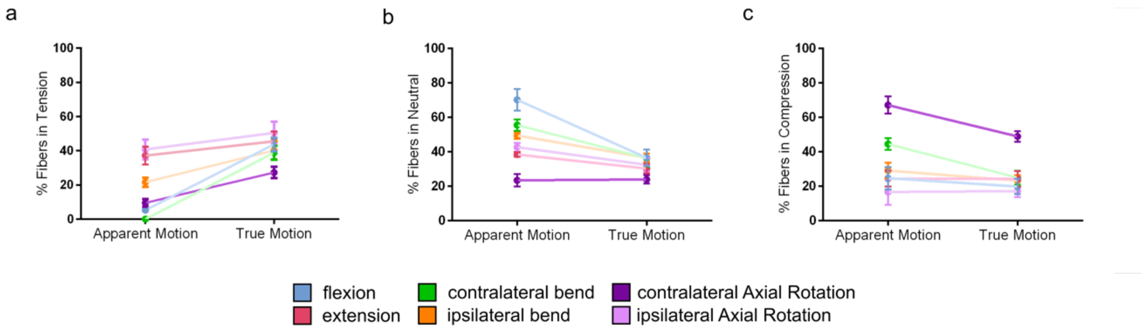

Figure 27 - Effect of residual stress and joint pressure on fiber stretch: *The average percentage of fibers in (a) tension (fiber stretch ≥ 1.16), (b) neutral (1.0 ≤ fiber stretch < 1.16), and (c) compression (fiber stretch < 1.0), across all motions and loading cases (apparent motion vs true motion). Error bars indicate 95% CI and n=6 for each case.*

4.4.6 Contribution of Distinct Collagen and Elastin Region on Model Predictions

We now turn to the effect of through-thickness heterogeneity within the lumbar facet capsular ligament by examining results for a multilayer model with elastin-rich and collagen-rich layers. **Figure 28** shows the maximum principal strains during peak flexion-extension and is broken down to show the contribution of the collagen fibers compared to the elastin. The topmost layer of each region is shown for cases of apparent motion and

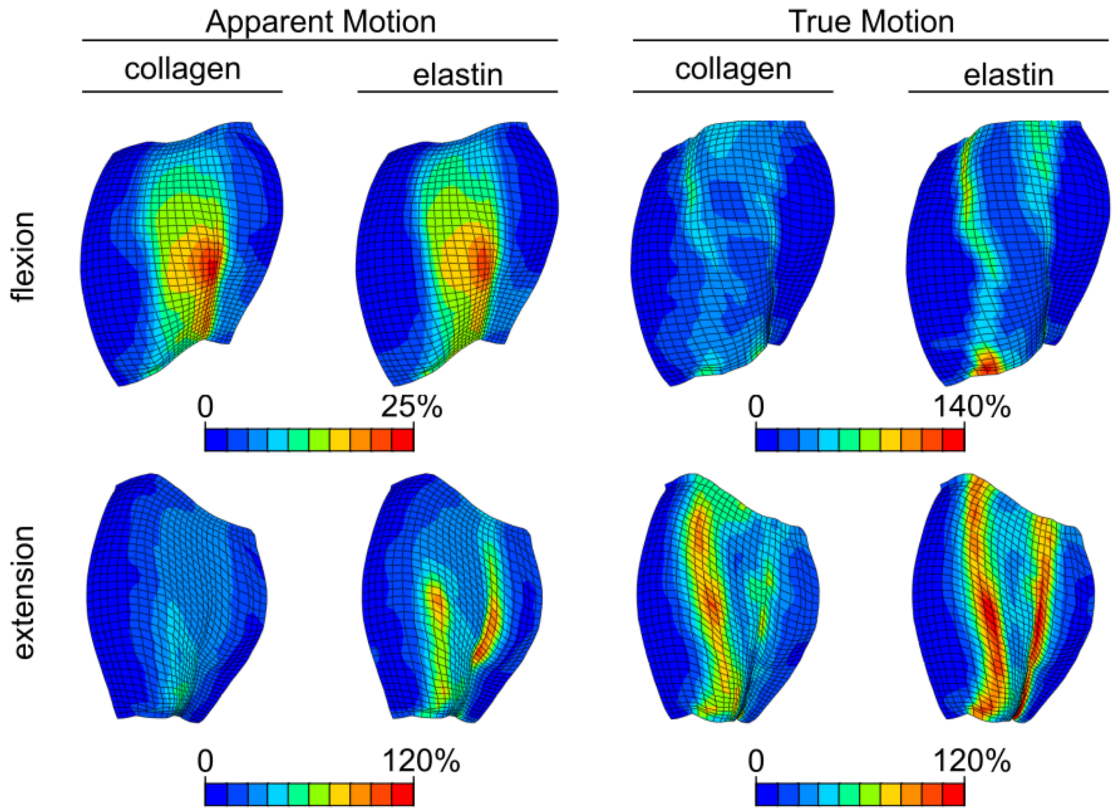

Figure 28 - Max principal strains for the topmost portion of the collagen and elastin regions: *For the collagen region, the topmost layer is the posterior portion of the ligament, and, for the elastin region, the topmost layer is the middle portion of the ligament. Max principal strain is shown for both apparent and true motion, and for spinal motions of flexion and extension. Note that scale bars are different for apparent and true models in flexion.*

true motion. The topmost layer of the collagen region corresponds to the topmost portion, or the posterior portion, of the ligament. The topmost layer of the elastin region is taken as the elastin interface to the collagen region. Since results were largely uniform through either layer, the topmost (i.e. posterior) surface of each layer was used for visualization of the strain and stress fields. In the case of apparent flexion, the strain fields across the collagen region and the elastin regions are very similar whereas the strain field of the elastin region is significantly higher than strains observed in the collagen region at apparent extension. When inflation and residual strain are incorporated into the model, the strain fields across the elastin and collagen region between apparent and true motion become

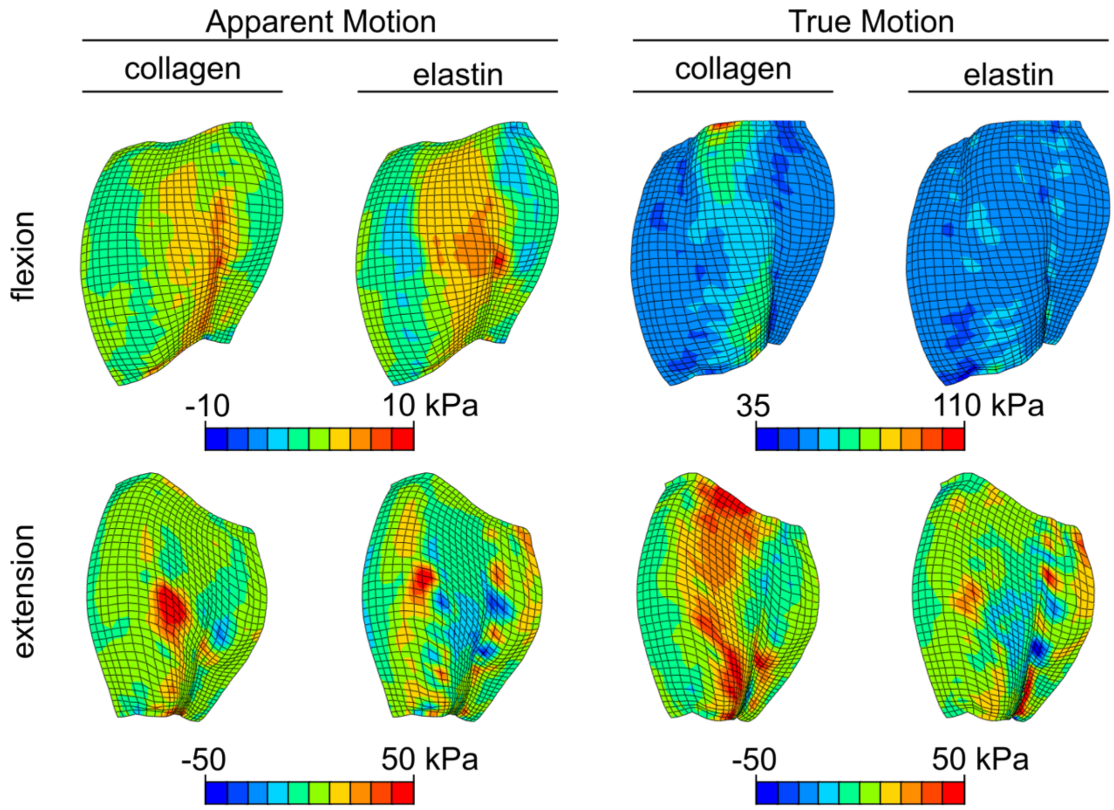

Figure 29- Max principal stress during apparent and true motion for spinal motions of flexion and extension: *The stress in the topmost layer of both the collagen and elastin portion of the ligament are shown. Note that scale bars are different for apparent and true models in flexion.*

more similar, for both flexion and extension. However, the magnitude of the strain is still significantly higher in the elastin region of a true extension model (**Figure 28**).

Figure 29 compares the maximum principal stresses in the same locations as the max principal strain shown in **Figure 28**. Again, we are plotting max principal stress across the ligament at the topmost portion of each region: collagen and elastin. The stress field across the collagen and elastin regions are similar in the case of apparent flexion. However, in the other three cases, apparent extension, true flexion, and true extension, the stress across the ligament varies in each region. In the case of principal stress, the magnitude of the stress is lower in all elastin regions, despite higher observed strains in the same region. This is expected with the chosen material model of each region. The collagen fibers create

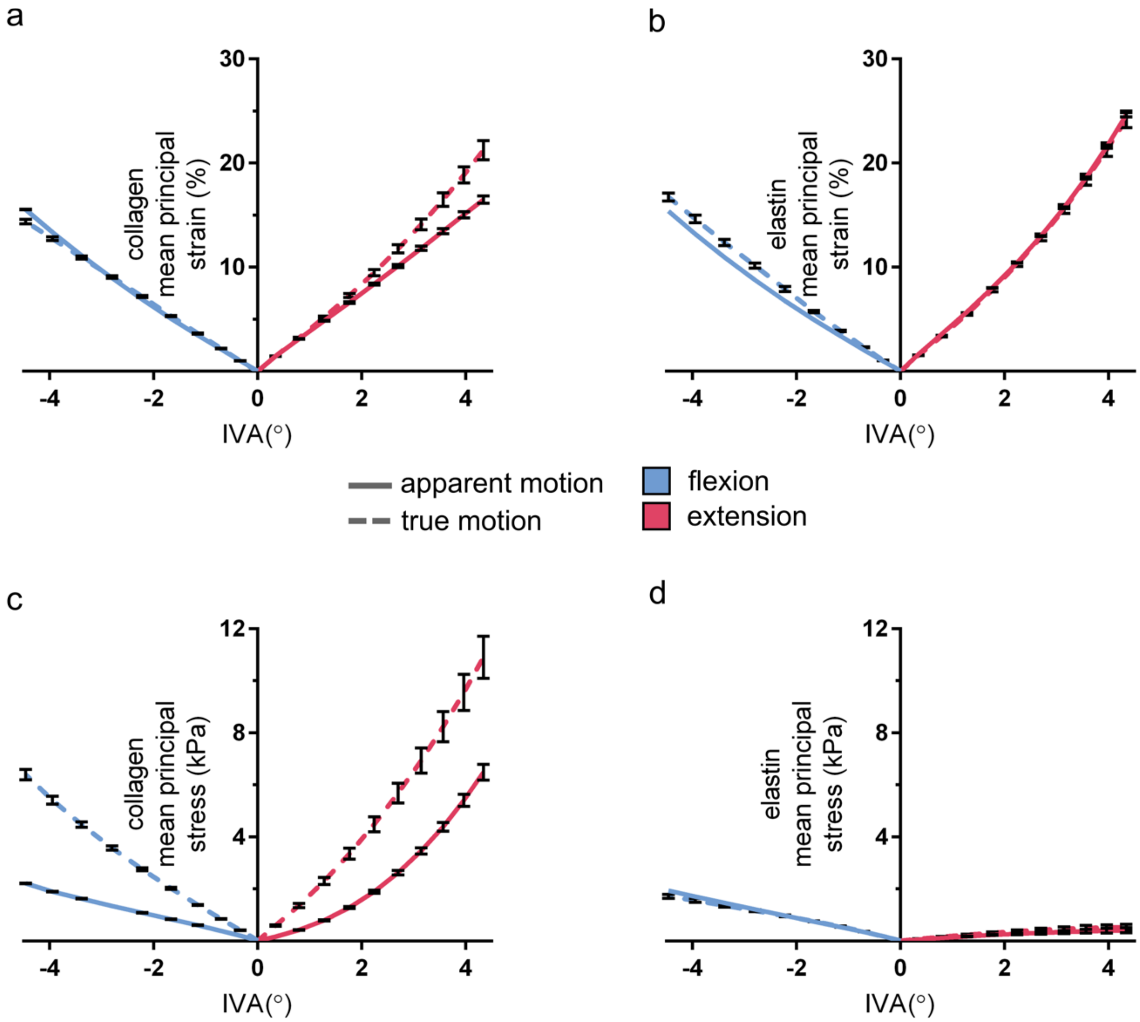

Figure 30- Comparison of mean max principal strain for the topmost portion of the collagen and elastin region for increasing IVA during spinal motions of flexion and extension: *The cases of apparent motion and true motion are compared. For easier comparison, all stresses and strains are plotted as the change in magnitude from the start and end of a given motion.*

regions of high stress when fully loaded, as was the case in our 1-layer models (**Figure 23-Figure 25**).

Further breaking down the contribution of the collagen-rich and elastin-rich regions to mean principal strain (**Figure 30** a-b) and principal stress (**Figure 30** c-d), we observed similar strains with increasing IVAs in the collagen region at flexion and in the elastin region at flexion and extension when comparing the apparent motion and true motion cases. For easier comparison, all stresses and strains are plotted as the change in magnitude from the start and end of the given motion. The overall mean principal strain in the elastin region is slightly higher than the collagen region for spinal extension but similar for flexion (**Figure 30**a-b). The mean principal strain in the collagen region is higher in the case of true extension when compared to apparent extension (**Figure 30**a). Our results suggest that the mean principal strains are comparable between the two regions in the case of flexion but the higher observed strains during extension are primarily taken up in the elastin region. This idea is further supported by comparing the mean principal stress results of the two regions (**Figure 30** c-d). The stress in the ligament is much higher in the collagen region than in the elastin region (**Figure 30**c), especially for the true model. The mean principal stresses in the elastin region for both flexion and extension remain the same between the apparent and true motion models and are overall lower than the mean stresses observed in the collagen region (**Figure 30**d).

4.5 Discussion

The major conclusion of this study is that the combined effect of prestress and joint pressure contributes significantly to the stress and strain fields that arise in the lumbar facet capsular ligament during spinal motion or even in the absence thereof. The results of our study indicate that a portion of the ligament is in tension on-joint due to residual strain and joint pressurization strain (**Figure 27**). In addition to its obvious ramifications for computational modeling of ligament mechanics, this conclusion also suggests certain considerations regarding the *in vivo* mechanics and function of the lumbar facet capsular ligament. Inflation of the joint space, specifically, had a large effect on the total observed strain (**Figure 21**) and stress (**Figure 22**) on the ligament, when comparing its contribution against that of residual strain and strain due to motion.

Our multiscale computational model represents a significant step forward in the study of the lumbar facet capsular ligaments. However, the model also highlights the complexity of the lumbar spine and the ongoing challenges in developing truly comprehensive, predictive models of spine biomechanics. Our study has highlighted the significant role of joint pressurization strain on overall ligament mechanics, both before and during spinal motions. Our model assumes that the joint pressure does not change throughout the application of motion, despite the available joint space volume changing. When the available joint volume changes, it will directly affect the pressure within the joint cavity and the resultant tension applied to the ligament. Further work is needed to characterize the change in joint volume with each motion and to define the rate at which the synovial fluid turns over, both important factors to consider when considering joint pressurization.

When we compared the E_{11} strain against the E_{22} strain, our results indicated that, for the cases of true flexion-extension and contralateral-ipsilateral bending, with increasing respective IVAs the bulk of the strain is observed in the 2-direction, or normal to the average predominate fiber alignment (**Figure 23**c, **Figure 24**c). Lower changes in strains in the 1-direction, or the bone-to-bone direction, did indicate that there was a higher percentage of fibers in tension (**Figure 23**c&e, **Figure 24**c&e, and **Figure 25**c&e). This suggests that the addition of residual strain and inflation strain can uncrimp fully and load crucial collagen fibers, with any additional loading on the ligament being resisted by the collagen fibers and taken up by the underlying elastin matrix. In the case of contralateral-ipsilateral axial rotation, increasing E_{11} strain is a result of motion being applied nearly parallel to the 1-direction, and, therefore, further strain and stress in that direction is expected (**Figure 25**c-d). This is further supported by our analysis of the average maximum and minimum principal stresses during motion, in which true ipsilateral axial rotation exhibit the second highest average max principal stress, after extension (**Figure 26**d&f).

A strength of our model is its ability to have distinct regions of collagen and elastin fibers throughout the thickness of the ligament. Collagen, the primary structural component in ligament, provides tensile strength and allows the ligament to withstand various mechanical loads. Conversely, elastin provides elasticity, enabling the ligaments to return to its original shape after being stretched. The distribution and organization of these fibers throughout the ligament play a crucial role in the ligament's anisotropic mechanical behavior and it affects the way the ligament responds to various spinal motions. During high strain motion, the highest magnitude of strain was observed in the elastin region of the tissue, perhaps due to its attachment to the bone (**Figure 28**). Our results further suggest that both the stress distribution and the average max principal stress is higher in the collagen region, due to the supportive role of collagen fibers to mechanical loads (**Figure 29**, **Figure 30**c-d). Overall, the stress in the elastin region is small although we did not model the ligaments return to rest after motion or analyze its hyperelastic response to loading. Ligaments adapt to changes in mechanical loading by synthesizing, degrading, or reorganizing their extracellular matrix components to better withstand loading. The results of our through-thickness study highlight the need to consider growth and remodeling phenomenon of the tissue, both during development and during disease and degeneration of the tissue. We can hypothesize that joint pressurization plays a large role during ligament remodeling. Joint pressurization may explain the separation of ligament microstructural composites into collagen-rich and elastin-rich regions, where collagen provides structural rigidity during pressure overload while elastin restores to neutral during small motions.

5 Hybrid Discrete-Continuum Multiscale Model of Tissue Growth and Remodeling

The contents of the chapter were previously published as a research article in the journal Acta Biomaterialia by Gacek, Mahutga, and Barocas. [19] The author of thesis conceptualized the idea, co-designed the study, developed the coupled micro-macroscale remodeling framework, ran all case studies, prepared all figures, and edited the manuscript.

5.1 Summary

Tissue growth and remodeling (G&R) is often central to disease etiology and progression, so understanding G&R is essential for understanding disease and developing effective therapies. While the state-of-the-art in this regard is animal and cellular models, recent advances in computational tools offer another avenue to investigate G&R. A major challenge for computational models is bridging from the cellular scale (at which changes are actually occurring) to the macroscopic, geometric-scale (at which physiological consequences arise). Thus, many computational models simplify one scale or another in the name of computational tractability. In this work, we develop a discrete-continuum modeling scheme for analyzing G&R, in which we apply changes directly to the discrete cell and extracellular matrix (ECM) architecture and pass those changes up to a finite-element macroscale geometry. We demonstrate the use of the model in three case-study scenarios: the media of a thick-walled artery, and the media and adventitia of a thick-walled artery, and chronic dissection of an arterial wall. We analyze each case in terms of the new and insightful data that can be gathered from this technique, and we compare our results from this model to several others.

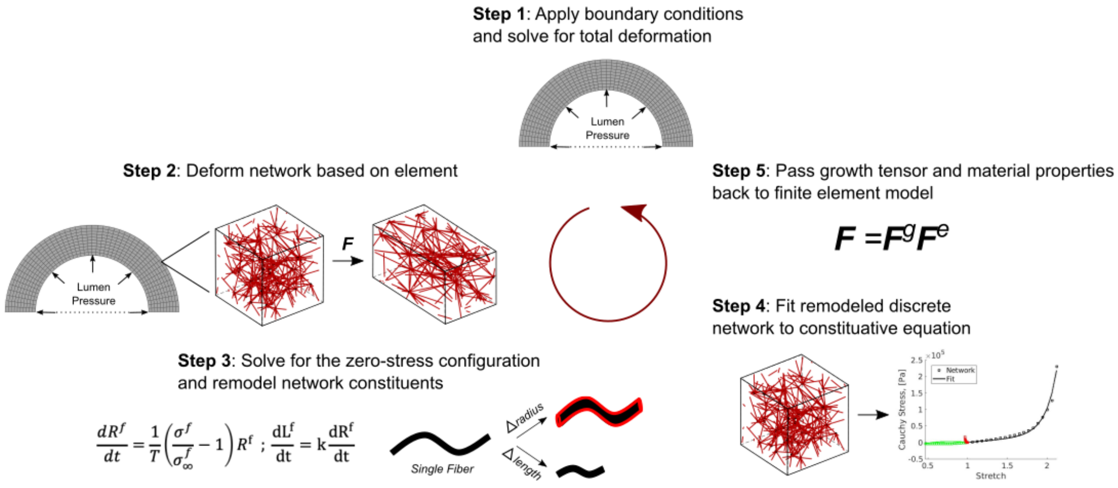

***Figure 31**: Graphical representation of the multiscale remodeling framework*

5.2 Introduction

Biological soft tissues are living composite materials consisting of cells and an extracellular matrix (ECM) comprising various fibrillar components (such as collagen, elastin, and fibrin) and non-fibrillar components (such as proteoglycans, glycosaminoglycans, and lipids), making tissues structurally complex [65]. Further, many tissues organize from networks at the cell-scale (micro-scale) into layered structures at the meso-scale (e.g. arteries, skin, uterine wall) and into morphologically complex macroscale geometries (e.g. the aortic arch, the skin of the hand, the uterus), making tissues inherently multiscale [66]–[68]. The organization at each level changes constantly in response to external cues. From the point of view of mechanotransduction, this organization presents a cascading mechanism from the application of loads at the macro-scale, to the translation of forces within the meso-scale structure, to the response of cells at the micro-scale. The subsequent tissue-level changes arise from the aggregate of the individual cellular responses.

Cells respond mechanically to their environment by remodeling both themselves [69]–[72] and the ECM that surrounds them [73]–[76]. Further, cells are responsible for forming the macroscopic geometries of the tissues they inhabit. Thus, it is important that we understand how cellular-level cues lead to changes in tissue-level properties – and to gross morphologic changes. Knowing how a tissue achieves – or fails to achieve – its target functionality is essential in understanding and assessing growth and remodeling in the context of the transition from a 'healthy' to a 'diseased' phenotype, which is a key factor in the development and implementation of medical interventions and therapies [77]–[80].

Previous work towards understanding the biomechanical behavior of soft tissues has primarily focused on the description of composite tissues using strain energy density functions (e.g., [49], [81]–[90]). This strain-energy-based continuum modeling approach provides a simple method for implementation into finite-element simulation of complex geometries. It also lends itself to efficient and insightful models of growth and remodeling. Further advances in the field have moved towards incorporating increasingly detailed loading scenarios, utilizing continuum constitutive relations including coupled computational fluid dynamics (CFD) or fluid-structure interaction (FSI) (e.g. [91]–[95]). However, the microstructural detail that is sacrificed in the description of a strain energy density function limits one's potential to understand cellular mechanotransduction due to localized material properties. Microstructural remodeling models have emerged [96]–[100], as have cell-signaling-based models [101]–[103], providing more detailed tools to simulate changes in tissue structure and behavior.

The objective of this study was to create and evaluate a multiscale framework to simulate multiple scales of the tissue growth and remodeling process without loss of microstructural detail. In this work, we utilize discrete network models of the micro-scale, on which the cell experiences its environment and subsequently makes changes to it. Further, it is at the micro-scale that disease and failure initiate. We layer the microscale models to describe the meso-scale architecture, then combine these micro/meso-scale models with a traditional finite element analysis by fitting the behavior of the micro/meso-scale with a continuum strain energy density model similar to our previous work [104]. Thus, we leverage the structural detail of a discrete fiber network model and the speed of continuum-scale finite-element analysis. We utilize this model to examine the microstructural features resulting from remodeling in various systems under the assumption that cells respond to local mechanics to return tissue constituents to tensional homeostasis [105]–[107]. We then probe the structure-function relationship under the hypothesis of tensional homeostasis in order to assess the role mechanical cues have on tissue growth and remodeling.

5.3 Methods

5.3.1 Multiscale Remodeling Framework and Nomenclature

In this work, we define superscripts to denote tissue constituents and/or fibers. Superscripts allow us to delineate between individual constituents without summation, and therefore we include summation symbols when appropriate for superscripts. We apply the Einstein summation convention for subscripts. We also define an elastic deformation gradient as F^e and a growth deformation gradient as F^g, where 'e' and 'g' are not treated as indices, but rather used to distinguish between deformation gradients in different reference frames.

5.3.2 Growth Preliminaries

There are two ideas that intersect in the area of tissue growth and remodeling. The first is the concept of kinematic growth [47], [108]–[111], under which the tissue's reference configuration can change based on some underlying remodeling law, and the growth of the tissue can be prescribed as a deformation tensor. This is shown schematically in **Figure 32**, and is given mathematically as

$$F_{ij} = F^e_{ik} F^g_{kj} \tag{5.1}$$

where F_{ij} is the total deformation tensor from the original configuration to the current - remodeled *and* deformed - configuration, F^e_{ik} is the elastic deformation tensor that describes the elastic deformation from the grown stress-free reference configuration to the deformed configuration, and F^g_{kj} is the growth tensor that maps from the initial reference configuration to the grown stress-free reference configuration. Even with all boundary conditions free (i.e., no surface stresses), F^e_{kj} is not, in general, the identity because the growth must be rectified by the compatibility equation, such that, in the absence of body forces,

$$\sigma_{ij,j} = 0 \tag{5.2}$$

where σ_{ij} is the Cauchy stress.

The second foundational idea is constrained mixture theory [112]–[116]. In its most basic form, constrained mixture theory defines each constituent as having its own associated mass fraction (or volume fraction), with the total solid volume fraction is given by

$$\phi^S = \frac{1}{v}\int_\Omega \, dv^S = \frac{1}{v}\sum_i \, v^i = \sum_i \, \phi^i \tag{5.3}$$

where ϕ^s is the total volume fraction of constituents, v is the volume of the tissue, v^S is the total volume of constituents, v^i is the volume of constituent i, and $\phi^i = v^i/v$ is the volume fraction of constituent i. A constrained mixture formulation further assumes that the constituents themselves are independent but are constrained to move together behaving as parallel structures that do no interact with one another such that the constituent stresses are additive to the total tissue stress

$$\sigma_{kl}(F^e_{mn}) = \frac{1}{v}\int_\Omega \, \sigma_{kl}(F^e_{mn})dv = \frac{1}{v}\sum_i \, \sigma^i_{kl}(F^e_{mn})v^i = \sum_i \, \phi^i\sigma^i_{kl}(F^e_{mn}) \tag{5.4}$$

where $\sigma_{kl}(F^e_{mn})$ is the stress in the tissue as a function of F^e_{mn}, which is the elastic deformation gradient applied to the tissue. The superscript i denotes a constituent of the tissue.

If we combine constrained mixture theory with kinematic growth theory, each constituent must evolve such that

$$F_{mp} = (F^e_{mn})^i\left(F^g_{np}\right)^i \tag{5.5}$$

so that the overall deformation gradients applied to each constituent are the same, but the growth $(F^e_{mn})^i$ and elastic deformation $\left(F^g_{np}\right)^i$ of any given constituent i, need not be. We also note that $\sigma^i_{kl}\left(F_{mp}\right)$ is not necessarily $\mathbf{0}$ when $F_{mp} = \delta_{mp}$ since the reference, strain-free configuration, $\left(F^g_{np}\right)^i$, is not, in general, equal to F_{mp}. One major benefit of using constrained mixture theory is the computational efficiency of being able to limit the behavior to a specified number of constituents (e.g., $i = 1,2,3$ for tissues composed primarily of cells, collagen and elastin), and treating those constituents as independent so that for a specified deformation, each may remodel with no direct effect on the other constituents. There are other ways to address growth using the combination of kinematic growth and constrained mixture theory as outlined further in [49], [117].

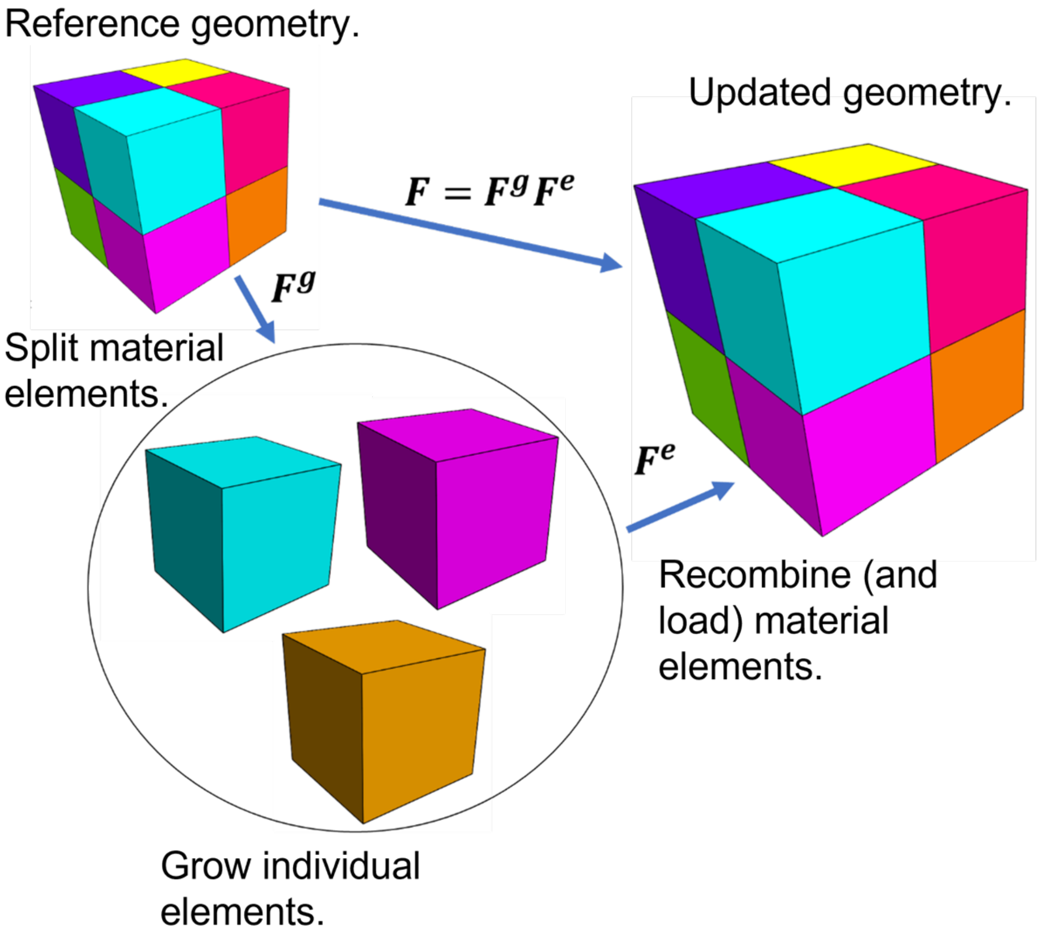

Figure 32: *Kinematics of growth showing the reference configuration, the split material growth configuration, and the recombined, elastically deformed configuration.*

Clearly, the above formulation is an approximation since cells do interact with both collagen and elastin, and they are therefore not independent. We can account for this interaction by generating a stress constitutive equation for a microvolume of interest based on individual constituents, in this case fibers of collagen and elastin, which interact with one another and with a cell through the cellular stress-fiber network. Because biological tissues are composites of fibers, they do not necessarily behave as an affine continuum. Thus, if we return to the stress balance in Eq. 5.4, we can modify it to account for all constituent fibers within a tissue, which gives us the relation from volume averaging theory [96], [118], [119]

$$\sigma_{kj}(F^e_{mn}) = \frac{1}{v}\int_\Omega \sigma^p_{kj}(F^e_{mn})dv = \frac{1}{v}\sum_p \frac{f^p}{a^p} a^p l^p n^p_k n^p_j \tag{5.6}$$

where σ^p_{kj} is the stress in fiber constituent p, f^p is the force generated by fiber p, a^p is the deformed cross-sectional area of fiber p, l^p is the deformed length of fiber p, and n^p_k is the orientation vector along fiber p. In Eq. 5.6, all tissue constituents are considered to be fibrous, and all fibers are assumed to generate forces only along their length. Further, to maintain network stability, we enforce an osmotic (or hydrostatic) pressure that prevents the network from collapsing. The expression for the osmotic pressure based on [60] is

$$c_{fcd} = c_0\phi \,; P = RT\left(\sqrt{c^2_{fcd} + 4c^2_*} - 2c_*\right) \tag{5.7}$$

where c_{fcd} is fixed charge density, c_0 is a fixed charge scaling factor (70 mM), ϕ is the total fiber (solid) volume fraction, P is the osmotic pressure, R is the universal gas constant, T is the tissue temperature (310K), and c_* is the external osmolarity (150 mM). Thus, the total stress in the fiber network system can be expressed as

$$\sigma^{total}_{ij} = \frac{1}{v}\sum_p f^p l^p n^p_i n^p_j - P\delta_{ij} \tag{5.8}$$

where δ_{ij} is the Kronecker delta.

5.3.3 Microscale Mechanics

In the present work, we utilize microstructural discrete fiber networks to represent a tissue. The networks are generated from a periodic Delaunay tessellation using the tetrahedron edges as fibers. Fibers are linked at the vertices (nodes) of the tessellation tetrahedra via a pin joint. Multiple fiber types can be used in one model [96], [120], [121], and the properties of the fibers used in the presented models are given in **Table 4**. We describe both actin and elastin as linear elastic fibers with constitutive behavior governed by

$$f^p = \begin{cases} E^p\left(\frac{l^p}{L^p_0} - 1\right)a^p & if\ \frac{l^p}{L^p_0} \geq 1 \\ \frac{E^p}{100}\left(\frac{l^p}{L^p_0} - 1\right)a^p & if\ \frac{l^p}{L^p_0} < 1 \end{cases} \tag{5.9}$$

where f^p is the force along the fiber p, E^p is the fiber modulus, l^p is the deformed fiber length, L_0^p is the fiber undeformed length, and a^p is the fiber cross-sectional area. In the calculation of f^p, we assume fibers are long relative to their radius, and that they have uniform cross-section a^p (i.e. they do not taper). This means that the fibers are likely to buckle under compressive loads, which we represent in Eq. 5.7 by reducing the force by a factor of 100 when the fiber stretch $\frac{l_k^p}{L_0^p} < 1$. Collagen fibers are treated as helical springs as described in [122] to represent the waviness or crimp often associated with collagen. To solve for the internal equilibrium of the network subject to a deformation, we use Newton-Raphson iteration to minimize the forces on all nodes, as described previously [96], [123], [124].

Table 4: *Fiber constitutive equation properties*

Constituent	***Model***	***Material Parameters***	***References***
Actin	Linear Elastic	$E = 4\,MPa$	[125]
Collagen	Helical Spring	$E = 700\,MPa; R_0 = 5.8\,nm;$ $r_0 = 1.6\,nm;$ $H_0 = 67.4\,nm$	[126]–[128]
Elastin	Linear Elastic	$E = 1\,MPa$	[129]

5.3.4 Generating Meso-scale Structures

A major benefit of using fiber networks is that we can generate meso-scale structures within our representative network. In this work, we combine three fiber types using three different network generation techniques to create a meso-scale arterial medial lamellar unit structure. First, we generate a 3D periodic Delaunay network of elastin fibers, which we collapse to a 2D circumferential-axial plane, then we take the collapsed nodes from the elastin network and perform a 2D Delaunay tessellation to create an interconnected collagen network. We then pare the collagen network down to a connectivity of nine in order to reduce the cross-link density to more closely mimic in vivo behavior. This gives us a highly connected (cross-linked), short fiber, elastin layer with a mechanically linked, lower-connectivity, longer fiber collagen network. This structure is representative of the elastic lamina separating concentric rings of smooth muscle cells found in arteries. Next, we create a 3D periodic network of actin stress-fibers. We then determine which actin stress-fibers cross the elastin/collagen lamina layer. We split these actin fibers and connect each end to the nearest node in the elastin/collagen lamina to form physical links between the actin cytoskeleton and the elastic lamina (akin to integrins binding cells to the ECM). Importantly, meso-structures of this kind need no additional constraints applied to them in the solution of the micro-problem. They are subjected to the same boundary conditions and calculation of internal equilibrium as more basic network structures.

5.3.5 Microscale Remodeling

Each fiber in each network remodels separately based on its own fiber stress. The assumption is made that the microstructure remodels to approach a defined target stress for each individual fiber (local application of tensional homeostasis [105]–[107]), which, in turn, results in a net tissue equilibrium state. This remodeling model can be expressed mathematically on a local fiber-by-fiber basis motivated by the observations of [127], [130] as

$$\frac{dR^p}{dt} = \frac{1}{\tau}\left(\frac{\|\sigma^p\|}{\sigma_\infty} - 1\right) R^p \,; \frac{dL_0^p}{dt} = k\,\frac{dR^p}{dt} \tag{5.10}$$

where R^p is the radius of fiber p, t is the remodeling time, τ is the remodeling time constant, $\|\sigma^p\| = f^p/a^p$ is the fiber stress magnitude, σ_∞ is the homeostatic, target fiber stress, L_0^p is the undeformed length of fiber p, and k is a parameter relating fiber lengthening to fiber thickening. In this form, fibers can be thought of as adding individual collagen molecules to become thicker and to lengthen. Redundant or unloaded fibers are allowed to decay and disappear from the network, but the current model form does not prescribe the addition of any new fibers or fiber-fiber crosslinks. The fiber remodeling properties for each demonstration case and fiber type are given in **Table 5**.

Table 5: *Fiber Remodeling Parameters*

	$Network\ Scale,\ [\mu m]$	$Constituent$	τ	$\sigma_{\infty}, [MPa]$	k	$R_0, [nm]$
Artery	10	Actin	4 days	0.750	0.2	80
		Elastin	NA	NA	NA	120
		Collagen	90 days	2.0	0.2	260

This method of fiber remodeling assumes the network structure has already been synthesized and cells have matured to a more quiescent state. One could imagine creating some fiber generation rules or fiber crosslinking rules by which the underlying network topology could change, but that is beyond the scope of this work. As the fibers remodel, the network zero-stress state is updated by finding a new deformation such that the average stresses in the network are zero. More precisely, we calculate values of F_{np}^{g}, which are the growth stretches λ_{ii}^{g} and shears τ_{ij}^{g}, such that the stresses of the volume-averaged Cauchy stress σ_{ij} are zero.

5.3.6 Network Boundary Conditions

In this work, networks are generated within representative cubes. Network boundaries are deformed using the deformation gradient to give a new network shape. The nodes internal to the network are then equilibrated while keeping the structure periodic. Physically, this means that a fiber passing through one boundary enters the opposite, parallel boundary at the same location. Thus, fibers passing through a boundary are free to slide both along a boundary or into/out of a boundary. Networks are always prescribed displacement boundary conditions. To solve for a specified applied stress, we solve the forward problem applying a deformation, calculating a stress error, then stepping forward to a new deformation, and so on until we reach stress convergence using Newton iteration. This technique is utilized to calculate the growth tensor (the deformation state of the network at zero-stress).

5.3.7 Micro-to-Macro Coupling

The output of the microscale remodeling code is a new, remodeled network representing a very small patch of tissue. Although it is possible to couple the remodeling microstructure directly to the macrostructure [131], [132], it can be more convenient and often more easily interpretable to convert the microstructural model into an approximate continuum-scale strain energy density function, W and kinematic growth tensor, F_{np}^g. For the former, we choose a mixture consisting of a neo-Hookean ground matrix and three exponential fiber families representing the three orthogonal axes of the network (i.e. x,y,z in Cartesian coordinates or r, Θ, z in cylindrical coordinates).

$$W = c_1(I_1 - 3) + \frac{K}{2}(ln\,(J)\,)^2 + \sum_{i=1}^{3} \frac{c_2^i}{2c_3^i}\left[exp\,\left(c_3^i\left(I_4^i - 1\right)^2\right) - 1\right] \tag{5.11}$$

where W is strain energy density, c_1 is the modulus of the ground matrix, $I_1 = tr(C_{kl})$ is the first strain invariant of the right Cauchy-Green tensor $C_{kl} = F_{mk}F_{ml}$, K is the bulk modulus, J is the determinant of F, c_2^i is the fiber *modulus* of family i, c_3^i captures the nonlinearity of fiber family i, $I_4^i = C_{kl}N_kN_l$ is the fourth strain invariant where N_k is the fiber family direction vector. The microscale network model was coupled to the macroscale geometry by creating a stress-strain curve for the material [34] and determining a suitable parameterization of Eq. 5.11 to match the microscale network results. For the first iteration, absent any prior knowledge of macroscale deformations, we perform a suite of uniaxial, biaxial, and shear tests to generate a characteristic behavior for the material. After the first iteration, we utilize the deformation from the finite element (FEM) simulation to perform a linear ramping from the undeformed network configuration to the deformed configuration. Briefly, a stress-strain curve was generated from a set of N points $\left((F_{ij}^e)^m, \sigma_{ij}^m\right), m = 1 \ldots N$ where the elastic deformation F_{ij}^e is given by

$$\left(F_{ij}^e\right)^m = \left(\frac{m}{N}(F_{ik}^{FEM} - \delta_{ik}) + \delta_{ik}\right)\left(F_{kj}^g\right)^{-1} \tag{5.12}$$

and F_{ik}^{FEM} is the finite element deformation gradient and F_{kj}^g is the network growth tensor. The elastic deformation is defined relative to the zero-stress deformation, as given by the growth tensor for the network, to give the material behavior from a zero-stress configuration to any arbitrary deformed configuration. The stress at each deformation is computed as derived in Eq. 5.8. We then fit the behavior subject to the applied deformation. The fitting process resulted in a defined material behavior from the strain energy density function in Eq. 5.11 such that it would approximate the behavior of the discrete-fiber networks with maximum fidelity near the current deformation state.

5.3.8 Biophysics of Network-Finite-Element Coupling

The coupling technique outlined above focuses on using a single periodic network to represent a small patch of tissue represented by an FE element. One may wonder why we use the element average data rather than the Gauss point data to remodel our networks. Physically, we must maintain separation between the scale of the tissue and the size of the network in order to ensure that networks would not be occupying or intersecting the same physical space in the FE simulation. Thus, if we applied growth at each Gauss point, we would require a very coarse mesh, so we choose to apply growth on a per-element basis to utilize a finer mesh, which will have better overall FE convergence. With this information, one might think the best way to improve convergence in the macro problem would be to make the elements and thus the networks smaller, however, the network itself is dictated by a characteristic length based on the microscopic features we wish to model (e.g. the fiber lengths in a single constituent network or the size of the cells in our meso-scale arterial network). Thus, we are constrained on how aggressively we can make refinements to the elements. We have chosen this coupling method to balance the computational and biophysical trade-off between physical separation of periodic structural networks and the convergence of FE mesh elements. In the following examples we use a mean mesh edge size of 332.3um for the cruciform model, and a mean mesh edge size of 8.5um for the cylinder model.

5.3.9 Coupling of the Micro and Macro Time Scales

The solution of the fiber-by-fiber remodeling differential equations is performed using a forward Euler approach with two time scales: the micro time scale of the individual fiber remodeling within the network given as dt, and a macro time scale representing the time between subsequent FE simulations given as DT, where we can relate the two time steps through $DT = \int dt \approx \sum_{i=1}^{p} dt(i)$, and the total remodeling time T is given by

$$T = \int DT = \iint dt \approx \sum_{j=1}^{Q} DT(j) = \sum_{j=1}^{Q} \sum_{i=1}^{p} dt(i) \qquad (5.13)$$

where Q is the total number of macro-scale FE iterations and p is the total number of micro-scale network iterations. The convergence of the time-scale coupling is discussed further in Model Verification and Convergence. The time scales used for simulation are given in **Table 6**.

***Table 6**: Time Series Parameters for Forward Euler Simulation*

	Micro time step, dt [days]	Micro iterations, p	Macro time step, DT [days]	Macro iterations, Q	Total Time [days]
Media	0.05	10	0.5	300	150
Media + Adventitia	0.05	10	0.5	300	150
Chronic Dissection	0.05	10	0.5	64	32

5.3.10 Full Multiscale Model Overview

The overall FE-network multiscale remodeling algorithm is summarized in the flowchart in **Figure 33**a. The network remodeling code is summarized in the flowchart in **Figure 33**b. We note that one can simply alter the fiber-by-fiber remodeling equation (given as Remodel Fibers in **Figure 33**b) to change the physics of remodeling, and one can alter the constitutive model for the FE simulation (given as Fit Material Properties in **Figure 33**b) depending on the microstructural model used and the imposed FE deformation. This topic is discussed further in Model Limitations. The macroscale finite-element models in this work were created and simulated using FEBio2.9.1 [41]. Each element of the FE mesh was prescribed as a prestrain elastic material to solve the compatibility in growth [133]. The process begins by initializing a finite element mesh. We then generate a discrete fiber network structure for each element in the mesh. In step one, the fiber networks are run through a suite of deformations, and the behavior is fit to the material model in Eq. 5.11, giving the initial properties for the element in the FE mesh. The FE simulation is then performed. The deformation and stresses from the FE simulation are next input into the remodeling code, and the networks are remodeled. The network growth is calculated, the network is re-tested under the deformations extracted from the FE simulation, and the resulting stress-strain behavior is refit to calculate new material properties.

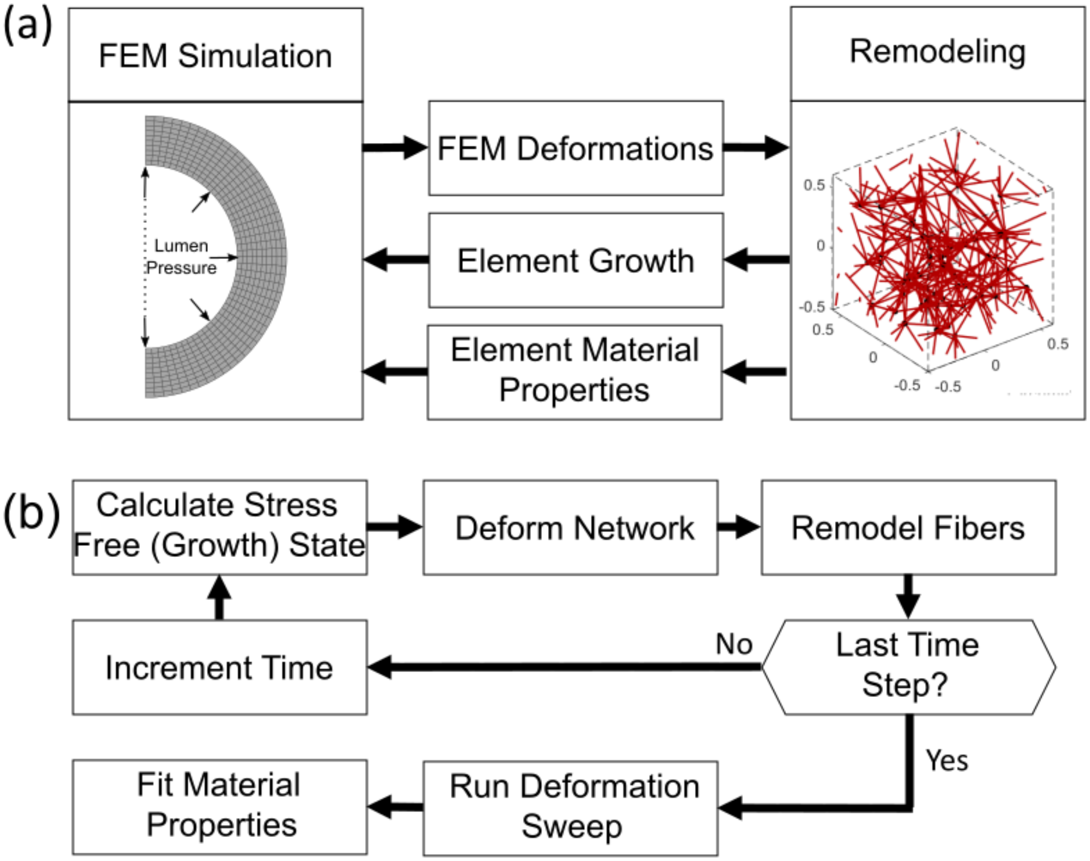

Figure 33: ***(a)*** *Hybrid discrete-continuum remodeling flowchart showing a representative macroscale geometry and a representative network used for constitutive modeling of each element of the FE geometry.* ***(b)*** *Network remodeling and material element update flowchart*

The code operates by calculating the material properties and zero-stress state (growth) from each network and then using that information as input into the FEBio simulation. The simulation is run, and the results for the element deformations and the element stresses are used for the network remodeling simulation. Briefly, the network is remodeled using deformation control, and operates using a forward Euler approach with the user defining the time-step length and the duration of remodeling for each FE simulation step. The code begins by calculating the zero-stress state for the network using Newton’s method. The code then deforms the network to the given deformation and calculates the internal equilibrium of fibers. Each fiber is then remodeled based on Eq. 5.10. The micro scale time is incremented, and the code continues remodeling the network until it reaches the defined macro time step duration. The end-state network material properties and the ending zero-stress state are calculated and used as input to the next macro iteration FE simulation.

5.3.11 Model Case Studies

5.3.11.1 The Thick-walled cylinder

Blood vessels are thick-walled cylinders that remodel in response to changes in blood pressure. Understanding how the architecture and residual stresses develop within blood vessels is central to relating tissue form and function. Further, understanding the remodeling process in terms of mechanical response to loading outside of the realm of ‘normal’ loads continues to be an active area of research especially in aortic dilatation, aneurysm, and dissection [94], [134], [135]. In this case study, we used a wedge of elements to simulate the medial layers of the mouse aorta as shown in **Figure 34**a. We simulated both normotension (mean arterial pressure (MAP) of 100mHg) and hypertension (50% increase in MAP to 150mmHg) The aortic elements are defined as a prestrain elastic material with the strain energy function of Eq. 5.11. The microscale network was defined to have a planar layer of collagen and elastin separating three-dimensional cellular layers mimicking the aortic medial lamellar unit [28,70] as shown in **Figure 34**a. This architecture represents the use of microscale Delaunay networks of different fiber types to simulate the mesoscale architecture of the aorta as described in section 5.3.4. The collagen, elastin, and actin fiber behaviors are prescribed in **Table 4**. Actin and collagen remodeled according to Eq. 5.10, with remodeling parameters given in **Table 6**. Elastin has a very long half-life, and was thus assumed to not remodel [136]. This case study referred to as Media or Media Only in this manuscript demonstrated the use of complex micro/meso-scale networks to simulate naturally occurring structures within a macroscale geometry.

5.3.11.2 The Role of the Adventitia in Arterial Remodeling

The adventitia is a collagen-rich layer that is thought to prevent damage to the vessel in the event of overload, and many studies have focused on the way the adventitia remodels in response to hypertension (e.g. [137]). In this case study, we add an adventitial layer to our thick-walled cylinder media model. The objective of this work was to investigate the role that the collagen-rich adventitia has on the remodeling of the media. The aortic FE geometry is shown in **Figure 34**b. The inner elements are prescribed to be medial layers and the outermost layer is prescribed to be adventitia. As before, a prestrain elastic material was prescribed with strain energy density given by Eq. 5.11. The media networks are the same as those used in the previous thick-walled cylinder. The adventitia network is generated as a Delaunay network consisting of only collagen fibers. The collagen, elastin, and actin model properties are given in **Table 4**. Collagen and actin remodel according to Eq. 5.10, with remodeling parameters given in **Table 6**. Collagen is assumed to remodel the same way in the media and the adventitia. Elastin is again assumed not to remodel. This case study referred to as Adventitia or Media + Adventitia in this manuscript demonstrates the use of multiple different micro/meso-scale architectures in a single macroscale geometry.

5.3.11.3 Remodeling in Chronic Aortic Dissection

Aortic dissection is the formation of a tear between layers within the aortic wall. This tear usually forms from the intimal side of the aorta, and thus is exposed to arterial pressure and flow. The result is that the dissection tends to be expanded by the arterial pressure, filling the tear region with blood forming a "false lumen." Dissection is associated with high levels of mortality both in the short term (acute phase) and in the long term (chronic phase) [138]. The treatment of aortic dissection varies widely based on where the tear and the subsequent false lumen form. In dissection affecting the ascending aorta (Type A), immediate surgery is generally performed. In dissections involving the descending or abdominal aorta (Type B), less aggressive treatments are often preferred including general monitoring to see whether the dissection stabilizes [138]. The false lumen is closed by

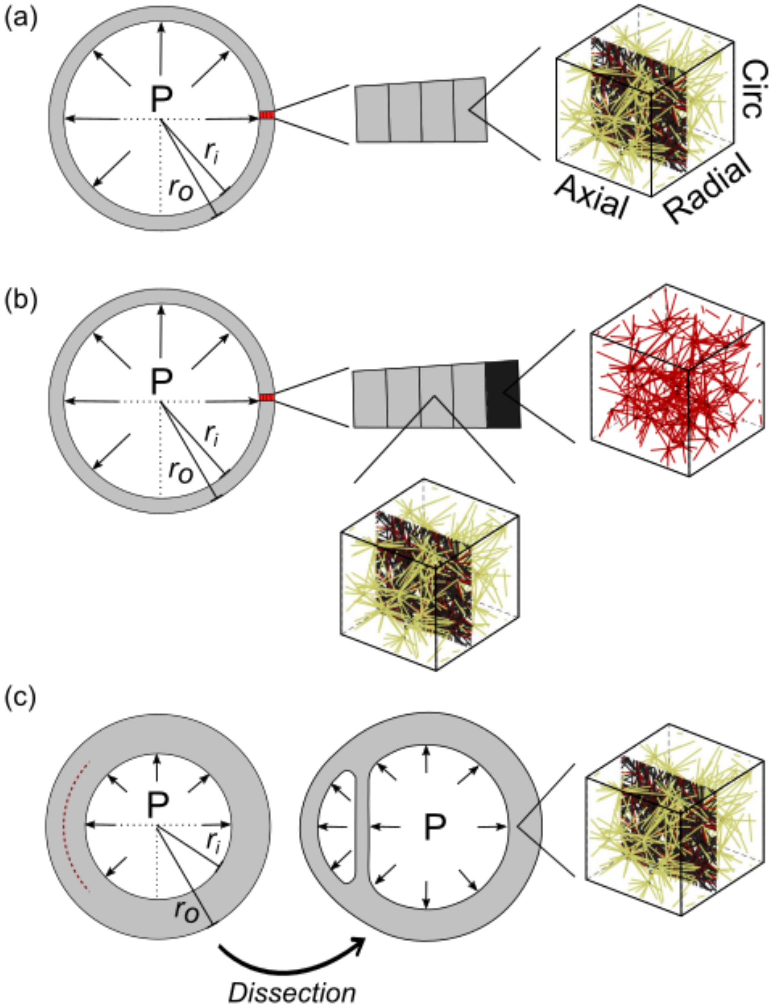

Figure 34: ***(a)*** *Configuration of the cylinder growth and remodeling case study with the four-element wedge used shown in red. A pressure boundary condition of 100 mmHg was applied to the inner curvature of the cylinder of inner radius (*r_i*) of 1.3 mm and outer radius (*r_o*) of 1.5 mm. The four-element wedge, representing the media layer, is shown with the periodic three fiber constituent network. Similarly, the five element wedge* ***(b.)*** *representing both the media and adventitial layer of arteries is shown with the same three fiber constituent fiber network representing the media and a collagen network representing the adventitia.* ***(c)*** *Configuration of the aortic dissection growth and remodeling case study with the dissection location shown in red in the healthy aorta slice. Similar to the previous case study, a healthy wedge was initially remodeled before the dissection was introduced. A pressure boundary condition of 100 mmHg was applied to the inner curvature of the cylinder of inner radius (*r_i*) of 0.127 mm and outer radius (*r_o*) of 0.195 mm. A periodic three fiber constituent network was used throughout the model.*

endovascular stent graft placement in many of these cases. Thus, one might wonder what factors are important in the stability of a chronic aortic dissection? Mechanically, there are four main components to how the tissue might respond: 1. The initial properties of the vessel at the time of dissection, 2. The new loading conditions of the tissue, 3. The geometry of the vessel and the tear, and 4. The tissue remodeling response. We created an idealized computational model of aortic dissection allowing us to independently control each of these factors and taking advantage of the flexibility of the multiscale FE code described herein. The dissected aortic FE geometry is shown in **Figure 34**c. The elements are prescribed to within the medial layer of the vessel wall. A prestrain elastic material was prescribed with strain energy density given by Eq. 5.11 for each element. The collagen, elastin, and actin model properties are given in **Table 4**. Collagen and actin remodeled according to Eq. 5.10, with remodeling parameters given in **Table 6**, while elastin did not remodel. This case study, referred to as Dissection or Chronic Dissection in this manuscript, demonstrates the ability of our technique to utilize structural complexity in both the microscale and the macroscale. It also demonstrates the usefulness of this technique to decouple factors that are difficult to isolate experimentally. Further, our model system allows us to assess clinically measurable features and correlate them with the underlying biophysics and pathophysiology.

5.4 Results

The objective of this work was not necessarily to show direct comparisons between our model results and any experiments, but rather to demonstrate the types of problems our scheme is capable of tackling and the types of insights we can gain from inclusion of a discrete microstructure. That noted, we provide broad comparisons to some other modeling frameworks and some experiments that are generally similar to our case studies.

5.4.1 The Thick-Walled Artery

We simulated a simple thick-walled cylinder consistent with the structure of an artery (**Figure 34**a). The simulation began by finding a normotensive, homeostatic state, after which we applied sustained hypertension of 50% over MAP. We refer to the normotensive state as "normotensive chronic" (NC), the state immediately after the application of hypertension as "hypertensive acute" (HA), and the state after re-equilibration to hypertension as "hypertensive chronic" (HC). During the remodeling process, the radius evolved as shown in Fig. 4a. In the thick-walled cylinder, the circumferential stress evolved through the wall thickness (**Figure 35**b). The hypertensive acute load caused a sharp increase in wall stress, alleviated over time by remodeling to the hypertensive chronic state; in all three states, the thick-walled geometry led to development of a stress gradient through the vessel wall. The results for the overall tissue growth in the remodeling of the thick-walled cylinder under normotensive and hypertensive loading scenarios are shown for the outermost element of the media in **Figure 35**c. The tissue thickens substantially and grows circumferentially in response to the pressure, as expected. The fiber volume faction given in **Figure 35**d for the outermost element showed substantial increases in actin stress-fiber content with much smaller magnitude decreases in collagen and elastin content. The differences between the inner and outer medial elements were small, so we only give the outermost element. The final network geometries for each stage of the remodeling process are given in **Figure 35**e. The inner and outer element differences are provided in *Appendix C* along with the observed elastic deformation for the tissue. We also show similar results for the case of hypotension given in *Appendix C*.

During remodeling, the circumferential stresses evolve as shown in **Figure 36**. There is an initial, homeostatic (normotensive chronic) residual stress (first plateau in **Figure 36**a) corresponding to a normotensive chronically loaded circumferential stress (first plateau in **Figure 36**b). After the homeostatic phase, we apply a 50% overload, where we see instantaneous increase in loaded stress (hypertensive acute spike in **Figure 36**b), which is

reduced back to a new homeostatic state for the hypertensive chronic scenario (second plateau in **Figure 36**b). The residual stress in response to chronic hypertension also increases in magnitude (second plateau of **Figure 36**a) with the tension on the outer surface and the compression on the inner surface roughly equal in magnitude. The residual stresses through the vessel wall (given at time points marked as normotensive chronic (NC), hypertensive acute (HA), and hypertensive chronic (HC) in **Figure 36**a) are shown in the cylinder cross-section in **Figure 36**c. These stresses are linked directly to the opening angle

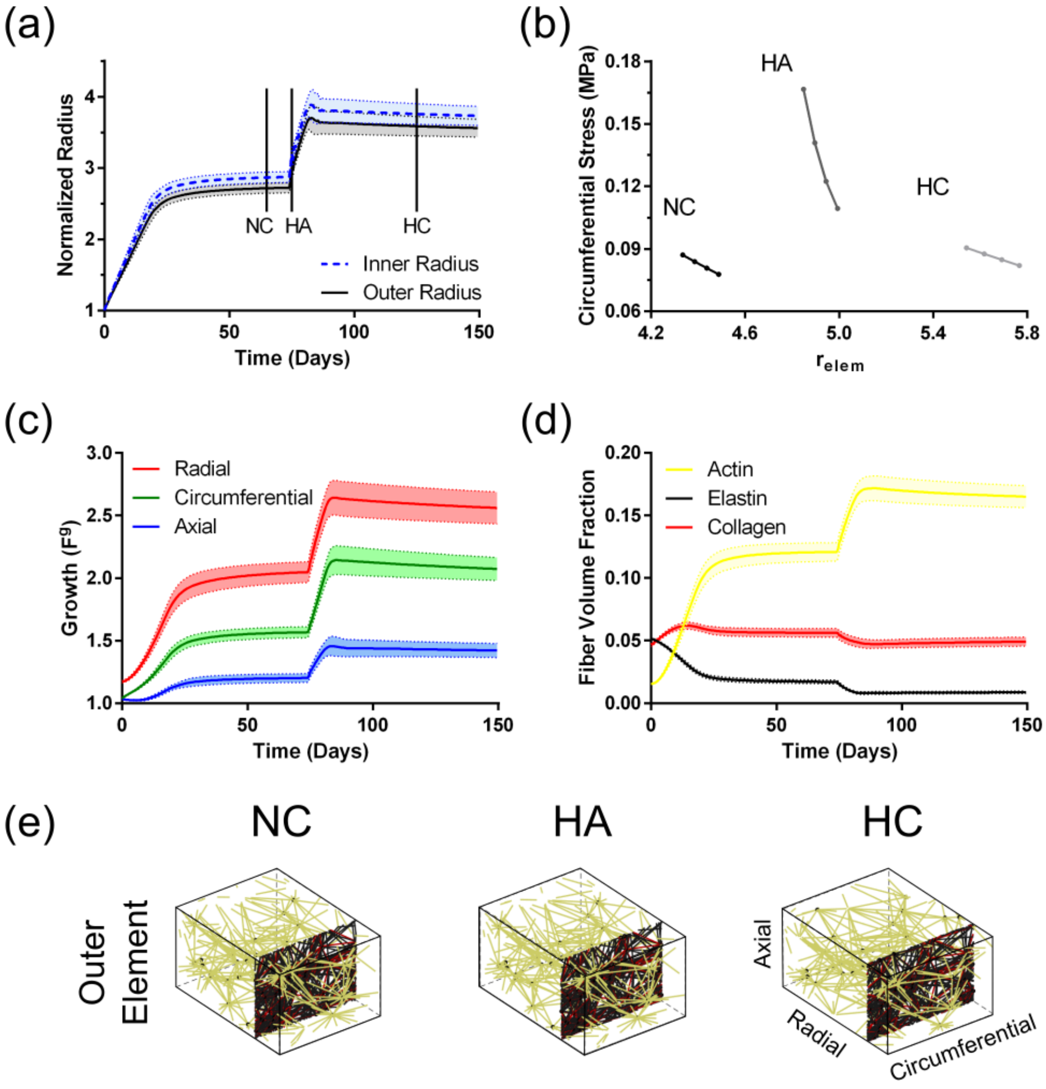

Figure 35: *The change in radius, normalized by the starting inner and outer radius for each network, is shown in **(a)**. Three time points, chosen to represent the normotensive-chronic (NC), hypertensive-acute (HA), and hypertensive-chronic (HC) states, and the mean circumferential stress vs. mean radius across all elements are shown in **(b)**.**(c)** The normal remodeling and response to 50% increase in load as well as the **(d)** fiber volume fraction of all three constituents are shown for the outermost element. Yellow, black, and red fibers represent actin, elastin, and collagen, respectively. The **(e)** outer element networks at the three chosen time points (NC, HA, HC.) are shown. Note: The networks are periodic so the location of the planar collagen/elastin layer is arbitrary. All data are shown as mean +/- 95% CI. (n=10)*

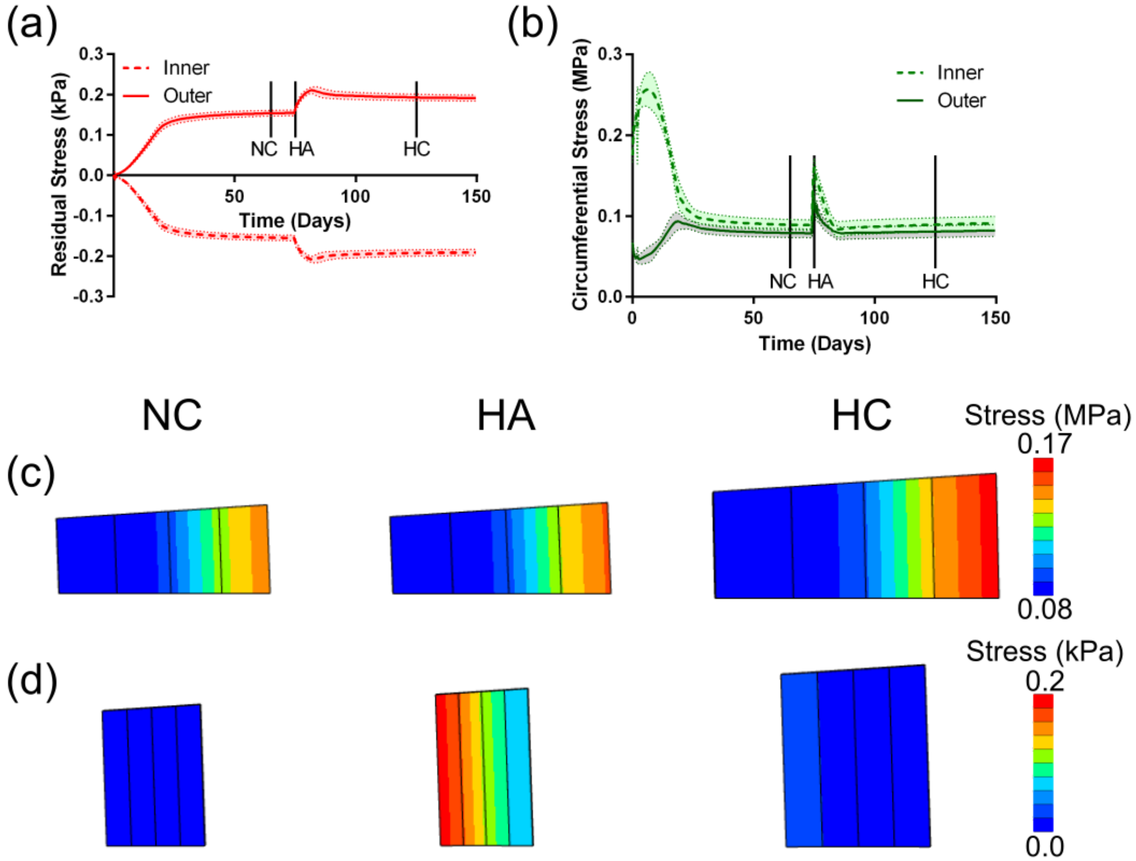

Figure 36: *The* ***(a)*** *circumferential residual stress and* ***(b)*** *circumferential stress in the outer and inner element over the course of remodeling. At time t=75 days, the pressure was increased from 100 mmHg to 150mmHg, simulating an overload case. The* ***(c)*** *residual and* ***(d)*** *circumferential stress at three time points (NC, HA, and HC) are shown for a given representative network. All data are shown as mean +/- 95% CI. (n=10)*

measurements typically taken during experiments, where a higher residual stress leads to larger opening angle. The loaded circumferential stresses corresponding to the notations NC, HA, HC in **Figure 36**b are shown in the cross-section in **Figure 36**d, demonstrating a nearly complete return to a homeostatic stress level.

5.4.2 The Role of the Adventitia in Arterial Remodeling

The adventitia serves a critical role in protecting the aorta from damage, but it remains unclear what role it serves in normal growth and remodeling. We investigated this role with our multiscale model by adding a collagen layer to the outside of the previously described thick-walled cylinder model. We simulated the same normotensive and hypertensive scenarios as defined for the thick-walled cylinder. The radius changes for the outermost medial layer and the adventitial layer are shown in **Figure 37**a. The radius stabilized in remodeling for the normotensive chronic case (first plateau) and the hypertensive chronic case (second plateau). The circumferential stress distribution through the vessel wall is given in **Figure 37**b, which indicated that large magnitudes of stress were carried by the adventitia. The growth results for the addition of an adventitial layer of collagen are shown for the outer medial layer (**Figure 37**c,d), and the adventitial layer (**Figure 37**e,f). The growth results show the radial thickening of the media along with the more prominent circumferential growth of the adventitia. The fraction evolution of constituents through the thickness is also given for the outermost medial layer (**Figure 37**d), and for the adventitial layer (**Figure 37**f). The medial layer predominantly increases in actin content, while the adventitia shows only slight increases in collagen content. The networks from the outer medial layer (**Figure 37**h) during the remodeling process indicated that the medial elements tended to thicken in response to load. The adventitial network (**Figure 37**i), tended to grow more circumferentially and thin radially.

The residual stress evolution in the inner medial, outer medial, and adventitial layer is given in **Figure 38**a. The residual stress shows two plateaus: one for the normotensive chronic case and one for the hypertensive chronic case. The magnitudes of both tensile and compressive stresses through the wall increased in response to hypertension. The residual stress also showed asymmetry through the thickness due to the adventitia. The media carried low levels of tension, while the adventitia was highly compressed in its unloaded

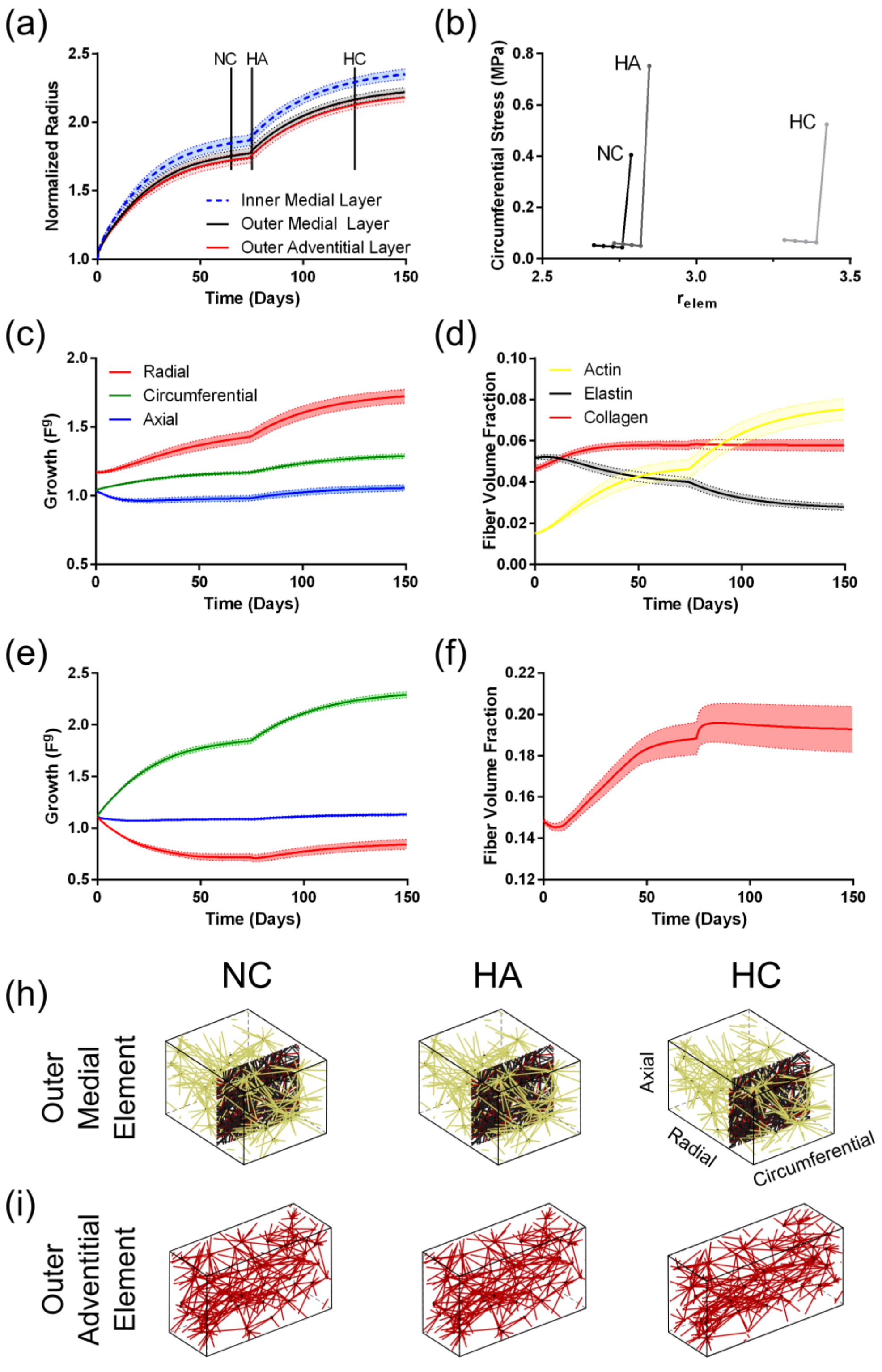

Figure 37*: The remodeling behavior of the five-element cylindrical model with medial and adventitial layers. The change in radius at the inner and outer medial layer, as well as the*

outer adventitial layer, normalized by the starting inner and outer radius for each network, are shown in ***(a)*** *three time points, chosen to represent the normotensive-chronic (NC), hypertensive-acute (HA), and hypertensive-chronic (HC) states, and the mean circumferential stress vs. mean radius across all elements are shown in* ***(b)****.* ***(c)*** *The normal remodeling and response to 50% increase in load as well as the* ***(d)*** *fiber volume fraction of all three constituents are shown for the outermost medial element. Similarly, the* ***(e)*** *normotensive and hypertensive remodeling response and the* ***(f)*** *collagen fiber volume fraction of the outer adventitial layer are shown. Yellow, black, and red fibers represent actin, elastin, and collagen, respectively. The* ***(h)*** *outer medial, and* ***(i)*** *outer adventitial element networks at the three chosen time points (NC, HA, HC.) are shown. Note: The networks are periodic so the location of the planar collagen/elastin layer is arbitrary. All data are shown as mean +/- 95% CI. (n=10)* state. The loaded circumferential stress for the inner medial, outer medial, and adventitial layer are given in **Figure 38**b. The circumferential loaded stress reaches a normotensive, homeostatic state, then hypertension is applied and a new homeostatic state is recovered. Here the results showed much of the stress due to loading being carried by the adventitia while the media was relatively shielded. The stress distribution through the wall for normotensive chronic (NC), hypertensive acute (HA), and hypertensive chronic (HC) are given for both the residual stress state (**Figure 38**c) and the loaded state (**Figure 38**d).These results further demonstrated the asymmetries in loading through the vessel wall due to the adventitia.

5.4.3 Microstructural Features of Arterial Remodeling

As previously mentioned, the network topologies for the media alone and the media and adventitia are given in **Figure 35**e and **Figure 37**h-i. When we look beyond the bulk network topology into individual fiber characteristics shown in **Table 7**, we see that, as expected hypertension increases both fiber diameter and fiber length for both actin and collagen. Further, we see that the adventitia does significantly alter the mean fiber diameters and lengths due to the stress shielding effects. Histograms of fiber lengths and radii are given in the *Appendix C* **Figure S9**-**Figure S10**.

5.4.4 Remodeling in the Chronic Aortic Dissection

To begin our simulation of chronic dissection, we remodeled a thick-walled cylinder consistent with our previous case study (see Section 5.3.11.1 and 5.4.1). This intact-tissue remodel gave us a starting state for our tissue. We then formed a tear within our tissue by splitting elements within the vessel as shown in **Figure 34**c, defining the onset of dissection. Mean arterial pressure was then applied to the newly formed false lumen as well as the true lumen, and the tissue was allowed to remodel. The differences between the initial cylinder immediately following dissection (left column) and the dissected cylinder after 32 days of remodeling (right column) are shown in **Figure 39**. The dissected cylinder significantly altered its residual stress state (**Figure 39**a), showing significant reductions in residual stress in the non-dissected region, and slight increases in

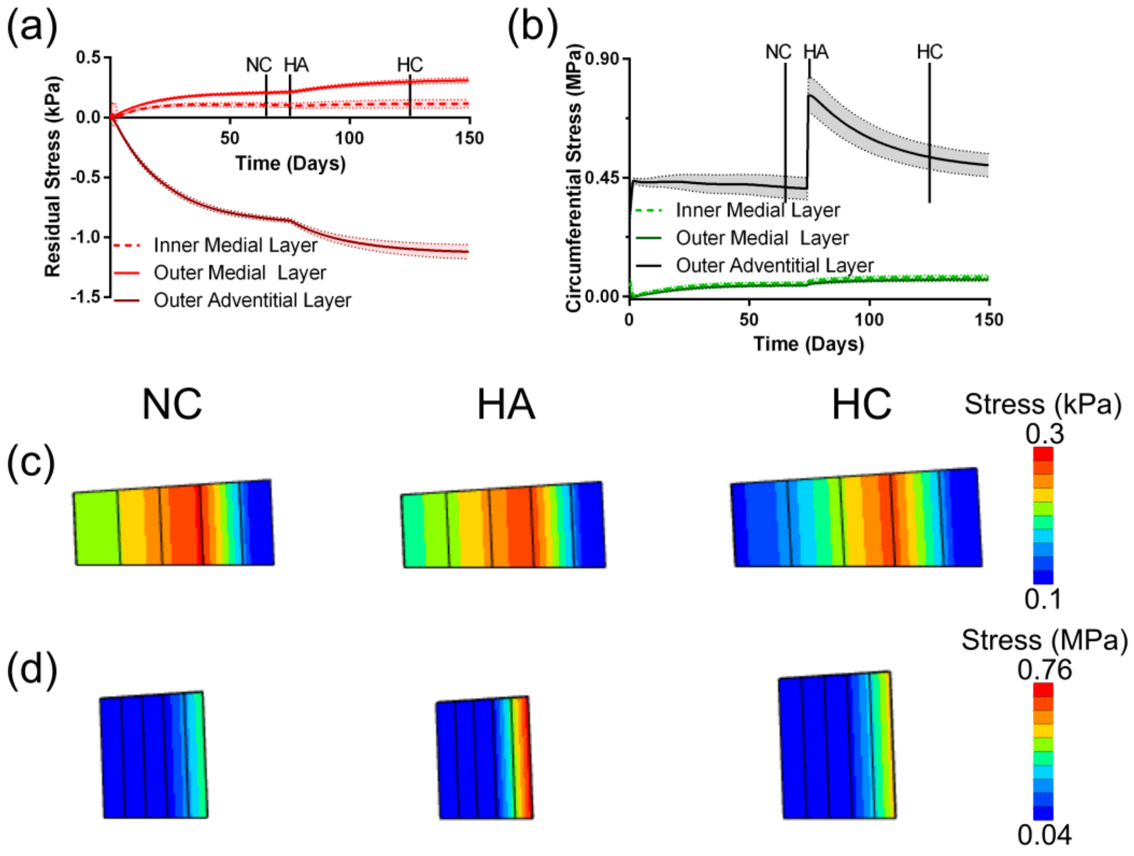

Figure 38: *Curves are shown for* ***(a)*** *residual stress and* ***(b)*** *circumferential stress over the course of remodeling. At time t=75 days, the pressure was increased from 100 mmHg to 150mmHg, simulating an overload case. The* ***(c)*** *residual stress and* ***(d)*** *circumferential stress for a representative case is shown, with the majority of the circumferential load being in the outer adventitial layer. All data are shown as mean +/- 95% CI. (n=10)*

the dissected septum (i.e., the wall separating the true lumen and false lumen). Initially under load, the dissected cylinder formed a band of stress emanating from the crack tip (**Figure 39**b), which was reduced and equilibrated during the remodeling. The remodeling itself resulted in significant volumetric growth of the tissue (**Figure 39**c) particularly towards the outer edge of the wall just away from the dissection. We also see that collagen content increased near the crack tip and opposite the dissection across the true lumen (**Figure 39**d). The collagen content decreased on the adventitial side of the media just past the crack tip (**Figure 39**d) consistent with the region of largest volumetric growth (**Figure 39**c). Further, significant alterations arose in material behavior, with the circumferential fiber modulus (c_2 in Eq. 5.11) increasing significantly (shown in *Appendix C* **Figure S11**a), particularly near the crack tip and along the region of largest growth. We also saw significant decreases in the axial modulus in the tissue as a whole, with small region of increased stiffness in the septal wall and outer wall of the false lumen (shown in the *Appendix C* **Figure S11**b).

5.5 Discussion

The scheme presented in this work provides a link between micro-scale cell/ECM remodeling and the macro-scale tissue consequences thereof. Local, independently-solved micro-problems for each macro-scale finite element allow study of detailed, local phenomena through application of local remodeling rules while capturing macroscopic geometric and physiologic effects. Below, we discuss each of the case studies in turn, followed by some limitations of this modeling scheme.

5.5.1 The Thick-walled Artery

The thick-walled cylinder results presented in **Figure 35** closely mimic our previous study using a thin-walled cylinder [96]. The model showed a significant increase in radius with the application of hypertension (**Figure 35**a). The remodeling process allowed the tissue to recover a homeostatic state, and we observed decreasing stress through the aortic wall in all cases (**Figure 35**b). Further, our results indicated that the stress though the aortic wall seemed to level out (slope of curves in **Figure 35**b) making the environment more consistent in terms of its stress-state. We also observed significant radial thickening and circumferential growth (**Figure 35**c) in the simulated artery. This demonstrates a tendency of arteries to thicken as a protective response to overload under normal extracellular conditions. In our simulations, a majority of remodeling happened within the cellular network, which might be expected because the actin cytoskeleton is prescribed a much faster turnover rate than collagen. We also saw that elastin fiber volume fraction dropped significantly. This decrease was not because elastin turned over, but rather because the tissue volume changed. In response to hypertension, we observed that the actin content increased sharply while the elastin content decreased slightly, and the collagen

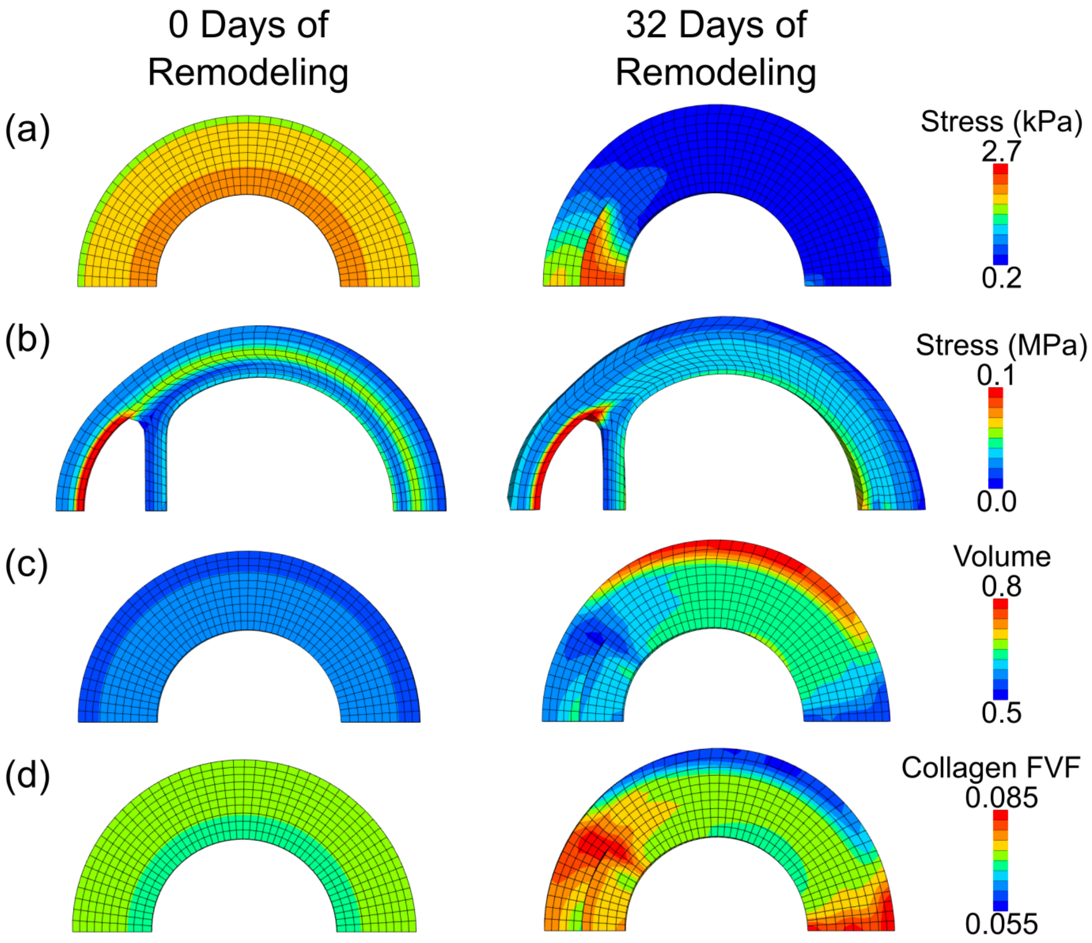

Figure 39*: The results of the aortic dissection case study before and after 32 days of remodeling. The results under "0 remodeling days" depict a healthy artery initially remodeled under normotensive pressure for 150 days. The* ***(a)*** *residual and* ***(b)*** *pressurized first principal stress, oriented circumferentially, are shown. The changes in the microscale fiber network are depicted as* ***(c)*** *volume change, and* ***(d)*** *collagen fiber volume fraction (FVF)*

Table 7: *Comparison of fiber lengths (L) and fiber radii (R) for actin stress fibers (SF) and collagen fibers (CF) in the initial network, the normotensive chronic (NC) case, and the hypertensive chronic (HC) case. Compared are the media only (M) and the media and adventitia (M+A) cases for both the innermost medial element (Inner), outermost medial element (Outer), and the adventitial layer (M+A Adventitia). The differential between inner and outer medial elements is given as Inner-Outer.*

			SF L (um)		**CF L (um)**		**SF R (nm)**		**CF R (nm)**		**CF L (um)**	**CF R (nm)**
			M	**M+A**	**M**	**M+A**	**M**	**M+A**	**M**	**M+A**	**M+A Adventitia**	
Initial	**Both**	**mean**	3.52	3.52	1.41	1.41	80.00	80.00	260.00	260.00	3.03	260.00
		std	1.43	1.43	0.69	0.69	0.00	0.00	0.00	0.00	1.15	0.00
NC	**Inner**	**mean**	6.40	4.31	2.90	1.89	224.18	119.45	334.40	284.21	3.18	267.70
		std	3.47	2.17	1.67	1.08	141.17	68.92	68.33	37.49	1.45	55.93
	Outer	**mean**	6.04	4.11	2.71	1.79	206.18	109.58	325.09	278.83		
		std	3.22	2.03	1.56	1.02	127.50	60.25	62.73	34.21		
		delta IO	0.36	0.20	0.19	0.11	18.01	9.87	9.32	5.38		
HC	**Inner**	**mean**	8.32	5.07	3.69	2.29	319.80	157.56	374.04	304.08	3.76	296.36
		std	4.51	2.72	2.18	1.33	194.41	101.48	94.23	50.79	1.77	73.14
	Outer	**mean**	7.87	4.79	3.46	2.15	297.42	143.51	362.63	296.82		
		std	4.19	2.52	2.04	1.25	178.13	90.38	87.31	46.26		
		delta IO	0.45	0.28	0.23	0.14	22.38	14.05	11.41	7.26		

content remained relatively consistent. This result indicates that, in healthy tissue, the cells would grow in response to increases in MAP. This is a favorable condition, especially in development. Further, increased cellularity may change the rate at which collagen turns over, which the model in its current form does not capture, but which could also be an important factor in normal development. For example, one could imagine the rate of turnover set proportional to the fraction of cells in the tissue (as proposed in [81]) effectively scaling the remodeling equation in Eq. 5.10 by the actin fiber volume fraction, although the investigation of alternative mathematical descriptions of single fiber remodeling laws are beyond the scope of this work.

In our previous study [96], there was not a convenient method for including residual stress, a problem resolved by the new method. We observed in this simulation that despite the small differences between the growth on the inner surface and outer surface, we still develop appreciable residual stresses (**Figure 36**). We can interpret the higher tension on the outer surface and compression on the inner surface as exerting a bending moment that would cause the tissue to spring open forming an opening angle when cut through the radial thickness. Our results demonstrate relatively similar residual tensions on the inner and outer surface. The residual stress was shown to increase in hypertensive cases relative to normotensive. This indicates that we might expect increases in opening angle with hypertension (at least in the absence of an adventitial layer). In their seminal work Fung and Liu [139] showed increases in opening angle with hypertension in the ascending aorta (which has a characteristically thinner adventitia that the descending/abdominal aorta), consistent with our model findings.

The thick-walled cylinder further showed modest, but appreciable, changes in growth between the innermost element and the outermost element (given in the *Appendix C*), which parallels results shown by [47], [49]. In response to hypertension, the circumferential elastic stretch (given in the *Appendix C*) returned to near homeostatic levels, while the radial compression showed hyper-restoration. This result indicates that the radial direction gets stiffer (more resistant to compression) in response to hypertension. Taken together, the differences in growth and mechanics indicated that the tissue remodeled by changing not only the physical size of the tissue, but also the mechanical response. This could be interpreted as a protective mechanism where when increased pressure is applied, the tissue grows circumferentially and radially, and stiffens radially to prevent damage, while maintaining circumferential properties.

5.5.2 The Role of the Adventitia in Arterial Remodeling

With the addition of an adventitial layer, the simulated remodeling process occurred more slowly in the media (**Figure 37**a, c, and e) and to a much lesser extent (**Figure 37**a and c) than the previous results for the thick-walled cylinder (**Figure 35**a and c). Much of the pressure load was shifted to the collagen-rich adventitia (**Figure 37**b), which made the actin content of the media (**Figure 37**d) much less prominent than for the media-only case. This result suggests a protective effect of the adventitial layer to medial cells. The stress through the wall (**Figure 37**b) tended to be much flatter in the media for this case versus the thick-walled, media-only case. Further, in response to load, the medial stress levels hardly change (NC vs. HA in **Figure 37**b). This is additional evidence for the protective effect the adventitia has in hypertension to the media. As for the adventitia itself, there was significant circumferential growth and radial compaction (**Figure 37**e), which is consistent with histology for the aorta [66]. We also observed modest increases in collagen content of the adventitia in response to hypertension (**Figure 37**f). The total fiber content (sum of actin, collagen, and elastin) in the medial wall was similar to the total collagen in the adventitia, indicating that the changes between the media and adventitia were likely a product of the microstructure and not due to the influence of hydrostatic pressure (based on fiber content).

The addition of an adventitia significantly altered the residual stresses in the wall with the media being held entirely in tension and the adventitia being in compression (**Figure 38**a). The net result of such loading would be a negative opening angle, which would mean when cut open the tissue would spring closed to form an overlap of the cut ends. This is in stark contrast to the media only case, where the inner media was in compression and the outer media was in tension (**Figure 38**a). Although surprising, this result, and the increase in the closing angle with hypertension, are not unheard of. In the afore mentioned paper by Fung and Liu, they demonstrate negative opening angles in the mouse aorta in the lower thoracic/upper abdominal region, which appears to be exacerbated with hypertension [139], [140]. The existence of negative opening angles in the lower part of the aorta, and the fact the adventitia in this region tends to be thicker [141], would indicate that the adventitial thickness plays a key role in mediating the arterial residual stress, particularly in the cell-laden media. Further, the addition of the adventitia seemed to make the residual stresses and the loaded stresses (**Figure 38**c and d) more consistent though the wall consistent with the model of Alford et al. [49]. It is possible that this is an important feature for maintaining the cellular mechanical environment within a vessel wall, as suggested by Bersi et al. [137].

5.5.3 Remodeling in Chronic Aortic Dissection

Our simulations on chronic aortic dissection suggest that the tissue undergoes significant remodeling with relatively small changes in macroscopic features. The overall shape of the tissue shows relatively little change (**Figure 39**a,b), but we see large discrepancies in underlying growth (**Figure 39**c), which manifested itself not through macroscale geometric shape changes, but through changes in the residual stresses in the vessel wall (**Figure 39**a). There were also significant changes in collagen content of the vessel wall with large regional variations around the circumference of the vessel (**Figure 39**d). Further, the properties of the underlying tissue were region-dependent, with significant differences near the false lumen and through the wall thickness, even far from the dissection (**Figure S11**a,b). There is disagreement in the literature on the properties of tissue near a dissection, as some studies report increases in small-strain stiffness [142], [143], while other studies (utilizing more advanced characterization techniques) have shown both increases and decreases in stiffness from sample to sample with a wide range in stiffness [144]–[146]. Our data might suggest that treating the sample as one tissue could be part of the problem, and that even tissue samples in close proximity may have vastly different properties. However, the observed differences may be more indicative of differences in initial pathology (prior to dissection) than in dissected vs. non-dissected tissues. The growth of the vessel during the chronic phase in type B dissection has been reported to be ~4%/year of the initial diameter [147], and the intimomedial flap of the false lumen has been shown to remain relatively stable in thickness (<0.5%/year increase in thickness) [148], [149]. Our results over the course of 30 days simulated time showed an increase in the false lumen impinged diameter of 4.25%, and an increase in the flap thickness of 0.66% under MAP loading. Clearly, our results show that the tissue remodeling is regionally variable around the circumference of the tissue slice and inducing minimal tissue macroscopic changes, but significant changes in the residual stress, tissue fiber content, and gross material properties.

5.5.4 Computational Efficiency

Although this method serves as a simplified way to interface any discrete microstructural description of a tissue with an FE model, the computational efficiency aspects must be addressed if this technique is to be tractable. Here we perform a rough cost estimate based on the stress and stiffness calculations only, neglecting the macroscopic-scale Newton solve that is the same for all approaches. Consider a network of fibers representing the microstructure. If we have a network of N fibers and M nodes used as a constitutive equation for an FE simulation, assuming the network behaves affinely, we would calculate N fiber forces and fiber lengths + 1 summation for total volume averaged stress. This would be required for every gauss point within every element. Thus, for a hex mesh of E elements, we would have 8xE stress calculations, which would become 8E(N+1) calculations for a network of N fibers. In the same way, we would have 8E(N+1) calculations of the stiffness tensor. This is for each step of the FE solution, so if we have S steps, then we would have 8ES stress calculation and 8ES elasticity calculations for the normal FE simulation and 8ES(N+1) calculations for the stress and elasticity of the network. This is not really a huge major hinderance to the solution because the calculation can be simply vectorized. However, since there is no requirement that the deformation on any given fiber is affine, we must iterate to ensure an equilibrium solution. The solution of equilibrium requires another solution of the internal Jacobian, which is an additional N calculations of the derivative of fiber forces with respect to fiber end nodal coordinates per iteration +1 summation of derivatives in addition to the calculated fiber forces. Thus, if the Newton loop ensure convergences after K iterations, we have a total of 8ES(2N + 2)K calculations to determine the stress in the network. By the same argument, the stiffness calculation would be 8ES(2N + 2)K calculations. If we contrast this with the fitting of a constitutive model, we would have 8ES calculations for the stress and the stiffness for the constitutive model. We would also have TE(2N+2)K calculations for the fitting process where T is the number of test points (deformation steps) for fitting. Now, assume that H iterations are required to fit the constitutive behavior for the network so that the overall fitting the constitutive behavior requires $(T(2N+2)K + H)E$ calculations. There is no additional calculation of the stiffness of the network required, as we let the fitting of stress also dictate the stiffness tensor. The results are summarized in **Table 8**.

***Table 8**: Computational Efficiency of Hybrid relative to Continuum Model and Full Multiscale Model*

	Continuum	**Full Multiscale**	**Hybrid (fitting + continuum)**
Stress Calcs.	$8ES$	$8ES(2N+2)K$	$TE(2N+2)K + HE + 8ES$
Elasticity Calcs.	$8ES$	$8ES(2N+2)K$	$0 + 8ES$
Total	$16ES$	$16ES(2N+2)K$	$TE(2N+2)K + HE + 16ES$
Calcs. Normalized to Continuum Solution	1	$(2N+2)K$	$\frac{T(2N+2)K}{16S} + \frac{H}{16S} + 1$
Calcs. Normalized to Full Multiscale	$\frac{1}{(2N+2)K}$	1	$\frac{T}{16S} + \frac{H}{16S(2N+2)K} + \frac{1}{(2N+2)K}$

Observing that, for nearly any reasonable problem, $N \gg 1$ (e.g., $N = 1076 \pm 13$ fibers for the medial networks of Fig. 4b-c, and $N = 322 \pm 3$ fibers for the adventitial networks of **Figure 35**c). Thus, we see we will never approach the efficiency of the continuum, constrained mixture model due to the structural complexity of our networks. However, the cost of the approach is mitigated by the highly parallelizable nature of the micro-problems, which would reduce the $(2N+2)$ calculations proportional to the number of CPUs used provided that number is less than or equal to the number of elements in the FE mesh.

We see from this illustrative example that the computational benefit over the full multiscale simulation comes into play when we are dealing with multiple FE steps (i.e., large S). In this scenario we will see speed improvement over the full multiscale simulation when $\frac{T}{16S} + \frac{H}{16S(2N+2)K} + \frac{1}{(2N+2)K} < 1$, where the first term is expected to dominate because of the large number of fibers N, reducing the expression to $\frac{T}{16S} < 1$. Thus, when we increase the number of FE steps, which is quite common especially in nonlinear, large deformation problems, or in dynamic problems (like the arterial pulse), we would anticipate significant speed benefits from this method over the full multiscale method. The computational value of the coupling approach is further outlined with more concrete wall-time numbers in [104].

5.5.5 Model Verification and Convergence

The behavior of the model system was verified by remodeling a simple cube in the FE domain consistent with a single network. We show in the *Appendix C* to this manuscript that that the code demonstrates the correct solution for both stress-control and displacement control provided we utilize small macroscopic time steps (i.e. the time between subsequent FE solutions). We further verified the code by simulating the remodeling a simple collagen cruciform during compaction by fibroblasts (a common G&R experimental model system), which is also given in the *Appendix C* to this paper.

A potential inaccuracy in this modeling system evolves from the fact that error can be propagated forward from treating the reciprocal nature of this scheme as an explicit forward algorithm. What we mean by this is that the macro FE problem is dependent on the micro network properties, which are fitted to the constitutive relation. Thus, if the fit is not accurate, we will have a stress differential between what the FE model predicts and what the micro network shows. To address this, one could alternate macro-micro steps until the stress differential converges. We have found that such a relationship is unnecessary beyond the first step of the simulation (or at the time of imposing specified boundary conditions more accurately). The reason is after the first step, the deformation of the FE model elements are used to define the local behavior of the micro networks, and in the absence of rapidly changing loading, the estimation of properties only improves beyond the first, initial step.

Still, we are propagating feed forward error, so we performed a time series convergence study on our multi-constituent cylinder model (**Figure 34**a) to ensure proper convergence. In our convergence study we looked at two time scales: the microscale, network (single fiber) remodeling time, and the macroscale, FE remodeling time. We choose the multi-constituent case because the actin remodels much faster than the collagen, so we must ensure convergence based on the fastest remodeling time scale utilized in this work. **Table 9** shows the time series performed and the end-state errors in growth relative to the most refined run (denoted by - - - in the table). The full plots of the time course of remodeling for the entire growth tensor are given in Figs. **Figure S4-Figure S5** in the *Appendix C*. In the micro-time step, we see small magnitudes of error all around. We note there is less than 0.02% error propagated over 50 macro time steps using the micro time step of 0.05 days, which is what is employed in this study. Further, we show that we are propagating less than 0.125% error over the course of 100 macro time steps at 0.5 days each, which is the length of step used for these studies. Thus, we recommend the use of dt=0.05 days for 10 iterations on the micro-scale, which gives us DT=0.5 days on the macro-scale for simulations following the parameters listed in this work. The time step length should be carefully considered if adapting this remodeling framework to different time-scales, or if one is employing different remodeling rules.

***Table 9**: Time Convergence study for both the micro-scale (network) and macro-scale (FE) simulation of the thick-walled multi-constituent artery cylinder run for a total of 50 days*

Micro time step [days]	Micro iterations, p	Macro time step [days]	Macro iterations, Q	Inner Element Growth Error (e_{11}, e_{22}, e_{33}) ; [%]			Outer Element Growth Error (e_{11}, e_{22}, e_{33}) ; [%]		
1.0	1	1.0	50	-0.099	-0.148	0.166	-0.189	-0.088	0.530
0.1	10	1.0	50	0.040	0.026	0.009	0.038	0.025	0.015
0.05	20	1.0	50	0.017	0.011	0.005	0.017	0.011	0.006
0.01	100	1.0	50		- - -			- - -	
0.05	100	5.0	10	-14.163	-14.143	-9.727	-13.253	-14.448	-8.959
0.05	20	1.0	50	-0.461	-0.394	-0.285	-0.413	-0.379	-0.252
0.05	10	0.5	100	-0.124	-0.108	-0.086	-0.108	-0.114	-0.061
0.05	5	0.25	200		- - -			- - -	

5.5.6 Limitations of the Modeling Scheme

The constitutive coupling used in this method approximates the network behavior, and therefore should be considered carefully. For example, in our current model, we found that the collagen networks and the composite medial networks show nonlinear behavior very similar to the GOH model [150] under the investigated loading conditions (i.e. biaxial tension and inflation). In contrast, an eight-fiber Arruda-Boyce-like [151], linear fiber network model (used in a verification study included in *Appendix C*) exhibited nearly linear behavior. Thus, it would be more reasonable to use the neo-Hookean (or Mooney-Rivlin) constitutive model for that material. In the cases studied here, we utilize loading scenarios that are characterized by stretch-dominated deformations. In this type of deformation, we capture the behavior of any network shear using the principal fiber directions. Further, the networks used herein develop small magnitudes of shear due to the ability of fibers to rotate and realign within the network. Thus, the simple GOH model make for a reasonable approximation. If, however, our macroscale geometry was subject pure shear loading without significant stretch, we might need to consider other constitutive models to represent the network material behavior accurately. For example, one could add shear coupling fibers similar to those employed by the four-fiber family model [152], one could use a distributed fiber version of the GOH model [153], [154], or one could use the Arruda-Boyce material model [151].

The use of a single network to define the properties of an element is also an approximation of the microstructure. We mitigate the effect of using only a single network for an element by prescribing periodicity on the microscale. The imposition of periodicity, however, means the deformation must follow the element-averaged deformation gradient, rather than being defined from the nodal positions of the elements themselves. The network deformation could be defined based on nodal coordinates of elements, but that would require the use of networks with non-periodic boundaries. Such networks tend to exaggerate edge effects and were therefore precluded from this study.

This technique in the form presented uses a very simple model of fiber turnover. The idea is that the fiber radius increases and this increase in radius is proportional to an increase in length (effectively adding fibril monomers to an existing fiber). Further, the model in its current form has no way to add new fibers to the network, it only grows and decays existing fibers. Thus, there is a mechanism for removal of unimportant fibers, but no mechanism for the addition of new fibers in any preferred alignment. Further, the decay and addition time constants are not variable and the fiber addition/removal is only based on stress. One could imagine that this relationship might also be dependent on other factors including cellularity of the tissue (e.g. the form proposed in [81]). The definition of growth in this work is phenomenological and is clearly an abstraction of the remodeling process. Future work is needed in biophysically motivating ECM growth models on both the single fiber and network level.

This work demonstrates a hybrid method for multiscale simulation of remodeling in biological tissues. We couple network microstructural elements to finite element modeling via FEBio by using simple constitutive modeling. The finite element code solves the compatibility of the growth, and determines the stress-strain state, while the remodeling is handled by the microstructural model given the stress-strain state of the tissue as a whole. Being able to apply the remodeling directly to the network level allows for gathering architectural information along with local material inhomogeneities, which are critical aspects in understanding initiating events in growth, remodeling, and failure. The applicability of this technique is broad in that one can model any tissue with any microstructure in any finite element software, making it a highly accessible approach for multiscale mechanic simulations.

6 Discussions and Conclusions

6.1 Summary

This dissertation characterized the on-joint, or *in vivo*, mechanical state of a capsular ligament during healthy adulthood. Three key features, and their relation to the stress and strain response of the ligament, were explored: (1) residual strain, (2) inflation strain due to joint pressurization, and (3) through-thickness variation in the collagen and elastin fibers.

First, I characterized the mechanical differences between the collagen and elastin regions using a novel stretch-and-bend experimental technique (Chapter 2). This study highlighted the effect of the inherent tension-compression asymmetry on ligament mechanics and offered novel insights on the effect of varying collagen and elastin fiber densities across the tissue. The main conclusion was that collagen composition, distribution, and crimp length are important considerations when bridging the knowledge gap between planar facet capsular ligament mechanics and on-joint behavior of the ligament. This work presents a significant advancement in our understanding of the behavior of capsular ligaments on-joint.

Next, I characterized the effect of joint pressurization on observed ligament surface strains using 3D strain tracking (Chapter 3). Although there has been limited research on inner capsular pressure at rest, dynamic rapid movement of the synovial fluid during spinal motions will cause changes in capsular pressure that has previously been overlooked. I performed a novel study to track the effect of joint pressure on ligament strains and, additionally, I directly measured the residual strain in the ligament as it was cut off the bone. The study reveals that the normal in vivo state of the facet capsular ligament is in tension, and that the collagen fibers are most likely uncrimped even when the spine is not loaded.

Finally, I expanded the capabilities of an existing multiscale FCL by Zarei *et. al* [16] model to include all 3 key features and determined the on-joint mechanical state of the ligament, both at rest and during spinal motion (Chapter 4). While the current validated model represented a significant advancement in our understanding of multiscale mechanics of the ligament, its performance was validated against an *in vitro* experimental dataset that does not necessary account for all factors. The enhanced computational model allowed us to observe realistic on-joint ligament stress distributions from the knowledge gained in previous planar and *in situ* mechanical tests of the ligament (Chapter 2-3). This enhanced computational model could significantly enhance our understanding of spine and ligament biomechanics, bone health, and could potentially contribute to prevention strategies for spinal diseases and instabilities.

Additionally, a discrete-continuum computational growth and remodeling framework was presented that has potential to track the progression of the ligament throughout growth and remodeling (Chapter 5). We coupled networks of collagen, elastin, and actin fibers to finite element modeling, via FEBio, using the hybrid continuum approached described in *Appendix A*. The macroscale solution of the growth and stress-strain state of the tissue is resolved within FEBio while the remodeling is done on the microstructural networks, allowing us to study changes on both the micro- and macroscale level. Although this study focused on G&R phenomenon in cardiovascular tissues, due to the wealth of prior knowledge, a small case study on G&R in the FCL is presented in *Appendix A*. This method can be broadly applied as it allows modeling of any tissue with any microstructure using any finite element software, and even allowing for expansion of the framework to include other mechanical loads, such as fluid-solid interactions, or remodeling factors, such as matrix metalloproteinases and tissue inhibitors of metalloproteinases, key indicators of tissue degeneration [155].

6.2 Future Direction

While the enhanced multiscale model presented in this dissertation advanced our understanding of the on-joint mechanics of the facet capsular ligament, it also highlighted the complex nature of the ligament and numerous factors that contribute to its mechanical state.

The incorporation of residual strain and inflation strain expanded our understanding of their effects on ligament mechanics, both at rest and during motion. The current methodologies can be expanded to include more realistic representations of these factors. Currently, a single representation of the L3L4 FCL was used, and a future next step could be to obtain sample-specific geometries of each tested specimen. While an average residual deformation was applied across the entire ligament, as observed in our experimental results described in Chapter 3, the residual strain is not homogenous. Using sample-specific geometries for each model would allow us to directly apply the observed residual strain field in our model. Additionally, the inflation strain was prescribed as a pressure load on the anterior portion of the ligament. We can further study the effect of joint pressurization by modeling the synovial fluid as an encapsulated fluid with prescribed fluid boundary conditions. This would allow us to study the pressure change within the joint space for a given applied spinal motion. We can also include fluid dissipation and speed of applied motion to study the effect of rapid spinal motions on ligament stress and strain fields.

Further, this model represents spine and ligament mechanics in a healthy patient, with no additional factors that would contribute to LBP. Future work can expand this model to simulate stages of aging and degeneration. The introduction of different pathologies, such as spondylolisthesis, or surgical interventions could provide a more holistic perspective on the lumbar facet capsular ligament's mechanics and their role in spinal biomechanics.

6.3 Conclusion

This work led to three novel findings. First, the ligament was stiffest when 3 conditions were met: the collagen fibers were (1) aligned in the direction of loading and (2) were in tension, and (3) the ligament was stretch ~16% from the off-bone, undeformed state. Second, results from planar mechanical tests overestimate the extent of stretch a ligament can endure before the collagen lock-out state is achieved. The normal *in vivo* state of the facet capsular ligament is in tension, and that the collagen fibers within the ligament are likely uncrimped even when the spine is not loaded. Third, pressurization (inflation) strain and residual strain have large effects on overall ligament stresses and strains. These factors (joint pressurization, residual strain, and through-thickness collagen variation) are contributors to or are driven by growth and remodeling phenomenon in soft tissues. Together these results provide a comprehensive analysis on the on-joint mechanical state of the lumbar facet capsular ligament and provide important insights that can influence future research, clinical applications, and therapeutic approaches of spinal biomechanics.

Bibliography

[1] G. Andersson, “Epidemiological features of chronic low-back pain,” *Lancet*, vol. 354, pp. 581–585, 1999.

[2] C. W. Pfirrmann, A. Metzdorf, M. Zanetti, J. Hodler, and N. Boos, “Magnetic resonance classification of lumbar intervertebral disc degeneration.,” *Spine (Phila. Pa. 1976).*, vol. 26, no. 17, pp. 1873–8, Sep. 2001, Accessed: May 15, 2019. [Online]. Available: http://www.ncbi.nlm.nih.gov/pubmed/11568697.

[3] M. Huang *et al.*, “Correlation between T2* (T2 star) relaxation time and cervical intervertebral disc degeneration,” *Medicine (Baltimore).*, vol. 95, no. 47, p. e4502, Nov. 2016, doi: 10.1097/MD.0000000000004502.

[4] J. S. Little and P. S. Khalsa, “Material Properties of the Human Lumbar Facet Joint Capsule,” *J. Biomech. Eng.*, vol. 127, no. 1, pp. 15–24, 2005, doi: 10.1115/1.1835348.

[5] S. A. O’Leary, N. K. Paschos, J. M. Link, E. O. Klineberg, J. C. Hu, and K. A. Athanasiou, “Facet Joints of the Spine: Structure–Function Relationships, Problems and Treatments, and the Potential for Regeneration,” *Annu. Rev. Biomed. Eng.*, vol. 20, no. 1, pp. 145–170, Jun. 2018, doi: 10.1146/annurev-bioeng-062117-120924.

[6] N. V. Jaumard, W. C. Welch, and B. A. Winkelstein, “Spinal facet joint biomechanics and mechanotransduction in normal, injury and degenerative conditions,” *J. Biomech. Eng.*, vol. 133, no. 7, pp. 1–31, 2011, doi: 10.1115/1.4004493.

[7] M. A. Adams and W. C. Hutton, “The Mechanical Function of the Lumbar,” *Spine (Phila. Pa. 1976).*, vol. 8, no. 3, pp. 327–330, 1983.

[8] L. Kalichman and D. J. Hunter, “Lumbar Facet Joint Osteoarthritis: A Review,” *Semin. Arthritis Rheum.*, vol. 37, no. 2, pp. 69–80, Oct. 2007, doi: 10.1016/j.semarthrit.2007.01.007.

[9] A. Ianuzzi, J. S. Little, J. B. Chiu, A. Baitner, G. Kawchuk, and P. S. Khalsa, “Human lumbar facet joint capsule strains: I. During physiological motions,” *Spine*

J., vol. 4, no. 2, pp. 141–152, Mar. 2004, doi: 10.1016/j.spinee.2003.07.008.

[10] A. A. Claeson and V. H. Barocas, “Planar biaxial extension of the lumbar facet capsular ligament reveals significant in-plane shear forces,” *J. Mech. Behav. Biomed. Mater.*, vol. 65, pp. 127–136, 2017, doi: 10.1016/j.jmbbm.2016.08.019.

[11] E. A. Bermel, S. Thakral, A. A. Claeson, A. M. Ellingson, and V. H. Barocas, “Asymmetric in-plane shear behavior of isolated cadaveric lumbar facet capsular ligaments: Implications for subject specific biomechanical models,” *J. Biomech.*, vol. 105, 2020, doi: 10.1016/j.jbiomech.2020.109814.

[12] E. Gacek, E. A. Bermel, A. M. Ellingson, and V. H. Barocas, “Through-thickness regional variation in the mechanical characteristics of the lumbar facet capsular ligament,” *Biomech. Model. Mechanobiol.*, vol. 20, no. 4, pp. 1445–1457, 2021, doi: 10.1007/s10237-021-01455-3.

[13] E. A. Bermel, V. H. Barocas, and A. M. Ellingson, “The role of the facet capsular ligament in providing spinal stability,” *Comput. Methods Biomech. Biomed. Engin.*, vol. 21, no. 13, pp. 712–721, 2018, doi: 10.1080/10255842.2018.1514392.

[14] A. M. Ellingson, M. N. Shaw, H. Giambini, and K. N. An, “Comparative role of disc degeneration and ligament failure on functional mechanics of the lumbar spine,” *Comput. Methods Biomech. Biomed. Engin.*, vol. 19, no. 9, pp. 1009–1018, 2015, doi: 10.1080/10255842.2015.1088524.

[15] A. A. Claeson and V. H. Barocas, “Computer simulation of lumbar flexion shows shear of the facet capsular ligament,” *Spine J.*, vol. 17, no. 1, pp. 109–119, 2017, doi: 10.1016/j.spinee.2016.08.014.

[16] V. Zarei *et al.*, “Multiscale modelling of the human lumbar facet capsular ligament: analysing spinal motion from the joint to the neurons,” *J. R. Soc. Interface*, vol. 15, no. 148, p. 20180550, Nov. 2018, doi: 10.1098/rsif.2018.0550.

[17] V. Zarei, S. Zhang, B. A. Winkelstein, and V. H. Barocas, “Tissue loading and microstructure regulate the deformation of embedded nerve fibres: Predictions from single-scale and multiscale simulations,” *J. R. Soc. Interface*, vol. 14, no. 135, 2017, doi: 10.1098/rsif.2017.0326.

[18] E. Gacek, A. M. Ellingson, and V. H. Barocas, “In Situ Lumbar Facet Capsular

Ligament Strains Due to Joint Pressure and Residual Strain," *J. Biomech. Eng.*, vol. 144, no. 6, 2022, doi: 10.1115/1.4053993.

[19] E. Gacek, R. R. Mahutga, and V. H. Barocas, "Hybrid discrete-continuum multiscale model of tissue growth and remodeling," *Acta Biomater.*, vol. 163, pp. 7–24, 2022, doi: 10.1016/j.actbio.2022.09.040.

[20] R. A. Deyo and J. N. Weinstein, "Low back pain.," *N. Engl. J. Med.*, vol. 344, no. 5, pp. 363–370, 2001, Accessed: Aug. 24, 2020. [Online]. Available: www.nejm.org.

[21] S. P. Cohen and S. N. Raja, "Pathogenesis, Diagnosis, and Treatment of Lumbar Zygapophysial (Facet) Joint Pain," *Anesthesiology*, vol. 106, no. 3, pp. 591–614, 2007.

[22] K. Suseki *et al.*, "Innervation of the Lumbar Facet Joints: Origins and Functions," *Spine (Phila. Pa. 1976).*, vol. 22, no. 5, pp. 477–485, 1997, doi: 10.1097/00007632-199703010-00003.

[23] V. Zarei, C. J. Liu, A. A. Claeson, T. Akkin, and V. H. Barocas, "Image-based multiscale mechanical modeling shows the importance of structural heterogeneity in the human lumbar facet capsular ligament," *Biomech. Model. Mechanobiol.*, vol. 16, no. 4, pp. 1425–1438, Aug. 2017, doi: 10.1007/s10237-017-0896-4.

[24] E. Ban, S. Zhang, V. Zarei, V. H. Barocas, B. A. Winkelstein, and C. R. Picu, "Collagen Organization in Facet Capsular Ligaments Varies With Spinal Region and With Ligament Deformation," *J. Biomech. Eng.*, vol. 139, no. 7, pp. 1–9, 2017, doi: 10.1115/1.4036019.

[25] S. Zhang, V. Zarei, B. A. Winkelstein, and V. H. Barocas, "Multiscale mechanics of the cervical facet capsular ligament, with particular emphasis on anomalous fiber realignment prior to tissue failure," *Biomech. Model. Mechanobiol.*, vol. 17, no. 1, pp. 133–145, 2018, doi: 10.1007/s10237-017-0949-8.

[26] T. Yamashita, Y. Minaki, A. C. Özaktay, J. M. Cavanaugh, and A. I. King, "A Morphological Study of the Fibrous Capsule of the Human Lumbar Facet Joint," *Spine (Phila. Pa. 1976).*, vol. 21, no. 5, pp. 538–543, 1996, doi: 10.1097/00007632-199603010-00002.

[27] C. Bonifasi-Lista, S. P. Lakez, M. S. Small, and J. A. Weiss, "Viscoelastic properties of the human medial collateral ligament under longitudinal, transverse and shear loading," *J. Orthop. Res.*, vol. 23, no. 1, pp. 67–76, Jan. 2005, doi: 10.1016/j.orthres.2004.06.002.

[28] H. B. Henninger, W. R. Valdez, S. A. Scott, and J. A. Weiss, "Elastin governs the mechanical response of medial collateral ligament under shear and transverse tensile loading," *Acta Biomater.*, vol. 25, pp. 304–312, 2015, doi: 10.1016/j.actbio.2015.07.011.

[29] M. S. Sacks and C. J. Chuong, "Orthotropic Mechanical Properties of Chemically Treated Bovine Pericardium," *Ann. Biomed. Eng.*, vol. 26, no. 5, pp. 892–902, 1998, doi: 10.1114/1.135.

[30] Q. Yu, J. Zhou, and Y. C. Fung, "Neutral axis location in bending and Young's modulus of different layers of arterial wall," *Am. J. Physiol. - Hear. Circ. Physiol.*, vol. 265, no. 1, pp. 52–60, 1993, doi: 10.1152/ajpheart.1993.265.1.h52.

[31] D. C. Gloeckner, K. L. Billiar, and M. S. Sacks, "Effects of mechanical fatigue on the bending properties of the porcine bioprosthetic heart valve.," *ASAIOJournal*, vol. 45, no. 1, pp. 59–63, 1999, Accessed: Jul. 07, 2019. [Online]. Available: http://www.ncbi.nlm.nih.gov/pubmed/9952009.

[32] A. Mirnajafi, J. Raymer, M. J. Scott, and M. S. Sacks, "The effects of collagen fiber orientation on the flexural properties of pericardial heterograft biomaterials," *Biomaterials*, vol. 26, no. 7, pp. 795–804, Mar. 2005, doi: 10.1016/j.biomaterials.2004.03.004.

[33] I. Vesely and D. Boughner, "Analysis of the bending behaviour of porcine xenograft leaflets and of natural aortic valve material: Bending stiffness, neutral axis and shear measurements," *J. Biomech.*, vol. 22, no. 6–7, pp. 655–671, 1989, doi: 10.1016/0021-9290(89)90016-X.

[34] J. Xie, J. Zhou, and Y. C. Fung, "Bending of Blood Vessel Wall: Stress-Strain Laws of the Intima-Media and Adventitial Layers," *J. Biomech. Eng.*, vol. 117, no. 1, pp. 136–145, 1995, doi: 10.1115/1.2792261.

[35] I. Vesely and D. R. Boughner, "A Multipurpose Tissue Bending Machine," *J.*

Biomech., vol. 18, no. 7, pp. 511–513, 1985.

[36] T. S. Keller, Z. Mao, and D. M. Spengler, “Young’s Modulus, Bending Strength, and Tissue Physical Properties of Human Compact Bone,” *J. Orthop. Res.*, vol. 8, no. 4, pp. 592–603, Jul. 1990, doi: 10.1002/jor.1100080416.

[37] E. Bermel, “Examining the Collagen Fiber Alignment in Cadaveric Lumbar Facet Capsular Ligaments and Their Effect on the Mechanics of the Spine at Multiple Scales,” 2019.

[38] N. O. Chahine, C. C. B. Wang, C. T. Hung, and G. A. Ateshian, “Anisotropic strain-dependent material properties of bovine articular cartilage in the transitional range from tension to compression,” *J. Biomech.*, vol. 37, no. 8, pp. 1251–1261, 2004, doi: 10.1016/j.jbiomech.2003.12.008.

[39] S. P. Lake, K. S. Miller, D. M. Elliott, and L. J. Soslowsky, “Effect of Fiber Distribution and Realignment on the Nonlinear and Inhomogeneous Mechanical Properties of Human Supraspinatus Tendon under Longitudinal Tensile Loading,” *J. Orthop. Res.*, vol. 27, no. 12, pp. 1596–1602, Dec. 2009, doi: 10.1002/jor.20938.

[40] R. R. Mahutga, C. T. Schoephoerster, and V. H. Barocas, “The Ring-Pull Assay for Mechanical Properties of Fibrous Soft Tissues – an Analysis of the Uniaxial Approximation and a Correction for Nonlinear Thick-Walled Tissues,” *Exp. Mech.*, vol. 61, pp. 53–66, 2021, doi: 10.1007/s11340-020-00623-3.

[41] S. A. Maas, B. J. Ellis, G. A. Ateshian, and J. A. Weiss, “FEBio: Finite Elements for Biomechanics,” *J. Biomech. Eng.*, vol. 134, no. 1, pp. 1–10, 2012, doi: 10.1115/1.4005694.

[42] S. A. Maas, J. A. Weiss, and G. A. Ateshian, “Chapter 4: Materials,” in *FEBio User’s Manual Version 3.0*, Salt Lake City, 2020.

[43] K. V. Mardia and P. E. Jupp, *Directional Statistics*. Hoboken, NJ, USA: John Wiley & Sons, Inc., 1999.

[44] N. R. Draper and H. Smith, “An Introduction to Nonlinear Estimation,” in *Applied Regression Analysis*, Second Edi., New York: Wiley, 1981, pp. 458–517.

[45] G. N. Maksym and J. H. T. Bates, “A distributed nonlinear model of lung tissue

elasticity," *J. Appl. Physiol.*, vol. 82, no. 1, pp. 32–41, 1997, doi: 10.1152/jappl.1997.82.1.32.

[46] J. S. Little and P. S. Khalsa, "Human Lumbar Spine Creep during Cyclic and Static Flexion: Creep Rate, Biomechanics, and Facet Joint Capsule Strain," *Ann. Biomed. Eng.*, vol. 33, no. 3, pp. 391–401, 2005, doi: 10.1007/s10439-005-1742-x.

[47] L. A. Taber, "A model for Aortic Growth Based on Fluid Shear and Fiber Stresses," *J. Biomech. Eng.*, vol. 120, no. 3, pp. 348–354, 1998, doi: 10.1115/1.2798001.

[48] L. A. Taber and J. D. Humphrey, "Stress-Modulated Growth, Residual Stress, and Vascular Heterogeneity," *J. Biomech. Eng.*, vol. 123, no. 6, pp. 528–535, 2001, doi: 10.1115/1.1412451.

[49] P. W. Alford, J. D. Humphrey, and L. A. Taber, "Growth and remodeling in a thick-walled artery model: Effects of spatial variations in wall constituents," *Biomech. Model. Mechanobiol.*, vol. 7, no. 4, pp. 245–262, 2008, doi: 10.1007/s10237-007-0101-2.

[50] S. Zhang, D. S. Bassett, and B. A. Winkelstein, "Stretch-induced network reconfiguration of collagen fibres in the human facet capsular ligament," *J. R. Soc. Interface*, vol. 13, no. 114, p. 20150883, 2016, doi: 10.1098/rsif.2015.0883.

[51] K. L. Troyer and C. M. Puttlitz, "Nonlinear viscoelasticty plays an essential role in the functional behavior of spinal ligaments," *J. Biomech.*, vol. 45, no. 4, pp. 684–691, 2012, doi: 10.1016/j.jbiomech.2011.12.009.

[52] K. L. Troyer and C. M. Puttlitz, "Human cervical spine ligaments exhibit fully nonlinear viscoelastic behavior," *Acta Biomater.*, vol. 7, no. 2, pp. 700–709, Feb. 2011, doi: 10.1016/j.actbio.2010.09.003.

[53] K. H. Yang and A. I. King, "Mechanism of facet load transmission as a hypothesis for low-back pain," *Spine*, vol. 9, no. 6. pp. 557–565, 1984, doi: 10.1097/00007632-198409000-00005.

[54] N. V. Jaumard, J. A. Bauman, W. C. Welch, and B. A. Winkelstein, "Pressure measurement in the cervical spinal facet joint: Considerations for maintaining joint anatomy and an intact capsule," *Spine (Phila. Pa. 1976).*, vol. 36, no. 15, pp.

1197–1203, 2011, doi: 10.1097/BRS.0b013e3181ee7de2.

[55] C. D. Chaput, J. J. Allred, J. J. Pandorf, J. Song, and M. D. Rahm, “The significance of facet joint cross-sectional area on magnetic resonance imaging in relationship to cervical degenerative spondylolisthesis,” *Spine J.*, vol. 13, no. 8, pp. 856–861, 2013, doi: 10.1016/j.spinee.2013.01.021.

[56] A. Fujiwara *et al.*, “The relationship between facet joint osteoarthritis and disc degeneration of the lumbar spine: an MRI study.,” *Eur. Spine J.*, vol. 8, no. 5, pp. 396–401, 1999, doi: 10.1007/S005860050193.

[57] D. Solav, K. M. Moerman, A. M. Jaeger, K. Genovese, and H. M. Herr, “MultiDIC : An Open-Source Toolbox for Multi-View 3D Digital Image Correlation,” *IEEE Access*, vol. 6, pp. 30520–30535, 2018, doi: 10.1109/ACCESS.2018.2843725.

[58] J. Blaber, B. Adair, and A. Antoniou, “Ncorr: Open-Source 2D Digital Image Correlation Matlab Software,” *Exp. Mech.*, vol. 55, no. 6, pp. 1105–1122, 2015, doi: 10.1007/s11340-015-0009-1.

[59] M. M. Panjabi, T. Oxland, K. Takata, V. Goel, J. Duranceau, and M. Krag, “Articular facets of the human spine:Quantitative three-dimensional anatomy,” *Spine (Phila. Pa. 1976).*, vol. 18, no. 10, pp. 1298–1310, 1993, doi: 10.1097/00007632-199308000-00009.

[60] T. M. Nagel, M. F. Hadi, A. A. Claeson, D. J. Nuckley, and V. H. Barocas, “Combining Displacement Field and Grip Force Information to Determine Mechanical Properties of Planar Tissue With Complicated Geometry,” *J. Biomech. Eng.*, vol. 136, no. 11, p. 114501, 2014, doi: 10.1115/1.4028193.

[61] S. P. Cohen *et al.*, “Consensus practice guidelines on interventions for lumbar facet joint pain from a multispecialty, international working group,” *Reg. Anesth. Pain Med.*, vol. 45, no. 6, pp. 424–467, 2020, doi: 10.1136/rapm-2019-101243.

[62] D. I. Rubin, “Epidemiology and Risk Factors for Spine Pain,” *Neurol. Clin.*, vol. 25, no. 2, pp. 353–371, 2007, doi: 10.1016/j.ncl.2007.01.004.

[63] J. N. Katz, “Lumbar disc disorders and low-back pain: Socioeconomic factors and consequences,” *J. Bone Jt. Surg.*, vol. 88, no. SUPPL. 2, pp. 21–24, 2006, doi:

10.2106/JBJS.E.01273.

[64] S. A. Maas, D. Rawlins, J. A. Weiss, and G. A. Ateshian, "FEBio User Manual v2.8," 2018. .

[65] J. E. Wagenseil and R. P. Mecham, "Vascular Extracellular Matrix and Arterial Mechanics," *Physiol. Rev.*, vol. 89, pp. 957–989, 2009.

[66] M. K. O'Connell *et al.*, "The three-dimensional micro- and nanostructure of the aortic medial lamellar unit measured using 3D confocal and electron microscopy imaging," *Matrix Biol.*, vol. 27, no. 3, pp. 171–181, 2008, doi: 10.1016/j.matbio.2007.10.008.

[67] A. C. Chang, B. H. Liu, P. L. Shao, and J. D. Liao, "Structure-dependent behaviours of skin layers studied by atomic force microscopy," *J. Microsc.*, vol. 267, no. 3, pp. 265–271, Sep. 2017, doi: 10.1111/JMI.12562.

[68] K. M. Myers and D. Elad, "Biomechanics of the human uterus," *Wiley Interdiscip. Rev. Syst. Biol. Med.*, vol. 9, no. 5, Sep. 2017, doi: 10.1002/WSBM.1388.

[69] K. E. Steucke, Z. Win, T. R. Stemler, E. E. Walsh, J. L. Hall, and P. W. Alford, "Empirically determined vascular smooth muscle cell mechano-adaptation law," *J. Biomech. Eng.*, vol. 139, no. 7, Jul. 2017, doi: 10.1115/1.4036454.

[70] B. Cook, C. Chau, and P. Alford, "Architecture-Dependent Mechano-Adaptation in Single Vascular Smooth Muscle Cells," *J. Biomech. Eng.*, vol. 143, no. 10, May 2021, doi: 10.1115/1.4051117.

[71] J. Xie, M. Bao, S. M. C. Bruekers, and W. T. S. Huck, "Collagen Gels with Different Fibrillar Microarchitectures Elicit Different Cellular Responses," *ACS Appl. Mater. Interfaces*, vol. 9, no. 23, pp. 19630–19637, 2017, doi: 10.1021/acsami.7b03883.

[72] J. F. Eichinger, D. Paukner, R. C. Aydin, W. A. Wall, J. D. Humphrey, and C. J. Cyron, "What do cells regulate in soft tissues on short time scales?," Apr. 2021.

[73] J. D. Humphrey, E. R. Dufresne, and M. A. Schwartz, "Mechanotransduction and extracellular matrix homeostasis," *Nat. Rev. Mol. Cell Biol.*, vol. 15, no. 12, pp. 802–812, 2014, doi: 10.1038/nrm3896.

[74] J. F. Eichinger, D. Paukner, J. M. Szafron, R. C. Aydin, J. D. Humphrey, and C. J.

Cyron, “Computer-controlled biaxial bioreactor for investigating cell-mediated homeostasis in tissue equivalents,” *J. Biomech. Eng.*, vol. 142, no. 7, pp. 1–8, 2020, doi: 10.1115/1.4046201.

[75] Z. S. Jackson, A. I. Gotlieb, and B. L. Langille, “Wall tissue remodeling regulates longitudinal tension in arteries,” *Circ. Res.*, vol. 90, no. 8, pp. 918–925, 2002, doi: 10.1161/01.RES.0000016481.87703.CC.

[76] E. A. Sander, V. H. Barocas, and R. T. Tranquillo, “Initial fiber alignment pattern alters extracellular matrix synthesis in fibroblast-populated fibrin gel cruciforms and correlates with predicted tension,” *Ann. Biomed. Eng.*, vol. 39, no. 2, pp. 714–729, Feb. 2011, doi: 10.1007/s10439-010-0192-2.

[77] T. M. Morrison, P. Pathmanathan, M. Adwan, and E. Margerrison, “Advancing Regulatory Science With Computational Modeling for Medical Devices at the FDA’s Office of Science and Engineering Laboratories,” *Front. Med.*, vol. 5, no. SEP, p. 241, Sep. 2018, doi: 10.3389/fmed.2018.00241.

[78] T. M. Morrison, M. L. Dreher, S. Nagaraja, L. M. Angelone, and W. Kainz, “The role of computational modeling and simulation in the total product life cycle of peripheral vascular devices,” *J. Med. Devices, Trans. ASME*, vol. 11, no. 2, Jun. 2017, doi: 10.1115/1.4035866.

[79] M. Y. Emmert *et al.*, “Computational modeling guides tissue-engineered heart valve design for long-term in vivo performance in a translational sheep model,” *Sci. Transl. Med.*, vol. 10, no. 440, May 2018, doi: 10.1126/scitranslmed.aan4587.

[80] B. Sanders *et al.*, “Improved Geometry of Decellularized Tissue Engineered Heart Valves to Prevent Leaflet Retraction,” *Ann. Biomed. Eng.*, vol. 44, doi: 10.1007/s10439-015-1386-4.

[81] S. Baek, K. R. Rajagopal, and J. D. Humphrey, “A theoretical model of enlarging intracranial fusiform aneurysms,” *J. Biomech. Eng. Asme*, vol. 128, no. 1, pp. 142–149, 2006, doi: 10.1115/1.2132374.

[82] P. W. Alford and L. A. Taber, “Computational study of growth and remodelling in the aortic arch,” *Comput. Methods Biomech. Biomed. Engin.*, vol. 11, no. 5, pp. 525–538, 2008, doi: 10.1080/10255840801930710.

[83] N. Horvat, L. Virag, G. A. Holzapfel, J. Sorić, and I. Karšaj, “A finite element implementation of a growth and remodeling model for soft biological tissues: Verification and application to abdominal aortic aneurysms,” *Comput. Methods Appl. Mech. Eng.*, vol. 352, pp. 586–605, Aug. 2019, doi: 10.1016/j.cma.2019.04.041.

[84] S. Roccabianca, C. Bellini, and J. D. Humphrey, “Computational modelling suggests good, bad and ugly roles of glycosaminoglycans in arterial wall mechanics and mechanobiology,” *J. R. Soc. Interface*, vol. 11, no. 97, Aug. 2014, doi: 10.1098/rsif.2014.0397.

[85] G. A. Ateshian, R. J. Nims, S. Maas, and J. A. Weiss, “Computational modeling of chemical reactions and interstitial growth and remodeling involving charged solutes and solid-bound molecules,” *Biomech. Model. Mechanobiol.*, vol. 13, no. 5, pp. 1105–1120, 2014, doi: 10.1007/s10237-014-0560-1.

[86] M. Latorre, M. R. Bersi, and J. D. Humphrey, “Computational modeling predicts immuno-mechanical mechanisms of maladaptive aortic remodeling in hypertension,” *Int. J. Eng. Sci.*, vol. 141, pp. 35–46, Aug. 2019, doi: 10.1016/j.ijengsci.2019.05.014.

[87] S. Loerakker and T. Ristori, “Computational modeling for cardiovascular tissue engineering: the importance of including cell behavior in growth and remodeling algorithms,” *Curr. Opin. Biomed. Eng.*, Dec. 2019, doi: 10.1016/j.cobme.2019.12.007.

[88] P. Sáez, E. Peña, J. M. Tarbell, and M. A. Martínez, “Computational model of collagen turnover in carotid arteries during hypertension,” *Int. j. numer. method. biomed. eng.*, vol. 31, no. 2, p. e02705, Feb. 2015, doi: 10.1002/cnm.2705.

[89] S. Sankaran, J. D. Humphrey, and A. L. Marsden, “An efficient framework for optimization and parameter sensitivity analysis in arterial growth and remodeling computations,” *Comput. Methods Appl. Mech. Eng.*, vol. 256, pp. 200–210, Apr. 2013, doi: 10.1016/j.cma.2012.12.013.

[90] P. R. Buskohl, J. T. Jenkins, and J. T. Butcher, “Computational simulation of hemodynamic-driven growth and remodeling of embryonic atrioventricular

valves," *Biomech. Model. Mechanobiol.*, vol. 11, no. 8, pp. 1205–1217, Nov. 2012, doi: 10.1007/s10237-012-0424-5.

[91] J. Wu and S. C. Shadden, "Coupled Simulation of Hemodynamics and Vascular Growth and Remodeling in a Subject-Specific Geometry," *Ann. Biomed. Eng.*, vol. 43, no. 7, pp. 1543–1554, 2015, doi: 10.1007/s10439-015-1287-6.

[92] A. B. Ramachandra, S. Sankaran, J. D. Humphrey, and A. L. Marsden, "Computational Simulation of the Adaptive Capacity of Vein Grafts in Response to Increased Pressure," *J. Biomech. Eng.*, vol. 137, no. 3, Mar. 2015, doi: 10.1115/1.4029021/370120.

[93] M. S. Sadrabadi, M. Eskandari, H. P. Feigenbaum, and A. Arzani, "Local and global growth and remodeling in calcific aortic valve disease and aging," *J. Biomech.*, vol. 128, p. 110773, Nov. 2021, doi: 10.1016/J.JBIOMECH.2021.110773.

[94] M. S. Bazzi *et al.*, "Experimental and Mouse-Specific Computational Models of the Fbln4 SMKO Mouse to Identify Potential Biomarkers for Ascending Thoracic Aortic Aneurysm," *Cardiovasc. Eng. Technol.*, pp. 1–15, Jan. 2022, doi: 10.1007/S13239-021-00600-4/FIGURES/8.

[95] S. J. Mousavi, S. Farzaneh, and S. Avril, "Patient-specific predictions of aneurysm growth and remodeling in the ascending thoracic aorta using the homogenized constrained mixture model," *Biomech. Model. Mechanobiol.*, vol. 18, no. 6, pp. 1895–1913, Dec. 2019, doi: 10.1007/S10237-019-01184-8/FIGURES/11.

[96] R. Mahutga and V. H. Barocas, "Investigation of Pathophysiological Aspects of Aortic Growth, Remodeling, and Failure Using a Discrete-Fiber Microstructural Model," *J. Biomech. Eng.*, vol. 142, no. 11, Aug. 2020, doi: 10.1115/1.4048031.

[97] Z. Jia and T. D. Nguyen, "A micromechanical model for the growth of collagenous tissues under mechanics-mediated collagen deposition and degradation," *J. Mech. Behav. Biomed. Mater.*, vol. 98, pp. 96–107, Oct. 2019, doi: 10.1016/j.jmbbm.2019.06.004.

[98] B. Fata, W. Zhang, R. Amini, and M. S. Sacks, "Insights into regional adaptations in the growing pulmonary artery using a meso-scale structural model: Effects of

ascending aorta impingement," *J. Biomech. Eng.*, vol. 136, no. 2, Feb. 2014, doi: 10.1115/1.4026457/442934.

[99] B. Fata *et al.*, "Mesoscale Structural Models in the Growing Pulmonary Artery," *Struct. Mech. Tissues Organs*, pp. 383–402, Jan. 2016, doi: 10.1007/978-1-4899-7630-7_19.

[100] J. F. Eichinger *et al.*, "A computational framework for modeling cell-matrix interactions in soft biological tissues," Mar. 2021.

[101] A. C. Estrada, K. Yoshida, J. J. Saucerman, and J. W. Holmes, "A multiscale model of cardiac concentric hypertrophy incorporating both mechanical and hormonal drivers of growth," *Biomech. Model. Mechanobiol.*, vol. 20, no. 1, pp. 293–307, Feb. 2021, doi: 10.1007/S10237-020-01385-6/FIGURES/7.

[102] L. Irons and J. D. Humphrey, "Cell signaling model for arterial mechanobiology," *PLOS Comput. Biol.*, vol. 16, no. 8, p. e1008161, Aug. 2020, doi: 10.1371/JOURNAL.PCBI.1008161.

[103] L. Irons, M. Latorre, and J. D. Humphrey, "From Transcript to Tissue: Multiscale Modeling from Cell Signaling to Matrix Remodeling," *Ann. Biomed. Eng.*, vol. 49, no. 7, pp. 1701–1715, 2021, doi: 10.1007/s10439-020-02713-8.

[104] M. Nikpasand, R. R. Mahutga, L. M. Bersie-Larson, E. Gacek, and V. H. Barocas, "A Hybrid Microstructural-Continuum Multiscale Approach for Modeling Hyperelastic Fibrous Soft Tissue," *J. Elast. 2021*, pp. 1–25, Jun. 2021, doi: 10.1007/S10659-021-09843-7.

[105] M. Walker, P. Rizzuto, M. Godin, and A. E. Pelling, "Structural and mechanical remodeling of the cytoskeleton maintains tensional homeostasis in 3D microtissues under acute dynamic stretch," *Sci. Rep.*, vol. 10, no. 1, Dec. 2020, doi: 10.1038/S41598-020-64725-7.

[106] F. A. Braeu, · R C Aydin, and C. J. Cyron, "Anisotropic stiffness and tensional homeostasis induce a natural anisotropy of volumetric growth and remodeling in soft biological tissues," *Biomech. Model. Mechanobiol.*, vol. 18, pp. 327–345, 2019, doi: 10.1007/s10237-018-1084-x.

[107] D. Stamenovic and M. L. Smith, "Tensional homeostasis at different length

scales," *Soft Matter*, vol. 16, pp. 6946–6963, 2020, doi: 10.1039/d0sm00763c.

[108] R. Skalak, G. Dasgupta, M. Moss, E. Otten, P. Dullemeijer, and H. Vilmann, "Analytical description of growth," *J. Theor. Biol.*, vol. 94, no. 3, pp. 555–577, Feb. 1982, doi: 10.1016/0022-5193(82)90301-0.

[109] L. A. Taber and D. W. Eggers, "Theoretical study of stress-modulated growth in the aorta," *J. Theor. Biol.*, vol. 180, no. 4, pp. 343–357, 1996, doi: 10.1006/jtbi.1996.0107.

[110] L. A. Taber, "Biomechanics of growth, remodeling, and morphogenesis," *Appl. Mech. Rev.*, vol. 48, no. 8, pp. 487–545, 1995, doi: 10.1115/1.3005109.

[111] R. Skalak, D. A. Farrow, and A. Hoger, "Kinematics of surface growth," *J. Math. Biol.*, vol. 35, no. 8, pp. 869–907, 1997, doi: 10.1007/s002850050081.

[112] J. D. Humphrey and K. R. Rajagopal, "A Constrained Mixture Model For Growth And Remodelling Of Soft Tissues," *Math. Model. Methods Appl. Sci.*, vol. 12, no. 03, pp. 407–430, 2002, doi: 10.1142/S0218202502001714.

[113] J. D. Humphrey and K. R. Rajagopal, "A constrained mixture model for arterial adaptations to a sustained step change in blood flow," *Biomech. Model. Mechanobiol.*, vol. 2, no. 2, pp. 109–126, 2003, doi: 10.1007/s10237-003-0033-4.

[114] J. D. Humphrey, "Remodeling of a collagenous tissue at fixed lengths," *J. Biomech. Eng.*, vol. 121, no. 6, pp. 591–597, 1999, doi: 10.1115/1.2800858.

[115] R. L. Gleason and J. D. Humphrey, "Effects of a sustained extension on arterial growth and remodeling: A theoretical study," *J. Biomech.*, vol. 38, no. 6, pp. 1255–1261, 2005, doi: 10.1016/j.jbiomech.2004.06.017.

[116] S. Baek, K. R. Rajagopal, and J. D. Humphrey, "Competition between radial expansion and thickening in the enlargement of an intracranial saccular aneurysm," *J. Elast.*, vol. 80, no. 1–3, pp. 13–31, 2005, doi: 10.1007/s10659-005-9004-6.

[117] C. J. Cyron, · R C Aydin, and · J D Humphrey, "A homogenized constrained mixture (and mechanical analog) model for growth and remodeling of soft tissue," *Biomech. Model. Mechanobiol.*, vol. 15, pp. 1389–1403, 2016, doi: 10.1007/s10237-016-0770-9.

[118] P. L. Chandran and V. H. Barocas, “Deterministic Material-Based Averaging Theory Model of Collagen Gel Micromechanics,” *J. Biomech. Eng.*, vol. 129, no. 2, p. 137, Apr. 2007, doi: 10.1115/1.2472369.

[119] T. Stylianopoulos and V. H. Barocas, “Volume-averaging theory for the study of the mechanics of collagen networks,” *Comput. Methods Appl. Mech. Eng.*, vol. 196, no. 31–32, pp. 2981–2990, Jun. 2007, doi: 10.1016/j.cma.2006.06.019.

[120] C. M. Witzenburg *et al.*, “Failure of the Porcine Ascending Aorta: Multidirectional Experiments and a Unifying Microstructural Model,” *J. Biomech. Eng. Asme*, vol. 139, no. 3, 2017, doi: 10.1115/1.4035264.

[121] C. E. Korenczuk, R. Y. Dhume, K. K. Liao, and V. H. Barocas, “Ex Vivo Mechanical Tests and Multiscale Computational Modeling Highlight the Importance of Intramural Shear Stress in Ascending Thoracic Aortic Aneurysms,” *J. Biomech. Eng.*, vol. 141, no. 12, Dec. 2019, doi: 10.1115/1.4045270.

[122] A. D. Freed and T. C. Doehring, “Elastic Model for Crimped Collagen Fibrils,” *J. Biomech. Eng.*, vol. 127, no. 4, p. 587, Feb. 2005, doi: 10.1115/1.1934145.

[123] R. Y. Dhume, E. D. Shih, and V. H. Barocas, “Multiscale model of fatigue of collagen gels,” *Biomech. Model. Mechanobiol.*, vol. 18, no. 1, pp. 175–187, 2019, doi: 10.1007/s10237-018-1075-y.

[124] L. Gyoneva, C. B. Hovell, R. J. Pewowaruk, K. D. Dorfman, Y. Segal, and V. H. Barocas, “Cell-matrix interaction during strain-dependent remodelling of simulated collagen networks,” *Interface Focus*, vol. 6, no. 1, 2016, doi: 10.1098/rsfs.2015.0069.

[125] K. C. Holmes, D. Popp, W. Gebhard, and W. Kabsch, “Atomic model of the actin filament,” *Nature*, vol. 347, no. 6288, pp. 44–49, Sep. 1990, doi: 10.1038/347044a0.

[126] Z. L. Shen, M. R. Dodge, H. Kahn, R. Ballarini, and S. J. Eppell, “Stress-strain experiments on individual collagen fibrils,” *Biophys. J.*, vol. 95, no. 8, pp. 3956–3963, 2008, doi: 10.1529/biophysj.107.124602.

[127] B. P. Flynn, G. E. Tilburey, and J. W. Ruberti, “Highly sensitive single-fibril erosion assay demonstrates mechanochemical switch in native collagen fibrils,”

Biomech. Model. Mechanobiol., vol. 12, no. 2, pp. 291–300, Apr. 2013, doi: 10.1007/s10237-012-0399-2.

[128] M. J. Buehler, “Nanomechanics of collagen fibrils under varying cross-link densities: Atomistic and continuum studies,” *J. Mech. Behav. Biomed. Mater.*, vol. 1, no. 1, pp. 59–67, Jan. 2008, doi: 10.1016/j.jmbbm.2007.04.001.

[129] J. Gosline, M. Lillie, E. Carrington, P. Guerette, C. Ortlepp, and K. Savage, “Elastic proteins: biological roles and mechanical properties,” doi: 10.1098/rstb.2001.1022.

[130] B. P. Flynn, A. P. Bhole, N. Saeidi, M. Liles, C. A. DiMarzio, and J. W. Ruberti, “Mechanical Strain Stabilizes Reconstituted Collagen Fibrils against Enzymatic Degradation by Mammalian Collagenase Matrix Metalloproteinase 8 (MMP-8),” *PLoS One*, vol. 5, no. 8, 2010, doi: 10.1371/journal.pone.0012337.

[131] M. F. F. Hadi, E. A. A. Sander, J. W. W. Ruberti, and V. H. H. Barocas, “Simulated remodeling of loaded collagen networks via strain-dependent enzymatic degradation and constant-rate fiber growth,” *Mech. Mater.*, vol. 44, pp. 72–82, Jan. 2012, doi: 10.1016/j.mechmat.2011.07.003.

[132] L. M. Bersie-Larson *et al.*, “Glomerular filtration and podocyte tensional homeostasis: importance of the minor type IV collagen network,” *Biomech. Model. Mechanobiol.*, doi: 10.1007/s10237-020-01347-y.

[133] S. A. Maas, A. Erdemir, J. P. Halloran, and J. A. Weiss, “A general framework for application of prestrain to computational models of biological materials,” *J. Mech. Behav. Biomed. Mater.*, vol. 61, pp. 499–510, 2016, doi: 10.1016/j.jmbbm.2016.04.012.

[134] B. A. Lane, M. J. Uline, & X. Wang, T. Shazly, N. R. Vyavahare, and J. F. Eberth, “The Association Between Curvature and Rupture in a Murine Model of Abdominal Aortic Aneurysm and Dissection,” *SP ISS Exp. Adv. Cardiovasc. Biomech.*, doi: 10.1007/s11340-020-00661-x/Published.

[135] A. G. Berman *et al.*, “Experimental aortic aneurysm severity and growth depend on topical elastase concentration and lysyl oxidase inhibition,” *Scientific*, vol. 12, no. 99, 2022, doi: 10.1038/s41598-021-04089-8.

[136] A. Heinz, “Critical Reviews in Biochemistry and Molecular Biology Elastases and elastokines: elastin degradation and its significance in health and disease,” 2020, doi: 10.1080/10409238.2020.1768208.

[137] M. R. Bersi, C. Bellini, J. Wu, K. R. C. Montaniel, D. G. Harrison, and J. D. Humphrey, “Excessive Adventitial Remodeling Leads to Early Aortic Maladaptation in Angiotensin-Induced Hypertension,” *Hypertension*, vol. 67, no. 5, pp. 890–896, May 2016, doi: 10.1161/HYPERTENSIONAHA.115.06262.).

[138] J. Golledge and K. A. Eagle, “Acute aortic dissection,” *Lancet*, vol. 372, no. 9632, pp. 55–66, 2008, doi: 10.1016/S0140-6736(08)60994-0.

[139] Y. C. Fung and S. Q. Liu, “Change of residual strains in arteries due to hypertrophy caused by aortic constriction,” *Circ. Res.*, vol. 65, no. 5, pp. 1340–1349, Nov. 1989, doi: 10.1161/01.RES.65.5.1340.

[140] S. Q. Liu and Y. C. Fung, “Zero-Stress States of Arteries,” *J. Biomech. Eng.*, vol. 110, no. 1, pp. 82–84, Feb. 1988, doi: 10.1115/1.3108410.

[141] D. P. Sokolis, “Regional distribution of layer-specific circumferential residual deformations and opening angles in the porcine aorta,” *J. Biomech.*, vol. 96, p. 109335, Nov. 2019, doi: 10.1016/J.JBIOMECH.2019.109335.

[142] M. Amabili *et al.*, “Biomechanical characterization of a chronic type a dissected human aorta,” *J. Biomech.*, vol. 110, p. 109978, Sep. 2020, doi: 10.1016/j.jbiomech.2020.109978.

[143] Z. Li *et al.*, “Mechanical and histological characteristics of aortic dissection tissues,” *Acta Biomater.*, vol. 146, pp. 284–294, Jul. 2022, doi: 10.1016/J.ACTBIO.2022.03.042.

[144] A. Emmott, I. El-Hamamsy, and R. L. Leask, “Histopathological and biomechanical properties of the aortic wall in 2 patients with chronic type A aortic dissection,” *Cardiovasc. Pathol.*, vol. 29, pp. 48–52, Jul. 2017, doi: 10.1016/J.CARPATH.2017.05.006.

[145] V. Deplano *et al.*, “Mechanical characterisation of human ascending aorta dissection,” *J. Biomech.*, Jul. 2019, doi: 10.1016/J.JBIOMECH.2019.07.028.

[146] Y. Shingu *et al.*, “Augmentation Index Is Elevated in Aortic Aneurysm and

Dissection," *Ann. Thorac. Surg.*, vol. 87, no. 5, pp. 1373–1377, May 2009, doi: 10.1016/J.ATHORACSUR.2009.02.049.

[147] E. Sueyoshi, I. Sakamoto, K. Hayashi, T. Yamaguchi, and T. Imada, "Growth rate of aortic diameter in patients with type B aortic dissection during the chronic phase," *Circulation*, vol. 110, no. 11 SUPPL., Sep. 2004, doi: 10.1161/01.CIR.0000138386.48852.B6/FORMAT/EPUB.

[148] S. Peterss *et al.*, "Changing Pathology of the Thoracic Aorta From Acute to Chronic Dissection: Literature Review and Insights," *J. Am. Coll. Cardiol.*, vol. 68, no. 10, pp. 1054–1065, Sep. 2016, doi: 10.1016/J.JACC.2016.05.091.

[149] C. Karmonik *et al.*, "Preliminary findings in quantification of changes in septal motion during follow-up of type B aortic dissections," *J. Vasc. Surg.*, vol. 55, no. 5, pp. 1419-1426.e1, May 2012, doi: 10.1016/J.JVS.2011.10.127.

[150] T. C. Gasser, R. W. Ogden, and G. A. Holzapfel, "Hyperelastic modelling of arterial layers with distributed collagen fibre orientations," *J. R. Soc. Interface*, vol. 3, no. 6, pp. 15–35, 2006, doi: 10.1098/rsif.2005.0073.

[151] E. M. Arruda and M. C. Boyce, "A THREE-DIMENSIONAL CONSTITUTIVE MODEL FOR THE LARGE STRETCH BEHAVIOR OF RUBBER ELASTIC MATERIALS," *J. Mech. Phys. Solivds*, vol. 41, no. 2, pp. 389–412, 1993.

[152] J. Ferruzzi, D. A. Vorp, and J. D. Humphrey, "On constitutive descriptors of the biaxial mechanical behaviour of human abdominal aorta and aneurysms," doi: 10.1098/rsif.2010.0299.

[153] G. A. Holzapfel, J. A. Niestrawska, R. W. Ogden, A. J. Reinisch, and A. J. Schriefl, "Modelling non-symmetric collagen fibre dispersion in arterial walls," doi: 10.1098/rsif.2015.0188.

[154] T. C. Gasser, R. W. Ogden, and G. A. Holzapfel, "Hyperelastic modelling of arterial layers with distributed collagen fibre orientations," doi: 10.1098/rsif.2005.0073.

[155] M. E. Ita, P. Ghimire, R. L. Welch, H. R. Troche, and B. A. Winkelstein, "Intra-articular collagenase in the spinal facet joint induces pain, DRG neuron dysregulation and increased MMP-1 absent evidence of joint destruction," *Sci.*

Rep., vol. 10, no. 1, 2020, doi: 10.1038/s41598-020-78811-3.

[156] G. A. Holzapfel, T. C. Gasser, and R. W. Ogden, “A new constitutive framework for arterial wall mechanics and a comparative study of material models,” *J. Elast.*, vol. 61, no. 1–3, pp. 1–48, 2000, doi: 10.1023/A:1010835316564.

[157] G. A. Holzapfel, “Biomechanics of Soft Tissue,” in *The Handbook of Materials Behavior Models*, Academic Press, 2001, pp. 1049–1063.

[158] J. D. Humphrey, *Cardiovascular Solid Mechanics*, vol. 1. 2002.

[159] K. Y. Volokh, “On arterial fiber dispersion and auxetic effect,” *J. Biomech.*, vol. 61, pp. 123–130, Aug. 2017, doi: 10.1016/j.jbiomech.2017.07.010.

[160] R. Gatt *et al.*, “Negative Poisson’s ratios in tendons: An unexpected mechanical response,” *Acta Biomater.*, vol. 24, pp. 201–208, Sep. 2015, doi: 10.1016/J.ACTBIO.2015.06.018.

[161] D. R. Nolan and J. P. Mcgarry, “On the Compressibility of Arterial Tissue,” *Ann. Biomed. Eng.*, vol. 44, doi: 10.1007/s10439-015-1417-1.

[162] F. Di Puccio, S. Celi, and P. Forte, “Review of Experimental Investigations on Compressibility of Arteries and Introduction of a New Apparatus,” doi: 10.1007/s11340-012-9614-4.

[163] Z. Yosibash, I. Manor, I. Gilad, and U. Willentz, “Experimental evidence of the compressibility of arteries,” *J. Mech. Behav. Biomed. Mater.*, vol. 39, pp. 339–354, Nov. 2014, doi: 10.1016/J.JMBBM.2014.07.030.

[164] O. E. Yossef, M. Farajian, I. Gilad, U. Willenz, N. Gutman, and Z. Yosibash, “Further experimental evidence of the compressibility of arteries,” *J. Mech. Behav. Biomed. Mater.*, vol. 65, pp. 177–189, Jan. 2017, doi: 10.1016/J.JMBBM.2016.08.013.

[165] X. Guo and G. S. Kassab, “Variation of mechanical properties along the length of the aorta in C57bl/6 mice,” *Am. J. Physiol. Circ. Physiol.*, 2003, doi: 10.1152/ajpheart.00567.2003.

[166] Y. C. Fung, “Elasticity of soft tissues in simple elongation.,” *Am. J. Physiol.*, vol. 213, no. 6, pp. 1532–1544, 1967, doi: 10.1152/ajplegacy.1967.213.6.1532.

[167] C. Bellini, J. Ferruzzi, S. Roccabianca, E. S. Di Martino, and J. D. Humphrey, “A

Microstructurally Motivated Model of Arterial Wall Mechanics with Mechanobiological Implications," doi: 10.1007/s10439-013-0928-x.

[168] G. A. Holzapfel and R. W. Ogden, "An Arterial Constitutive Model Accounting for Collagen Content and Cross-Linking," *J. Mech. Phys. Solids*, p. 103682, Aug. 2019, doi: 10.1016/J.JMPS.2019.103682.

[169] K. Li, R. W. Ogden, and G. A. Holzapfel, "An exponential constitutive model excluding fibres under compression: Application to extension–inflation of a residually stressed carotid artery," *Math. Mech. Solids*, vol. 23, no. 8, pp. 1206–1224, Aug. 2018, doi: 10.1177/1081286517712077.

[170] J. K. Cheng, I. Stoilov, R. P. Mecham, and J. E. Wagenseil, "A fiber-based constitutive model predicts changes in amount and organization of matrix proteins with development and disease in the mouse aorta," *Biomech. Model. Mechanobiol.*, 2013, doi: 10.1007/s10237-012-0420-9.

[171] T. C. Gasser, C. A. J. Schulze-Bauer, and G. A. Holzapfel, "A three-dimensional finite element model for arterial clamping," *J. Biomech. Eng.*, vol. 124, no. 4, pp. 355–363, Aug. 2002, doi: 10.1115/1.1485284.

[172] J. F. Rodríguez, C. Ruiz, M. Doblaré, and G. A. Holzapfel, "Mechanical stresses in abdominal aortic aneurysms: Influence of diameter, asymmetry, and material anisotropy," *J. Biomech. Eng.*, vol. 130, no. 2, Apr. 2008, doi: 10.1115/1.2898830.

[173] D. Guan, F. Ahmad, P. Theobald, S. Soe, X. Luo, and H. Gao, "On the AIC-based model reduction for the general Holzapfel–Ogden myocardial constitutive law," *Biomech. Model. Mechanobiol.*, vol. 18, no. 4, pp. 1213–1232, Aug. 2019, doi: 10.1007/s10237-019-01140-6.

[174] L. A. Mihai, S. Budday, G. A. Holzapfel, E. Kuhl, and A. Goriely, "A family of hyperelastic models for human brain tissue," *J. Mech. Phys. Solids*, vol. 106, pp. 60–79, Sep. 2017, doi: 10.1016/j.jmps.2017.05.015.

[175] G. A. Holzapfel and R. W. Ogden, "Constitutive modelling of passive myocardium: a structurally based framework for material characterization," *Trans. R. Soc. A*, vol. 367, pp. 3445–3475, 2009, doi: 10.1098/rsta.2009.0091.

[176] D. W. Laurence *et al.*, "A pilot *in silico* modeling-based study of the pathological

effects on the biomechanical function of tricuspid valves," *Int. j. numer. method. biomed. eng.*, vol. 36, no. 7, Jul. 2020, doi: 10.1002/cnm.3346.

[177] N. M. Shahraki, A. Fatemi, V. K. Goel, and A. Agarwal, "On the use of biaxial properties in modeling annulus as a Holzapfel-Gasser-Ogden material," *Front. Bioeng. Biotechnol.*, vol. 3, no. JUN, p. 69, Jun. 2015, doi: 10.3389/fbioe.2015.00069.

[178] T. C. Gasser and G. A. Holzapfel, "Modeling plaque fissuring and dissection during balloon angioplasty intervention," *Ann. Biomed. Eng.*, vol. 35, no. 5, pp. 711–723, May 2007, doi: 10.1007/s10439-007-9258-1.

[179] E. McEvoy, G. A. Holzapfel, and P. McGarry, "Compressibility and Anisotropy of the Ventricular Myocardium: Experimental Analysis and Microstructural Modeling," *J. Biomech. Eng.*, vol. 140, no. 8, Aug. 2018, doi: 10.1115/1.4039947.

[180] H. Khayyeri, G. Longo, A. Gustafsson, and H. Isaksson, "Comparison of structural anisotropic soft tissue models for simulating Achilles tendon tensile behaviour," *J. Mech. Behav. Biomed. Mater.*, vol. 61, pp. 431–443, Aug. 2016, doi: 10.1016/j.jmbbm.2016.04.007.

[181] C. Laville, C. Pradille, and Y. Tillier, "Mechanical characterization and identification of material parameters of porcine aortic valve leaflets," *J. Mech. Behav. Biomed. Mater.*, vol. 112, p. 104036, Aug. 2020, doi: 10.1016/j.jmbbm.2020.104036.

[182] K. Li, R. W. Ogden, and G. A. Holzapfel, "A discrete fibre dispersion method for excluding fibres under compression in the modelling of fibrous tissues," *J. R. Soc. Interface*, vol. 15, no. 138, p. 20170766, Jan. 2018, doi: 10.1098/rsif.2017.0766.

[183] K. Li, R. W. Ogden, and G. A. Holzapfel, "Modeling fibrous biological tissues with a general invariant that excludes compressed fibers," *J. Mech. Phys. Solids*, vol. 110, pp. 38–53, Feb. 2018, doi: 10.1016/j.jmps.2017.09.005.

[184] D. R. Nolan, A. L. Gower, M. Destrade, R. W. Ogden, and J. P. McGarry, "A robust anisotropic hyperelastic formulation for the modelling of soft tissue," *J. Mech. Behav. Biomed. Mater.*, vol. 39, pp. 48–60, Nov. 2014, doi: 10.1016/j.jmbbm.2014.06.016.

[185] M. Latorre and F. J. Montáns, “On the tension-compression switch of the Gasser-Ogden-Holzapfel model: Analysis and a new pre-integrated proposal,” *J. Mech. Behav. Biomed. Mater.*, vol. 57, pp. 175–189, Apr. 2016, doi: 10.1016/j.jmbbm.2015.11.018.

[186] A. V. Melnik, H. Borja Da Rocha, and A. Goriely, “On the modeling of fiber dispersion in fiber-reinforced elastic materials,” *Int. J. Non. Linear. Mech.*, vol. 75, pp. 92–106, Sep. 2015, doi: 10.1016/j.ijnonlinmec.2014.10.006.

[187] Y. Lanir, “Constitutive equations for fibrous connective tissues,” *J. Biomech.*, vol. 18, no. 1, p. 1, 1983.

[188] P. L. Chandran and V. H. Barocas, “Affine Versus Non-Affine Fibril Kinematics in Collagen Networks: Theoretical Studies of Network Behavior,” *J. Biomech. Eng.*, vol. 128, no. 2, pp. 259–270, Apr. 2006, doi: 10.1115/1.2165699.

[189] H. Hatami-Marbini and R. C. Picu, “Effect of fiber orientation on the non-affine deformation of random fiber networks,” *Acta Mech.*, vol. 205, no. 1–4, pp. 77–84, Jun. 2009, doi: 10.1007/s00707-009-0170-7.

[190] M. Marino and G. Vairo, “Stress and strain localization in stretched collagenous tissues via a multiscale modelling approach,” *Comput. Methods Biomech. Biomed. Engin.*, vol. 17, no. 1, pp. 11–30, 2014, doi: 10.1080/10255842.2012.658043.

[191] E. J. Weinberg and M. R. Kaazempur Mofrad, “A multiscale computational comparison of the bicuspid and tricuspid aortic valves in relation to calcific aortic stenosis,” *J. Biomech.*, vol. 41, no. 16, pp. 3482–3487, Dec. 2008, doi: 10.1016/j.jbiomech.2008.08.006.

[192] E. J. Weinberg and M. R. K. Mofrad, “Three-dimensional, multiscale simulations of the human aortic valve,” *Cardiovasc. Eng.*, vol. 7, no. 4, pp. 140–155, Dec. 2007, doi: 10.1007/s10558-007-9038-4.

[193] V. H. Barocas and V. H. Barocas, “Multiscale, Structure-Based Modeling for the Elastic Mechanical Behavior of Arterial Walls,” *J. Biomech. Eng.*, vol. 129, no. 4, p. 611, Jan. 2007, doi: 10.1115/1.2746387.

[194] E. Sander, T. Stylianopoulos, R. Tranquillo, and V. Barocas, “Image-based biomechanics of collagen-based tissue equivalents,” *IEEE Eng. Med. Biol. Mag.*,

vol. 28, no. 3, pp. 10–18, May 2009, doi: 10.1109/MEMB.2009.932486.

[195] P. Gonc -Alves Coelho, P. R. Fernandes, and H. Carric -O Rodrigues, “Multiscale modeling of bone tissue with surface and permeability control,” doi: 10.1016/j.jbiomech.2010.10.007.

[196] K. M. Virgilio, K. S. Martin, S. M. Peirce, and S. S. Blemker, “Multiscale models of skeletal muscle reveal the complex effects of muscular dystrophy on tissue mechanics and damage susceptibility,” *Interface Focus*, vol. 5, no. 2, p. 20140080, Apr. 2015, doi: 10.1098/rsfs.2014.0080.

[197] C. E. Korenczuk, V. H. Barocas, and W. J. Richardson, “Effects of Collagen Heterogeneity on Myocardial Infarct Mechanics in a Multiscale Fiber Network Model,” *J. Biomech. Eng.*, vol. 141, no. 9, Sep. 2019, doi: 10.1115/1.4043865.

[198] F. Maceri, M. Marino, and G. Vairo, “A unified multiscale mechanical model for soft collagenous tissues with regular fiber arrangement,” *J. Biomech.*, vol. 43, no. 2, pp. 355–363, Jan. 2010, doi: 10.1016/j.jbiomech.2009.07.040.

[199] H. Hatami-Marbini, A. Shahsavari, and R. C. Picu, “Multiscale modeling of semiflexible random fibrous structures,” *CAD Comput. Aided Des.*, vol. 45, no. 1, pp. 77–83, Jan. 2013, doi: 10.1016/j.cad.2011.10.002.

[200] G. A. Holzapfel, M. Stadler, and T. C. Gasser, “Changes in the mechanical environment of stenotic arteries during interaction with stents: Computational assessment of parametric stent designs,” *J. Biomech. Eng.*, vol. 127, no. 1, pp. 166–180, Feb. 2005, doi: 10.1115/1.1835362.

[201] T. C. Gasser and G. A. Holzapfel, “Modeling the propagation of arterial dissection,” *Eur. J. Mech. A/Solids*, vol. 25, no. 4, pp. 617–633, Jul. 2006, doi: 10.1016/j.euromechsol.2006.05.004.

[202] B. Fereidoonnezhad, R. Naghdabadi, S. Sohrabpour, and G. A. Holzapfel, “A Mechanobiological model for damage-induced growth in arterial tissue with application to in-stent restenosis,” *J. Mech. Phys. Solids*, vol. 101, pp. 311–327, Jan. 2017, doi: 10.1016/j.jmps.2017.01.016.

[203] M. Rolf-Pissarczyk, K. Li, D. Fleischmann, and G. A. Holzapfel, “A discrete approach for modeling degraded elastic fibers in aortic dissection,” *Comput.*

Methods Appl. Mech. Eng., vol. 373, p. 113511, Jan. 2021, doi: 10.1016/j.cma.2020.113511.

[204] W. Mao, A. Caballero, R. McKay, C. Primiano, and W. Sun, “Fully-coupled fluid-structure interaction simulation of the aortic and mitral valves in a realistic 3D left ventricle model,” *PLoS One*, vol. 12, no. 9, p. e0184729, Sep. 2017, doi: 10.1371/journal.pone.0184729.

[205] D. Balzani, S. Brinkhues, and G. A. Holzapfel, “Constitutive framework for the modeling of damage in collagenous soft tissues with application to arterial walls,” *Comput. Methods Appl. Mech. Eng.*, vol. 213–216, pp. 139–151, Mar. 2012, doi: 10.1016/j.cma.2011.11.015.

[206] A. Erdemir, C. Bennetts, S. Davis, A. Reddy, and S. Sibole, “Multiscale cartilage biomechanics: technical challenges in realizing a high-throughput modelling and simulation workflow,” *Interface Focus*, vol. 5, no. 2, p. 20140081, Apr. 2015, doi: 10.1098/rsfs.2014.0081.

[207] C. M. Witzenburg *et al.*, “Failure of the porcine ascending aorta: Multidirectional experiments and a unifying microstructural model,” *J. Biomech. Eng.*, vol. 139, no. 3, Mar. 2017, doi: 10.1115/1.4035264.

[208] S. S. Sajjadinia, B. Carpentieri, and G. A. Holzapfel, “A backward pre-stressing algorithm for efficient finite element implementation of in vivo material and geometrical parameters into fibril-reinforced mixture models of articular cartilage,” *J. Mech. Behav. Biomed. Mater.*, p. 104203, Nov. 2020, doi: 10.1016/j.jmbbm.2020.104203.

[209] O. Gültekin, H. Dal, and G. A. Holzapfel, “Numerical aspects of anisotropic failure in soft biological tissues favor energy-based criteria: A rate-dependent anisotropic crack phase-field model,” *Comput. Methods Appl. Mech. Eng.*, vol. 331, pp. 23–52, Apr. 2018, doi: 10.1016/j.cma.2017.11.008.

[210] G. A. Holzapfel, R. W. Ogden, and S. Sherifova, “On fibre dispersion modelling of soft biological tissues: A review,” *Proceedings of the Royal Society A: Mathematical, Physical and Engineering Sciences*, vol. 475, no. 2224. Royal Society Publishing, 2019, doi: 10.1098/rspa.2018.0736.

[211] S. Federico and T. C. Gasser, “Nonlinear elasticity of biological tissues with statistical fibre orientation,” *J. R. Soc. Interface*, vol. 7, no. 47, 2010, doi: 10.1098/rsif.2009.0502.

[212] C. J. Stender, E. Rust, P. T. Martin, E. E. Neumann, R. J. Brown, and T. J. Lujan, “Modeling the effect of collagen fibril alignment on ligament mechanical behavior,” *Biomech. Model. Mechanobiol.*, vol. 17, no. 2, pp. 543–557, Apr. 2018, doi: 10.1007/s10237-017-0977-4.

[213] R. Y. Dhume and V. H. Barocas, “Emergent structure-dependent relaxation spectra in viscoelastic fiber networks in extension,” *Acta Biomater.*, vol. 87, pp. 245–255, 2019, doi: 10.1016/j.actbio.2019.01.027.

[214] K. L. Billiar and M. S. Sacks, “Biaxial mechanical properties of the native and glutaraldehyde- treated aortic valve cusp: Part II - A structural constitutive model,” *J. Biomech. Eng. Asme*, vol. 122, no. 4, pp. 327–335, 2000.

[215] B. A. Lane, K. A. Harmon, R. L. Goodwin, M. J. Yost, T. Shazly, and J. F. Eberth, “Constitutive modeling of compressible type-I collagen hydrogels,” *Med. Eng. Phys.*, vol. 53, pp. 39–48, Mar. 2018, doi: 10.1016/j.medengphy.2018.01.003.

[216] M. Böl, S. Reese, K. K. Parker, and E. Kuhl, “Computational modeling of muscular thin films for cardiac repair,” *Comput. Mech.*, vol. 43, no. 4, pp. 535–544, Sep. 2009, doi: 10.1007/s00466-008-0328-5.

[217] T. Eriksson, A. Prassl, G. Plank, and G. Holzapfel, “Influence of myocardial fiber/sheet orientations on left ventricular mechanical contraction,” *Math. Mech. Solids*, vol. 18, no. 6, pp. 592–606, Aug. 2013, doi: 10.1177/1081286513485779.

[218] Z. Win, J. M. Buksa, and P. W. Alford, “Architecture-Dependent Anisotropic Hysteresis in Smooth Muscle Cells,” *Biophys. J.*, vol. 115, no. 10, pp. 2044–2054, Nov. 2018, doi: 10.1016/j.bpj.2018.09.027.

[219] S. M. S. M. Vanderheiden, M. F. M. F. Hadi, and V. H. V. H. Barocas, “Crack Propagation Versus Fiber Alignment in Collagen Gels: Experiments and Multiscale Simulation,” *J. Biomech. Eng.*, vol. 137, no. 12, p. 121002, 2015, doi: 10.1115/1.4031570.

[220] S. Zeinali-Davarani, Y. Wang, M. J. Chow, R. Turcotte, and Y. Zhang,

"Contribution of collagen fiber undulation to regional biomechanical properties along porcine thoracic aorta," *J. Biomech. Eng.*, 2015, doi: 10.1115/1.4029637.

[221] M. Smoljkić *et al.*, "Biomechanical Characterization of Ascending Aortic Aneurysms," *Biomech. Model. Mechanobiol.*, 2017, doi: 10.1007/s10237-016-0848-4.

[222] G. A. Holzapfel and R. W. Ogden, "Modelling the layer-specific three-dimensional residual stresses in arteries, with an application to the human aorta," *J. R. Soc. Interface*, vol. 7, no. 46, pp. 787–799, May 2010, doi: 10.1098/rsif.2009.0357.

[223] S. Baek, A. Valentin, and J. D. Humphrey, "Biochemomechanics of cerebral vasospasm and its resolution: II. Constitutive relations and model simulations," *Ann. Biomed. Eng.*, vol. 35, no. 9, pp. 1498–1509, Sep. 2007, doi: 10.1007/s10439-007-9322-x.

[224] C. S. Jhun, M. C. Evans, V. H. Barocas, and R. T. Tranquillo, "Planar biaxial mechanical behavior of bioartificial tissues possessing prescribed fiber alignment," *J. Biomech. Eng.*, vol. 131, no. 8, Aug. 2009, doi: 10.1115/1.3148194/398341.

[225] E. A. Sander, T. Stylianopoulos, R. T. Tranquillo, and V. H. Barocas, "Image-based multiscale modeling predicts tissue-level and network-level fiber reorganization in stretched cell-compacted collagen gels," *Proc. Natl. Acad. Sci. U. S. A.*, vol. 106, no. 42, pp. 17675–17680, 2009, doi: 10.1073/pnas.0903716106.

[226] S. Thomopoulos, G. M. Fomovsky, and J. W. Holmes, "The Development of Structural and Mechanical Anisotropy in Fibroblast Populated Collagen Gels," *J. Biomech. Eng.*, vol. 127, pp. 742–750, 2005, doi: 10.1115/1.1992525.

[227] Z. Feng *et al.*, "The mechanisms of fibroblast-mediated compaction of collagen gels and the mechanical niche around individual fibroblasts," *Biomaterials*, vol. 35, no. 28, pp. 8078–8091, Sep. 2014, doi: 10.1016/J.BIOMATERIALS.2014.05.072.

[228] J. John, A. T. Quinlan, C. Silvestri, and K. Billiar, "Boundary Stiffness Regulates Fibroblast Behavior in Collagen Gels," *Ann. Biomed. Eng.*, vol. 38, no. 3, pp. 658–673, 2010, doi: 10.1007/s10439-009-9856-1.

[229] E. Kuhl, K. Garikipati, E. M. Arruda, and K. Grosh, “Remodeling of biological tissue: Mechanically induced reorientation of a transversely isotropic chain network,” *J. Mech. Phys. Solids*, vol. 53, no. 7, pp. 1552–1573, Jul. 2005, doi: 10.1016/J.JMPS.2005.03.002.

[230] G. Grindheim, M. E. Estensen, E. Langesaeter, L. A. Rosseland, and K. Toska, “Changes in blood pressure during healthy pregnancy: A longitudinal cohort study,” *J. Hypertens.*, vol. 30, no. 2, pp. 342–350, 2012, doi: 10.1097/HJH.0B013E32834F0B1C.

[231] R. A. Bomberger, C. K. Zarins, K. E. Taylor, and S. Glagov, “Effect of hypotension on atherogenesis and aortic wall composition,” *J. Surg. Res.*, vol. 28, no. 5, pp. 402–409, 1980, doi: 10.1016/0022-4804(80)90102-X.

Appendix A: A Hybrid Microstructural-Continuum Multiscale Approach for Modeling Hyperelastic Fibrous Soft Tissue

The contents of the appendix were previously published as a research article in the Journal Elasticity by Nikpasand, Mahutga, Bersie-Larson, Gacek, and Barocas. The author of thesis developed the Network-to-HGO model framework (*7.3.7 Comparison between Network-to-HGO and Full Multiscale Simulation)*, compared results to the Full Multiscale Framework, and provided an analysis on the results. [104]

6.1 Summary

The heterogeneous, nonlinear, anisotropic material behavior of biological tissues makes precise definition of an accurate constitutive model difficult. One possible solution to this issue would be to define microstructural elements and perform fully coupled multiscale simulation. However, for complex geometries and loading scenarios, the computational costs of such simulations can be prohibitive. Ideally then, we should seek a method that contains microstructural detail, but leverages the speed of classical continuum-based finite-element (FE) modeling. In this work, we demonstrate the use of the Holzapfel-Gasser-Ogden (HGO) model [150], [156] to fit the behavior of microstructural network models. We show that Delaunay microstructural networks can be fit to the HGO strain energy function by calculating fiber network strain energy and average fiber stretch ratio. We then use the HGO constitutive model in a FE framework to improve the speed of our hybrid model, and demonstrate that this method, combined with a material property update scheme, can match a full multiscale simulation. This method gives us flexibility in defining complex FE simulations that would be impossible, or at least prohibitively time consuming, in multiscale simulation, while still accounting for microstructural heterogeneity.

6.2 Introduction

Biological soft tissues are complex, hydrated composites, typically simplified as a mixture of fibrous proteins (primarily collagen and elastin) and cells [157], [158]. The multi-constituent nature of tissues and the dependence on crimped collagen fibers to add structural reinforcement makes tissue mechanical behavior inherently nonlinear. The heterogeneous distribution of constituents due to the varied mechanical loading environments, and the various microstructural requirements of cell populations also tend to make tissues anisotropic (**Figure 40**). The behavior of these tissues, including dissonant behavior from tissue to tissue (e.g. auxetic behaviors in tendon/ligaments [159], [160] compared to the relative rubber-like behavior of arteries [161]–[165]), makes defining a consistent constitutive model challenging.

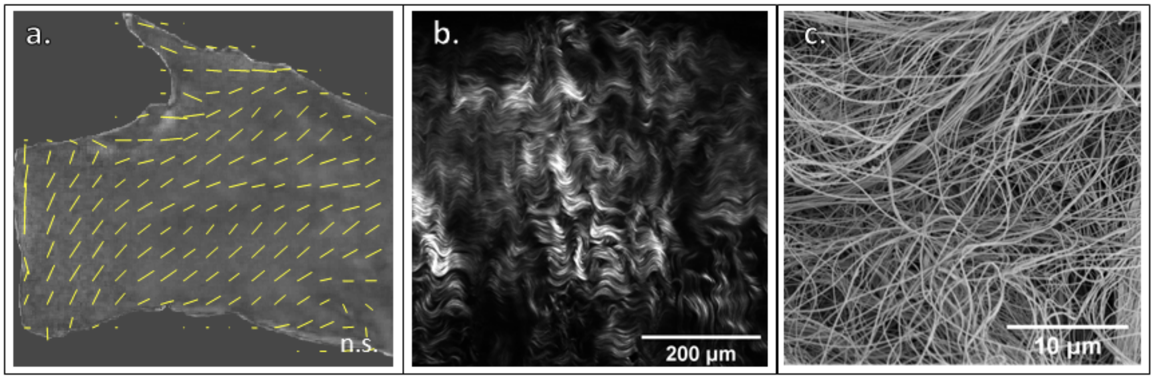

Figure 40 .a.) *Quantitative Polarized Light Imaging (QPLI) of the brachiocephalic artery bifurcation showing macro-scale fiber orientation vectors.* ***b.)*** *Second Harmonic Generation (SHG) imaging of collagen microstructure in the Facet Capsular Ligament (FCL).* ***c.)*** *Scanning Electron Microscopy (SEM) of the collagen microstructure in the FCL*

Despite the complexity of tissue microstructure, a number of models have been proposed in the continuum framework to define the nonlinear, anisotropic material behavior. By far the most common method for defining the nonlinearity of soft tissues is by treating the material as having stress developed as an exponential of strain [156], [166]–[170]. Perhaps the most significant, and widely used constitutive model for nonlinear, anisotropic materials is the Holzapfel-Gasser-Ogden (HGO) model [150], [156]. The beauty of this model is in its simplicity, its broad applicability [10], [171]–[181], and its adaptability and ability to be extended [153], [173], [182]–[186]. In its most basic form, the model is described by a strain energy density function of a neo-Hookean ground substrate with an exponential anisotropic fiber component. The HGO model is given by:

$$W = W^m + W^f = C_1(I_1 - 3) + C_2/(2C_3)\,[\exp(C_3(I_4 - 1)^2) - 1] \tag{A.1}$$

where W^m is the non-fibrillar matrix strain energy density, W^f is the fiber strain energy density, C_1 is the neo-Hookean material parameter, $I_1 = C_{II}$ is the first strain invariant of the right Cauchy-Green tensor (C_{IJ}), C_2 is the fiber modulus term, C_3 is the fiber nonlinearity, and $I_4 = a_I^0 C_{IJ} a_J^0$ is the fourth strain invariant of the right Cauchy-Green tensor C_{IJ} and $\boldsymbol{a^0}$ is a vector describing the fiber direction.

A critical simplification in the analysis of such tissue behavior is the assumption that the deformation of the underlying fiber network is affine [187]. This assumption has been used countless times to lead to different soft tissue models based on invariants and/or the complete fiber distribution. However, the detailed microstructural behavior of a tissue is not, in general, affine [188], [189]. This fact leads to the use of multiscale models where one can precisely define the microstructure while still leveraging the advantages of finite-element modeling [23], [25], [121], [190]–[199]. Of course, the necessity of solving many microstructural problems in the pursuit of modeling the deformation of a specific tissue leads to a huge computational cost. This computational cost is especially exacerbated when one adds in multi-physics such as tissue failure, fluid dynamics, or microstructural remodeling [83], [96], [132], [176], [178], [179], [200]–[209]. Thus, the ideal scenario would be to use the microstructural models when we need the structural and mechanical detail, but use a constitutive model (like the HGO) with a finite element solver when we need to run large-scale, multi-physics models.

In this work, we propose a hybrid modeling approach in which we fit an HGO model to deformations imposed on a microstructural element, then use the HGO constitutive model to enhance the speed of the finite element simulation. This technique allows one to examine microstructural features when necessary without generating and solving all the microstructural problems during the finite element solution. In this way, we enhance the flexibility in multiscale modeling by allowing for the use of larger domains with heterogeneous material definitions and complex boundary conditions without the need to run computationally expensive fully coupled multiscale simulations via a supercomputer.

6.3 Methods

6.3.1 Mechanics Mathematical Preliminaries

Kinematic quantities important in the following analysis are given here. The first important descriptor is the deformation gradient, $\boldsymbol{F}$, which maps the deformation from the undeformed domain to the deformed domain. Out of the deformation gradient comes the Jacobian, $\boldsymbol{J}$ which is given as the determinant of $\boldsymbol{F}$, and represents the volume change due to the deformation. Additional important kinematic variables are the right Cauchy-Green tensor $\boldsymbol{C}$, defined by $C_{IJ} = F_{kI}F_{kJ}$, and the Green-Lagrange strain tensor $\boldsymbol{E}$, defined by $E_{IJ} = \frac{1}{2}(C_{IJ} - \delta_{IJ})$ where δ_{IJ} is the Kronecker delta. In this work, we also use several strain invariants. The isotropic first strain invariant, $I_1 = C_{II}$, and the transverse isotropic fourth strain invariant, $I_4 = a_I^0 C_{IJ} a_J^0$, dictated by a direction vector, $\boldsymbol{a^0}$. We further define the fourth strain invariant as the square of the averaged fiber stretch $\langle I_4 \rangle = H_{IJ}C_{IJ} = \hat{\lambda}_f^2$, where H_{IJ} is the generalized structure tensor (defined below) and $\hat{\lambda}_f$ is the averaged fiber stretch. A number of mechanics quantities are also addressed in the following analysis. The first is the concept of stress. The Cauchy stress carries the physical interpretation of force per current cross-sectional area and is defined as $\boldsymbol{\sigma} = \frac{2}{J}\boldsymbol{F}\frac{\partial W}{\partial C}\boldsymbol{F}^T$ where W is the strain energy density function for the material. The second Piola-Kirchoff stress is defined as $\boldsymbol{S} = \frac{\partial W}{\partial \boldsymbol{E}} = J\boldsymbol{F}^{-T}\boldsymbol{\sigma}\boldsymbol{F}^{-1}$, which carries no meaningful physical interpretation, but does represent a useful quantity for purposes of calculation due to both force and area being mapped to the reference configuration.

6.3.2 Methodological Principles

Our goal is to convert a discrete fiber network model, which allows a high degree of structural fidelity but is computationally intensive, into an HGO model, which is computationally much more tractable. Because our goal is computational simplicity, we use the simple form of the HGO model shown above in Eq. A.1. It is routinely assumed in affine models of this type that the constitutive equation can be written in terms of independent contributions from a non-fibrous matrix and the fiber network. The non-fibrous matrix is often incompressible or includes a volume-dependent term to limit material compressibility. Similarly, in multiscale models [23], [193], [194], a separate neo-Hookean matrix is introduced in parallel to the network. For the present analysis, it is therefore assumed that the fiber network contribution is distinct from the neo-Hookean, incompressible non-fibrillar matrix, and the current work focuses on the fiber network contribution only. The fundamental challenge to be addressed is to convert a fiber network model into one based on the fiber stretch via I_4 (i.e. $a_I^0 C_{IJ} a_J^0$ in a model of the classical HGO form). That is, the problem is to determine parameters C_2 and C_3 such that the model

$$W^f = C_2/(2C_3)\,[exp(C_3(\langle I_4\rangle - 1)^2) - 1] \tag{A.2}$$

yields a fiber-network strain energy density function W^f that matches the results from the network computations. Here we delineate the difference between the square stretch, I_4, in a given direction $\boldsymbol{a^0}$, and the square stretch in the average fiber direction $\langle I_4\rangle = H_{IJ}C_{IJ}$. The invariant $\langle I_4\rangle$ is calculated as the double contraction of a generalized structure tensor H_{IJ} with the right Cauchy-Green tensor C_{IJ}. The generalized structure tensor H_{IJ} is defined as

$$H_{IJ} = \frac{1}{V}\int_{\Omega} N_I^m N_J^m dV = \frac{\sum_{m=1}^{k} V^m N_I^m N_J^m}{\sum_{m=1}^{k} V^m} \tag{A.3}$$

where $\boldsymbol{N}^m$ is the unit vector in the direction of fiber m, and $V^m = \pi(R^m)^2 L^m$ is the volume of a fiber with radius, R^m and length, L^m. The calculation of the generalized structure tensor and its use to calculate $\langle I_4\rangle$ are based on the underlying assumption that, in general, the network behaves affinely. This calculation does not account for different properties of fibers such as the tension-compression asymmetry of fiber response, or the different fiber types that might occur (e.g., collagen and elastin). There are also differences incurred because the fibers are exponential and the deformation in a network is not affine, meaning the apparent modulus of any given fiber need not be the same as any other or, in fact, the average fiber. There are several ways one could approach this problem, including calculating the end-state $h_{ij} = F_{iK}H_{KL}F_{jL}$ for the network and mapping it back to the undeformed domain with or without those fibers that are in compression. This strategy, however, would rely on an accurate representation of the deformation, which is often unknown *a priori*. A second option would be to not calculate the structure tensor from the fiber network, but instead treat its components as additional fitting parameters. Doing so, however, would leave the underlying structural information we have from the microstructural networks unutilized.

One of the challenges with a structure-tensor-based model is the so-called tension-compression switch. Fibers are very stiff in tension but buckle and support almost no load in compression. If the structure tensor and the resulting calculated $\langle I_4 \rangle$ do not exclude fibers in compression, then the model is at risk of overpredicting the stress response, especially if the model has been fitted to data from a different strain field. This issue has received much discussion (e.g., [182], [210]), and variations have been proposed in which compressed fibers are excluded [183], [186]. In the current work, we chose to use a simpler, all-fiber structure tensor. As noted earlier, the tension-compression switch is approximated smoothly in the discrete-fiber model by the exponential fiber constitutive equation; the specific representation of the switch has relatively little effect on the overall network mechanics [188]. We refer the reader to the in-depth discussions on structure tensors and tension-compression asymmetry in biological tissues given in other works [186], [210], [211].

There are, of course, infinitely many possible deformations, but the fitting problem can be reduced conveniently by considering the fiber network strain energy W^f as a function of $\hat{\lambda}^f = \sqrt{\langle I_4 \rangle} = \sqrt{\mathrm{H_{IJ}C_{IJ}}}$, which represents an averaged fiber stretch in the affine, continuous model. Although the product $\mathrm{H_{IJ}C_{IJ}}$ does not have any physical meaning within the context of the non-affine discrete fiber model, it is easily calculated and convenient for use in the fitting process. Likewise, W^f can be calculated either from computing an average stress in the domain [118] and integrating it with respect to its energy conjugate in the continuum sense to determine a strain energy, or by summing the total strain energy of all fibers and dividing by the domain volume. These two methods are given by

$$W^f = \int_{E_{IJ}=0}^{E_{IJ}} S_{IJ} dE_{IJ} = \frac{1}{V} \int_{\Omega} w^m dV \approx \frac{1}{V} \sum_{m=1}^{k} w^m V^m \qquad \text{(A.4.1)}$$

where W^f is the total strain energy density of the fiber network, S_{IJ} is the second Piola-Kirchhoff stress, E_{IJ} is the Green strain, $w^m$is the strain energy density of fiber m, V is the domain volume, and V^m is the volume of fiber m. The individual strain energy of a fiber is given by

$$w^m = \int_{E_{IJ}^m=0}^{E_{IJ}^m} S_{IJ}^m dE_{IJ}^m \tag{A.4.2}$$

The results from a network simulation of any macroscopic deformation can then be represented as W^f vs. λ^f. This method is further summarized in the flowchart in **Figure 41**. With W^f vs. λ^f from the network determined, the total-fiber constitutive law can be fit to the aggregated network-scale simulation results. Although in principle any total-fiber constitutive law could be used, a continuum model in an exponential format that is similar to the fiber's qualitative behavior is an intuitive choice to predict fibers' overall behavior. Therefore, throughout this work we use the expression of Eq. A.2 and fit C_2 and C_3 to the W^f vs. λ^fcurve.

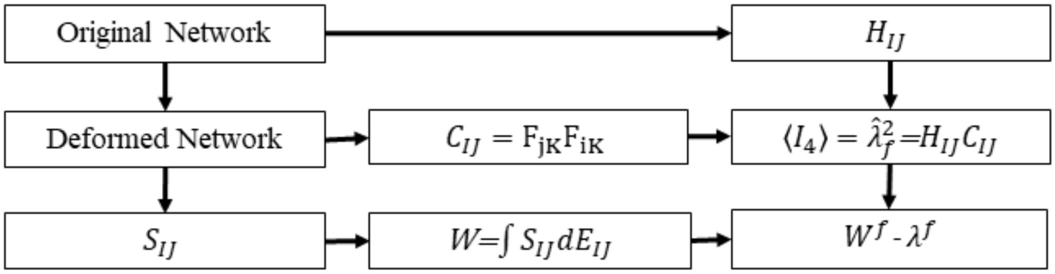

Figure 41 *Flowchart for converting fiber network model to affine model*

6.3.3 Case Study: Multiple Deformations of a Single Network

To verify the ability of an HGO-type model to reproduce network mechanical response, a moderately aligned ($H_{11} = 0.69, H_{22} = 0.21$ and $H_{33} = 0.10$) 3D Delaunay network was generated using the Delaunay triangulation function, *delaunay*, in MATLAB (R2019a, MathWorks, Natick, MA). This alignment was chosen due to the tendency of collagenous tissues to possess a preferred alignment, observed in, for example, ligaments [4], [212]. Briefly, randomly generated seed points in the 3D space were used to generate a Delaunay tetrahedral network. The seed points represent network nodes, and the edges of the tetrahedral regions represent the fibers. After initial generation, the network was subjected to artificial stretches to reach the desired alignment. Finally, the aligned network was clipped from the stretched network to a unit cube, and the fibers and nodes inside the cube were extracted to form the aligned networks used in these simulations. This process was done iteratively, with the number of the seed points adjusted in order to obtain a final volume fraction of 0.04 for each network, holding the fiber cross-sectional areas constant. This fiber fraction represents a collagenous tissue as in [123], [213]. The fiber volume fraction in a network is given by

$$\phi^f = \frac{V^f}{V} = \frac{\chi \sum_{m=1}^{k} \pi (R^m)^2 L^{*m}}{\chi^3 V^*} \tag{A.5}$$

where ϕ^f is the fiber volume fraction, V^f is the total fiber volume, V is the network volume, χ is a scale factor converting from computational length units to real length unit [m], R^m is the radius of fiber m, L^{*m} is the length of fiber m in computational space, and V^* is the network volume in computational space.

The fibers in these networks were then modeled as one-dimensional nonlinear springs connected at freely-rotating pin joints (nodes) at two ends. The slender fibers are subjected to moderate to large strains and have negligible bending stiffness. The governing equation describing the *fibers in the network* was adapted from [214] and is defined as

$$f = \frac{kA}{B}(exp[BE] - 1) \tag{A.6}$$

where f is the force generated within the fiber, A is the fiber undeformed cross-sectional area, k and B are constant and represent fiber stiffness and nonlinearity, respectively, and $E = \frac{1}{2}(\lambda_m^2 - 1)$ is the Green strain of the fiber, m, stretched to stretch ratio λ_m. The values for k and B in Eq. A.6 and the fiber radius were set to 10 MPa, 2.5, and 100nm, respectively, following Dhume et al. [123]. We emphasize that the function in Eq. A.6 represents a single fiber in the network, where the function itself is chosen so that the force is zero at zero strain, with large magnitude forces developed in tension and low magnitude forces developed in compression, simulating the tension-compression switch seen in native collagen fibers. The solution of the network state given a prescribed deformation was calculated using Newton iteration to balance all forces on internal nodes. The overall Cauchy stress state for the network was then calculated as

$$\sigma_{ij} = \frac{1}{V}\int_{\Omega} \sigma_{ij} dV \approx \frac{1}{V}\sum_{m=1}^{k} \sigma_{ij}^{m} V^{m} = \frac{1}{V}\sum_{m=1}^{k} \left(\frac{f_i^m}{A^m}\right) n_j^m (A^m l^m) = \frac{1}{V}\sum_{m=1}^{k} f_i^m n_j^m l^m \tag{A.7}$$

where σ_{ij} is the network volume averaged Cauchy stress, V is the network volume, σ_{ij}^m is the Cauchy stress of fiber m, V^m is the volume of fiber m, f_i^m is the force from fiber m, A^m is the instantaneous cross-sectional area of fiber m, $\boldsymbol{n^m}$ is the fiber normal direction in the deformed state, and l^m is the current length of fiber m.

The network was subjected to five different deformations: x-direction uniaxial stretch, simple shear on the xy- and yz-faces, and equibiaxial stretch in the xy- and xz-plane (**Figure 42**a, b). The network underwent a stretch of 1.8 in the x-direction. The stretches for other deformations were calculated such that the final $\hat{\lambda}_f = \sqrt{H_{IJ}C_{IJ}}$ in all deformations was equal to the calculated $\hat{\lambda}_f$ for the x-direction uniaxial stretch experiment. These deformations were selected because the network of interest has $H_{11} > 0.33$, meaning that the main fiber direction falls mostly in the x-direction. This approach ensures $H_{IJ}C_{IJ} > 1$, which allows for proper fitting of the W^f curves. In this work, the directionality of the networks drove the deformations used for the initial HGO fits (i.e. networks aligned in x are subjected to x, xy, and/or xz deformations). For each deformation, the boundary nodes were displaced, and internal node equilibrium was attained using Newton iteration. In all deformations, the boundaries were displaced such that incompressibility was guaranteed on the network's bounding box. For each deformation, the (macroscopic) right Cauchy-Green tensor, C_{ij}, and the macroscopic volume-averaged Cauchy stress, σ_{ij}, were calculated and stress converted to W^f vs. λ^f as described previously (Eq. A.4). The W^f vs. λ^f curves were plotted simultaneously for all the generated deformations, and a single constitutive HGO fiber model given in Eq. A.2 was fit to the data using MATLAB (R2019a, MathWorks, Natick, MA) built in constrained minimization routine *fmincon*. An example of the W^f vs. λ^f curves and the fit are shown in **Figure 43**.

To show that how fiber realignment can differ in various deformations, the largest eigenvalue of the instantaneous orientation tensor at each steps, h_{ij}, was calculated and plotted vs. the average value of fiber stretch (**Figure 45**c, d).

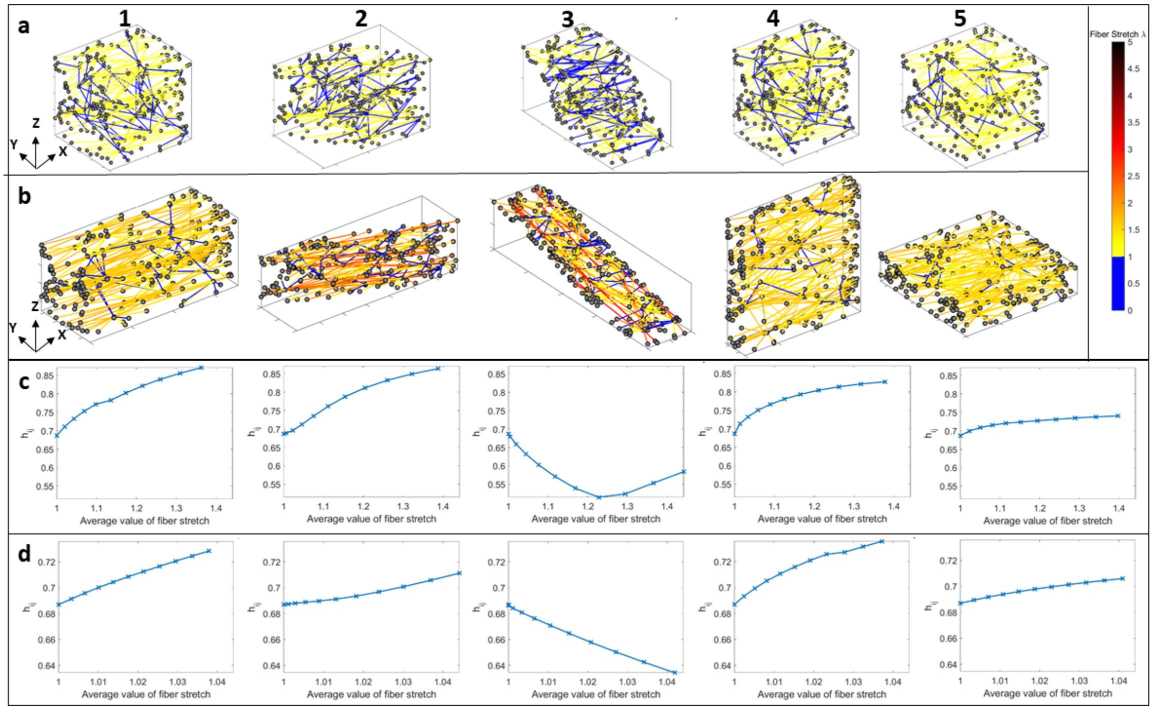

Figure 42 a1-5.) *Network deformations for x-uniaxial, xy-shear, yz-shear, xz-biaxial, xy-biaxial for 112% fiber Green strain.* ***b1-5.)*** *Network deformations for x-uniaxial, xy-shear, yz-shear, xz-biaxial, xy-biaxial for 10% fiber Green strain.* ***c1-5.)*** *The largest eigenvalue of the instantaneous orientation tensor, h_{ij} versus the average value of fiber stretch for 112 %fiber Green strain.* ***d1-5.)*** *The largest eigenvalue of the instantaneous orientation tensor, h_{ij} versus the average value of fiber stretch for 10% Green strain*

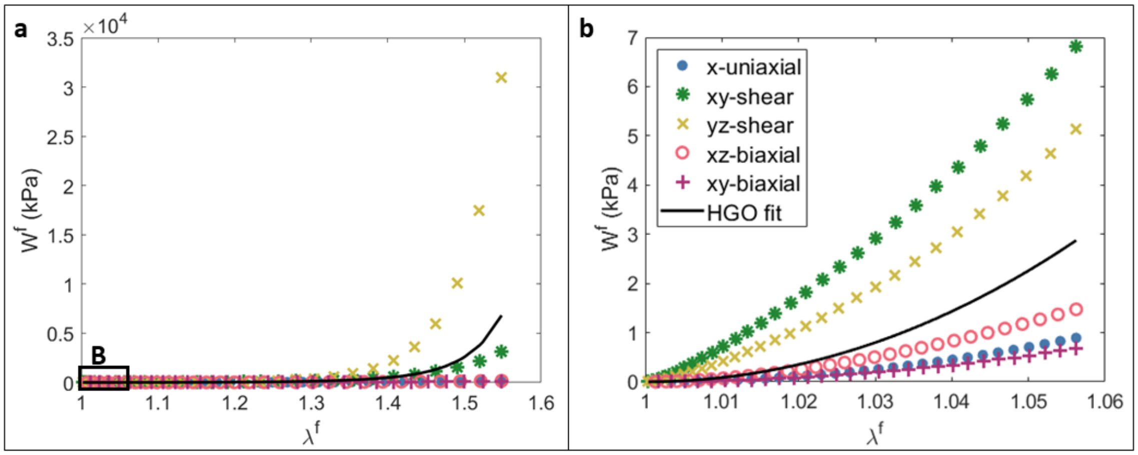

Figure 43 *Holzapfel-Gasser-Ogden material property determination from microstructural networks under varied deformations for* ***a.)*** *112% Green strain,* ***b.)*** *10% Green strain*

6.3.4 Alignment Dependance for Delaunay Networks

We evaluated the proposed method by generating HGO model parameters for 750 Delaunay networks with a range of alignments. The various deformations described in **Figure 45** were imposed on the networks, and W^f vs. λ^f plots were constructed for each deformation. For each network, the W^f vs. λ^f deformation plots were fit together with the single HGO model given in Eq. 2. Contour plots of the material parameters were then created to evaluate the material property variation with alignment and assess if the HGO model could be broadly applied across Delaunay networks of varying alignment.

6.3.5 Hybrid Microstructural-Continuum Approach

The novelty of this approach is that it removes much of the computational overhead needed in fully coupled multiscale approaches. Particularly, the use of the network model to fit a continuous material model (HGO) lets us leverage the increased speed in calculating both stress and the material (or spatial) elasticity tensor of the continuum material model over the micro-network model. Take, for example, a network consisting of Q fibers and R nodes where we have Cauchy stress given by Eq. A.7 converted to the PK2 stress to calculate the material elasticity tensor

$$C_{IJMN} = \frac{\partial S_{IJ}}{\partial C_{MN}} = \frac{\partial}{\partial C_{MN}}\left[\frac{1}{V_0} F_{Im}^{-1}\left(\sum_{k=1}^{Q} f_m^k l^k n_n^k\right) F_{Jn}^{-1}\right] \tag{A.8}$$

where S_{IJ} is the network PK2 stress, and C_{MN} is the right Cauchy-Green tensor, V_0 is the undeformed network volume, $\boldsymbol{F^{-1}}$ is the inverse deformation gradient tensor, $\boldsymbol{f^k}$ is the fiber force vector, $\boldsymbol{n^k}$ is the fiber direction vector, and l^f is the fiber current length. If we examine these equations, it becomes clear that, at a minimum, we would need to calculate the fiber force, $\boldsymbol{f}$ for each fiber, k, and we would need to calculate something akin to the fiber elasticity, $\frac{\partial}{\partial C_{MN}}\left((\sum_{k=1}^{N} f_m^k l_n^k)\right)$ for each fiber, k. For each network at each Gauss point in each element (i.e. 8 networks per hex element), we would have to calculate both of these quantities. That means we would have to run one network simulation per Gauss point and make Q calculations for the stress and Q calculations for the elasticity per network, if there existed an analytical solution to the elasticity tensor, which, in the case of non-affine networks, is not necessarily the case. Additionally, the network solution relies on determining the static force balance of internal nodes, which, if solved explicitly, would yield another R calculations. However, this solution typically involves implicit solution via Newton iteration, resulting in between 5-10 iterations to achieve static equilibrium for a well-conditioned network. Thus, in the best case scenario, we would have $2Q+R$ calculations per Gauss point. If we contrast this with the HGO model, which involves one stress calculation and one elasticity calculation per Gauss point, we expect a minimum decrease in computational cost of $Q + \frac{1}{2}R$ per network. The overall computation time is presented in **Supplementary Table 1**.

One can fit the behavior of a network by subjecting it to many potential deformations and fitting the total data (as in Case Study 7.3.3), or one could simply fit one single deformation of interest. The former will give a better rough estimate if the actual deformation of the material is unknown, while the latter will be more accurate if there is confidence in the magnitude and type of deformation the network will undergo. We henceforth refer to the initial average fit to many deformations as the ***HGO fit*** and to the later fit to a single deformation as the ***refit***. Care must be taken when refitting to a single deformation, as not all deformations will cause the average stretch to be greater than one. In these cases, the fit will not capture the behavior of the network, and an alternative fit

Supplementary Table 1: *Coefficients for the fit of HGO parameters C_2 and C_3*

ij	α_{ij} $[MPa]$	β_{ij} $[-]$
00	1.56 ± 0.22	-11.84 ± 4.46
01	-8.30 ± 1.89	94.49 ± 28.61
10	14.10 ± 3.77	70.46 ± 15.98
11	-5.56 ± 0.58	-517.60 ± 97.80
02	33.70 ± 7.63	-106.90 ± 29.40
20	-59.90 ± 16.27	-59.44 ± 13.25
12	5.47 ± 0.79	474.80 ± 69.40
21	-35.90 ± 7.57	396.00 ± 75.60
22	67.25 ± 17.50	0

should be used. In our model, we use two methods for dealing with this issue: 1. If the average stretch never exceeds one, we simply make the fiber modulus zero, thereby removing the fiber contribution, and 2. If the average stretch does eventually exceed one, but the fit is poor due to the behavior of the strain energy curve (i.e., **Figure 44**), we attempt to fit only the slope of the strain energy curve for which the average stretch is greater than one. This effectively allows us to fit something closer to the stress, as the stress is directly related to the slope of the W^f vs. λ^f curve.

Once the HGO properties are fitted to the network simulations, we can use those material inputs in a finite element (FE) framework as shown in **Figure 44**a. This allows us to rely on the constitutive relation to solve the FE simulation rather than having to use costly microscale network simulations. Further, once we have the solution from the FE simulation, we can extract the deformation gradient at any point of interest and run the networks to evaluate any microstructural quantities such as fiber orientation or fiber stresses. This offers us the ability to evaluate discrete quantities in regions of interest, or to pass strains down to the microstructure to evaluate fiber remodeling or failure.

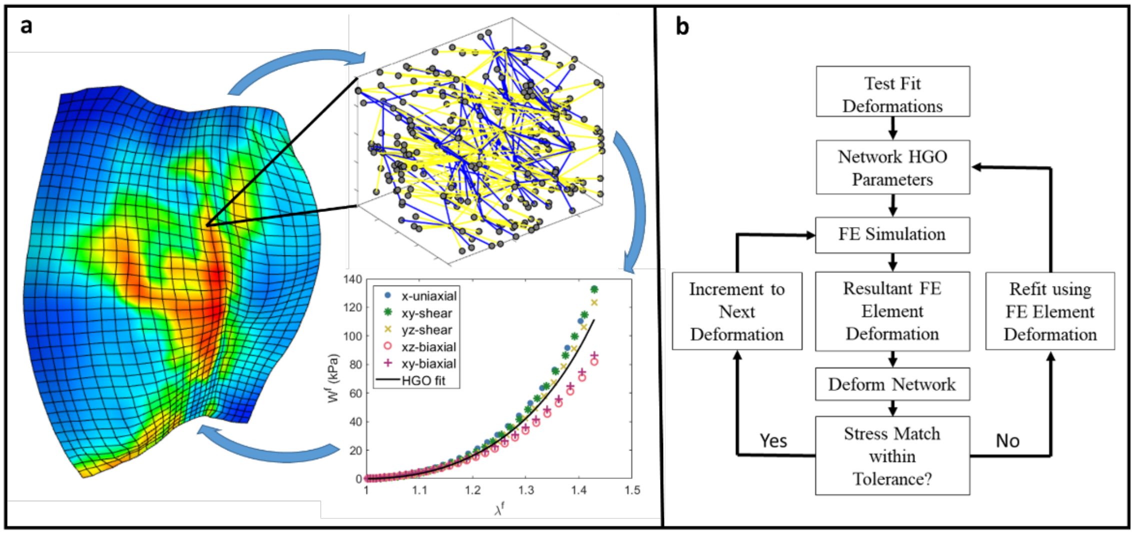

Figure 44 a.) *Schematic of the hybrid continuum-discrete multiscale approach.* ***b.)*** *Flowchart for the hybrid continuum-discrete multiscale approach.*

In an FE simulation, one often is concerned with an imposed deformation that occurs in a series of small steps. In this case, one can choose whether to iterate at a given step until the deformation field and model are consistent, or to adjust the model based on a given step and use the updated parameters for *the next* step. The latter approach introduces some error in that the continuum model does not match the microscopic model at the end of the step, but it has the considerable efficiency advantage of allowing an update at relatively low computational cost. The lagging update errors can also be further mitigated by imposing smaller deformation steps where in the limit of an infinitesimally small step the error becomes zero. If one only cared about the end state of the deformation, then this method would introduce little error, especially if the state or states of interest are iterated to match microscopic and macroscopic stress. For this work, we chose the less costly approach of allowing the continuum model correction to proceed with the previous step update, and only iterate the state of interest, which in our example (7.3.7) is the final step. This process is shown in **Figure 44**b.

6.3.6 Case Study: Single-Network Model Performance for Non-Fitted Deformation

In this study, we compared the fit of the HGO model to an array of deformations and the fit of an HGO model to a specific deformation. To do this, we first fit the network to x-uniaxial (magnitude 1.25), xy-biaxial, xz-biaxial (magnitude 1.1), xy- shear and xz-shear (magnitude 0.15). Once the HGO model had been fit, we tested it on a deformation that differed from the ones used in fitting the model parameters. Specifically, we modeled an element from complex motion of the stretching and three-point bending of a facet capsular ligament as in [12]. We imposed the deformation gradient of an element experiencing maximum stretch during the simulated experiment:

$$\boldsymbol{F} = \begin{bmatrix} 1.239 & 0 & 0.0035 \\ 0 & 1.048 & -0.0014 \\ -0.0080 & 0.102 & 0.770 \end{bmatrix} \tag{A.9}$$

which was dissimilar to the uniaxial, biaxial, and shear deformations used to fit the initial HGO model. The deformation was imposed on the discrete network model, and the volume-averaged Cauchy stress was determined. Concurrently, the Cauchy stress was calculated by the HGO model using the parameters fitted to the suite of deformations (given above as ***HGO fit***). In addition, in keeping with the ***refit*** update strategy discussed above, after the simulation was done, we refit the HGO model to W^f vs. λ^f giving us stress estimates for the deformation imposed in Eq. A.9.

6.3.7 Comparison between Network-to-HGO Model and Full Multiscale Model

The goal of the proposed method is to facilitate higher-efficiency multiscale simulations based on network structure. To evaluate its potential, we performed a full multiscale simulation of a representative L4-L5 facet capsular ligament (FCL) sample during spinal flexion (reproducing the model of Zarei et al. [16]). The model boundary conditions are defined through application of nodal displacements based on the bone surface from the kinematic simulation of Bermel et al. [13]. Additional details of the simulation setup are available in [16]. The same micro-networks used in [16] were applied in the network-to-continuum scheme, and the resulting continuum biomechanics problem was solved using the open-source finite-element platform FEBio [41]. Because FEBio does not support the HGO model, the ligament was modeled as a coupled solid mixture of a Mooney-Rivlin (effectively reduced to a neo-Hookean) ground matrix with three fiber families, leading to the strain energy density function

$$W = W^m + W^f \tag{A.10a}$$

where W is the total strain energy density. The first term in the total strain energy density is the non-fibrillar matrix component of the strain energy density W^m given by

$$W^m = C_1(I_1 - 3) - 2C_1\, lnJ + \frac{\lambda}{2}(ln\,J)^2 \tag{A.10b}$$

where C_1 is half the second Lamé parameter relating to the neo-Hookean material parameter, I_1 is the first strain invariant of the right Cauchy-Green tensor, C_{IJ}, $J = \det(\boldsymbol{F})$ is the differential volume change of the deformation, and λ is the first Lamé parameter relating to the bulk modulus. The tissue was considered as a compressible material with a matrix modulus and bulk modulus that matched those used by Zarei et al. [16]. The compressibility of the FCL was experimentally observed by Little et al., who suggest that the Poisson's ratio is as low as 0.3 [4]. The second half of the strain energy density is the fiber component of the strain energy density W^f given by

$$W^f = C_2/(2C_3)\sum_{p=1}^{3} h^p\left(exp\left(C_3(I_4^p - 1)^2\right) - 1\right) \tag{A.10c}$$

where C_2 represents the fiber modulus, C_3 captures fiber nonlinearity, h^p is the weighting factor for fiber family p, $I_4^p = C_{IJ}N_I^pN_J^p = (\lambda^p)^2$ is the fourth strain invariant of the right Cauchy-Green tensor, C_{IJ}, $\boldsymbol{N}^p$ is the unit vector pointing in the direction of fiber family p in the undeformed state, and λ^p is the average fiber stretch of fiber family p. The undeformed direction vectors $\boldsymbol{N}^p$, were generated directly from the structure tensors H_{IJ} by taking the eigenvectors, which, since H_{IJ} is a symmetric positive definite matrix, give three orthogonal fiber directions. For the current work, we use these three orthogonal fiber families pointing in the principal directions of H_{IJ} and assign the weight h^p to each family based on the eigenvalues of H_{IJ} corresponding to each eigenvector $\boldsymbol{N}^p$. Fiber material parameters C_2 and C_3 were fit to the W^f vs. λ^f plots using the method described above. The neo-Hookean material parameter, C_1, and the bulk modulus parameter, λ, were set to 0.025 MPa and 0.417 MPa, respectively, to match [16]. The analogous stress for this strain energy function can be found in the FEBio manual [64] under compressible materials Fiber with Exponential Power Law (4.1.3.8) and Coupled Mooney-Rivlin (4.1.3.17).

Briefly, to generate the finite-element simulation, we imported the L4-L5 FCL geometry mesh of hexahedral elements [16], and applied HGO parameters to each individual element corresponding to the microstructural networks applied in [16]. To simulate flexion, the displacement of the nodes at the entheses (left and right sides of **Figure 44**a) were specified based on the L4-L5 motion segment model [13] as further described in [16].

Initially, micro-networks from the full multiscale model were fit to the HGO using multiple deformations, as described previously. A FEBio model of the representative FCL sample bending in flexion was then simulated using the initial HGO fit for fiber material parameters in Eq. A.10c. For added accuracy, the deformation gradient tensor for each element in the FEBio HGO model was then used to refit the fiber material parameters. For comparison, maximum shear stress and maximum shear strain fields were computed for the full multiscale model, the FEBio initial HGO model, and the FEBio refit HGO model.

6.4 Results

6.4.1 Multiple Deformations of a Single Network

A representative fiber network was chosen for detailed analysis. The network is shown after moderate (10% Green strain, **Figure 42**a) and extremely large (112% Green strain in **Figure 42**b) deformations. The deformed network is shown for x-uniaxial, xy- and xz-shear, and xy- and xz-biaxial deformations (**Figure 42** a and b). In this case, the network of interest has $H_{11} = 0.69$, meaning that the use of x-direction deformations ensures $H_{IJ}C_{IJ} > 1$ which allow us to more accurately fit the W^f curves.

The largest eigenvalue of the instantaneous orientation tensor, h_{ij}, is plotted versus the average value of fiber stretch over the full stretch range (**Figure 42**c) and in close-up of the small-stretch range (**Figure 42**d). The eigenvalues show large variation with deformations which is particularly pronounced at low strains. This result shows that the fiber realignment is highly deformation-dependent.

The fitting of network behavior to a series of different deformations is shown in **Figure 43**. We see that under relatively large strains, the W^f vs. λ^f curves become more similar. At small to moderate strains, the non-affinity of the deformation can play a significant role in the mechanics of the network, causing the plot of W^f vs. λ^f to become strongly deformation-dependent (**Figure 43**b). In the case of **Figure 43**, for example, a single HGO model cannot match the network model for all possible deformations, or even for specific families of deformations.

6.4.2 Alignment Dependence for Delaunay Networks

A total of 750 networks with different orientations ranging from isotropic ($H_{11} = 0.33$) to strongly aligned ($H_{11} = 0.8$) were studied, with the five representative networks (numbers 1-5) examined in detail in **Figure 45**. The network views in **Figure 45**a (xy-view) and **Figure 45**b (xz-view) show markedly different alignments. The orientations of these networks start with network 1 being nearly isotropic, network 2 being slightly aligned in the x-direction, network 3 being slightly aligned in the z-direction, network 4 being more strongly aligned in the x-direction, and network 5 being even more strongly aligned in the x-direction, as demonstrated by the numbering in **Figure 45**d-f. The W^f vs. λ^f curves were plotted for each network, and an HGO curve was fit to them (**Figure 45**c). It is evident from these W^f vs. λ^f plots that the fit of the HGO model becomes more variable for more highly aligned fiber networks, especially at large strains. Another particularly interesting aspect of these plots is the behavior of network 3. The W^f vs. λ^f plot would indicate that the direction transverse to the alignment direction is actually stiffer than that in the direction of alignment. However, this is not the whole story. The fiber stretch values are the double contraction of the orientation tensor and the right Cauchy-Green tensor, so when stretching in directions transverse to the primary alignment, much greater magnitudes of stretch are necessary to produce the same averaged fiber family stretch. In fact, the magnitude of the xy-biaxial stretch in network 3 was 3.33, while the magnitude of the xz-biaxial stretch was only 1.17. This effect is further evidence of the non-affine fiber

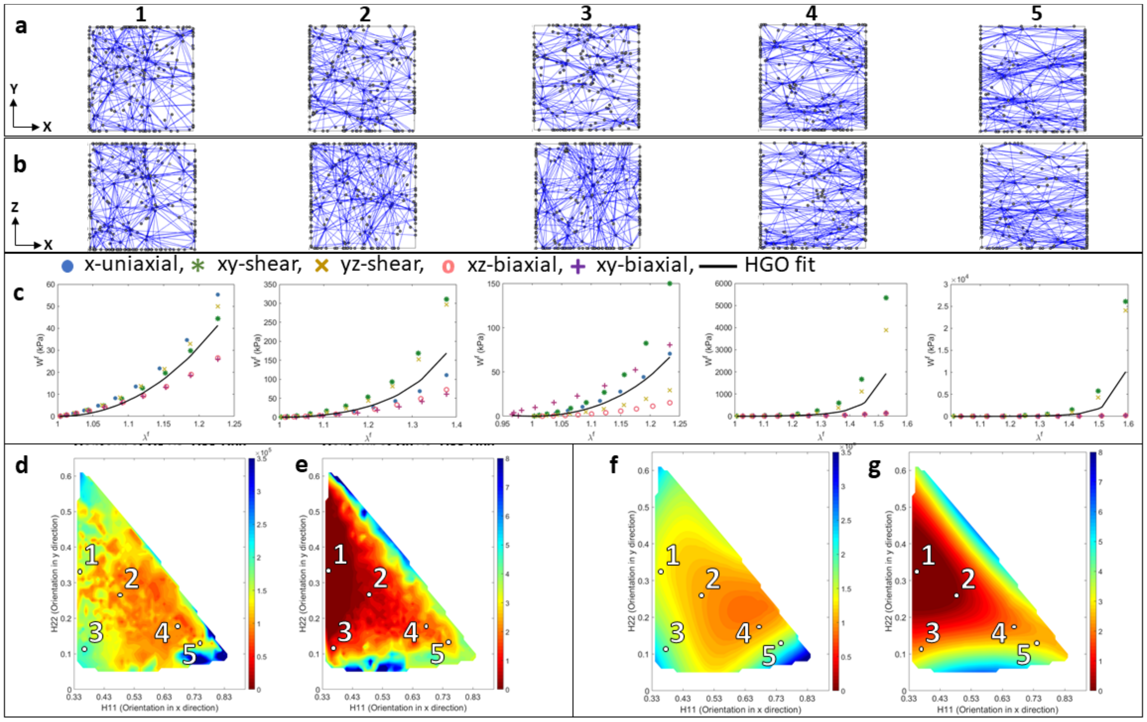

Figure 45 a1-5.) *xy view of networks 1-5.* ***b1-5)*** *xz view of networks 1-5.* ***c1-5.)*** *W^f-λ^f of networks 1-5 with alignment, network 1: H_{11}= 0.35 and H_{11}= 0.32, network 2: H_{11}= 0.5 and H_{11}= 0.32, network 3: H_{11}= 0.36 and H_{11}= 0.12, network 4: H_{11}= 0.66 and H_{11}= 0.18, network 5: H_{11}= 0.74 and H_{11}= 0.14.* ***d.)*** *and* ***e.)*** *Contour plots of HGO material property, C_2 and C_3, respectively, as a function of alignment in x, H_{11}, and y direction, H_{22}.* ***f.)*** *and* ***g).*** *Contour plots of fitted value of HGO material property, C_2 and C_3, respectively, to the multivariate nonlinear model of Eq. A.11*

realignment occurring in fiber networks that is not well captured by the HGO model. **Figure 45**c also shows that the deformations corresponding with alignment are similar to what was observed in **Figure 43**. For network 1, all deformations form a tight cluster of W^f vs. λ^f curves because the fibers are nearly isotropic. Network 2 shows slightly more spread since the primary orientation is more strongly aligned in the x-direction, and networks 4 and 5 exhibit even greater spread due to increased alignment in the primary x-direction.

Despite the differing W^f vs. λ^f behavior with different deformations, we still require an initial set of parameters for our simulations. We therefore fit a pair of model parameters C_2 and C_3 from Eq. 2 to the W^f vs. λ^f curves to allow us to readily determine material parameters without the need to run any additional simulations. We observed that the fitted parameters C_2 and C_3 were not constant over all networks, but showed considerable variation with network alignment. This result indicates that the degree of non-affinity, as indicated by the amount of correction necessary to convert the discrete fiber network model into an affine model, is dependent on fiber alignment. This result was previously obtained by Hatami-Marbini and Picu [189], who found a greater degree of non-affinity in aligned networks loaded transverse to the preferred direction of alignment. The importance of this result lies in the fact that the constants C_2 and C_3 depend the fiber network orientation, *even for networks constructed of identical fibers and even when orientation is included in the continuum model via the construct* $H_{IJ}C_{IJ}$.

To further explore the observed dependence, contour graphs of the calculated parameters, C_2 and C_3, were generated as a function of the alignment in the 1 and 2 directions (H_{11} and H_{22}, respectively) for all networks simulated (**Figure 45** d and e). The location of networks of **Figure 45** a and b are indicated on the contours with numbers 1-5. The non-smooth appearance of the contour lines must derive from other factors that contribute to the network behavior. However, H_{11} and H_{22} are sufficient to capture the general trend via the quadratic curve fits shown in **Figure 45** f and g. The equations for those fits,

$$C_2 = \sum_{i=0}^{2} \sum_{j=0}^{2} \alpha_{ij} H_{11}^{i} H_{22}^{j} \quad \text{(A.11a)}$$

$$C_3 = \sum_{i=0}^{2} \sum_{j=0}^{2} \beta_{ij} H_{11}^{i} H_{22}^{j} \quad \text{(A11b)}$$

allow estimation of C_2 and C_3 for any Delaunay network of fibers with the underlying properties specified above (Eq. A.6). The goodness of fit was marginal ($R^2 = 0.47$ for C_2 and $R2 = 0.73$ for C_3) due to the inherent differences between networks and other factors influencing behavior (i.e. even networks with the same alignment have varied nodal positions and fiber lengths, which can change the network response to stretch). The coefficient values are given in **Supplementary Table 1**.

Large values of C_2 and the smallest values of C_3 occur when the network is close to isotropic (point 1 in **Figure 45** d and e). *If one desires to represent the behavior of an isotropic, non-affinely deforming discrete-fiber network with an affine-deformation model,* *the underlying fiber model in the network needs to be stiffer and less nonlinear compared to that representing a more strongly aligned network (point 5 in* **Figure 45** *d and e).* As a simple verification, suppose we have the network shown in **Figure 46**a having $H_{IJ} = \begin{bmatrix} 2/3 & 0 \\ 0 & 1/3 \end{bmatrix}$. If we stretch in the direction of fibers as shown in **Figure 46**b where $F_{iJ} = \begin{bmatrix} 3/2 & 0 \\ 0 & 2/3 \end{bmatrix}$ and $C_{IJ} = \begin{bmatrix} 9/4 & 0 \\ 0 & 4/9 \end{bmatrix}$, we have an estimated average fiber stretch of $\langle \lambda_f \rangle = \sqrt{H_{IJ} C_{IJ}} = \sqrt{3/2 + 4/27} = 1.284$. If we simply compute the average stretch of the three fibers we have $\lambda_1 = 2/3$ and $\lambda_2 = \lambda_3 = 3/2$ which gives us a mean stretch of $\bar{\lambda} = 1.222$. Now if we take the same network and stretch transverse to the direction of alignment as shown in **Figure 46**c where $F_{iJ} = \begin{bmatrix} 2/3 & 0 \\ 0 & 3/2 \end{bmatrix}$ and $C_{IJ} = \begin{bmatrix} 4/9 & 0 \\ 0 & 9/4 \end{bmatrix}$, we get an estimated average stretch of $\langle \lambda_f \rangle = \sqrt{8/27 + 3/4} = 1.023$. If we then compute the actual stretches by computing the equilibrium positions assuming that the fiber forces are linear in strain such that sum of vertical forces is zero:

$$\sum f_y = 0 = (L_1/l - 1) - 2(L_2/l - 1)\cos(\theta) \tag{A.12}$$

and enforcing the geometric constraints that $L_2 \cos(\theta) + L_1 = 1.5/2$ and $2L_2 \sin(\theta) = 1/1.5$, we can solve giving $L_1 = 0.439$, $L_2 = 0.456$, and $\theta = 47.0^o$. Thus, the stretches are $\lambda_1 = 0.88$ and $\lambda_2 = \lambda_3 = 0.91$ giving an average stretch of $\bar{\lambda} = 0.900$. This example leads us to two observations: 1. The estimated stretch transverse to the direction of alignment is far from that in the direction of alignment, and 2. The estimated behavior of the stretch transverse to the direction of alignment is not representative of the true average, and is, in fact, indicating the network is in tension when the true behavior of the network shows all the fibers in compression. This simple example drives home the point that the networks estimated using the structure tensor, H_{IJ} can be quite different from the real network behavior when the network is loaded transverse to its preferred direction of alignment. In this case, the network itself is very non-affine and should require a larger correction which is observed in **Figure 45**d-e. Further, this result demonstrates the issue one can encounter when trying to fit the network behavior to the HGO model where the network itself develops almost no stress (effectively zero since the fibers buckle in

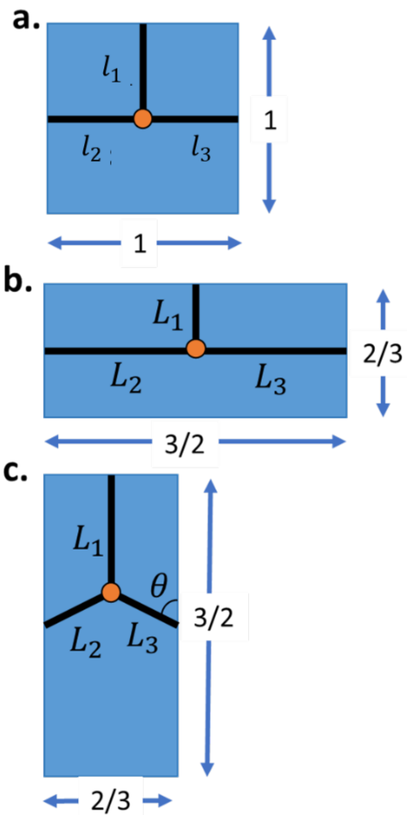

Figure 46 a.) *Undeformed network where* $l_1 = l_2 = l_3 = l = 1/2$*.* ***b.)*** *Network stretched in the direction of strongest alignment where* $L_2 = L_3 = 3/4$ *and* $L_1 = 1/3$*.* ***c.)*** *Network stretched transverse to the direction of stongest alignment where* $L_2 = L_3$*.*

compression) despite the fact that the HGO model using the structure tensor and calculating $\langle I_4 \rangle$ indicates the fibers should be in tension. This results in a fitted HGO fiber stiffness of ~0, which is clearly unphysical in general, but may be true for certain deformations. This effect is one that we must account for in our fitting method as discussed in Section 7.3.5 above.

6.4.3 Case Study: Single-Network Model Performance for Non-Fitted Deformation

A simple validation of the initial HGO fit and refit process is shown in **Figure 47**. The initial HGO fit of uniaxial, biaxial, and shear deformations produces stresses of a similar magnitude as the network simulation under the deformation given in Eq. A.9 (**Figure 47**a).

However, the results show large discrepancies in the shape of the curve (**Figure 47**a), which are largely corrected in the refit process (**Figure 47**b). The study presented indicates the viability of fitting an HGO model using the underlying orientation and a generated W^f vs. λ^f for many deformations to give a rough estimate of parameters, while highlighting importance of the refit process to producing the proper behavior. Further, this case study demonstrates how network mechanics vary significantly from the extrapolated HGO model under different deformations.

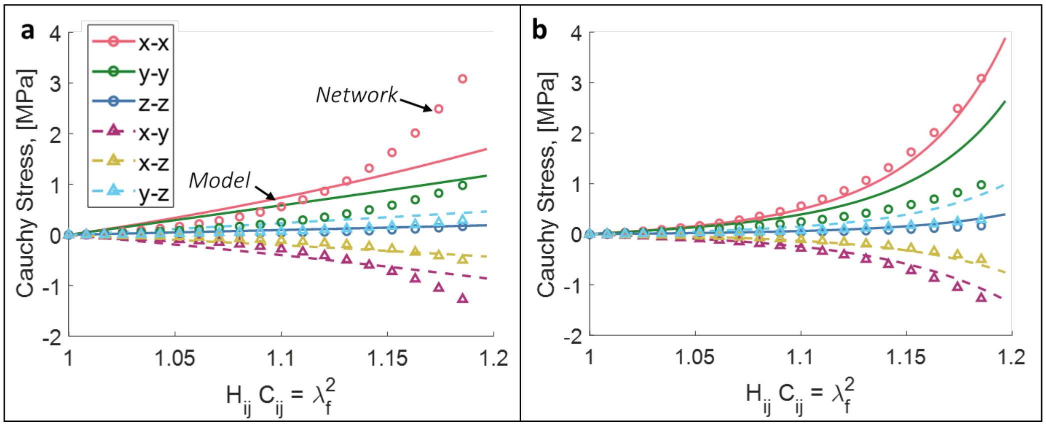

***Figure 47** Comparison between HGO model and network simulation under complex deformation for **a.)** initial fit and **b.)** refit*

6.4.4 Comparison to Full Multiscale Simulations

Maximum shear stress and strain fields are shown for the multiscale model, initial HGO model, and refit HGO model (**Figure 48**). The maximum shear stress and strain distribution of the HGO model compared to the multiscale model are visually similar, and the HGO model was able to predict the regions of high shear stress and strain. The initial HGO model parameters underpredicted the magnitude of the maximum shear stress and overpredicted the max shear strains in these regions, but the accuracy of the tissue's stress prediction improved with a refit of the HGO parameters with each element's average deformation gradient tensor. The refit HGO model more accurately localized regions of high tissue shear stress, at the cost of a small increase in the tissue's strain, when compared to the initial HGO model. This observation is supported by the improvement of RMS error of the refit HGO model maximum shear stress compared to

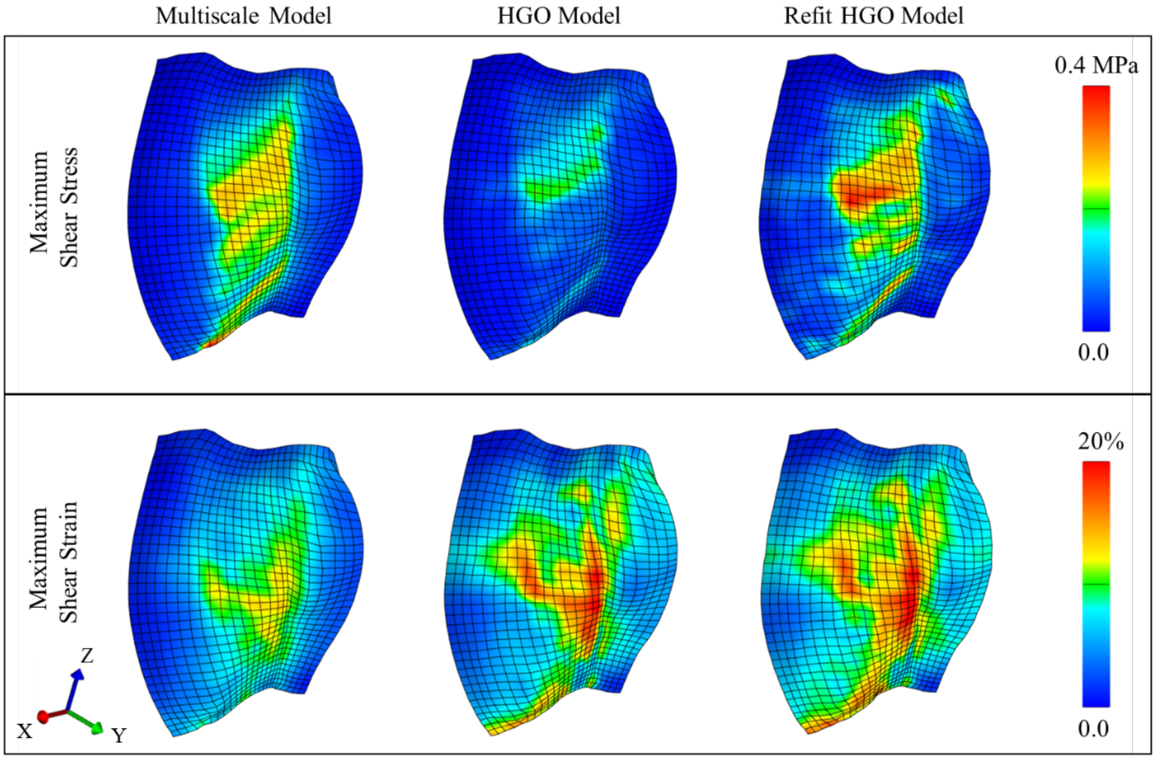

Figure 48 *Maximum Shear Stresses and Strains of the multiscale, HGO, and refit HGO models for a single representative FCL sample during spinal flexion. The HGO model predicted the location of high shear stresses and strains while the refit HGO model improved the accuracy of magnitude of the maximum shear stress*

the initial HGO model. The RMS errors for the initial HGO model maximum shear stress and strain are 0.074 MPa, and 3.28%, respectively. The RMS errors for the refit HGO model maximum shear stress and strain are 0.062 MPa, and 4.12%, respectively. Further, the computation time for the entire HGO simulation including the final step refit is shown in **Supplementary Table 2**. The time to run the HGO simulation is orders of magnitude decreased over the full multiscale simulation.

***Supplementary Table 2**: Computation Time for Multiscale vs HGO FE model*

	Multiscale	***HGO***
Task	*Time [CPU hour]*	
Initial Simulation and Fit of 900 Networks (x 5 deformations x 20 steps)	NA	1.12
Re-simulation and Refit of 900 Networks (x 1 deformation x 20 steps)	NA	0.34
FE Simulation	2622.69	0.02
Total	2622.69	1.48

6.5 Discussion

6.5.1 Major Findings and Potential Significance

In this work, we developed a hybrid microstructural-continuum multiscale model to reproduce the macroscopic constitutive behavior of a structure-based multiscale simulation. This paper presents methods to speed up the model construction and full analysis of a discrete-fiber multiscale model while accounting for the microstructural details of a heterogeneous tissue such as FCL. The proposed work uses the structural parameters of discrete fiber networks in a continuous-fiber model such as HGO to decrease the computational cost of a full multiscale simulation of a heterogeneous tissue from 2622.69 to 1.48 CPU-hours as is shown in **Supplementary Table 2**.

We found that the macroscopic-scale behavior of a Delaunay network can be reasonably described using the HGO model, but the accuracy of the approximation is dependent on the degree of alignment of the fiber network, the type of deformation imposed, and the magnitude of the deformation. The results of **Figure 44** and **Figure 45**c indicate that simulations within a certain family of deformation types (uniaxial, biaxial, shear) can be fit with a high degree of confidence. The results of **Figure 45**c and **Figure 47** suggest that extrapolating beyond the fitting range can give an overall rough estimate of behavior, but it is important to update the parameters based on the deformation. If the deformation of interest is known (e.g., one knows that the system will be loaded in equibiaxial extension), then one can simply fit a model to that deformation and use the model, but the deformation of interest is almost never known *a priori*. Even if the type of deformation or the boundary conditions are known, however, the magnitude of the deformation is often unknown, and tissue heterogeneity virtually assures that the local deformation is different from the applied (global) deformation, so it is essential to have a procedure that can be used to provide a good initial guess of the continuum model parameters one needs, as well as a method for updating the parameters. This work demonstrates reasonable methods for selection of initial parameters via fitting multiple deformations, and a refitting process based on the simulation deformation gradient.

In addition, we have described how stronger alignment of Delaunay networks results in more dissimilar behavior between deformations in terms of W^f vs. λ^f curves (**Figure 45**c). This result, while not unexpected based on previous studies [189], is significant because it further emphasizes the importance of the refit process and the challenges of trying to use an affine model to describe a material that exhibits non-affine behavior. The networks also showed increased nonlinearity and fiber modulus with alignment, which further indicates that inherent non-affinity alters the apparent mechanical response of the tissue. We further offered a simple verification of this result in the example in **Figure 46**, which further demonstrates the pitfalls in assuming affine behavior in the modeling of fibrous tissues. Particularly, one must be cautious when one starts to probe local phenomena such as cell-ECM interactions or tissue failure in affine continuous models.

Taken together, these results indicate that the HGO model itself does not fully capture the change in network behavior with the generalized structure tensor, H_{IJ}. One issue with this structure tensor is that, to properly capture the behavior of a dispersed fiber population with a tension-compression switch, one needs to recalculate the tensor using only the tensile fibers. In an ideal case, this would be done for each deformation step (alternative approaches are not given here, but are discussed in [186], [210]). Such an approach could help alleviate some of these differences observed in the current study, but the cost of performing a spherical integration over 3D distributions of fibers might well prove greater than that of the simple refit process, especially for multiple fiber families or multiple fiber types. Some network models, might be better fit, to a certain extent, by a compressed-fiber-excluding macroscopic model, and a more thorough testing regimen achievable via computational vs. experimental tests may provide more insight into exactly what behaviors are captured or lost by such models. Future in-depth studies of on the translation of a discrete, fiber-level tension-compression switch to a macroscopic fiber compression exclusion model are merited.

As discussed above, we do not account for the fiber tension-compression asymmetry in the calculation of H_{IJ}. That is, H_{IJ} is calculated based on all fibers in the initial state. We instead capture the fiber tension-compression switch through the fiber constitutive law, which is much stiffer in tension than in compression. The tension-compression switch of fibers is intrinsic to the microstructural model, so we remove the requirement for fiber exclusion from the structure tensor [159], [210]. The HGO parameters C2 and C3, which are fit to the results of the microstructural simulations, are thus informed by the tension-compression asymmetry inherent to the model. It may be possible that a better fit of the microstructural model could be obtained by an HGO model with a tension-compression switch, but that possibility was not explored in the current work.

We further described how a curve-fit of multiple simulations could allow one to select continuous model parameters to represent Delaunay networks with arbitrary orientation without rerunning simulations (**Figure 45**). The construction of such databases of properties for networks can further simplify the assessment of material parameters that describe network behavior. While the equations show a high degree of variance, construction of a broad curve-fit of parameter values can give us a reasonable starting point for a wide range of networks. The initial fitting of the network behavior to multiple deformations is the largest contribution to the overall time spent on simulation for the HGO FE model (**Supplementary Table 2**). Thus, if one can select starting parameters based on network orientation and some other metric of network construction like network type (Delaunay, Voronoi, etc.), one can greatly reduce the time to produce simulations. In fact, this method of reproducing network parameters from pre-defined relations rather than having to generate and run the networks could have a significant impact on creation and simulation of multiscale tissue models, allowing for many hypotheses to be tested quickly with regards to fiber orientations, tissue composition, or localized defects. If such a strategy is to be pursued, however, it is imperative that the starting parameter values be based on networks similar to the ones being used in the simulation.

We describe the application of the microstructural-to-HGO modelling strategy to a finite-element simulation. This simulation shows similar results to a full multiscale simulation (**Figure 48**) while reducing the model construction and simulation time by orders of magnitude over a full multiscale approach (**Supplementary Table 2**). As mentioned previously, this approach, combined with estimation of material parameters without generating and simulating networks, could enable multiscale simulations without the need for a supercomputing cluster. Eliminating the necessity of bridging micro- to mm-scale could also open up opportunities to take tissue multiscale approaches up another scale level to organ or full-body kinematics, further helping us identify things like the role local FCL defects play in the spine or elucidating the role of microstructure in aneurysm mechanics.

6.5.2 Model Limitations

As with all models, the proposed system has several limitations. First, because the HGO model is an imperfect estimator of actual network behavior, there will be intrinsic errors even after the proposed refitting procedure. One could perform this analysis with other constitutive models that may capture specific behavior differently as compared to the HGO model (take for example the Blatz-Ko material for compressible materials like collagen gels [215], or any of a number of actively contracting models for vascular tissues such as [216]–[218]). The proposed technique is adaptable to different constitutive models, and could be fit to multiple affine models to select the best choice.

As noted above, the HGO model did not fully capture the observed network behavior. We observe that a strength of our approach is that the computational experiments are not limited by the physical realities of equipment design and sample damage, so one can perform any experiment desired and as many experiments as desired. As a result, any inability of the continuum-scale model to capture the micro-scale network model's behavior will be apparent. Whether this effect is a positive or negative feature depends on the perspective of the user: it virtually guarantees inconsistency between the micro- and macro-scale models in some deformation, but it enables the user to see exactly where and how severe such inconsistency is, which could be valuable. For example, one could decide that the inaccuracy is in a range of deformations that are not physiologically relevant, or the inconsistency could inspire the development of new constitutive models at the continuum scale.

Another limitation of the approach in current form is the restriction to a single, non-evolving network. A major advantage of the full multiscale approach is the ability to accommodate changes in the network due to, e.g., failure [121], [207], [219] or remodeling [131], [132]. In the case of an evolving network, the macroscale parameters would necessarily have to be refit at each step. Knowing the deformation state at the previous step could allow for efficient re-fitting, but there is much work still to be done to identify the optimal strategy for such problems. Similarly, in particular in the case of the arterial wall, multicomponent models are important at both the microstructural [96], [121], [207] and macrostructural [220]–[223] scales, and the best strategy to fit a multicomponent, discrete-fiber microstructural model is by no means clear and has not been explored in this work.

Lastly, compressing the network in the direction in which most fibers are aligned might result in average of fiber stretch ($\hat{\lambda}_f$) less than one. In this case, some fibers are still stretched leading to a rise in the strain energy. The fitting procedure will be unable to capture these behaviors, and such artifacts will cause an increase in the stiffness of the model, since the slope of W^f vs. λ^f curve, i.e. stress, will be artificially increased as the fit attempts to match the network when average stretch becomes greater than one (i.e. W_f has been increasing from the network model since some fibers are in tension, but the overall average $\hat{\lambda}_f$ is still less than one, thus the fit must be stiffer than the network in order to minimize the distance between the curves). Conversely, as observed in the example given in **Figure 46**, it is also possible for the average fiber stretch $\hat{\lambda}_f$ to give a value greater than one, while the true average is less than one. This would indicate that the fibers themselves have a negligible effect on the behavior. While this might be true for a specific deformation, it is, in general, not an accurate representation of the material, and thus requires special care to be taken in the fitting process. These problems are mostly theoretical, since tissues are almost always loaded in the direction that their fibers are aligned, but it is nonetheless important to make sure there is a method for dealing with this issue in this framework. We offer one solution in this work, but it is by no means the only way to deal with this issue.

6.6 Conclusion

In this work, we have demonstrated a novel technique for simulating multiscale biological tissues. This work focuses on simple microstructures applied to complex finite element geometries, but this technique can be expanded for any microstructural model. The present method gives us flexibility to perform large-scale simulations while maintaining microstructural detail.

Appendix B: Supplementary Material - Chapter 2

The contents of this appendix were previously published as the supplemental material for the research article in the Journal of Biomechanics and Modeling in Mechanobiology by Gacek, Bermel, Ellingson, and Barocas. [12]

Supplementary Table 3: *Samples dimensions as measured for parallel and perpendicular orientations*

	Parallel Orientation			Perpendicular Orientation		
	Width (mm)	**Length (mm)**	**Thickness (mm)**	**Width (mm)**	**Length (mm)**	**Thickness (mm)**
Sample 1	9.99	9.43	1.58	9.43	9.99	1.58
Sample 2	8.73	12.93	1.35	12.93	8.73	1.35
Sample 3	9.31	12.4	1.99	12.40	9.31	1.99
Sample 4	12.64	16.06	1.53	16.06	12.64	1.53
Sample 5	9.07	17.77	1.68	17.77	9.07	1.68
Sample 6	8.74	16.99	2.17	16.99	8.74	2.17
Sample 7	9.27	16.82	1.93	16.82	9.27	1.93
Sample 8	9.19	15.24	2.06	15.24	9.19	2.06
Sample 9	7.63	14.35	1.88	14.35	7.63	1.88
Sample 10	8.02	13	1.74	9.59	8.02	1.74
Sample 11	9.99	8.94	1.29	14	12	1.29
Sample 12	7.43	10.34	1.16	10.34	7.43	1.16
Sample 13	11.51	12.62	1.79	12.62	11.21	1.79
Sample 14	9.65	12.10	1.75	12.10	9.65	1.75

Supplementary Table 4: *Each sample's optimized parameter values and 95% confidence intervals*

	E (MPa)	E 95% CI (MPa)	ξ (MPa)	ξ 95% CI (MPa)	β	β 95% CI	α	α 95% CI
Sample 1	0.019	[0.00077, 0.041]	19.43	[18.22, 20.52]	8.27	[8.20,8.35]	0.026	[Inf, Inf]
Sample 2	0.018	[0.014, 0.037]	5.84	[5.06, 6.60]	7.57	[7.37, 7.80]	0.0035	[Inf, Inf]
Sample 3	0.014	[0.011, 0.017]	64.00	[20.03, 23.42]	8.16	[7.40, 7.60]	0.049	[Inf, Inf]
Sample 4	0.024	[0.019, 0.029]	45.88	[39.05, 52.36]	10.0	[9.85, 10.20]	0.064	[Inf, Inf]
Sample 5	0.0042	[0.0037, 0.0065]	6.71	[5.06, 8.36]	9.72	[9.39, 10.14]	0.0026	[Inf, Inf]
Sample 6	0.019	[0.017, 0.021]	1.56	[1.43, 1.68]	9.60	[9.42, 9.82]	0.115	[Inf, Inf]
Sample 7	0.0065	[0.0042, 0.0071]	1.48	[1.27, 1.79]	6.37	[6.22, 6.66]	0.0045	[Inf, Inf]
Sample 8	0.0075	[0.0067, 0.021]	1.34	[0.77, 1.95]	7.58	[6.84, 8.46]	0.46	[Inf, Inf]
Sample 9	0.0084	[0.0076, 0.011]	9.84	[8.36, 11.22]	7.64	[7.45, 7.90]	0.031	[Inf, Inf]
Sample 10	0.0084	[0.0048, 0.038]	2.00	[1.67, 2.36]	5.07	[5.27, 5.37]	0.046	[Inf, Inf]
Sample 11	0.018	[0.013, 0.021]	19.92	[17.90, 21.94]	6.63	[6.53, 6.75]	0.076	[Inf, Inf]
Sample 12	0.012	[0.0098, 0.014]	5.48	[5.11, 5.83]	4.84	[4.78, 4.95]	0.036	[Inf, Inf]
Sample 13	0.013	[0.00050, 0.059]	59.36	[56.39, 62.33]	7.19	[7.15, 7.24]	0.12	[Inf, Inf]

Supplementary Table 5*: The starting inputs into the optimization routine for each sample*

	E (MPa)	**ξ (MPa)**	**β**	**α**
Sample 1	0.0193	23	6.5	0.03
Sample 2	0.0175	23	6.5	0.03
Sample 3	0.0139	64.06	8.15	0.048
Sample 4	0.0235	6.5	9.15	0.05
Sample 5	0.0042	3.6514	8.6462	0.003
Sample 6	0.0186	3.3	6.5	0.13
Sample 7	0.0065	1.5325	6.4169	0.1297
Sample 8	0.0235	1.4639	7.688	0.4359
Sample 9	0.008	9	8.7	0.03
Sample 10	0.008	2	5.07	0.046
Sample 11	0.0175	24.57	6.74	0.0765
Sample 12	0.012	2.9	4.8	0.105
Sample 13	0.012	23.5	5.737	0.05

Appendix C: Supplementary Material - Chapter 5

The contents of this appendix were previously published as the supplemental material for the research article published in the journal Acta Biomaterialia by Gacek, Mahutga, and Barocas. [19]

Model Verification Case Study:

Verification Methods:

To verify the simulation framework, we performed a suite of simple remodeling cases. We defined a simple eight-element cube macroscale geometry (**Figure S1**a). Each element of the cube is represented by an eight-fiber, one-node periodic network (similar to the Arruda-Boyce material model [151]) (**Figure S1**b). The network behavior was fit (**Figure S1**c) to the strain energy density function in Eq. 5.11 to define the materials for each element of **Figure S1**a. Test cases utilizing boundary conditions of free in all dimensions and fixed in all dimensions were used to validate the code and compare to the results of a single network remodeled under the same conditions.

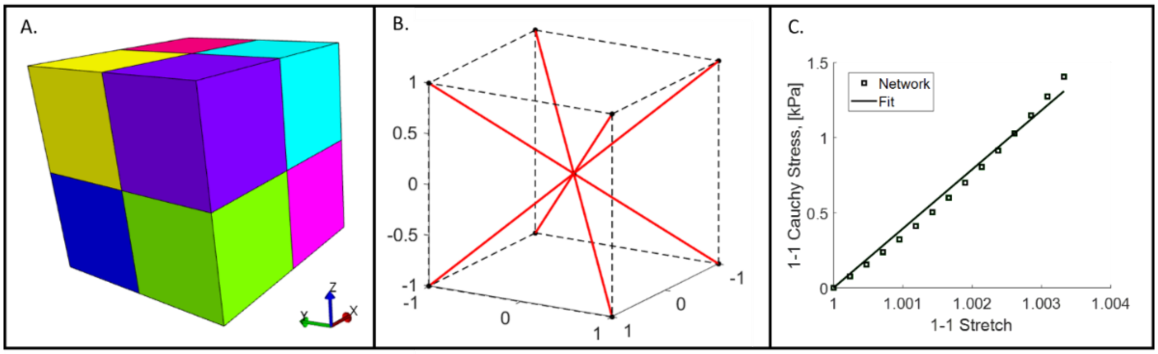

***Figure S1**:Verification problem setup showing **(a)** the FE Geometry, **(b)** the network structure, and **(c)** the fitted constitutive network behavior.*

Verification Results:

To verify the results of our simulation framework, we addressed two network remodeling methods one using deformation-control (i.e., fixing the deformation, then remodeling) and one using stress-control (i.e., deforming the network to match the stress, then remodeling). We consider boundary conditions of all faces fixed and all faces free.

With all faces fixed, we see very good agreement between the single network simulation, the deformation-control simulations, and the stress-control simulations (**Figure S2**).

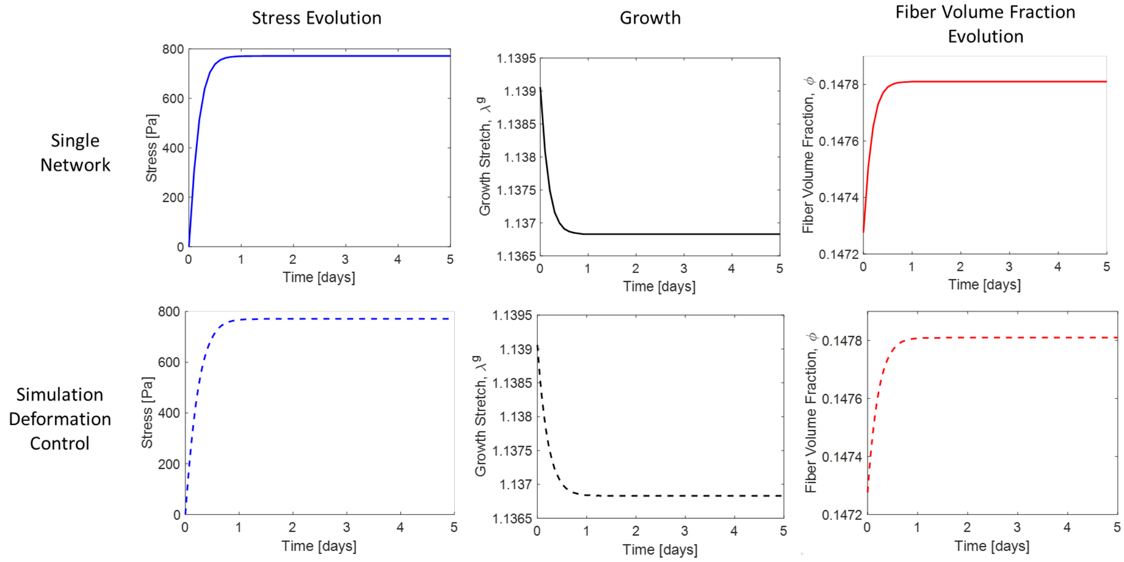

Figure S2: *Fixed boundary remodeling verification problem showing stress evolution (left column), growth (middle column), and fiber volume fraction evolution (right column) for a single microscale network (top row) and for the hybrid discrete-continuum method using deformation control (bottom row).*

In the first column, we show that the stress approaches the same target stress for all simulation types. In the stress-control simulation we do observe steps in the stress profile of the stress-control simulation (last row) due to the nature of the network deformation changing with remodeling as the stress is matched. In both growth (second column) and fiber volume evolution (third column), we show negligible differences between the various simulation types.

With all faces free, we show good agreement between the single network simulations and the deformation-control and stress-control simulations (**Figure S3**). In the stress evolution (first column), we see that the deformation-control simulation (second row) at each step begins at zero stress, but then ramps up. This is to be expected as the deformation is fixed so the network naturally tends to remodel to develop some level of stress. As time progresses the amount of stress developed in remodeling does decrease, indicating the simulation is closing in on a solution. The growth in the simulations (second column) also shows good agreement, with the deformation-control simulations (second row) showing slight differences in the remodeling profile. The fiber volume fraction profiles also show good agreement (third column), with the deformation-control simulations (second row), again, showing slight differences in the remodeling profile.

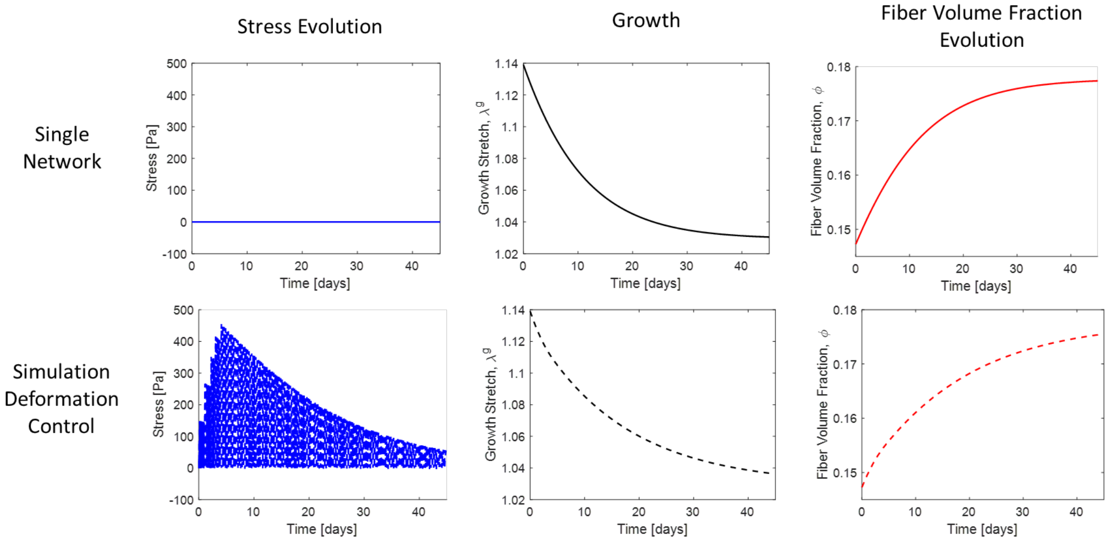

Figure S3: Zero-stress boundary remodeling verification problem showing stress evolution (left column), growth (middle column), and fiber volume fraction evolution (right column) for a single microscale network (top row) and for the hybrid discrete-continuum method using deformation control (bottom row).

Verification Discussion:

The verification problem sets demonstrate the ability to match single-network remodeling using the FE multiscale framework. We are able to show that two different methods (deformation-control and stress-control) can match the single network simulation provided we use small time steps. This is important because it illuminates the importance of selecting the time step duration between macro-scale FE simulations which is further discussed in the manuscript Discussion section under Model Verification and Convergence. These simulations serve as proof of concept that deformation applied to a network can recapitulate both deformation-control and stress-control boundary conditions on the macro-scale.

The Collagen Cruciform

Methods

A common in vitro system for studying collagen remodeling is created by placing fibroblasts in a reconstituted collagen gel [74], [224]. In this work, we simulate the remodeling of a collagen cruciform due to fibroblasts as given by [74], [131], [225]. The objective of this study was to demonstrate the microscale reorientation of collagen fibers related to the macroscale cruciform geometry while capturing the macroscale compaction of the cruciform itself. We investigate three cases of different vertical to transverse arm width ratios 1:1, 1:0.5, and 1:0.375 as in [224]. The behavior of each element was prescribed as a prestrain elastic material having the strain energy function given in Eq. 5.11 above. The microscale network was prescribed as an Arruda-Boyce-like network of collagen fibers with fiber behavior given in **Table 4**. This was done to simulate the lower fiber connectivity seen in in vitro collagen gels. The network had a collagen volume fraction of 2mg/mL initially. The collagen fibers in the gel were remodeled subject to the growth law of Eq. 5.10, with remodeling parameters given in **Table 5**. In this simulation, fibroblasts were considered as passive elements only responsible for remodeling collagen fibers. This case study demonstrated the use of the multiscale framework to assess microscopic features in different locations of a heterogeneous system.

Results

A simple and controlled way to investigate the role of mechanical forces on tissue remodeling is the collagen gel cruciform. We simulated remodeling of the collagen cruciform using our multiscale framework (**Figure S4**a) consistent with the experiments and models of [74], [131], [224], [225]. The cruciform showed significant compaction based on decreases in relative volume (Fig. S4a) during the remodeling process. In the microstructure, the collagen alignment tended to follow the contour of the cruciform (**Figure S4**b) and the strength of alignment followed the arms of the cruciform (**Figure S4**c). We simulated the experiments of [224] utilizing different arm size ratios, and showed an increased strength of alignment within the center region with decrease in transverse arm size (**Figure S4**c). Further, the simulations showed regions of low alignment just off the cruciform centerline toward the smaller arms consistent with [224]. The simulation also allowed us to visualize the residual strain field over the cruciform (**Figure S4**d) arising from the remodeling process. The residual strain concentrates in the arms, with higher magnitudes of strain in smaller arms.

Discussion

The basic behavior of the collagen gel cruciform model causes the gel to compact and to stiffen as the fiber content increases [226], [227]. The increased compaction in the model (**Figure S4**a) is consistent with the observations of [228]. We also observed different orientations in different regions of the gel (Fig. S4b), which is consistent with what has been shown previously [131], [224], [225], [229]. When we altered the gel initial arm thicknesses, we also showed increased alignment in the center region, away from the transverse arms consistent with the experimental observations of [224]. Further, the model also captures the shift of the low alignment regions in the center of the sample toward the transverse arms as width of the arms were decreased (**Figure S4**c) as also shown in [224]. We showed a heterogeneous residual strain distribution through the cruciform arising from the remodeling due to heterogeneity of the macrostructure based on arm width differences (**Figure S4**d). Our model is capable of capturing many of the phenomena observed in collagen-fibroblast tissue equivalents while allowing direct observation of the collagen network underlying the macrostructure (e.g. fiber orientations shown in **Figure S4**c). The microstructural detail allows us to view microscale heterogeneities and local initiation of growth and remodeling within the structure.

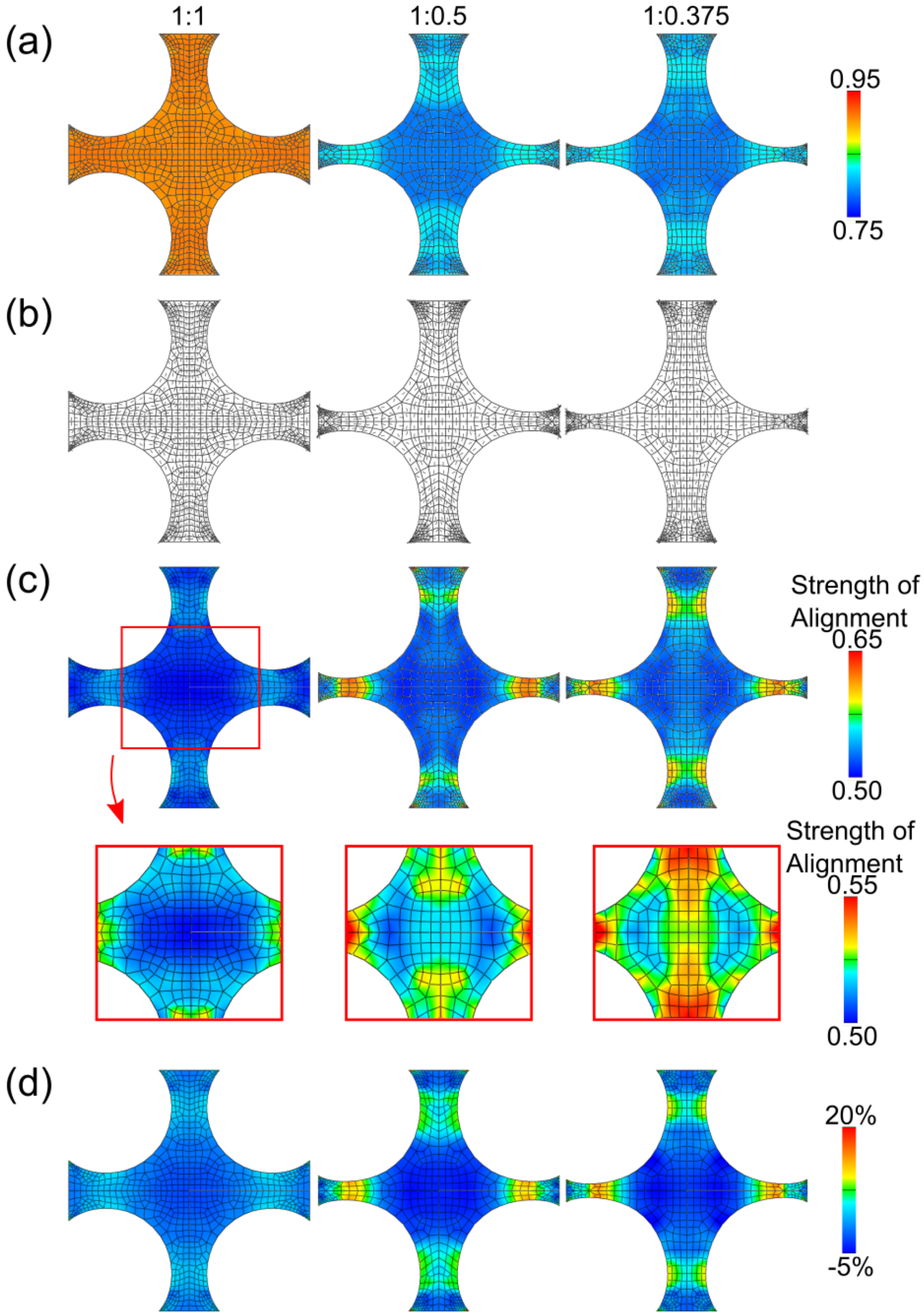

Figure S4:*Collagen alignment in* ***(a)*** *cruciform, shown with relative volume changes, with arm width ratio of 1:1, 1:0.5, 1:0.375.* ***(b)*** *Primary direction and* ***(c)*** *strength of aligment are shown, with the center region of each cruciform enlarged to show detail.* ***(d)*** *The first principal strain for each cruciform at the end of remodeling.*

Thick-Walled Cylinder:

Model Validation:

Time Series Convergence Methods:

For analysis of convergence behavior, we used the multi-constituent cylinder model given in **Figure 34**b. The time series convergence was performed as outline in the manuscript discussion following the micro and macro times steps given in **Table 6**. Micro times steps are denoted ‘dt’ while macro time steps are denoted ‘DT’.

Time Series Convergence Results:

The effect of micro time-step length (dt) while holding the macro time step constant (DT=1.0 days) is shown in **Figure S5**. The results of all 6 independent components of growth are given as the rows in the figure, while the columns show the difference between the innermost medial element and the outermost medial element. The effect of macro time-step length (DT) while holding the micro time-step constant (dt=0.05 days) is given in **Figure S6**. Results are displayed in the same way as **Figure S5**.

Time Series Convergence Discussion:

Based on the data of **Figure S5** and **Figure S6**, we see that the micro time-step length seems to have little effect on the remodeling behavior, while the macro time-step length can significantly affect both the trajectory of remodeling and the end-state of the simulation. The implications of this study are that special attention should be given to the choice of macro time-step length. It is imperative that when the model parameters or the remodeling equation itself is altered, one performs a similar convergence analysis to avoid propagation of large errors. Further, one must also be careful when remodeling with abruptly changing boundary conditions (e.g. applying ‘instantaneous’ hypertension to an artery) as this event can induce large errors in remodeling if we do not properly adjust our macro time-step length. In this work, we mitigate potential inaccuracies by locally shortening the time step duration following the application of hypertension to minimize forward propagated error.

Micro Time Step Convergence

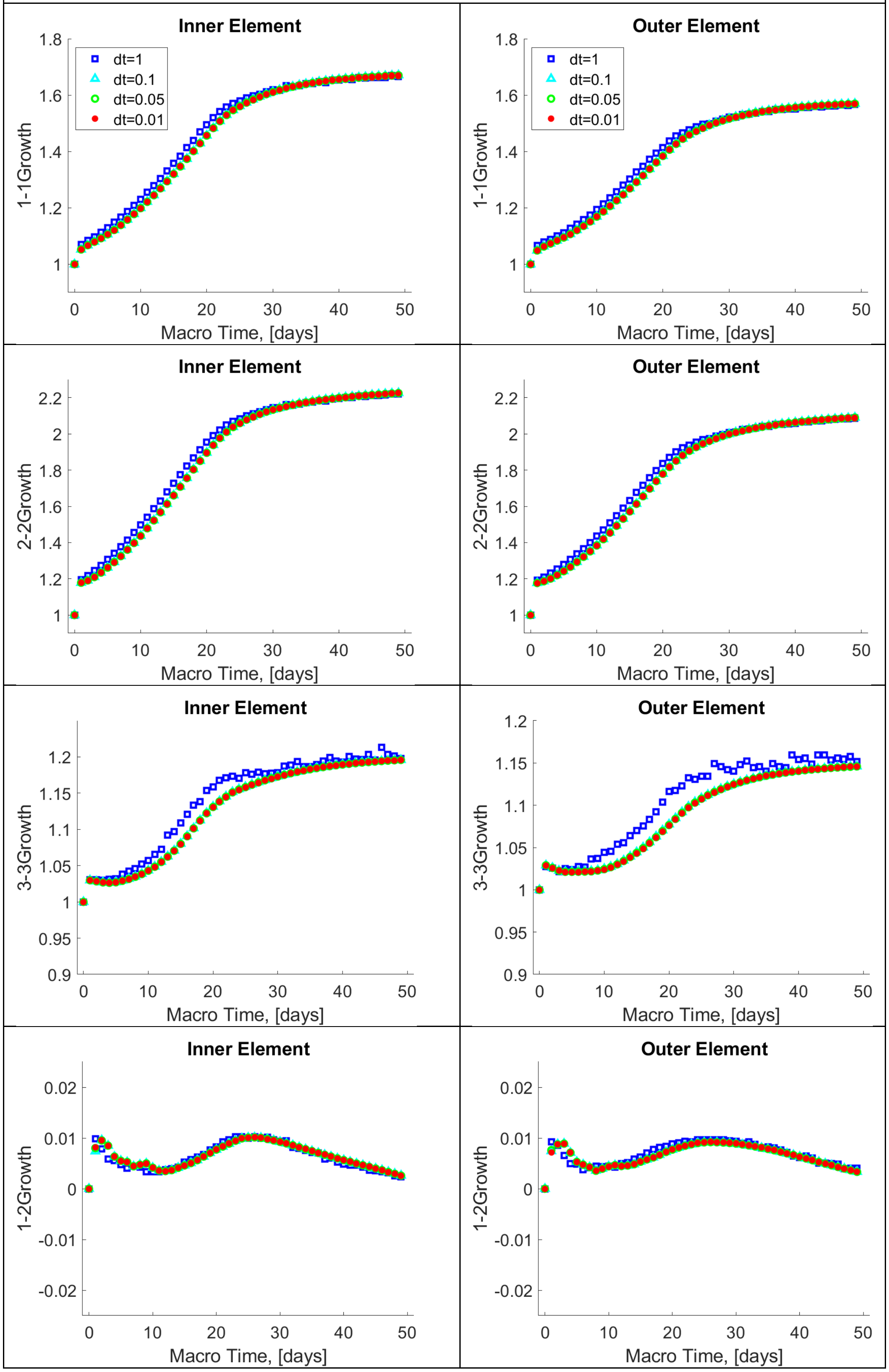

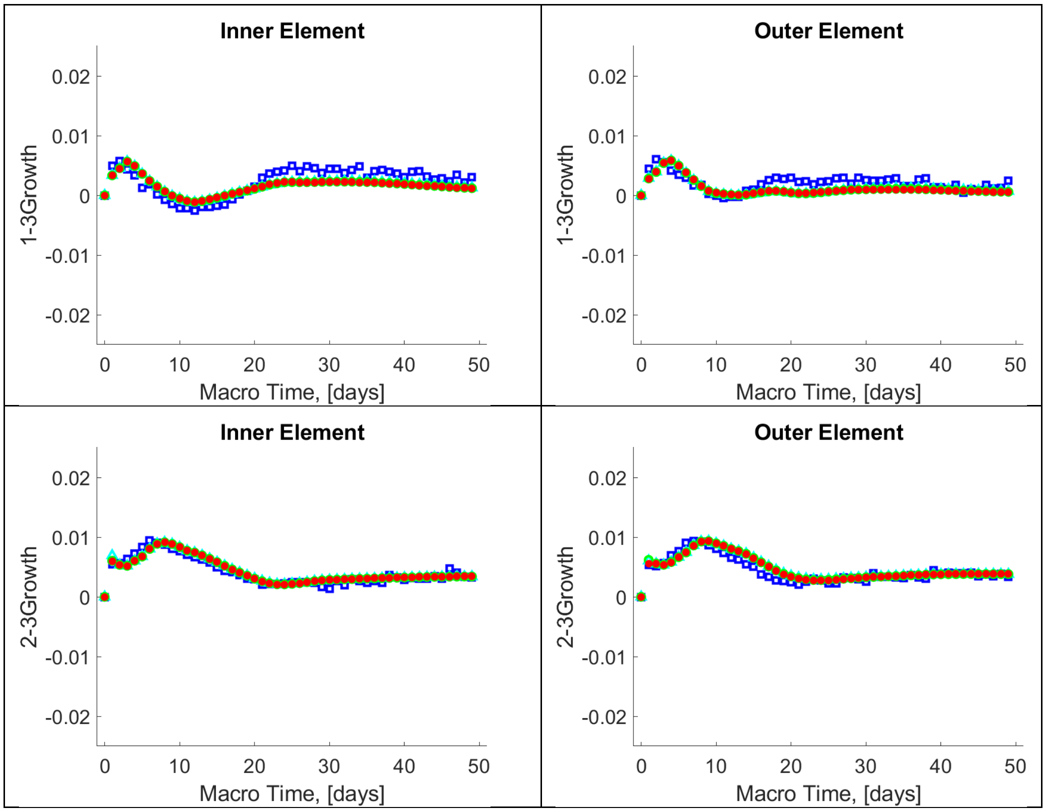

Figure S5*: Micro-scale convergence analysis holding the macro-scale time step constant at DT=1.0.*

Macro Time Step Convergence

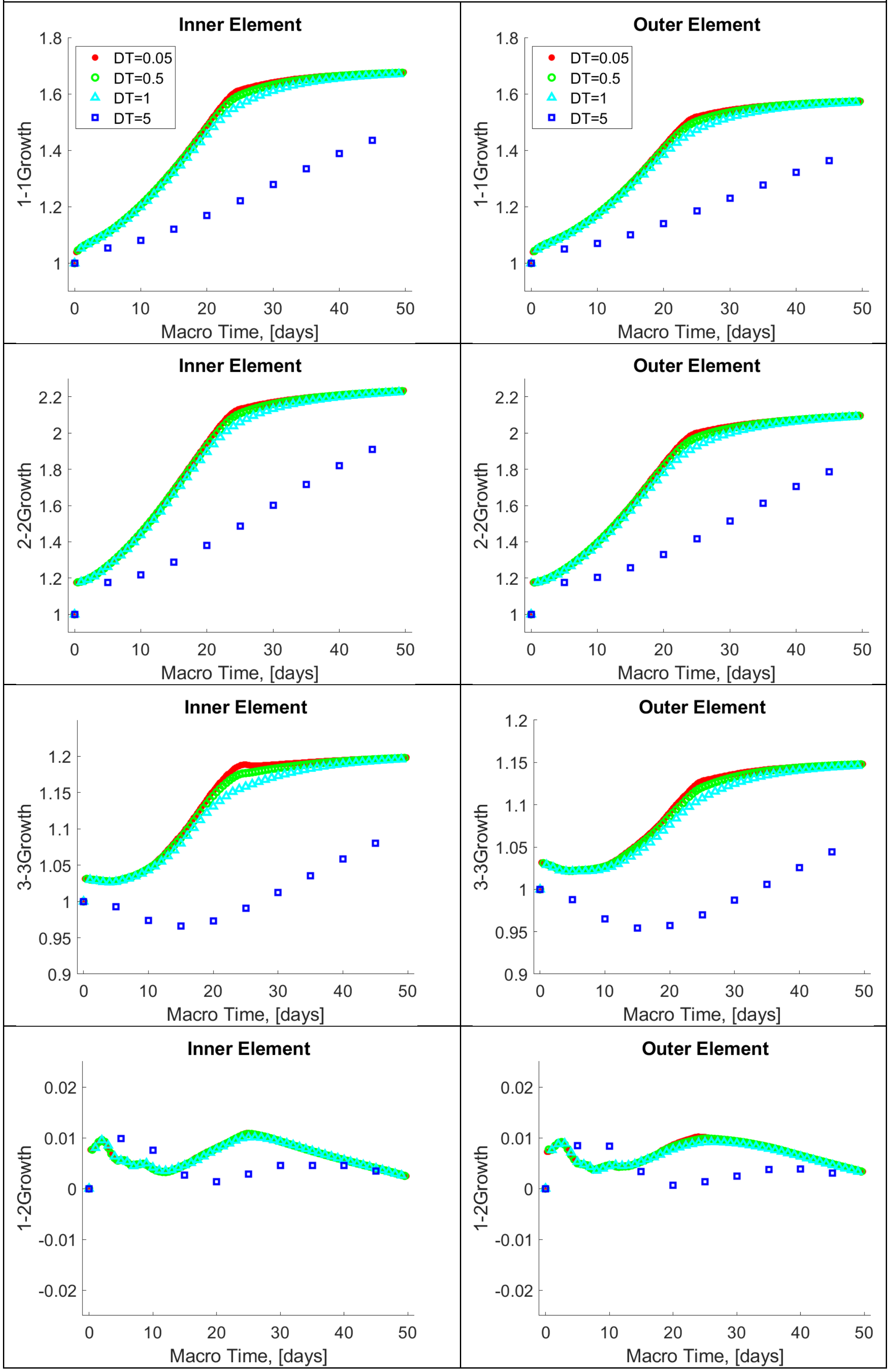

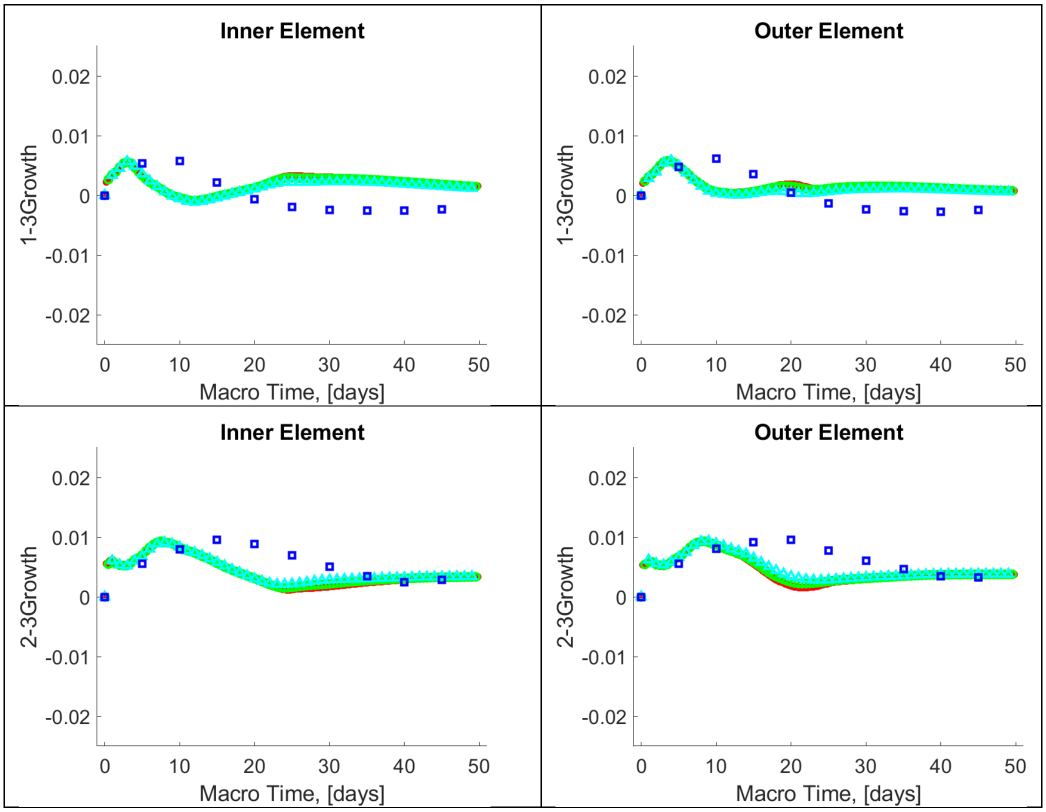

Figure S6: *Macro-scale convergence analysis holding the macro-scale time step constant at dt=0.05.*

Under Hypertension:

***Results**:*

The growth of the inner medial (**Figure S7**a) and outer medial (**Figure S7**d) elements showed relatively small differences. The elastic stretch in the cylinder in **Figure S7**b and **Figure S7**e showed large stretches in the circumferential direction and compression in the radial direction. Further, we saw an instantaneous spike in elastic stretch in the circumferential direction as well as a spike in radial compression in response to hypertension, which is recovered through the remodeling process. We saw relatively small differences in the cell and fiber content in the inner element (**Figure S7**c) and the outer element (**Figure S7**f).

***Discussion**:*

Because the elastic stretch is recovered after hypertension (**Figure S7**b and e), we conclude the tissue stiffens since it deforms less under an increased load compared to the homeostatic, normotensive case. Further, we saw the radial compression also decreased in response to hypertension. This also demonstrates tissue stiffening in response to hypertension.

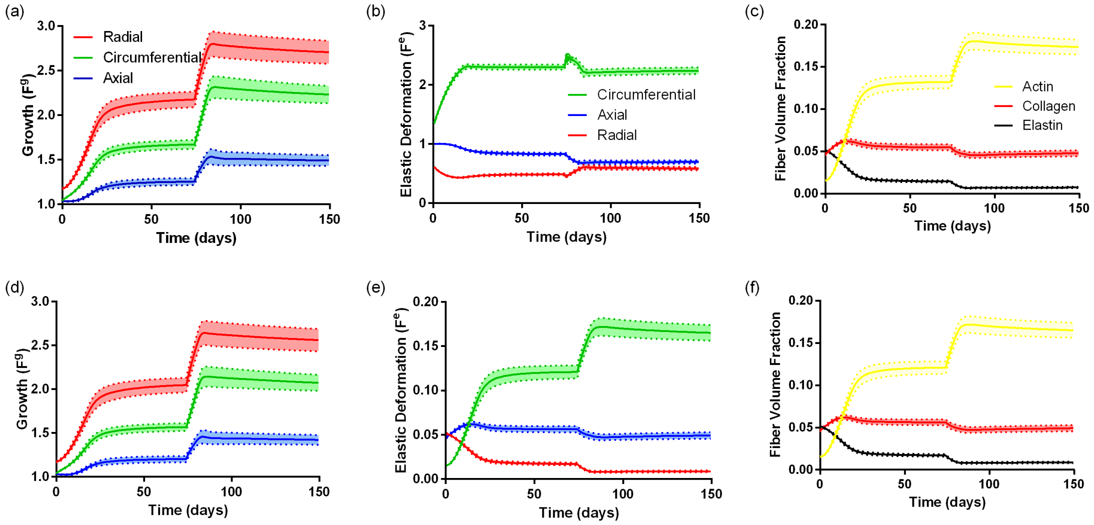

Figure S7:*Normal remodeling and response to 50% increase in mean arterial pressure.* ***(a)*** *Growth in the innermost element,* ***(b)*** *Elastic stretch in the innermost element,* ***(c)*** *fiber volume fraction evolution in the innermost element,* ***(d)*** *growth in the outermost elements,* ***(e)*** *elastic stretch in the outermost element,* ***(f)*** *fiber volume fraction in the outermost element. Data is shown as mean +/- 95% CI (n=10).*

Under Hypotension:

Motivation:

Hypotension is a reduction in blood pressure below normal levels. Hypotension is a relatively uncommon chronic condition, typically only linked to aortic valve insufficiency and aortic coarctation, although it is commonly reported in pregnancy around mid-gestation [230]. The case studied here is an extreme exaggeration of hypotension (50% drop) compared to the modest drops seen in mid-gestation (~5-10% drop), but parallels closely to coarctation induced hypotension in cynomolgus monkeys given in [231].

Methods:

The methods followed in this study are identical to those outlined for the thick-walled media-only cylinder given in the manuscript. In the case of hypotension, we induce a 50% drop in mean arterial pressure and measure the morphometric and compositional changes induced.

Results:

The stress evolution for hypotension is given for the innermost element (**Figure S8**a) and the outermost element (**Figure S8**d). We see from these results that the remodeling process is much slower to re-equilibrate. In the data for the elastic deformation (**Figure S8**b and e), we see an instantaneous drop in circumferential stretch and an instantaneous increase in radial stretch. This is a mirror image to the hypertension case. The constituent volume fraction evolution is given in **Figure S8**c and f for the inner and outer elements respectively.

Discussion:

After hypotension initiation (**Figure S8**b and e), the circumferential elastic stretch shows a slight increase indicating stiffening relative to the homeostatic state. When pressure is decreased the tissue shrinks radially and circumferentially, becomes slightly stiffer circumferentially and becomes slightly more compliant radially to prevent collapse or buckling of the wall under very small pressures. In our simulations of hypotension, we see that the cellular network remodels to decrease actin content. This could be a metabolically favorable effect as the lower pressure likely means lower flow and thus less opportunity for transport through the wall which balances with a decrease in metabolic demand by decreasing cellularity. The elastin volume fraction increases, which indicates the tissue decreases in overall volume. We would anticipate that the net result of this remodeling is that load is shifted from collagen and actin onto the elastin. The increase in elastin content and the decrease in cellularity parallel the coarctation-induced hypotension results given in [231].

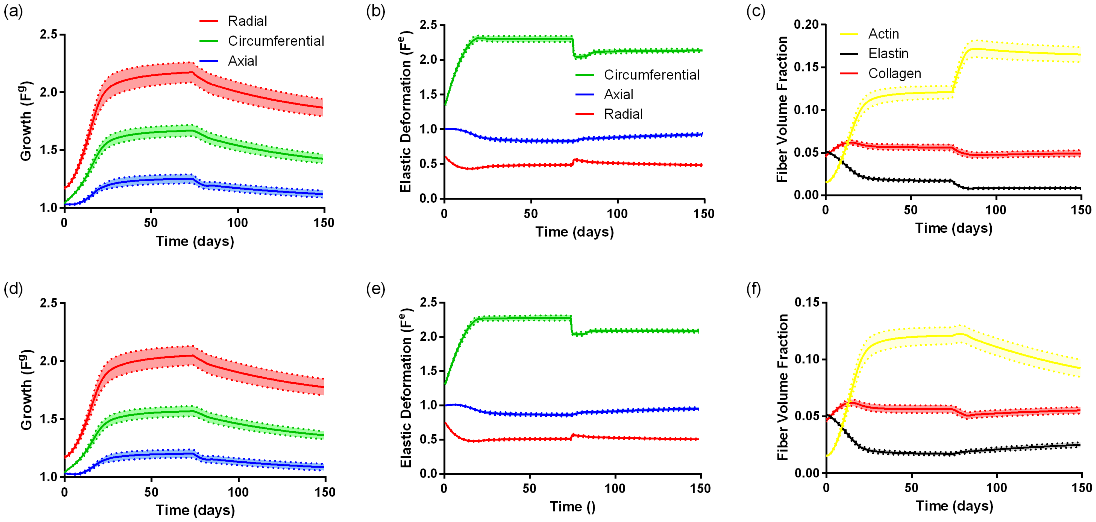

Figure S8*: Normal remodeling and response to 50% decrease in mean arterial pressure.* ***(a)*** *Growth in the innermost element,* ***(b)*** *Elastic stretch in the innermost element,* ***(c)*** *fiber volume fraction evolution in the innermost element,* ***(d)*** *growth in the outermost elements,* ***(e)*** *elastic stretch in the outermost element,* ***(f)*** *fiber volume fraction in the outermost element. Data is shown as mean +/- 95% CI (n=10).*

Effect of the Adventitia on Individual Fiber Properties:

***Results**:*

During the remodeling process fibers both lengthen and thicken according to the remodeling law given in Eq. 5.12. In the thick-walled cylinder, we have three primary fiber types: cellular stress fibers (actin), collagen ECM fibers, and elastin ECM fibers. The cellular stress fiber bundles start out at 80nm in radius and the collagen fiber bundles start at 260nm radius. The elastin fibers do not remodel, and stay at 120nm in radius. The changes in actin fibers are given in **Figure S9**. The top two rows show the actin fiber radius changes for the innermost and outermost medial elements with and without an adventitial layer. The third and fourth rows show the changes in actin fiber length for the inner and outer medial layers. The left column is under normotensive conditions and the right column is under hypertensive conditions. The changes in collagen fibers are given in **Figure S10**. The figure setup is the same as **Figure S9**, except we include fiber data the adventitial layer given in yellow.

***Discussion**:*

In **Figure S9**, we see that the actin fiber bundles tend to remodel to form a skew normal distribution from the initial state. We also see that the innermost element tends to have longer and thicker fibers than the outermost element due to its higher stress state. We see a significant shielding effect of the adventitia on the actin fibers demonstrated by a leftward shift of both the actin fiber radii and the actin fiber lengths in the media+adventitia case vs. the media only case. In **Figure S10**, we see that the collagen fibers tend to have a more normal, less skewed distribution in radii, but a similar skewed distribution in lengths. We again see the shielding effect of the adventitia on the medial layers noted by the distribution leftward shift in the media+adventitia case relative to the media only case. We further see that the adventitial fibers (given in yellow), show a similar mean radius to those of the media.

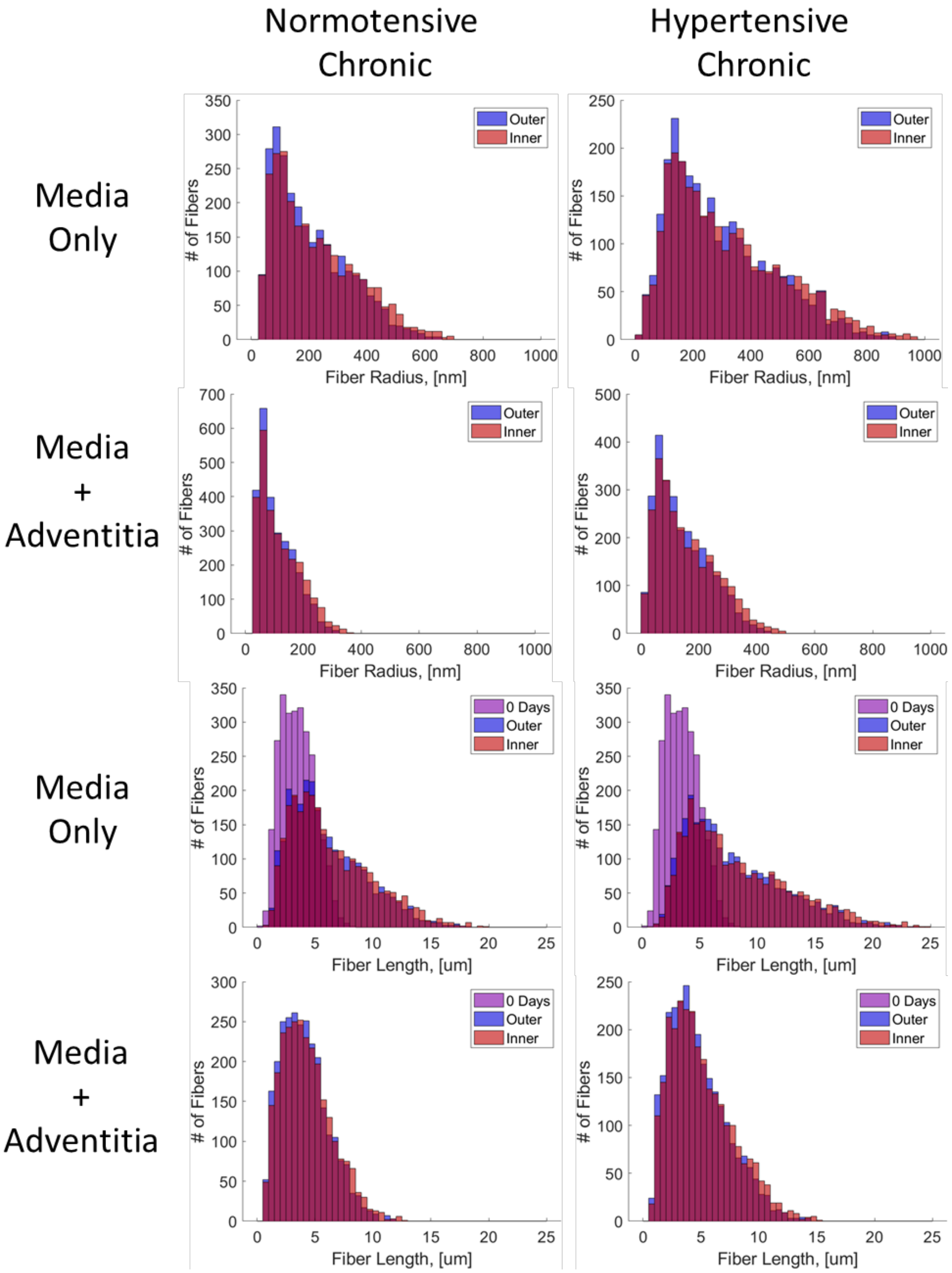

Figure S9: Actin fiber radii and lengths for media and media + adventitia in normotension and hypertension.

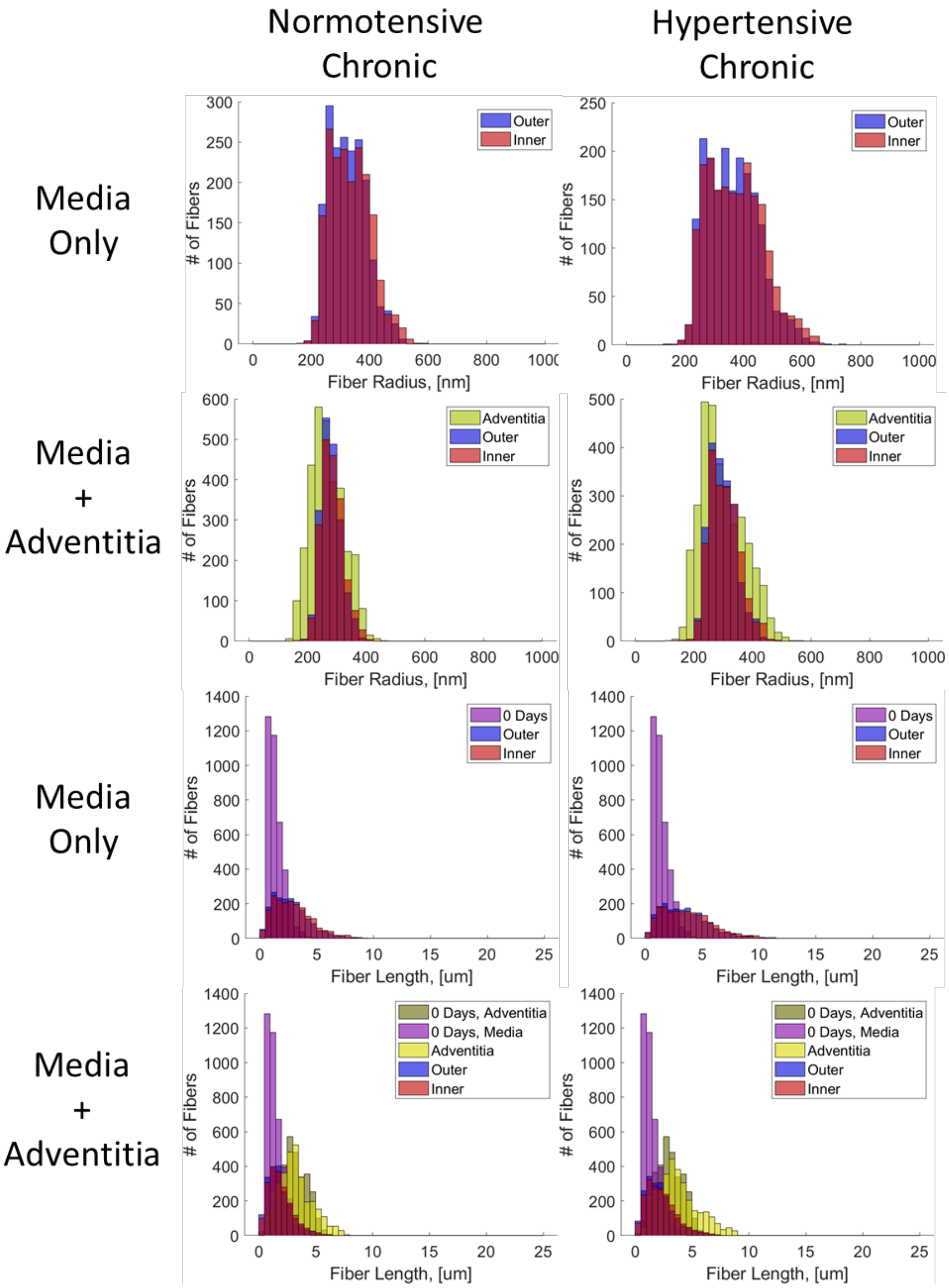

Figure S10 Collagen fiber radii and lengths for media and media + adventitia in normotension and hypertension.

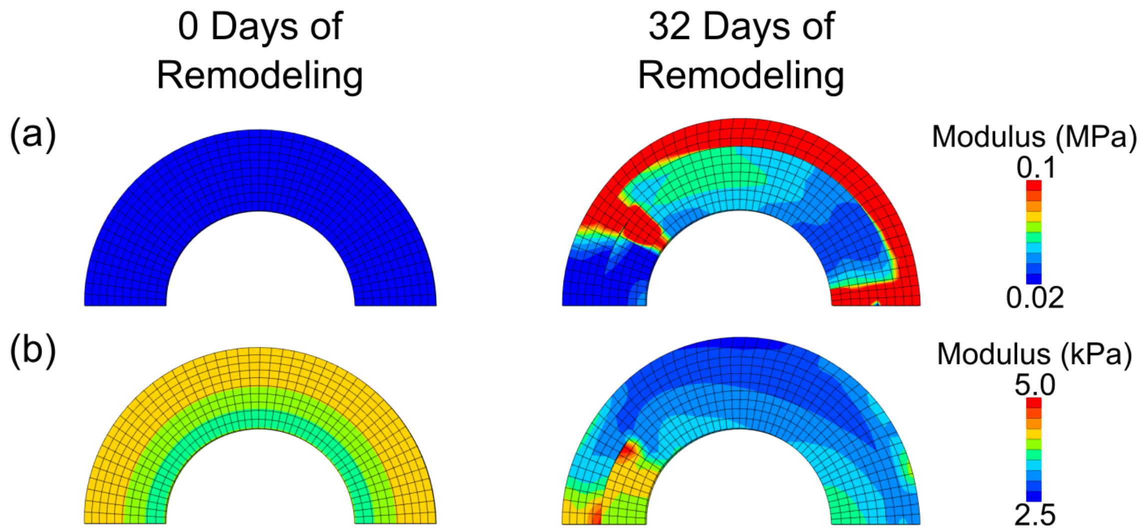

Figure S11: a) Circumferential and b) axial fiber modulus (C_2 in Eq. 5.11) in the normal (0 days of remodeling) and dissected (32 days of remodeling) cylinder